Dual-Purpose Canister Filling Demonstration Project Progress Report

Spent Fuel and Waste Disposition

Prepared for
US Department of Energy
Spent Fuel and Waste Science and Technology

Bret D. Brickner, Jennifer Meszaros, Venugopal K. Varma, Emilian Popov, Eliott J. Fountain, Adrian S. Sabau, Fayaz Rasheed, Kaushik Banerjee Nesrin O. Cetiner, Elvis Dominguez-Ontiveros
Oak Ridge National Laboratory

September 24, 2021
M3SF-21OR010305019
ORNL/SPR-2021/2223

This is a technical report that does not take into account contractual limitations or obligations under the Standard Contract for Disposal of Spent Nuclear Fuel and/or High-Level Radioactive Waste (Standard Contract) (10 CFR Part 961). For example, under the provisions of the Standard Contract, spent nuclear fuel in multi-assembly canisters is not an acceptable waste form, absent a mutually agreed to contract amendment.

To the extent discussions or recommendations in this report conflict with the provisions of the Standard Contract, the Standard Contract governs the obligations of the parties, and this report in no manner supersedes, overrides, or amends the Standard Contract.

This report reflects technical work which could support future decision making by DOE. No inferences should be drawn from this report regarding future actions by DOE, which are limited both by the terms of the Standard Contract and a lack of Congressional appropriations for the Department to fulfill its obligations under the Nuclear Waste Policy Act including licensing and construction of a spent nuclear fuel repository.

ABSTRACT

This report discusses the progress made at the Oak Ridge National Laboratory to support direct disposal of dual-purpose canisters (DPCs). Acceptable filler materials should demonstrate that the probability of criticality in DPCs during the disposal timeframe is below the probability threshold for inclusion in a repository performance assessment. This effort, which will ultimately result in a full-scale demonstration, includes computational fluid dynamics (CFD) modelling developed to gauge the filling process and to uncover any unforeseen issues. Filling simulations of the lower region (mouse holes) of a prototypic DPC show successfully simulate filling of the void space inside the canister and a smooth, even progression of the liquid level. Flow through a pipe that is similar to the drainpipe in a DPC is being investigated separately to gain valuable insight of the flow regime inside a pipe. Three physical experiments validating the computational filling model have been completed using surrogate liquids. One experiment using molten metal has been completed and the results demonstrate adequate filling of the canister void spaces. Although the scale experiment observed some void spaces related to shrinkage of the metal during cooling, the volume filled is expected to be sufficient to meet the purpose of moderator exclusion. Further experiments will scale up the geometry, moving towards a full-sized DPC demonstration, and provide a more rigorous investigation of candidate filler materials.

This page is intentionally left blank.

CONTENTS

LIST OF FIGURES

This page is intentionally left blank.

LIST OF TABLES

This page is intentionally left blank.

REVISION HISTORY

Revision	Changes Made
0 (2018)	Initial issue
1 (2019)	This revision incudes a description of a flow experiment through a pipe that is similar to the drainpipe in a DPC. This experiment will be used to gain insight into the flow regime inside a narrow, long pipe. All updates are identified by black vertical lines in the margin.
2 (2019)	Minor editorial changes throughout the document. All updates are identified by black vertical lines in the margin. This revision includes Appendix A, which reports on progress in the CFD filling simulations and initial physical testing efforts supporting simulation validation.
3 (2019)	Appendix B is added in this revision. Appendix B presents (1) the updated validation results of the CFD filling simulation using water and glycerin as surrogate filler materials, (2) paraffin wax experiment for gaining insight into the phase change effects and the formation of voids in complicated geometries (e.g., grid spacers), (3) Computerized Tomography (CT) of the solidified paraffin wax that can be used to determine void fraction after solidification, (4) preliminary simulation to evaluate DPC preheating/preconditioning by blowing hot gas (needed for uninterrupted filling of DPCs using metallic or cementitious fillers), and (5) updates of the series of pipe experiments that are being planned/executed to determine the feasibility of filling a DPC using the existing drainpipe.
4 (2020)	Appendix C is added in this revision. Appendix C presents (1) findings about the paraffin wax experiment conducted to gain insight into the phase change effects and the formation of voids in complicated geometries (e.g., grid spacers), (2) a CT analysis of the solidified paraffin wax that can be used to determine void fraction after solidification (3) results of the casting simulation, (4) preparations of first casting experiment, (5) benchmarking experiment to verify CFD results, (6) updates of the series of pipe experiments being planned/executed to determine the feasibility of filling a DPC using the existing drainpipe, and (7) results of preliminary simulations to evaluate DPC

	preheating/preconditioning (needed for uninterrupted filling of DPCs using metallic or cementitious fillers).
5 (2021)	Revision of the main document to reflect the status and results of the work. Appendix D is added in this revision. Appendix D presents (1) demonstration of the feasibility of molten metal fillers to completely fill the spent fuel areas inside the DPCs, (2) metal casting simulations using ProCAST software, (3) fabrication of the DPC fill pipe flow experiment, (4) modeling the filling of the DPC with water and validating the flow model with experimental results, (5) and acquisition of a full-scale DPC for future studies.

ACRONYMS

BWR	boiling water reactor
CCI	confocal chromatic imaging
CFD	computational fluid dynamics
CFL	Courant–Friedrichs–Lewy
CSFS	COBRA Spent Fuel Storage
DOE	US Department of Energy
DOE-NE	US Department of Energy Office of Nuclear Energy
DPC	dual-purpose canister
FCRD	Fuel Cycle Research and Development
FPB	fill-pipe bottom
FY	fiscal year
HRIC	high-resolution interface-capturing
IFM	intermediate flow mixer
LDV	laser Doppler velocimetry
MH	mouse hole
NRC	US Nuclear Regulatory Commission
ORNL	Oak Ridge National Laboratory
PDT	photochromic dye tracing
PIL	python image library
PIV	particle image velocimetry
PWR	pressurized water reactor
RTV	room temperature vulcanizing
SFP	spent fuel pool
SNF	spent nuclear fuel
SNS-TTF	Spallation Neutron Source - Target Test Facility
UNF-ST&DARDS	Used Nuclear Fuel – Storage, Transportation & Disposal Analysis Resource and Data Systems
VOF	volume of fluid

This page is intentionally left blank.

DUAL-PURPOSE CANISTER FILLING DEMONSTRATION PROJECT PROGRESS REPORT

1. INTRODUCTION

This report documents work performed supporting the US Department of Energy (DOE) Nuclear Energy Spent Fuel and Waste Disposition, Spent Fuel and Waste Science and Technology, under work breakdown structure element 1.08.01.03.05, "Direct Disposal of Dual Purpose Canisters." In particular, this report fulfills M3 milestone, M3SF-21OR010305019, "DPC filler simulation and demonstration progress report," as Revision 4 to M3SF-20OR010305017, "DPC filler simulation and demonstration progress report," within work package SF-19OR01030501, "Direct Disposal of Dual Purpose Canisters–ORNL." Appendix D is added in this revision.

The commercial US nuclear utilities are currently storing spent nuclear fuel (SNF) onsite in spent fuel pools (SFPs) and dry storage systems. SFPs were initially constructed for temporary storage, but without SNF reprocessing options in the United States and with no final disposal pathway, SFPs started to reach capacity limits. Hence, to allow continued operation of the nation's commercial nuclear fleet, utilities started transferring SNF from SFPs (wet storage) to dry storage. As of June 4, 2018, there were 2,802 dry storage systems in use in the United States containing 117,737 spent fuel assemblies [1]. The majority of the dry storage systems currently being loaded are dual-purpose (storage and transportation) canister (DPCs). DPCs can accommodate up to 37 pressurized water reactor (PWR) assemblies and 89 boiling water reactor (BWR) assemblies, and they are designed primarily for storage and transportation. The DOE Office of Nuclear Energy (NE) is currently investigating the feasibility of direct disposal of DPCs in a geological repository to potentially offset the need to repackage currently loaded SNF into smaller disposal canisters. DPC direct disposal has many potential benefits, including cost savings in terms of billions of dollars, minimization of worker dose incurred from repackaging activities, and reduction of low-level radioactive waste in the form of discarded DPCs [2]. Although it has been indicated [2] that direct disposal of DPCs is feasible from a purely technical perspective, several engineering challenges, along with legal and policy issues, must be addressed to make DPC disposal a reality. One challenge is the potential for post-closure criticality in a repository time frame.

As-loaded criticality analyses of the currently loaded DPCs are being performed using the Used Nuclear Fuel-Storage, Transportation & Disposal Analysis Resource and Data System (UNF-ST&DARDS) [3] to evaluate uncredited margins that can be used to offset an increase in canister reactivity (calculated in terms of neutron multiplication factor, k_{eff}) due to various postulated degradation mechanisms in a repository time frame. Based on current modeling approaches [3], it has been shown that many of the loaded canisters have the potential to achieve criticality under the right conditions over a repository time frame (i.e., 10,000 years or longer) (Figure 1).

As shown in Figure 2, three approaches are under investigation to support post-closure criticality of DPCs in a repository time frame. The first approach is to perform detailed modeling and analysis of each loaded DPC; this effort is underway using UNF-ST&DARDS (Figure 1) with analysis documented in [16]. The second approach includes on-going work for a criticality consequence analysis to determine the impact of a potential criticality event on a repository performance assessment [17, 18, 19]. The third approach, which is the topic of this report, is to investigate potential preconditioning of DPCs with filler materials that can be credited over a repository time frame to displace the moderator material and thus prevent canister criticality. This report presents the progress made at Oak Ridge National laboratory (ORNL) to investigate adding a filler material to existing DPCs before placing them into a repository. Currently, two classes of filler materials are under consideration: cementitious materials and low-temperature melting metals/alloys.

The work presented in this report focuses on initial evaluation of a potential filling option using simulations and prototypic (mockup) testing using surrogate filler materials to examine filler behavior during filler. While the majority of the surrogate fillers used in the initial examinations are highly unlikely to be good candidates for actual fillers, they provided good qualities (e.g., transparency, removability) to examine the potential for a filler to be used within the canister's and content's complex geometry and its ability to move through the relatively narrow fill port proposed for introduction of the filler to the canister. As the work progresses, these examinations are expected to progress to candidate materials that are more suited to the intended purpose (e.g., long term exclusion of moderators).

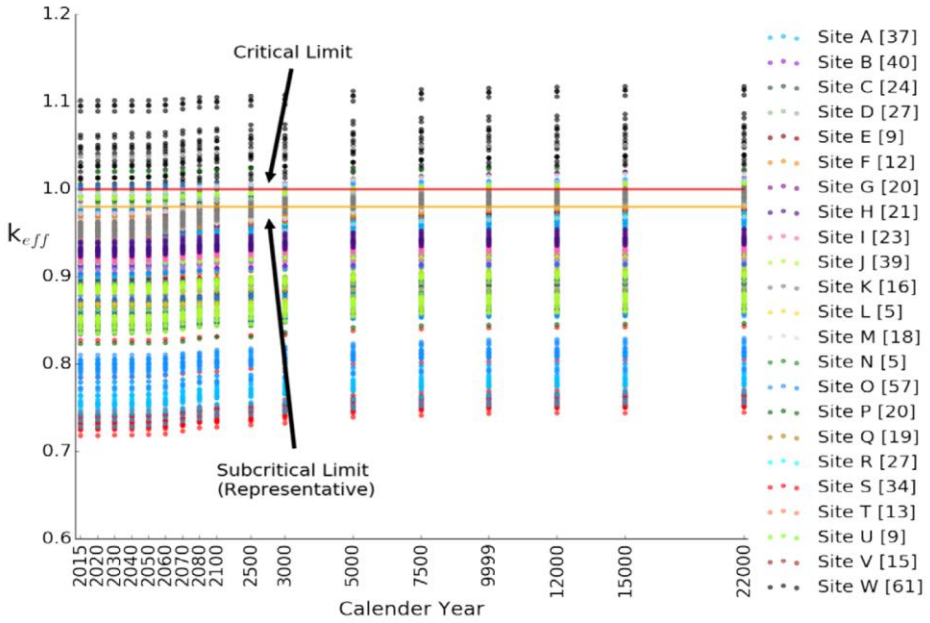

Figure 1. k_{eff} as a Function of the Calendar Year (up to Year 22,000) for 551 DPCs Loaded at 23 Sites. (Postulated degradation scenario includes loss of neutron absorber panels from basket over repository time frame.).

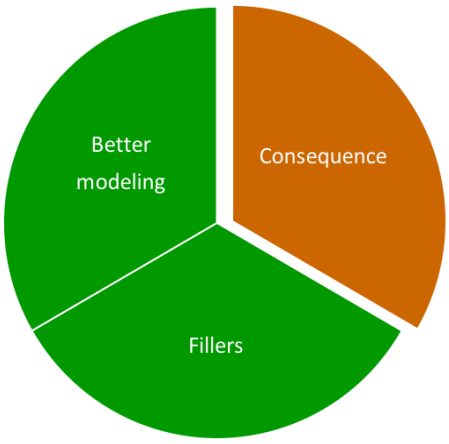

Figure 2. Three Approaches Taken within the Long-Term DPC Disposition Evaluation Program.

This report is presented in two parts. The first part presents the progress made to develop accurate filling modeling and simulation tools. The second part presents the progress made on physical experiments to (1) validate the numerical simulation and (2) to understand various foreseen and unforeseen issues of filling a DPC from the bottom. The objective is to understand various elements of the filling process and to gradually develop a fully validated simulation and test setup to present all the coupled processes involved in filling a canister with filler materials. This approach will identify a filling method (e.g., filling through the drainpipe, vent, or purpose-built access to the DPC's interior) that can be used with high confidence and to vet various potential filling materials as presented in "Joint Workplan on Filler Investigations for DPCs" [4].

This page is intentionally left blank.

2. FILLING MODELING AND SIMULATIONS

The flow simulations are being developed in phases, with the goal of producing a fully validated multiphysics simulation to support and assess the DPC filling process. The multiphysics simulation will also be used to screen filler materials. The DPC filling simulation mirrors a simple experiment where surrogate filling materials are injected through the canister drainpipe. The experimental data from the simple test will also be used to validate the simulation model. The objective of this simulation and simple test is to determine (1) whether a DPC can be filled using the drainpipe, (2) feasible filling rates, and (3) the volume fraction to be filled.

The objectives of the filling simulations are (1) to numerically analyze the filling process, initially on ideal surfaces, (2) to determine remaining voids and filling times, and (3) to identify potential problems. Simulations provide the flexibility needed to experiment with different liquids (metals) and surrogates, to explore filling methods based on existing or new canister features, to aid the experiment design by scaling major quantities. Both Computational Fluid Dynamics (CFD) and a professional casting software called ProCast are being used to predict filler flow.

The simulations are paired with physical testing to verify the predictive capability of the software for the geometry, filler material, and flow regime. A canister mockup test section is designed (Figure 3., see Section 2.4) and simulated. It represents a portion of the lower 16% of a real canister (height 74 cm, Ø26 cm), and it includes the passages among the assemblies' shrouds (mouse holes), the support stands (assembly spacer), the assembly's lower grids, and the first spacer grid. The design uses a 5 × 5 rod array, which is considered representative of a PWR fuel bundle. A circular container encloses five 5 × 5 bundles and accounts for most real canister features [5].

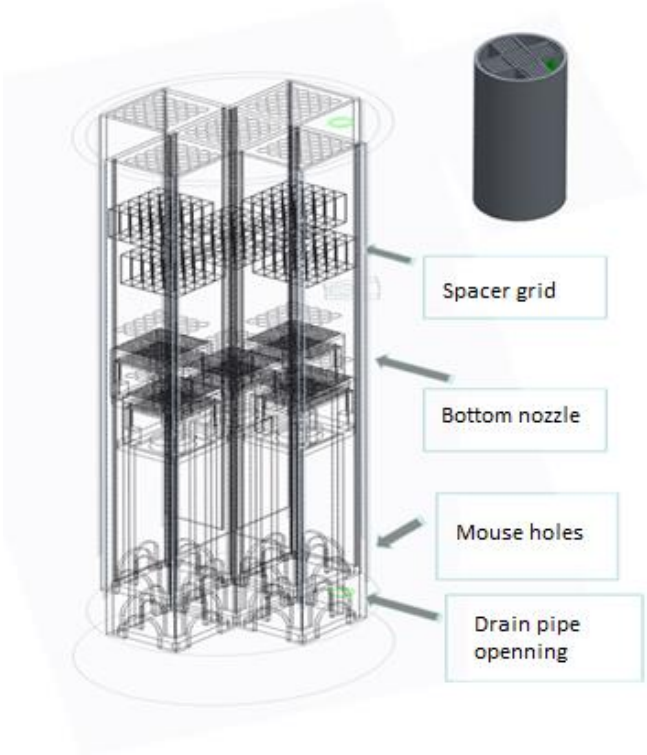

Figure 3. DPC Mockup (Based on 5 × 5 Bundles) of the Lower Section of the Real Canister, Including Mouse Holes, Supports, Bottom Nozzle, and One Spacer Grid.

The simulation employs a 3-dimensional (3D) computational fluid dynamics (CFD) method for a two-phase two-component system in isothermal condition. The gas (helium) and the liquid (metals) front propagation is resolved by solving a viscous flow of mixture [6]. To implement this approach, the commercial software STAR-CCM+ version 13.02 is selected [7]. This model is not suitable for casting (solidification).

The problem is formulated within the framework of the segregated flow approach and discretized by the finite volume method. This includes and allows for coupling between the continuity and momentum equations. The following integral equations represent the conservation of mass and momentum (Navier-Stokes):

$$\text{Continuity: } \frac{\partial}{\partial t}\int_V \rho dV + \oint_A \rho \bar{V} \cdot da = 0\,, \tag{1}$$

$$\text{Momentum: } \frac{\partial}{\partial t}\int_V \rho \bar{V} dV + \oint_A \rho \bar{V} \otimes \bar{V} \cdot da = -\oint_A pI \cdot da + \oint_A T + \int_V f_g dV\,, \tag{2}$$

where V is volume, A is area, a is area vector, p is pressure, f_g is gravity force, ρ is density, $\bar{V}$ is velocity vector, T is stress tensor, and μ is dynamic viscosity. For laminar flows, the stress tensor is formulated as follows: $T = \mu[\nabla\bar{V} + \nabla\bar{V}^T - \frac{2}{3}(\nabla \cdot \bar{V})I]$, where I is the identity tensor.

To apply the flow model shown above to a filling problem that involves liquid and vapor phases, it is necessary to formulate it as a mixture. Mixture models are formulated using a Eulerian multiphase platform. Additional (phasic) quantities are introduced, all based on the volume fraction of one of the phases, *i*:

$$\rho = \sum_i \rho_i \alpha_i; \quad \mu = \sum_i \mu_i \alpha_i; \quad c_p = \sum_i \frac{(c_p)_i \rho_i}{\rho}\alpha_i; \;\; where: \; \alpha_i = \frac{V_i}{V} \;\; and \sum_i \alpha_i = 1. \tag{3}$$

Then a transport equation for the volume fraction is added to the system. The model is called *volume of fluid* (VOF) and has been proven to demonstrate accurate results with low computing cost.

$$\frac{\partial}{\partial t}\int_V \alpha_i dV + \oint_A \alpha_i \bar{V} \cdot da = \int_V \left(S_{\alpha_i} - \frac{\alpha_i}{\rho_i}\frac{D\rho_i}{Dt}\right) dV\,, \tag{4}$$

where S_{α_i} is the source void fraction, and $\frac{\alpha_i}{\rho_i}\frac{D\rho_i}{Dt}$ is the material derivative of phase density.

To date, two types of materials are considered as filler candidates. ORNL is investigating low melting temperature metals, surrogate liquids, and waxes, and Sandia National Laboratory is studying the use of slurries (concrete mixtures). A preliminary list of fillers used in numerical simulations is given in Table 2-

A. Note that these are not necessarily the final candidates but a preliminary list for numerical simulation in the simple unit test to identify possible challenges. Two transport properties are important for this phase of the filling evaluation: density and dynamic viscosity. Silicone oils are highly ranked candidates due to their low cost and the large available range of viscosities.

One half (central symmetry) of the geometry in Figure 3 is initially considered. It has a volume of 11.46 liters per Figure 4). With a volumetric scaling factor to the real geometry of about 6.5, and with an estimate of 17 hours for filling time of the real canister, the equivalent filling rate to be applied within the model is determined to be 1.26 cm^3/s. Note that this is true for one half of the geometry. For testing, the filling rate of the entire volume must be two times higher. The Reynolds numbers (Re) for such filling rates and length scales, which are typical for rod bundles, are in single digits at Re~3, which justifies the laminar flow regime assumption. The initial mesh of the entire geometry resulted in a computational grid consisting of about 6M elements. The liquid is fed through the inlet section of the drainpipe, as shown in Figure 4. A velocity boundary condition is defined at the drainpipe orifice (area 180 mm^2) with a velocity magnitude of 1.26/180 = 0.007 m/s. Thus, the filling simulation is separated from the drainpipe simulation. The flow regime in the vertical drainpipe is subject to separate evaluation, which is currently under investigation. The formulation of that study is provided below.

Table 1. Preliminary List of Surrogate Liquids for Testing and Filling Simulations.

Material	Melting Temp. (°C)	Density (g/cm^3)	Viscosity (Pa·s)	Reference
Glycerin ($C_3H_8O_3$)	Liquid	1.26@RT	0.95@RT	www.MatWeb.com
Silicon oil (Catalog ID: 378372)	Liquid	0.96@25C	0.33@25C	www.sigmaaldrich.com
Lead	327 (600K)	10.70 @600K	0.0026@600K	V. Sobolev (2007)
Lead-bismuth	124 (398K)	10.53 @398K	0.0032@398K	B. Alchagirov (2003)
Mercury	Liquid	13.53@RT	0.0015@RT	Thermal Fluids Central
Water	Liquid	0.997@RT	0.00088@RT	Web (for comparison)

Calculations are run in parallel on 32–640 computing processors. To properly capture the liquid level progression, the time step must be kept between 1–5 ms. The shortest runtime during this preliminary phase was 0.7 hour for one second of the filling process. Filling the entire geometry would take days of computing, so the strategy was changed. The major objective of a filling simulation is to predict the level progression and the void removal. Both of these occur near the current level position. The areas of computational domain below and above the level have little-to-no influence on the filling, but they consume computing resources. To reduce the computing burden, the domain is decomposed into smaller regions, and a data mapping algorithm is applied. The regions overlap, and the velocity and the void fraction (liquid) are mapped from one region to another. The canister geometry further facilitates this approach because the area above the mouse holes is composed of parallel channels (bundle region), and only one channel needs to be modeled. This radically reduces the computing load.

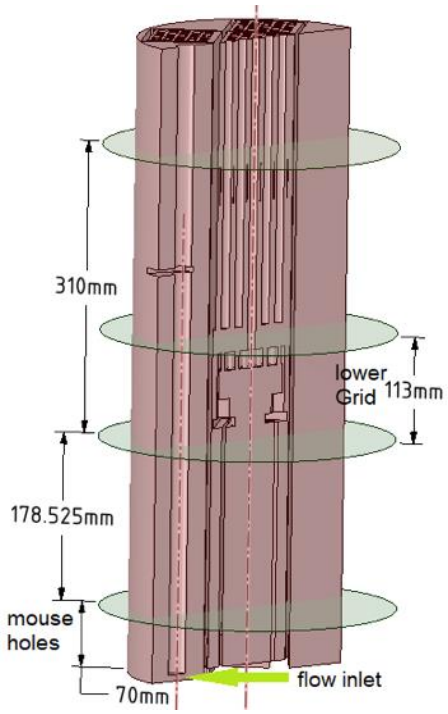

Figure 4. Model Split Indicating the Sections of the Geometry Modeled.

2.1 Filling of the Mouse Hole Region

First the mouse hole region is separated and modeled, as shown in Figure 4. The overall height of the section shown is 70 mm, and it comprises the entire geometry. A polyhedral grid of about 45,000 elements was used. The wall mesh is displayed in Figure 6. It gives a perspective of the geometry with a clear view of the mouse holes. The objective of this simulation is to demonstrate that the mouse holes can be successfully filled if the drainpipe opening provides a continuous constant flow of 1.26 cc/s. The runs are performed on 32 processors for ~5 days (average runtime is 0.12 hour/sec of transient) with a time step of 5 ms. Simulations of the following liquids have demonstrated successful filling of voids in the mouse holes region: glycerin, lead-bismuth, silicone oil, and mercury. Mercury (Hg) is not an option for a real application, but due to its low viscosity and high density, it represents a bounding scenario for the simulation. No noticeable level deformations are observed when different liquids are used. The filling rate is low enough to avoid any local effects that could compromise the filling. This is illustrated in Figure 5. , which plots sections of the mouse hole region for two liquids: lead-bismuth (Pb-Bi) and silicone oil. Even though the densities of these liquids differ by about ten times and the viscosities differ by about hundred times, the filling looks the same. The plot in Figure 5. shows the liquid level at 400 s and at the end of the filling process (total time 1020 s), when the level is at the middle and at the top of the mouse holes. No visible differences are noticeable. The volumes of injected liquids are the same: 496.5 cc for silicone oil, and 498.2 cc for Pb-Bi at 400 s. The small differences are due to computational inaccuracies because the filling rate is the same for both liquids.

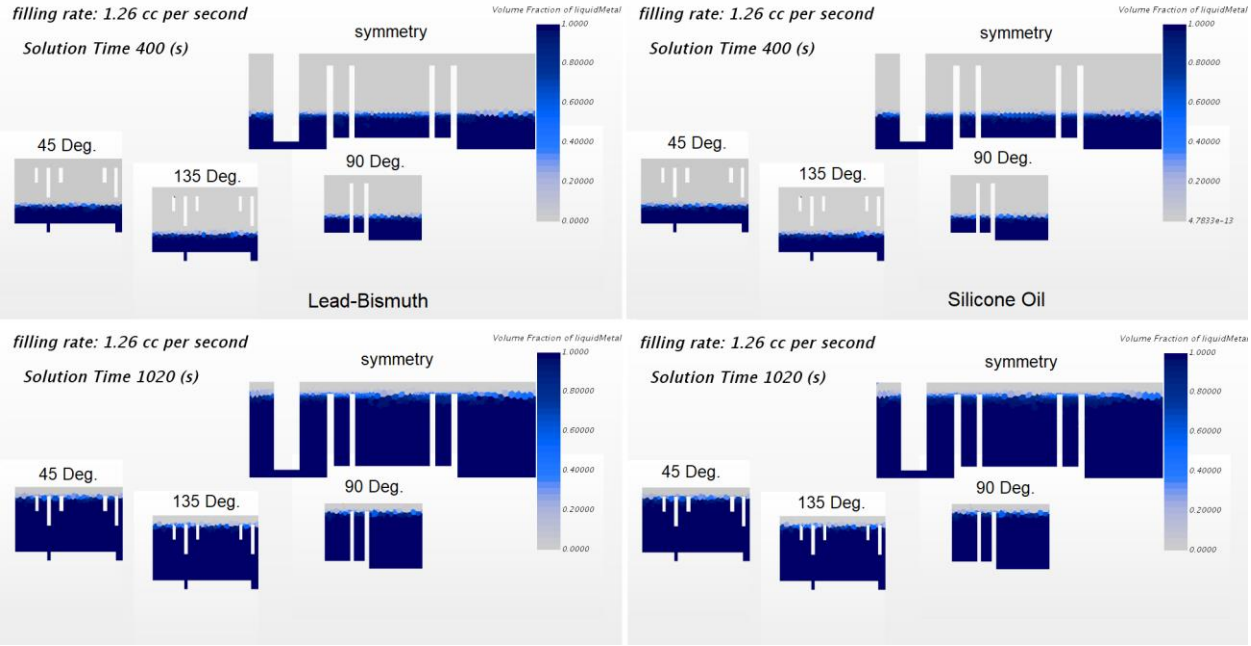

Figure 5. Liquid Levels at 400 and 1,020 s (end) of Transient from Two Runs with Different Liquids (Left: Lead-Bismuth; Right: Silicone Oil), and Contours of Levels at Several Sections of the Mouse Hole Region (Symmetry, 45-, 90-, and 135-Degree Cross Planes).

Even though the silicone oil density is much lower, it allows for the liquid to level off and to smoothly cover the entire region. The level velocity of 4.2 mm/min is such that the viscosity/density combination of the liquids does not affect the filling process. A detailed examination of the plotted sections does not show the presence of any voids. The same is confirmed by the overall volume balance, which is controlled during the simulation.

An isometric view of the simulated section is shown in Figure 6. The top wall and the symmetry planes are removed for better visibility inside the domain. The top part, as seen in Figure 5. , is added to the model to make the outlet pressure equal for all parallel cells. The DPC is designed so that each individual fuel bundle is confined in a separate shroud (cell). The cell walls do not allow for cross flow in the canister. The parallel cells are formed just above the mouse hole region, and the mouse holes are the only flow passage that permits the liquid to enter the fuel bundle cells. In order to properly simulate the filling of these individual cells, an extra volume is artificially added on top of this section to connect the parallel cells. This volume is not filled and does not affect the overall filling time or mass balance.

The views in Figure 6. provide another look at the filling process in the mouse hole region of the canister. This is the region where the bundle shrouds interconnect. The view on the left in Figure 6. shows an early stage of filling in which the central part is still not flooded. The liquid initially propagates on the circumference around the outside wall before entering the central area. Even though that space is narrow, the liquid can freely penetrate the space and distribute evenly in the remainder of the domain. The right view in Figure 6. shows a later stage of the filling in which the mouse holes are partially filled. By observing the levels in different cells, one can conclude that the process is very smooth, and the level rises evenly in all cells. Although the resolution of the model is quite low (to keep the compute time short), the numerical scheme used (high resolution level tracking) maintains the level within 1–2 grid elements. No numerical diffusion is observed due to the second order upwind scheme used to run the simulations. Note that the interface between the gas and liquid cannot be sharper than one element (the liquid boundary to match the element boundary) because the VOF method treats the liquid as a fraction of the total fluid, and as soon the level crosses the element boundary, the void fraction in the same element starts to increase

and varies from 0–1 before the element is completely filled. This explains the different color of gradient in the elements near the level.

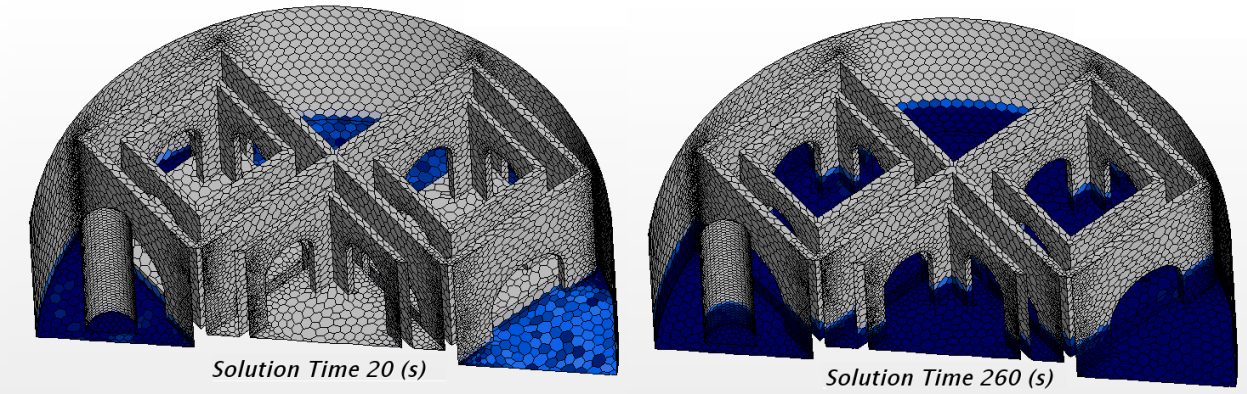

Figure 6. Liquid Content during Filling of the Mouse Hole Region at 20 and 260 s. Total Filling Time = 1,040 s; the Computational Grid is Also Shown.

An important aspect of the filling calculations is the conservativeness of the solution. The relatively coarse domain discretization poses questions about the solution's accuracy. To address these questions, a control of the mass in the system is established during the time advancement. The result is plotted in Figure 7. for three of the test liquids (Pb-Bi, Si-oil, Hg), and it shows that the error varies within 1.5%. In the simulation, the model fills for 1,040 s while the actual filling time is 1,024 s. The error tends to increase toward the second half of the process, which will be investigated in the future. The error could be due to the grid becoming larger in the space over the mouse holes. Usually, the element size is driven by the geometry features, and to resolve small details, more elements are used. Once details such as the mouse holes are meshed, the grid elements become larger in the spaces over the mouse holes. This may be increasing the error, but it remains within practical limits. In view of the long practical filling times, such a small difference is considered acceptable.

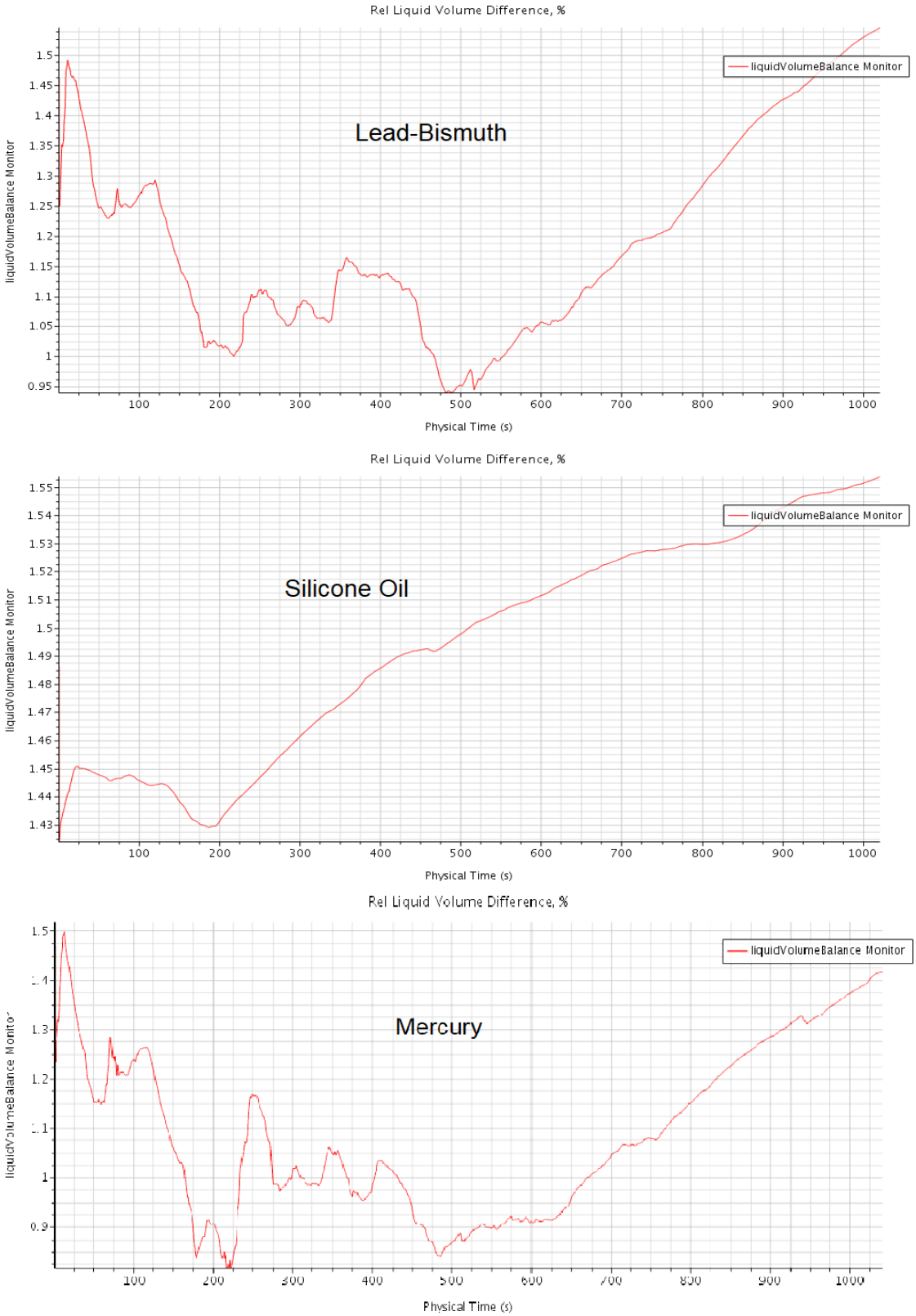

Figure 7. Mass Error Evolution during Filling of the Mouse Holes Region with Pb-Bi (Left), Silicone Oil (Center), and Mercury (Right).

2.2 Lower Grid Filling Simulation

The lower grid filling simulation is discussed in this subsection with additional information provided in Appendix A.

As shown in Figure 4, upstream of the mouse holes, there is a section (~180 mm) where the geometry does not change. This section contains the liquid in the fuel assemblies' supports. The fuel assemblies are placed in the canister on rectangular supports that separate them from the canister floor. After filling of the mouse holes has been successfully demonstrated, there is no need to carry the numerical solution in that region because no new geometry features exist. Instead, this section is skipped by shortening the domain to save computing time. The level, which is computed in the region below (mouse holes), is transposed as an input condition, assuming it has the same topology. The rationale is based on the fact that no specific features of the level are observed, like moving or standing waves, substantial radial convection, etc., which would invalidate the above assumption. The liquid front propagates in all cells with the same velocity. Technically, this is accomplished by mapping data between nonconformal domains, which is challenging in CFD computing, but it can be done. This approach is followed in the present analyses.

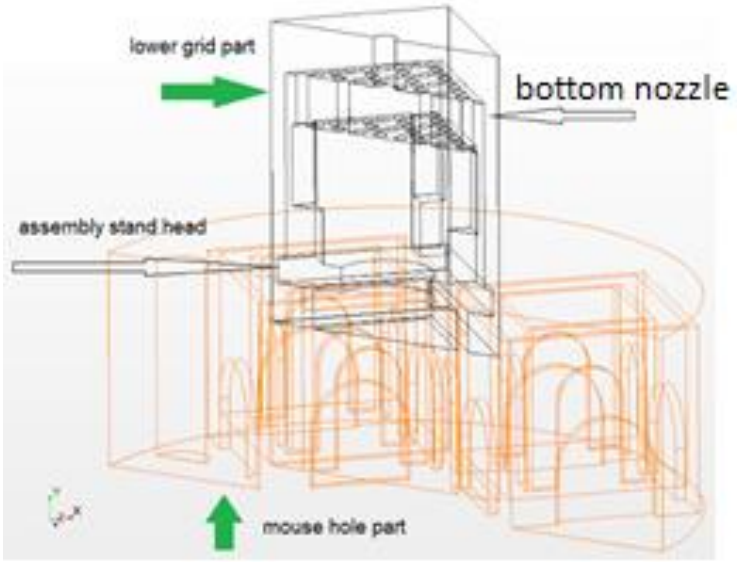

Figure 8. Lower Grid and Its Relative Position to the Mouse Hole Region Used in the Simulation. The Important Features of That Section Are Indicated.

The simulated section is shown in Figure 4. This bottom nozzle includes several small holes that, in the reactor design, were originally meant to provide more even flow distribution at the bundle's inlet. These holes may pose a problem in the filling process and will require special attention. The modeled section also includes the upper part of the assembly stand and the transition region. It is part of one of the five 5 × 5 bundles. As mentioned before, the bundle cells (shrouds) permit the domain to be further decomposed and simplified by simulating only one of the five bundles (because they form identical parallel channels).

More detail about these components and their relative positioning is shown in Figure 8. The mouse hole region is shown with different colors to distinguish the components. The section has an overall height of 113 mm. It is set to overlap the mouse hole region, with 15 mm to allow for data mapping. The overlap is shown in Figure 8. The lower grid section is meshed with about 100,000 elements. When compared to the mouse hole region, this increased number of elements is about 5 times larger and has 45,000 elements. This is caused by the holes in the lower assembly grid.

To provide continuity of the filling process, two variables from an existing solution in the mouse hole region must be mapped to the lower grid region. One of them is the current level, expressed as liquid volumetric content (fraction of total fluid). The level is usually spread across at least three layers of elements, which determines the mapped domain. Figure 9 (below) shows the outcome after the mapping is performed. A partial level of data only in the central cell is mapped to the lower grid region. It covers part of the bundle support fluid volume just below the lower grid. The volume of this initial liquid is 15 cc, and it must be accounted for in the over-volume balance during the simulation. The computational mesh is demonstrated in Figure 9. (below), with a zoom into the lower grid holes. The geometry is captured in full detail, resulting in an increased element count.

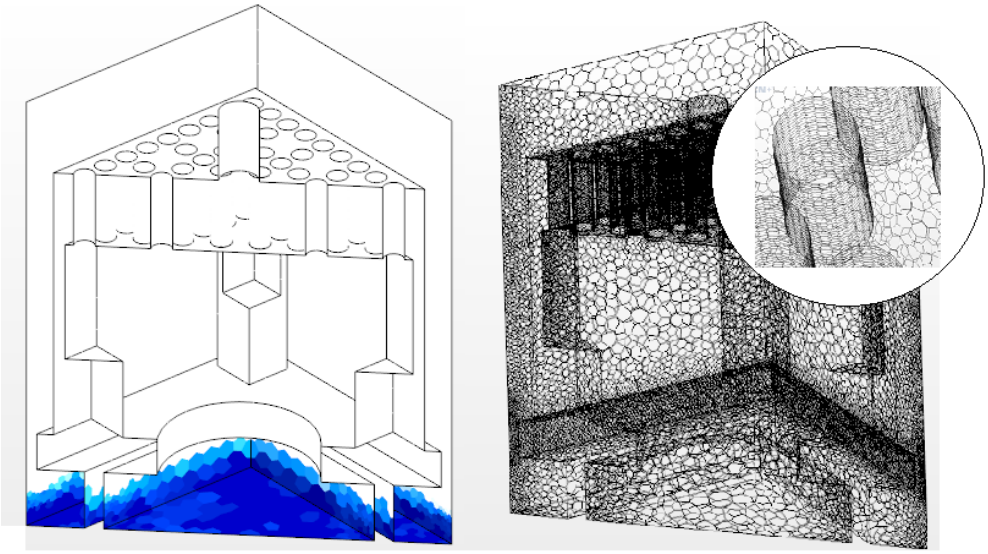

Figure 9. Initial Liquid Fraction as Mapped from the Mouse Hole Region (Left), and Computational Mesh of the Lower Grid Region with a Zoom into the Hole Area's Mesh (Right).

The second variable that must be transferred from the previous solution is the velocity vector at the inlet of the new section. A close examination of velocity vectors in a plane just above the mouse holes (Figure 10.) shows a random high frequency distribution of instantaneous velocities. The dominant magnitude is around 0.05 m/s, with no preferential direction. The insert window in Figure 10. enlarges the velocities in the mapped area and shows the computational grid. Such a velocity profile is calculated by the viscous solution when no ensemble time averaging of velocity is performed. The difference between the instantaneous velocity and the axial average velocity (~4mm/min) indicates that a small-scale turbulence is computed in a general laminar flow. Further examination of the velocity contours in the mouse hole region does not indicate formation of eddies, indicating that the flow is not turbulent. The Re numbers for that region, based on the level velocity and typical length scales (~70mm), are ~15. This finding requires more attention and further analysis of the origin of these fluctuations, which are most likely numeric.

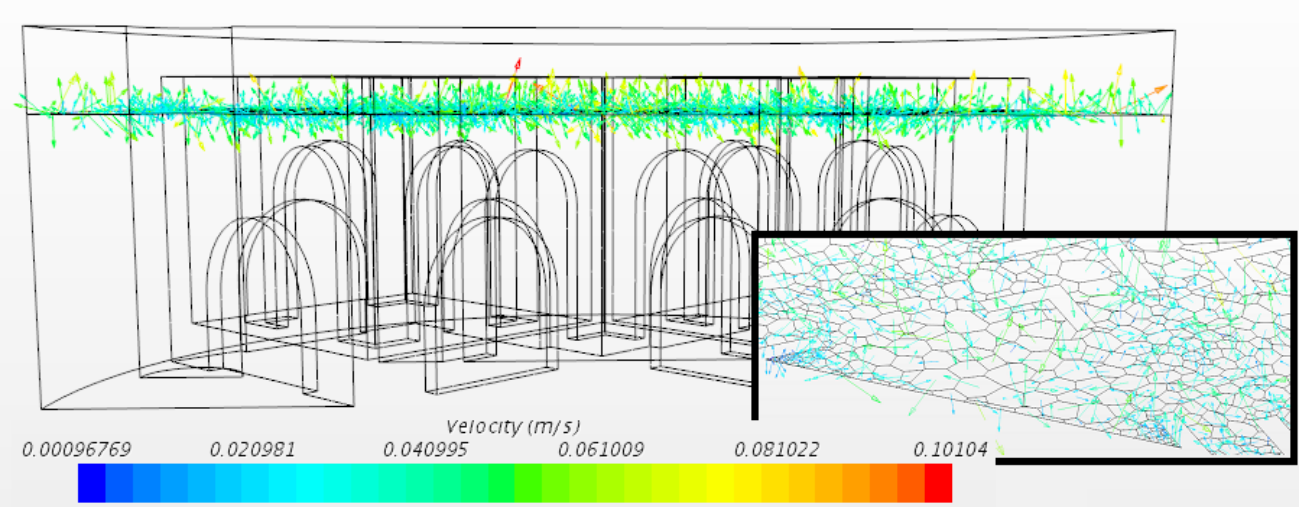

Figure 10. Velocity Vectors of the Advancing Liquid Level on a Plane Just above the Mouse Holes. The Random Fluctuation of Liquid is Noticeable, with no Preferential Direction. The Insert Shows the Mesh and the Velocities in the Mapped Region.

Based on the results discussed above, instantaneous velocities are not suitable as a boundary condition for the lower grid region unless they are time averaged. Instead of time averaging, the velocity at the inlet section of the lower grid region is calculated after the filling rate for the same region is calculated. Additional data are needed to perform this calculation, as summarized in Table 2-B.

Table 2. Geometry Data for the Bottom Nozzle Section and for the Half Symmetry Model with the Same Axial Elevations.

Parameter	Value
Volume of lower grid region	224 cubic centimeters (cc)
Axial height of lower grid region	113 mm
Inlet flow area of lower grid region	2137 mm^2
Volume 113 mm tall	2047.8 cc
Overall filling rate for the entire model	1.26 cc/s

The approach is based on calculating the overall time for filling a section of the entire geometry with the same axial marks as the lower grid section: 113 mm. The filling time of the entire geometry with 113 mm height = volume (local) of entire geometry / overall filling rate:

$$T_{total} = 2047.8/1.26 = 1625 \text{ s} \quad (5)$$

If the same filling time is valid for the lower grid section of the geometry, then a part specific filling rate can be calculated:

$$\text{Filling rate (lower grid)} = \text{volume of lower grid} / T_{total} = 224 / 1625 = 0.138 \text{ cc/s} \quad (6)$$

Once the part-specific filling rate is known, the inlet velocity is calculated:

$$\text{Inlet velocity for the lower grid section} = \text{Filling rate (lower grid)} / \text{inlet flow area} = 0.138 / 2137 = 6.45\text{E-}5 \text{ m/s} \quad (7)$$

This velocity is slightly lower than the level advancement velocity of 4.2 mm/min (7.0E-5 m/s) mentioned before. The difference appears because the flow area in the lower grid section is smaller than the average flow area in the same section of the entire geometry. The inlet velocity is applied to the inlet geometry of the lower grid section together with mapping the level from the mouse hole section. These two initial conditions are sufficient to perform the calculations. The mapping is successfully accomplished following a code-specific procedure, and the analyses runs will be initiated soon.

The computational runs are successfully started and are under way at the time of this writing. They are being executed on 96 cores (three nodes 32 cores each). The first 500 s of the transient are calculated. The level progresses smoothly as in the previous DPC section (mouse holes) without any anomalies. The liquid level has not reached the lower grid area and it is still in the transitional region between the assembly stands/spacers and the lower grid. Four snapshots of the entire lower grid section showing the level advancement are plotted in Figure 11. The grid hole area is clearly visible above the current level position.

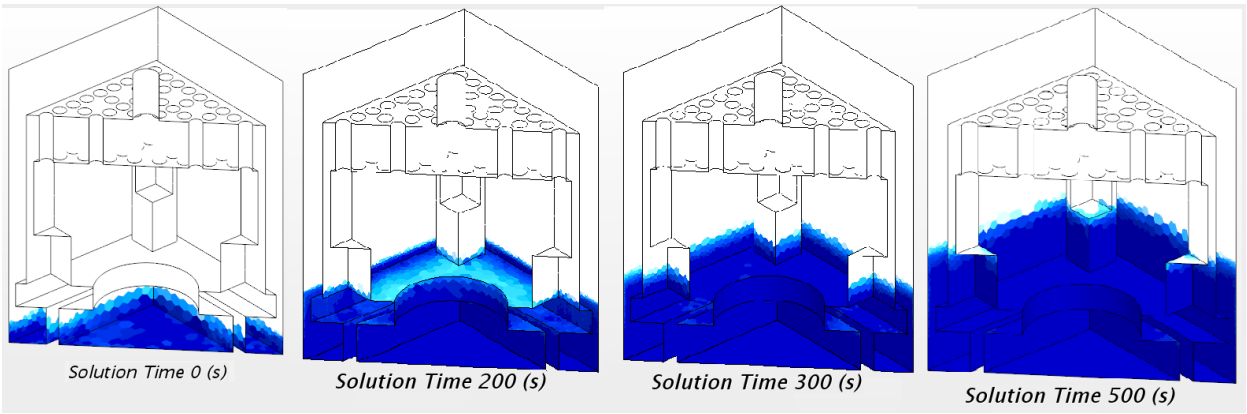

Figure 11. Evolution of the Level in the Lower Grid Section of the Model during the First 500 s of Transient.

In terms of resolution, the holes are the denser part of the domain and will require more computing time. The period of 500 s is computed for about 19 hours of CPU time per processor, or with about 0.2 hour of clock time per second of real process. At this speed, the entire filling simulation should be completed within a week.

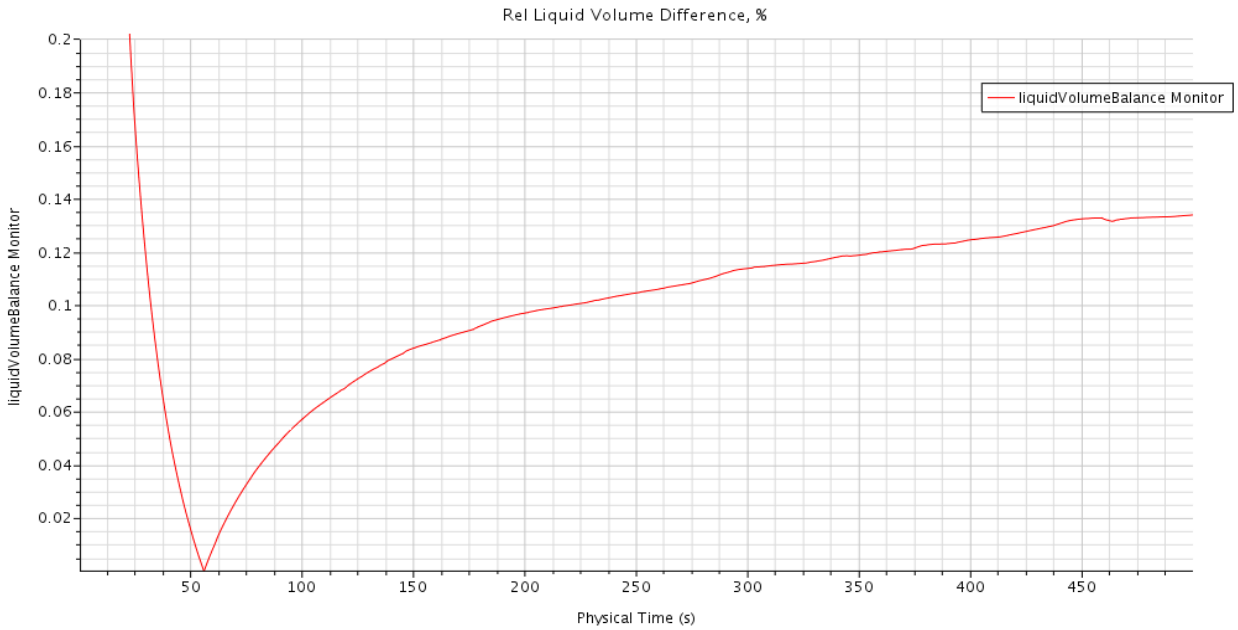

Figure 12. Mass Error Monitor. The Total Mass in the System is Constantly Evaluated and Compared to an Ideal Process.

The mass error is continuously being monitored (Figure 12). The current value is about 0.14%, which when converted to real volume yields 0.3 cm^3; it tends to stabilize at this level. This number indicates a very good solution convergence and accurate spatial discretization.

To allow for axial tracking of the filing process and identification of eventual voids, several cross sections of the domain are plotted in Figure 13. They are taken in the symmetry plane (midsection) and at 45, 90, and 135-degree sections. The information from these plots shows an even level progression and no void formation. The most critical area for voids is the grid, and the solution has not yet reached that location. The section that has already been filled is quite free of obstruction, as the flow enters by a central opening with a large area which does not present a challenge.

The simulations continue, and without any further complications, they are expected to complete in a week, depending on the load on the computing cluster.

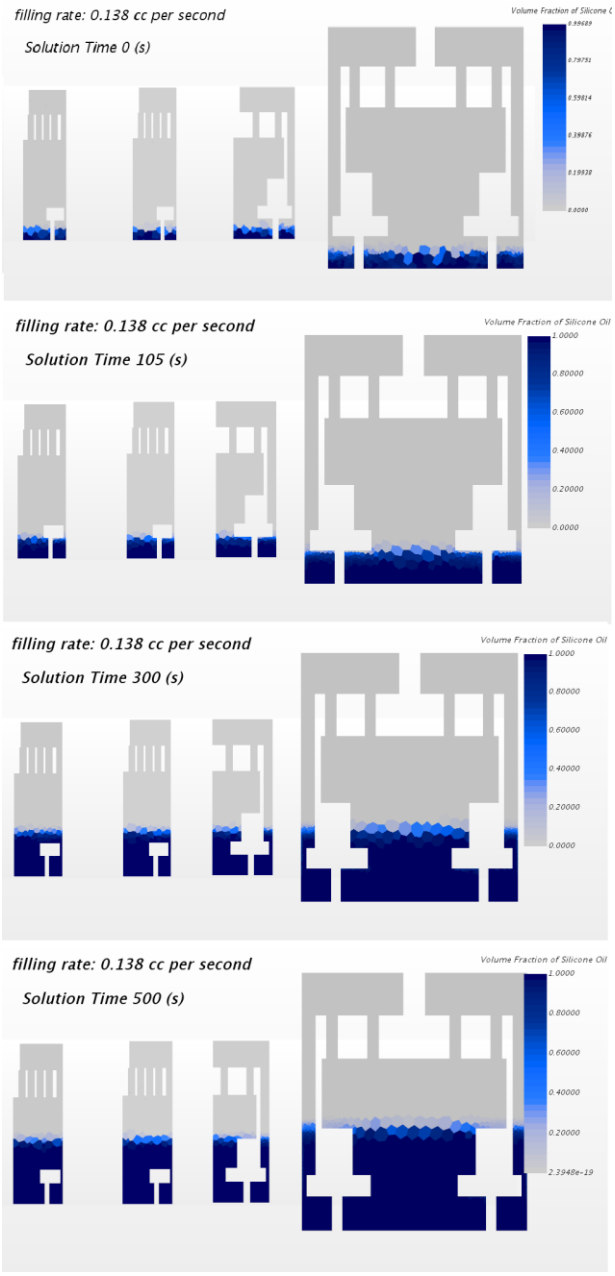

Figure 13. Filling of Lower Grid Region, Sectional Liquid Fraction Plots, Showing the Volume of the Lower Grid Filled at Different Time Instances. The Calculated Period Covers the Transition between the Stand and the Grid Entrance Region.

2.3 Drainpipe Analysis and Modeling Approach

The drainpipe analysis and modeling approach is discussed in this subsection with additional information provided in Appendix D. The information presented in this subsection is preliminary should be considered an introduction to the problem.

One consideration is to evaluate the possibility of filling the canister through the drainpipe. Each DPC is equipped with a drainpipe and a vent port of the same size (ID 1.25 in.). The drainpipe stretches from the top of the canister to the bottom, so it has the same length as the canister. The pipe is about 4.26 m (14 ft.)

long. While there is no strict requirement for how much time the filling of a single canister should take, the drainpipe's capacity to deliver a steady flow of liquid metal to the canister may be the limiting factor for the filling time and could be the component that will define this time. In the simulations, a filling time of 17 hours is assumed based on a filling rate of 100 ml/s. The assumed free canister volume is 6 m^3.

Extensive research has been conducted on flows in vertical pipes. In the past, intrusive methods such as hot wire anemometry were used, but more recent experimental works use non-intrusive techniques such as laser doppler velocimetry (LDV), photochromic dye tracing (PDT), confocal chromatic imaging (CCI), or particle image velocimetry (PIV). Two recent experimental and theoretical studies by Zadrazil and Markides [8] and by Padmanaban [9] address vertical pipe flows, mainly of water. When the pipe entrance is not obstructed by liquid (as in a pipe draining a tank) but is left open to the air or a gas atmosphere, the flow that develops in the pipe is a two-phase annular flow. In this type of flow, the liquid flows steadily on the pipe walls, forming an annular film. The core of the flow is gaseous and is typically stagnant. Some experiments consider co- or counter-current gas flows [9], but they are outside the initial scope of this work. Co- or counter-current gas flows are of interest for the canister filling because they would provide a means to control the flow rate without chocking the pipe. The term *chocking* is used here to indicate a regime in which the entire pipe area can become fluidized, and there would be no free flow of gas in the pipe. These evaluations will initially be assumed that this type of regime is unwanted, as it would impede the steadiness of canister filling by creating flow pulses, shocks (hydro) or other hydraulic phenomena. This could damage canister structures or disrupt the filling process due to the high gravity effect of liquid metals, which have densities approximately 10 times greater than that of water. This option will be further reevaluated during this study and may be revised. Figure 11 presents a typical drain port design.

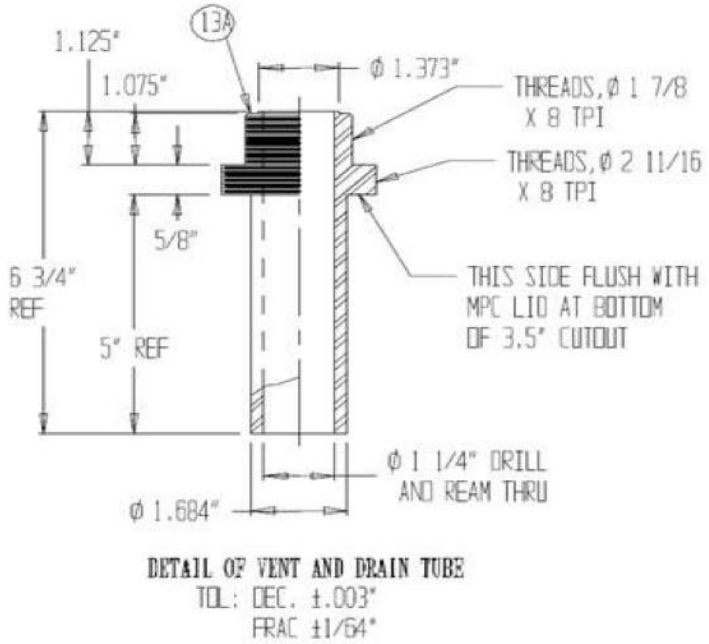

Figure 14. Drawing of the Drain Port Showing the Side of the Opening [5].

The Nusselt film theory can be used as a starting point in these analyses because it gives a good first order approximation to the main flow characteristics. It is based on the assumption that a steady liquid film forms on the pipe inner wall (or other structure wall) which is one dimensional (only in axial direction) and the film flow is laminar. Under such circumstances, the wall shear stress balances (in a steady condition, when the axial velocity is constant) with the force of gravity. This can be written as

$\frac{\partial \tau_{yz}}{\partial y} = -\rho g$, where τ is the shear stress in z (axial) and y (normal to the wall) direction; g is gravity; and ρ is the liquid density. Normally, the z-y shear component can be presented as $\tau_{yz} = \mu(\frac{\partial W}{\partial y} + \frac{\partial V}{\partial z})$, with the second term in one dimensional flow is given by $\frac{\partial V}{\partial z} = 0$. Thus, the final equation that defines the film velocity becomes:

$$\mu \frac{d}{dy}\left(\frac{dW}{dy}\right) = -\rho g, \tag{8}$$

where W is the axial and V is the radial velocity component. In one dimensional formulation, only W is non- zero. The above equation can be integrated with the following boundary conditions: W =0 at the wall, and $\frac{\partial W}{\partial y} = 0$ at the film thickness of y = δ. The result gives the velocity distribution in the film:

$$W(y) = \frac{g}{\nu}\left(\delta . y - \frac{y^2}{2}\right), \tag{9}$$

where ν is the liquid kinematic viscosity and δ is the film thickness.

Assuming further a flat film (not exactly the same that forms in a circular pipe), the flow rate of liquid per unit width of film can be calculated by integrating the following expression over the film thickness:

$$q = \int_0^{\delta} w(y)dy\,. \tag{10}$$

The result of the above integration provides a simple relation between the film thickness and the volumetric flow rate:

$$\delta = \left(\frac{3\nu q}{g}\right)^{\frac{1}{3}}. \tag{11}$$

This relation can be used as a first approximation for evaluating the film thickness that forms in laminar conditions in a gravity driven flow. To make that relationship applicable when the flow rate Q (m^3/s) is known, an additional assumption for the film width is necessary. In case of very thin films, the film width of a film flowing on the inner pipe wall, will be very close to the pipe perimeter. In such condition, the relation between Q and q is given by $q = Q/\pi D$, (m^2/s), where D – is the pipe diameter.

With the help of the above relation the film thickness can be finally evaluated as:

$$\delta = \left(\frac{3\nu Q}{\pi g D}\right)^{\frac{1}{3}}. \tag{12}$$

The non-dimensional parameter that characterizes the flow of liquid films is the Reynolds number *(Re)*. Traditionally in the liquid film flow theory, the *Re* number is defined in two different ways: by the Nusselt velocity W_{Nu}, or by the superficial velocity W_{sl}. The Nusselt velocity is formulated directly from the flow rate defined above:

$$W_{Nu} = \frac{q}{\delta} = \frac{\frac{g}{\nu}\delta^2}{3}. \tag{13}$$

The definition of the *Re* number is based on the Nusselt velocity and the film thickness and is given by:

$$Re_{Nu} = \frac{W_{Nu}\delta}{\nu} = \frac{g\delta^3}{3\nu^2}. \tag{14}$$

$$Re_{Nu} = \frac{q}{\nu} = \frac{Q}{\pi \nu D}. \quad (15)$$

The formula allows the film thickness to be calculated by knowing the Nusselt Reynolds number.

Substituting the film thickness in the above, leads to a relatively simple relation between the *Re* number and the flow rate:

$$W_{sv} = \frac{q}{\delta} = \frac{Q}{\pi D \delta} = \frac{4Q}{\pi 0.03175 \cdot 0.45e-3} = 2.23\frac{m}{s} \quad (16)$$

For Lead-Bismuth (Pb-Bi) eutectic ($\nu = 3.039E\text{-}7$ m^2/s) and for the chosen flow rate of 100 ml/s (Q = 1.0E-4 m^3/s), and for the size of the drainline (ID = 1.25" = 0.03175 m), the Nusselt Re number is: Re_{Nu} = 3298. The Nusselt film thickness can also be calculated, using the above formulas for Pb-Bi: δ = (3.3.039E-7.1.0E-4/π/9.81/3.175E-2)$^{1/3}$ = 0.45 mm. The corresponding Nusselt velocity can be used as a measure of some average film velocity. It is formulated above and is calculated below:

The second method to define the *Re* number is by the superficial velocity. The superficial velocity is the velocity of liquid if occupying the entire pipe and is given by: $W_{sv} = 4Q/\pi/D^2$. The *Re* number is then defined based on that velocity and the pipe diameter: $Re_{sv} = W_{sv}.D/\nu = 4Q/\pi/D/\nu \rightarrow Re_{sv}$ = 13,195.

The flow characterization based on the Nusselt theory helps to obtain a first guess for the expected flow behavior in the drainpipe. Due to the high gravity of the liquid metals, the Re numbers are 2-3 times higher than that of water. The resulting laminar flow film thicknesses are small (thin films) because of the same reason. It is highly expected that the flows will develop unsteady turbulent patterns. Therefore, the above introduced method won't be sufficient for correct prediction of the film motion. It is possible the problem to be approached numerically by performing CFD analyses of turbulent liquid films. The CFD is superior to the simple laminar one-dimensional theory, because it can provide multidimensional solution of the turbulent liquid gas interface.

In this short introduction to vertical free falling liquid films only water experiments are briefly reviewed. One of them is [8], where tests on a 3m long (ID 32.4 mm) pipe were performed. The pipe diameter and length are almost the same as those of the DPC drainpipes. Two high resolution techniques were employed for flow characterization: PTV/PIV (particle tracking velocimetry) and PLIF (planar laser induced fluorescence). Both methods allow for accurate velocity measurements (instantaneous), gas liquid interface capturing, identification of wave appearance and propagation, and recirculation zones formation. The measurements were taken on a test section 72D from the pipe inlet. The test setup allows co-current gas to be injected in the core of the flow. The review is limited to the tests with zero gas flows. They cover a range of ReNu between 306 – 1532, which is substantially lower than the range expected during the DPC filing.

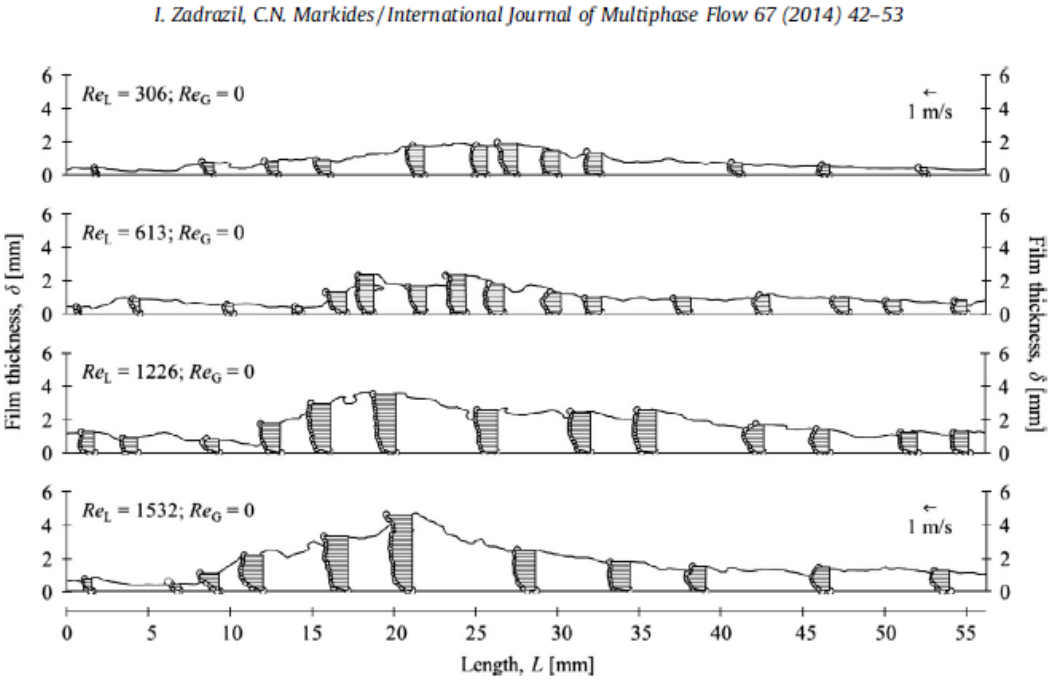

Figure 15. Liquid Film Instantaneous Velocities Showing Appearance of Waves. The Waves Grow with the *Re* Number.

A detailed image from CD-Adapco [6] shows the film thickness and the instantaneous velocities (Figure 15). For $Re_{Nu}>300$, waves start to appear and grow as the *Re* number increases. The wave velocity was also measured, which for the studied range of *Re* was around 1.5 m/s. It is noticeable that the mass transport is dominated by the wave size and not by the speed. The flow structure is defined by some basic substrate thickness (a constant thin portion of the film) and the waves traveling in this substrate. Recirculation zones are also seen in the wave crests; these are an indication of turbulent flow.

The flow visualization method used in Zadrazil and Markides [8] allowed the film velocities to be time averaged and accurately measured. Figure 16 is likely the most representative plot (also from Zadrazil and Markides) for zero gas flow, which is of interest in this study. The figure illustrates the mean film velocity profiles. The highest *Re* number results demonstrate that the film thickness stretches to 20% of the pipe's radius (~3.24 mm). These film thicknesses are in the waves. The substrate film thickness is marked with empty signs on the velocity plots. It indicates thicknesses of ~0.05R, or ~0.8 mm. Because the *Re* is about two times lower than in the case of Pb-Bi, the film's measured thickness is almost two times higher than the estimate given above for Pb-Bi. This observation points to a different flow structure that is characterized with thinner and faster films. The same conclusion is supported by comparing the profiles in Figure 16 with the estimate for the Nusselt velocity (2.23 m/s) of the Pb-Bi film. For the base film thickness (Figure 16), the velocities are between 1–1.5 m/s, and they grow slightly in the wave's crest. Apparently, the time averaging does not capture the instantaneous wave velocities, which creates a perception that the waves travel with the same velocity as the film (substrate), or almost the same (~20% faster). This observation must be carefully addressed to avoid reaching a wrong conclusion. The paper by Zadrazil and Markides [8] also provides data for CFD model validation, because turbulence-related properties such as kinetic energy or Reynolds stresses are calculated from the recorded instantaneous velocity field.

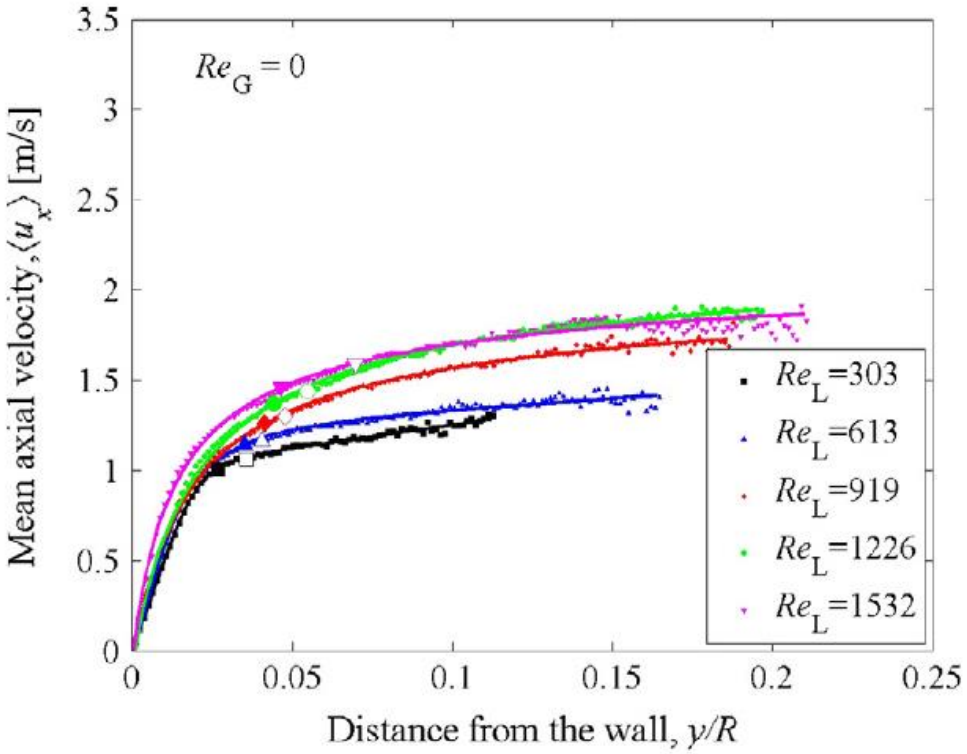

Figure 16. Axial Mean (Time Average) Velocity Profiles from Zadrazil and Markides [8] for Free-Falling Liquid Films (No Co-Current Gas Flow). The Substrate and the Average Film Thicknesses are Shown with Solid and Hollow Markers on Each Corresponding Plot.

Another interesting work is presented in Padmanaban's thesis [9]. This work did not employ such high - resolution visualization technique as used by Zadrazil and Markides [8], but the experiments were run up to higher *Re* numbers, close to or even exceeding those that are targeted in the DPC filling study. A straight vertical pipe with an ID of 1 in. (0.0254 m) and length of 4 m served as the test section. Photographs were made of the falling free films of water. The images were corrected to allow for better contrast in the wave area. Selected liquid film photos are shown in Figure 17 for three regimes with *Re* numbers of 13,348; 18,208 and 23,696. The regimes are selected to match (first one with *Re=13,348)* or to exceed the expected DPC filling *Re* numbers. The white arrows in Figure 17 indicate the region where the film flows next to the wall, to the waved area over the film, and to the gas bubbles. Annotations to the arrows provide more detail about the objects they specify.

The left image shows a liquid film with no gas, a wavy structure over the film (substrate), and a gas core with some liquid droplets. It seems that the film thickness is on the limit of beginning to disintegrate. The next image (center) has almost no gas core. The waves have grown large enough to block the entire cross section of the pipe. The flow regime starts to transition from annular film to churn-like flow in which the core is a mixture of gas and liquid. The right image demonstrates the breakup of the film and a falling flow of mixed gas and liquid. Gas is entrained in the liquid, and the liquid is entrained in the gas core. The liquid film is difficult to distinguish. This occurs at *Re* less than two times higher than the *Re* of interest in the filling analyses.

Based on this information, it can be concluded that the initially selected filling rate of 100ml/s will produce a turbulent film with large waves contributing substantially to the mass transport. The flow regime is close to a transitional mixed liquid-gas regime, which at this time is considered questionable for delivering a steady flow of liquid to the canister.

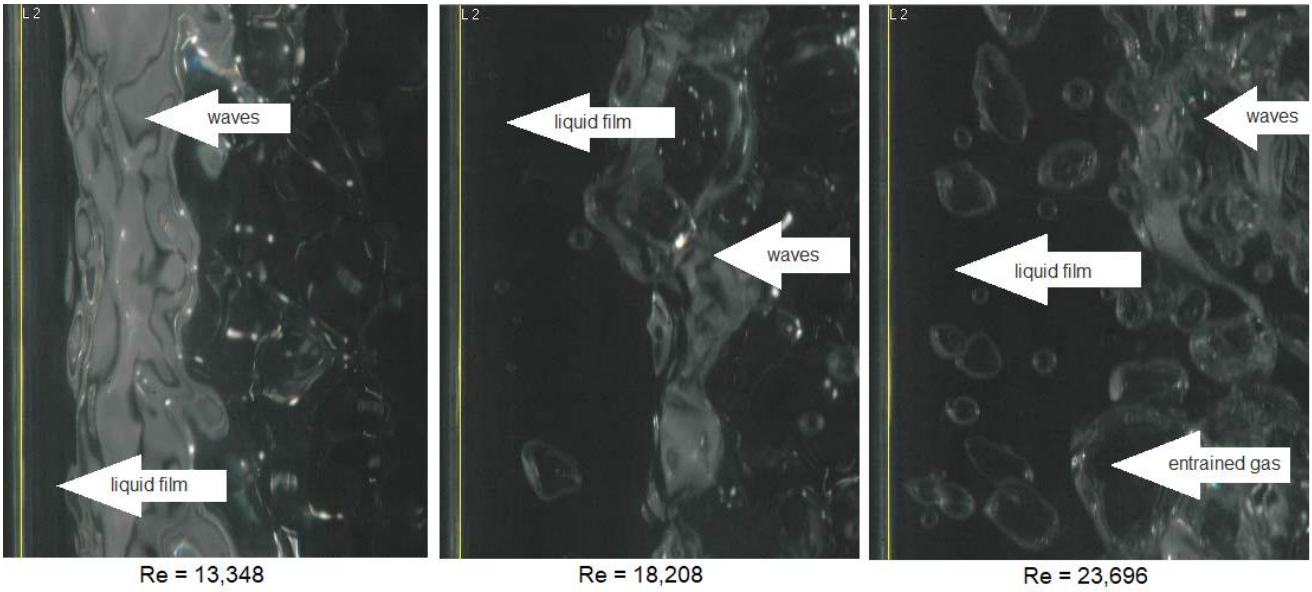

Figure 17. Photos of Free-Falling Films [9]. Only the Left Half of a Cross Sectional Area of the Pipe is Shown. The Wall is on the Far Left, and the Film is the Dark Area Next to the Wall. Gray-Colored Regions Show the Waves, and the Far-Right Image Shows the Entrained Gas.

Besides capturing the film topography, Padmanaban [9] provides measurements of the turbulent mean film thickness. The results are based on statistical processing of more than 40,000 images for each of the different flow rates. The data are correlated in analogy with the film's thickness (δ) from the Nusselt theory. To compare with other data, these data are nondimensionalized with a factor of $(\nu^2/g)^{1/3}$. The result is plotted in Figure 18. The *Re* number in Figure 18 is four times smaller than that used in this work due to different formulation (*Re = 13.195/4 = 3300).*

The nondimensional film thickness for this *Re* is *~35* (from Figure 18). Applying the factor given above, the dimensional film thickness for Pb-Bi can be calculated: *δ = 35(3.039E-14/9.81)^1/3 = 0.51 mm.*

The result is about 12% different from the Nusselt thickness of *0.45mm* given above. The difference is due to the wave formation that is captured in the experimental studies, but once averaged, it produces almost the same thickness. The average film thickness is only one of the flow characteristics. Another equally important characteristic is the wave height, which has only been measured in more recent works in which advanced visualization techniques were employed.

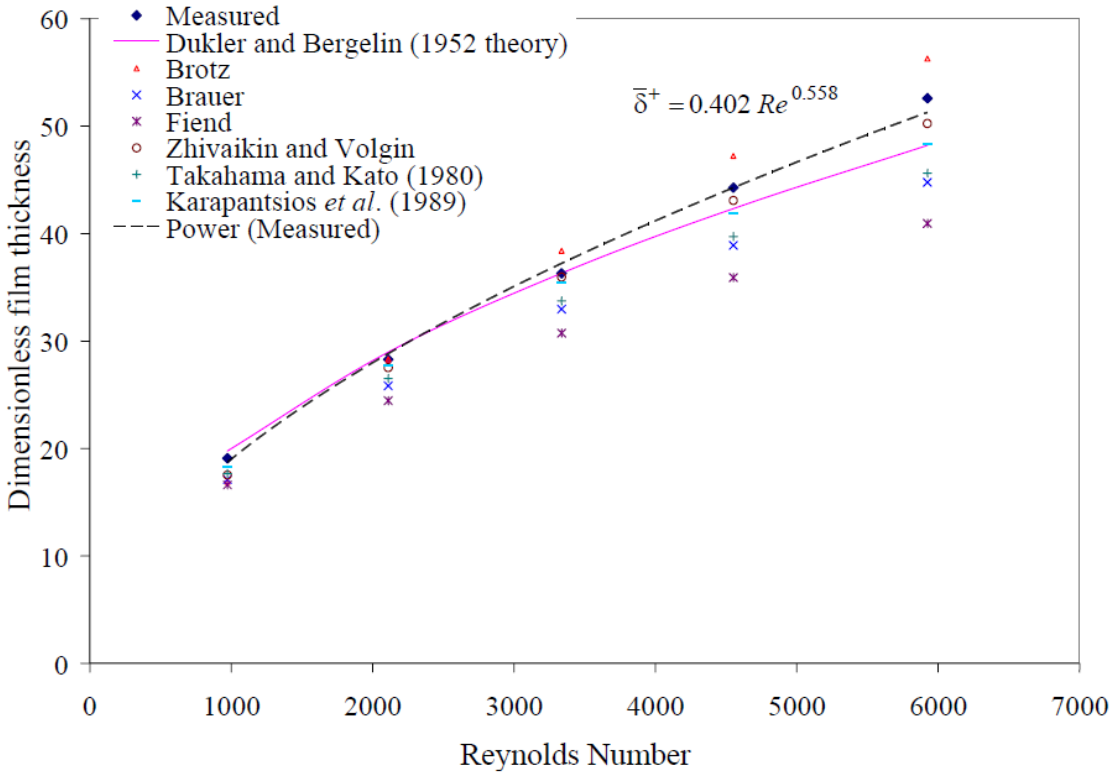

Figure 18. Dimensionless Film Thickness in Function of Re Number [9] for Comparison with Previous Experimental and Theoretical Data.

The limited review of existing data for free-falling liquid films in circular pipes reveals several useful findings.

1. There is an abundance of data for liquid films in pipes for low *Re* number flows. Data are more limited for high *Re* turbulent films because neither the theoretical models nor the experiments are easy to conduct. Most of the industrial applications involve turbulent flows, including the DPC-filling problem.
2. Within the scope of this initial work, no data were found for falling films of liquid metals. The search will continue in the future; however, it seems that experimenting with annular liquid-gas flows might be advisable in the filling demonstration project. The objective of such experimentation will prove that a steady, stable, liquid metal (Pb, Hg, Pb-Bi) film can be created and maintained for hours during the DPC filling.
3. Experimenting with liquid metals may pose new questions and may require new visualization methods, because, unlike materials most used for testing liquids, the metals are not transparent. Metals have much higher surface tension (about 6 times higher than water) than most liquids used for testing in most experiments. In the work of Kapitza [10], the surface tension is analyzed, and a parameter is introduced—$\gamma = \sigma / \rho\nu^{4/3}\, g^{1/3}$—where σ is surface tension. It is shown that the surface tension has a strong effect of the formation of waves in the film. It is expected that the liquid metal will have different film topology and perhaps different thicknesses for the same *Re* numbers.
4. Another aspect to be addressed is the drainpipe geometry and positioning in the canister. In the experiments with falling films, the pipes are well aligned and positioned perfectly vertical. In a real situation inside the canister, the drainpipe may not be vertical or even straight due to aging or other thermal or structural factors. Evaluations of the effect of pipe position and geometry on the formed liquid film might be necessary.

This initial introduction to the flow phenomena in circular pipes with free-falling liquid-gas films indicates that more studies are necessary in order to draw conclusions about using the canister drainpipe for filling with liquid metals.

2.3.1 DPC Drainpipe Flow Experiment

As discussed above, it is imperative to thoroughly understand the filler materials that flow through a pipe. A separate computational simulation and experiment are necessary to understand any unforeseen issue of filling a DPC using a drainpipe. This experiment will inform decision making regarding filling DPCs using a drainpipe. Due to the high specific gravity of metals, filling by creating a liquid film on the pipe walls is conceivable. The resultant flow regime is two-phase, annular. If properly organized and controlled, the filling could be smooth, continuous, without pulses, vibrations, or other hydraulic effects that may compromise the entire filling process.

The literature includes many experimental and analytical studies of vertical annular flows in pipes. However, most of these have been conducted using water or other light liquids. It is difficult to find any existing literature describing studies using liquid metals. Liquid metals differ from water in two major properties—density and surface tension—two extremely important properties when considering the annular film that develops on the pipe's wall. Experimenting with liquid metals can prove the feasibility of filling through the drainpipe. Simulations (CFD) can be carried out along with the tests to compliment the assessment and to allow for scaling the problem to a real DPC.

Most of the metals are solid at normal (room) conditions. Bringing the metals into liquid state for experimentation would be expensive. To avoid this expense, mercury can be used as a surrogate metal. Mercury is heavier than most metals and has comparable surface tension, which qualifies it as an ideal surrogate. ORNL has already developed an infrastructure for experimenting with mercury which can easily be leveraged for this type of testing.

Average liquid film thickness and topology are important for detailed understanding and simulation of annular film flow of liquid metal in vertical pipes. The existing models and correlations either have large relative errors or narrow application ranges. Therefore, a new set of experiments with mercury is being planned to provide greater understanding of the process and to complement the existing knowledge base of annular vertical pipe flows. The proposed data collection will include pressure, liquid and gas velocities, liquid film thickness, effect of viscosity, etc. Previous studies indicate that the film thickness is a function of Reynolds and Weber numbers for both liquid and gas. The collected flow regime data will be used mainly to establish limits for maximum and minimum liquid filling rates in the system. Analytical models will be developed and benchmarked along with the experiments.

2.3.2 Film Thickness Measurement Technique

Unfortunately, liquid metals are opaque and reflective, and light methods will not be applicable for flow visualization. Instead, the film's thickness can be measured using a conductivity-based technique. For a conducting liquid (e.g., mercury), the liquid film's thickness is proportional to the conductance of the film, whereas the droplet-laden gas core is not. Therefore, the approach is to impose an electrical potential between a pair of electrodes in contact with the liquid film and measure the resulting current, which is a function of the conductance of the film, hence of its thickness. This technique has been used extensively [11, 12].

A cluster of four film thickness sensors is shown in Figure 19(a). The sensor consists of one "transmitter" ring electrode, 32 "receiver" island electrodes equally spaced around the circumference, and one insulation ring. The ring and island electrodes are flush with the inner pipe wall, making the film thickness sensor nonintrusive. During the signal acquisition, the transmitter electrodes are activated successively by supplying them with a rectangular voltage pulse. For each transmitter activation, the resulting current is measured successively at the receiver electrodes in the corresponding unit. A full cycle, which is necessary to activate all transmitters and to measure the current at all receivers, takes

0.2 ms. Therefore, the total measuring rate is 5 kHz, which is much higher than the physical phenomena observed in annular flow. The principle and the signal acquisition hardware are the same as those in the electrode-mesh sensor of Prasser et al. [13].

The sensor is calibrated experimentally using a static liquid film. It is made by inserting a nonconducting insert of known diameter into the sensor, mimicking the gas core, and filling the remaining volume between the sensor and the insert with mercury. A calibration curve is determined for each receiver with the fit-model. A typical example of a curve fit is shown in Figure 19(b). It shows that the sensitivity of the sensor decreases for increasing film thickness and that a film's thickness up to about 3.5×10^{-3} m can be measured with sufficient sensitivity.

The current measured film thickness at a receiver is a function of the film's conductance integrated over the control-volume in between the transmitter and receiver. Therefore, at each measurement location, a mean film thickness averaged over this control-volume is measured at each instant. This approach is intrinsic to the conductivity-based film thickness measurement technique and is also true for the conductivity-based measurements in the literature.

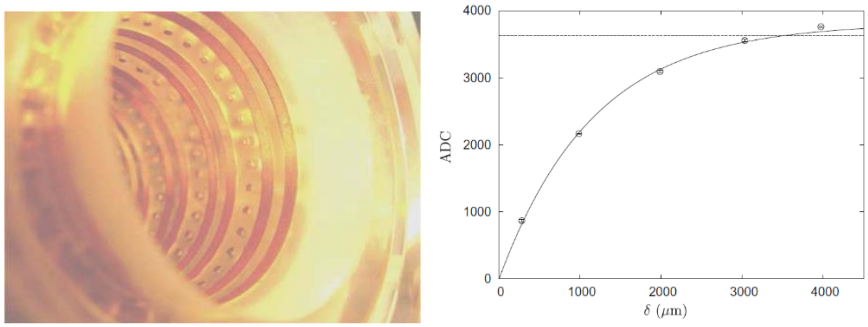

(a) (b)

Figure 19. (a) Photo of Film Thickness Sensor; Conductance is Measured between a Ring-Electrode and an Island-Electrode Flush within the Wall. (b) Typical Calibration Curve Using Stagnant Mercury Film.

The filling simulations that have been performed on the lower region (mouse holes) of a prototypic DPC show successful filling of the inner space voids and smooth, even liquid level progression. Several liquid metals and surrogates are being tested as potential candidates for fillers. The problem requires intensive computing and is a good candidate for a high-performance computing application. Additionally, a pipe flow experiment to gain insight into filling a DPC using drainpipe has been discussed. Future work includes filling the upper regions of the canister, assessing options for filling through the drainpipe, and model validation on lab-scale experiments.

3. FILLING EXPERIMENTS AND DEMONSTRATIONS

The objective of experimental testing is to validate the computational models designed to simulate the filling process. The scope of the experimental studies documented in this report is to provide validation for single physics, or unit testing of flow simulation to determine injectability, void filling, filling time, filling method (gravity vs. pump), etc. In the subsequent phases of this work, other phenomena, such as the thermodynamic process of phase change behavior and heat transfer, will be addressed experimentally using a separate-effects approach. Ultimately, the purpose of experimental studies is to build confidence in the computational models and simulations to help ascertain the feasibility of the DPC filling process.

A separate-effects approach helps to discern the impact of complex phenomena that ultimately affect injectability and void filling due to mechanical interactions between the molten liquid and various interior surfaces of DPCs. While computational fluid dynamics (CFD) models are capable of resolving the physics of fluids, they do not include the complex physical interactions between fluids and surfaces or the intricate geometric details of DPC interiors. Typically, meso-scale effects such as surface wettability (i.e., contact angle between the fluid and the surface) and surface tension of fluids are modeled in a parametric form that defines a simple *viscous shear*. However, the stochastic variability of surfaces (such as surface roughness), and the effects of joining and intersections may have drastic impacts on the interaction between fluids and surfaces. In a physical configuration in which fluid flow is determined by a significant pressure differential, these surface effects may not be dominant. However, for this physical configuration and the planned filling process, the importance of a thorough understanding of interactions and the validation of computational models cannot be understated. Moreover, the physics of gas entrapment and void formation is not well understood.

As single-physics computational models are validated and confidence is built, a multiphysics simulation framework that couples fluid flow, thermodynamics of fluids, and heat transfer phenomena will be investigated. The multiphysics computational models and simulations will then be validated through experiments that properly address these phenomena. These models will be critical in narrowing down the choices of candidate filling materials. This capability will also be instrumental in determining whether an external heating source will be needed, and if so, whether it will be used to design such a system. The multiphysics simulation capability may require expansion to include structural analysis. The impact of radiation hardening on mechanical properties may require additional experimental studies. Finally, identification and/or development of process instruments may be required to certify the filling process with a reasonable confidence level.

The following sections present the experimental system setup and results of physical experiment of filling portions of a DPC through its drainpipe. The initial experimental setups are intended to provide high-level integral data such as filling time and entrapped void fraction (determined through narrow-range level monitoring) to allow for verification and/or calibration of viscous shear parameters. The full details of each experiments are provided within appendices to the main report.

3.1 Experiment 1: Drainpipe and Mousehole Filling Process (Water, Glycerin)

To simplify the computational models to reduce runtime and avoid numerical instabilities, spacer grids are simplified by removing detailed mechanical features. These features are fully represented in the experimental setups to guarantee that their characteristic effects are captured experimentally.

The ORNL team has decided to demonstrate the filling process in two experimental setups for initial testing. The first experimental setup mimics the computational model—with the exception of detailed mechanical features in spacer grids as stated earlier—and is intended to provide supporting data for injectability of various fluids through the drainpipe, identification of a sustainable filling rate, and resulting filling time and entrapped void space. This setup will primarily be used for experimental demonstration of the filling process with various fluids used in the CFD simulations, as shown in Table 1.

The DPC filling tests currently use scaled down models to minimize material cost and expedite the testing process while maintaining a high level of feature integrity with the actual canister design. The initial phase of testing will involve the use of liquid (water / glycerin) media to test the experimental apparatus and setup controls and to establish empirical data benchmarks for fluid dynamics simulations. The ORNL team procured three types of spacer grids from Westinghouse: (1) a 17 × 17 standard structural grid, (2) a protective (P)-grid, and (3) an intermediate flow mixer (IFM) grid. While these spacer grids are available to the team, some custom spacer grids are also being fabricated through a subcontractor to closely match the specifications [14]. The custom fabricated spacer grids will be used in the initial experiments, while the Westinghouse spacer grids will be used in later phases of the demonstration work [15].

The liquid-only design, as shown in Figure 20, uses polycarbonate and acrylic parts for the majority of the housing components to facilitate observations of the filling process. The canister is made from 10-in. outer diameter (OD) × ¼-in. thick acrylic tubing, and the outer basket is made from machined sheets of polycarbonate which are assembled with slot features and small fasteners. The upper and lower flanges are also made from ½-in. thick polycarbonate sheets. Two split ring flanges and 16 flanged socket head cap screws mate with a groove cut into each end of the outer container's face, compressing a gasket at each end to effectively seal the ends and prevent leakage of the liquids. A ball valve is installed near the bottom of the container to aid in draining the apparatus at the end of the experiment. The internal components are modeled as closely to the true dimensions (scaled) as possible.

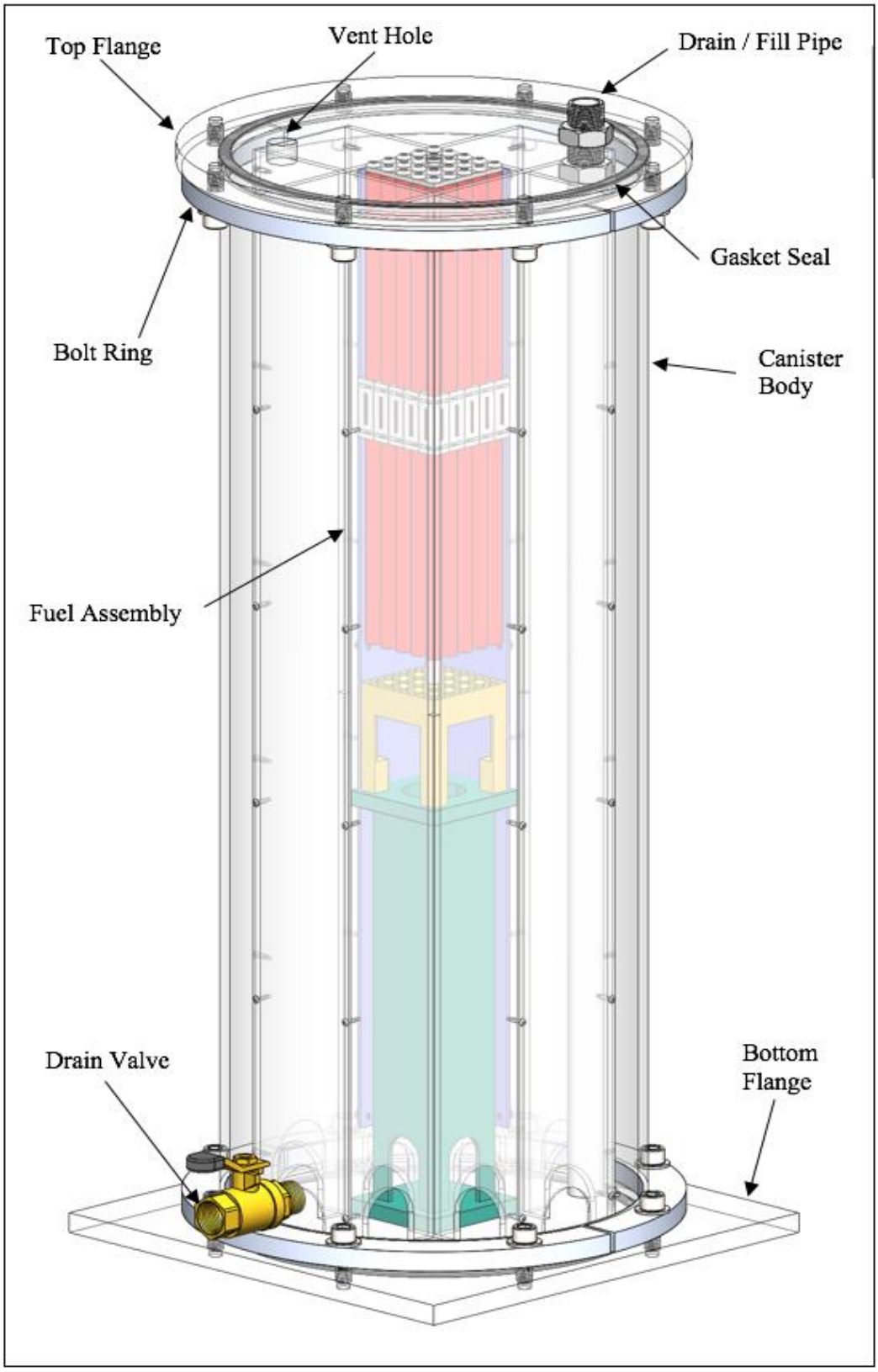

Figure 20. Polycarbonate Canister with Five-Cell Basket for Liquid Experiment.

The basket structure is the left image in Figure 21, and the bottom spacer (green), bottom nozzle (yellow), the fuel assembly (red), and the spacer grid (white), neutron absorber (gray), and the guide tube (pink) are shown as the right image in Figure 21. Figure 22 presents an artist rendering of the experimental setup.

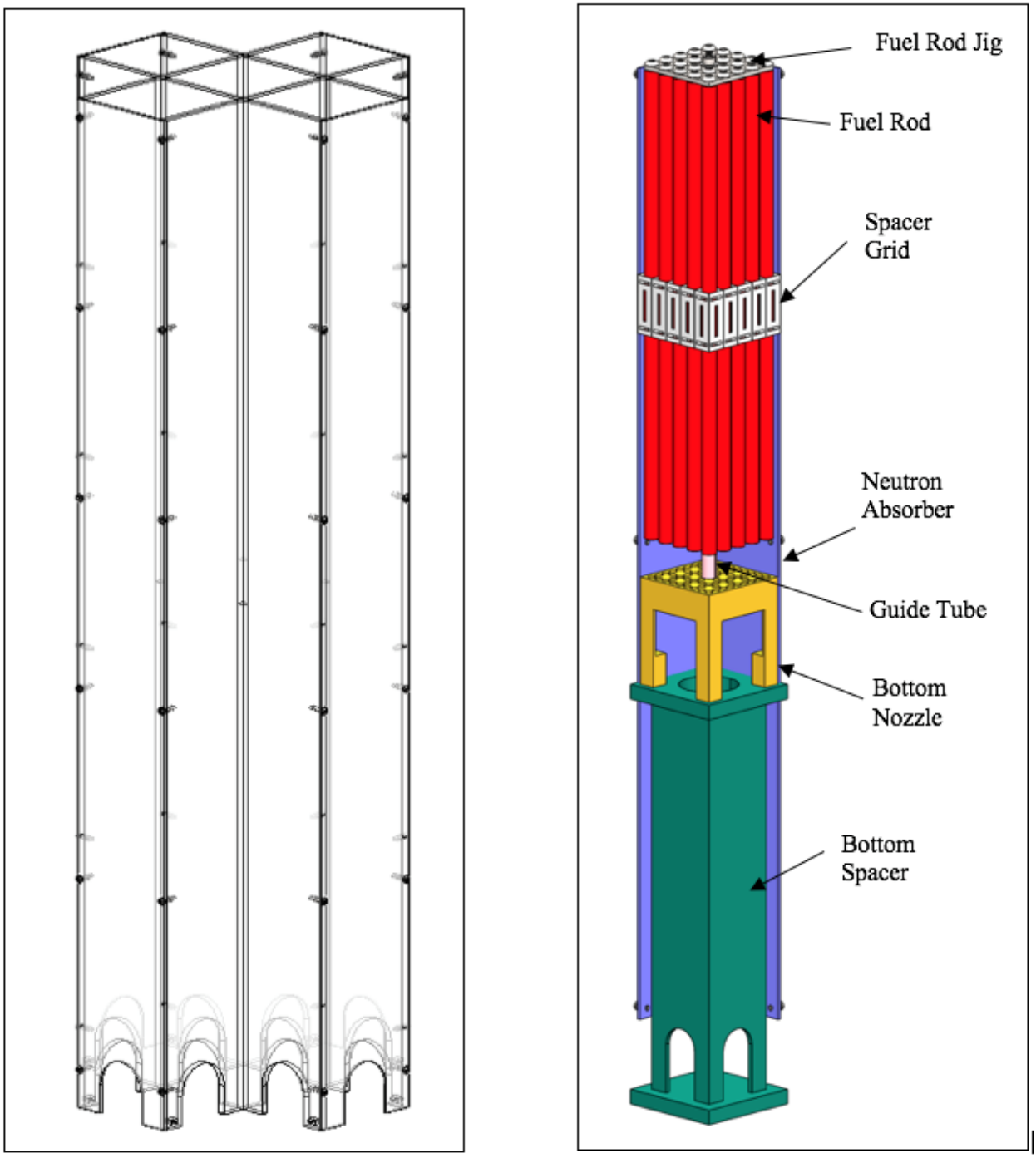

Figure 21. Polycarbonate Outer Basket (Left), and a Stack of the Fuel Assembly (Right).

Figure 22. Artist's Rendering of the Experimental Setup.

As mentioned above, ORNL received three types of spacer grids from Westinghouse. To use these grids in the experimental setup, multiple 5 × 5 grids can be created by carefully cutting the original parts. Alternatively, the original Westinghouse spacer grids can be preserved to be used in an experimental setup that uses a full-scale assembly (e.g., 17 × 17) in the later phases of the project.

Bardet et al. [14] custom fabricated a series of scaled spacer grids that closely match the original grid specifications. An example 5 × 5 spacer grid design is shown in Figure 23 and Figure 24. ORNL is collaborating with this team for fabrication of custom-made spacer grids. An important feature to be added in future experiments are the grid mixing vanes, as they are expected to introduce further potential void areas at the top of the mixing grids.

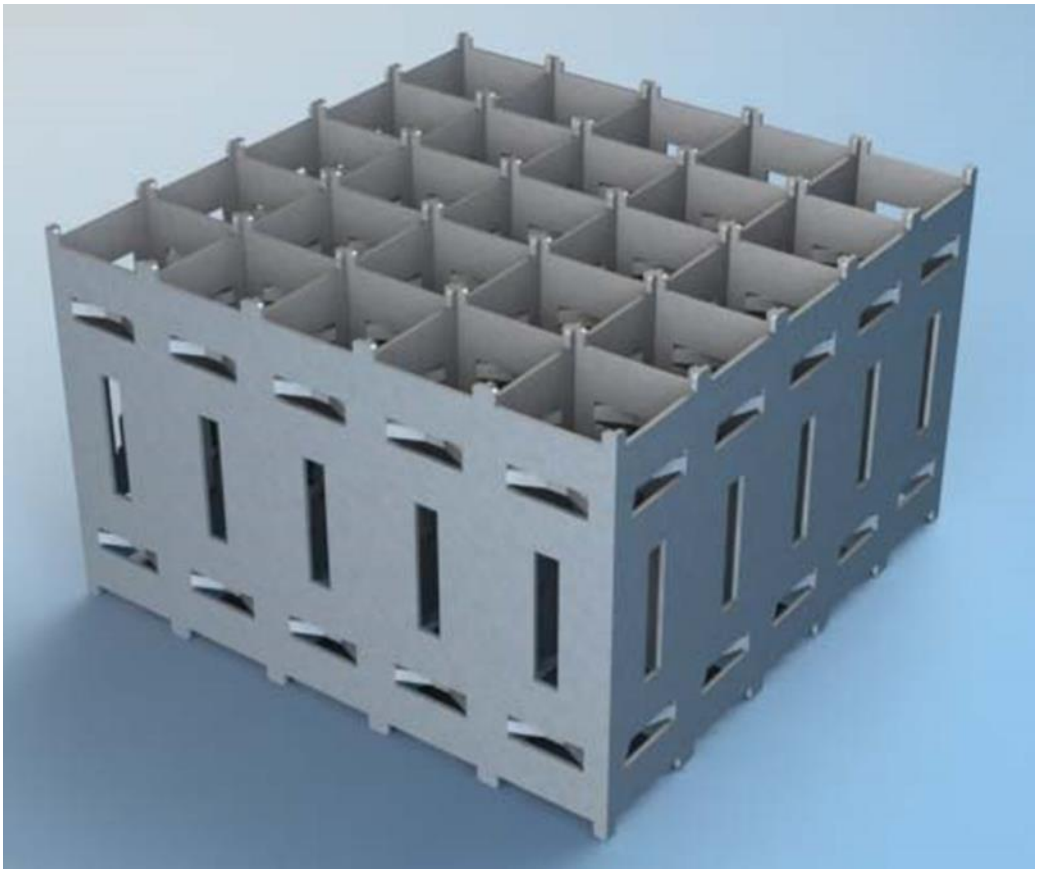

Figure 23. Side View of Spacer Grid (5 × 5) without Mixing Vanes [10].

3.2 Experiment 2: Formation of Voids within Grid Geometries (Paraffin)

The second experimental setup is intended to provide insight into the formation of voids in intricate geometries, such as the small and irregular spaces between the fuel rods and the springs and dimples in spacer grids. The primary focus of this setup is to provide a flexible experimentation capability while being as close to the real geometric configuration as possible. A salient feature of the second experimental setup is its modular construction and its easy disassembly. This setup will use a surrogate filler material with a low melting point, such as the paraffin wax, which melts at 64°C. This will allow for visual inspection of the filled volume, particularly to understand coalescence of multiple smaller void formations into larger voids.

This design also uses polycarbonate and acrylic parts for the majority of the housing components to facilitate observation of the filling process. The container is made from 10-in. OD × ¼-in. thickness acrylic tubing which has been split into two identical halves, as shown in Figure 25. These halves are assembled using two split ring flanges and 16 flanged socket head cap screws that mate with a groove cut into each end of the outer container face. Two or more hose clamps are also used around the outer circumference to secure the canister. The edges are sealed with compressed rubber gaskets, which can be accompanied by room temperature vulcanizing (RTV) sealant if necessary. Gaskets are also located at each end of the container and are compressed by the split ring flanges. The outer basket is made from machined sheets of polycarbonate that are assembled with slot features and small fasteners. The upper and lower flanges are also made from ½-in. thick polycarbonate sheets.

The internal components are modeled as closely to the true scaled dimensions as possible, but to facilitate the disassembly of components once the paraffin has solidified, certain components have been modified.

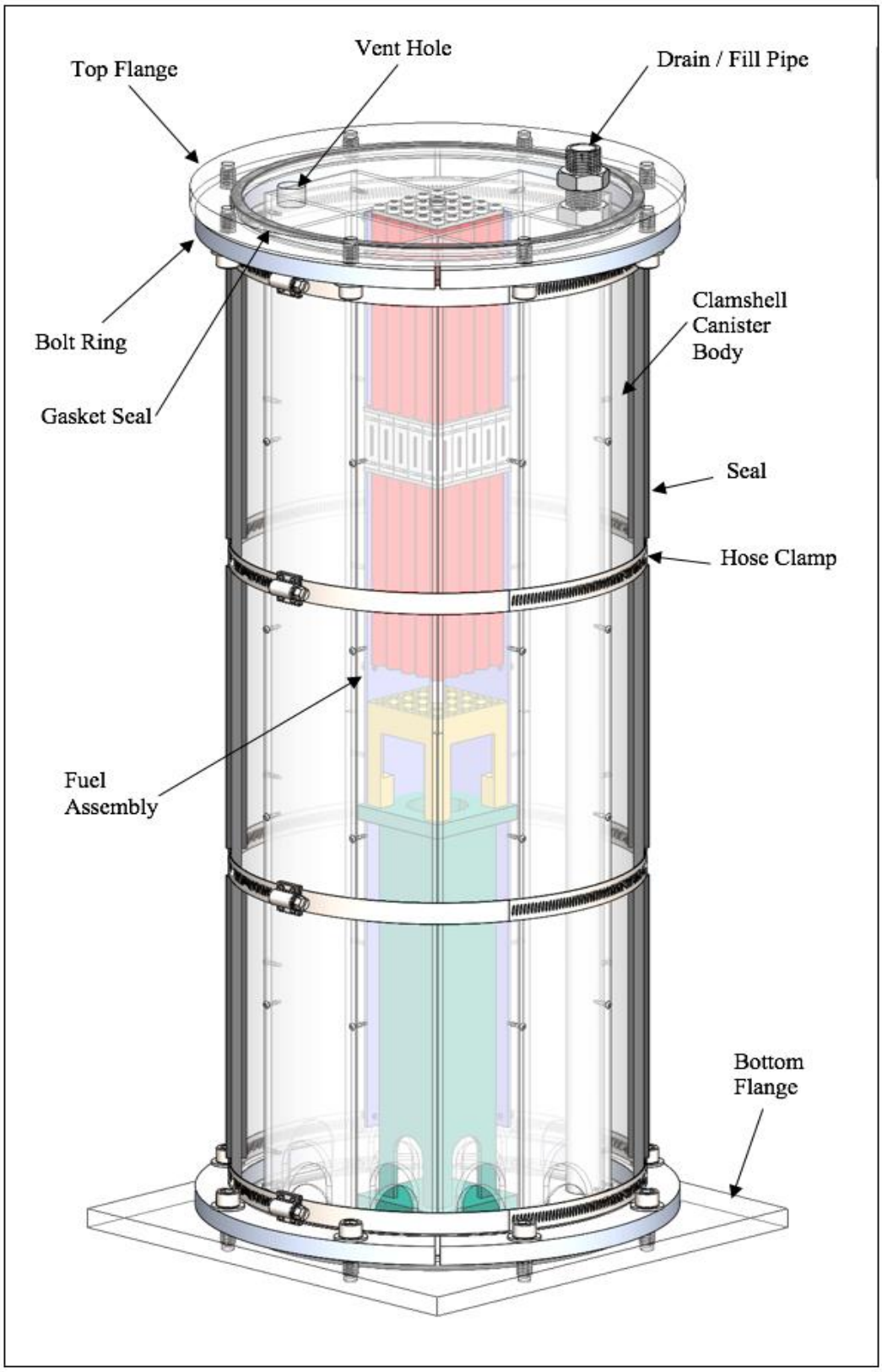

Figure 24. Polycarbonate Canister with Five-Cell Basket for Paraffin Experiment.

The grid spacer design has been modified to be easily disassembled by using upper and lower plates which contain slots to capture the grid panels. The grid panels are also modified to have tabs at each end to mate with the upper and lower plates. Figure 16 shows details of the grid panels. Figure 26 shows the exploded view of the customized modular grid assembly. The fully assembled custom grid is show in Figure 27.

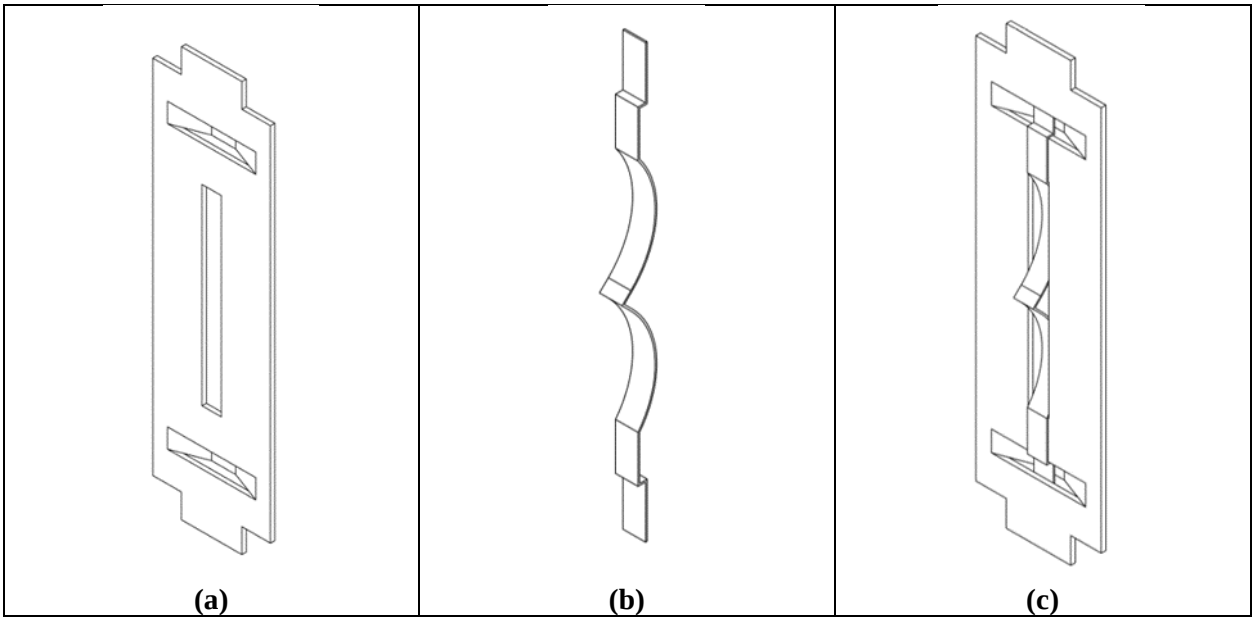

Figure 25. (a) Custom Spacer Grid with Dimple, (b) Custom Spacer Grid Compressed Spring, and (c) Custom Spacer Grid Panel with Dimple Weldment.

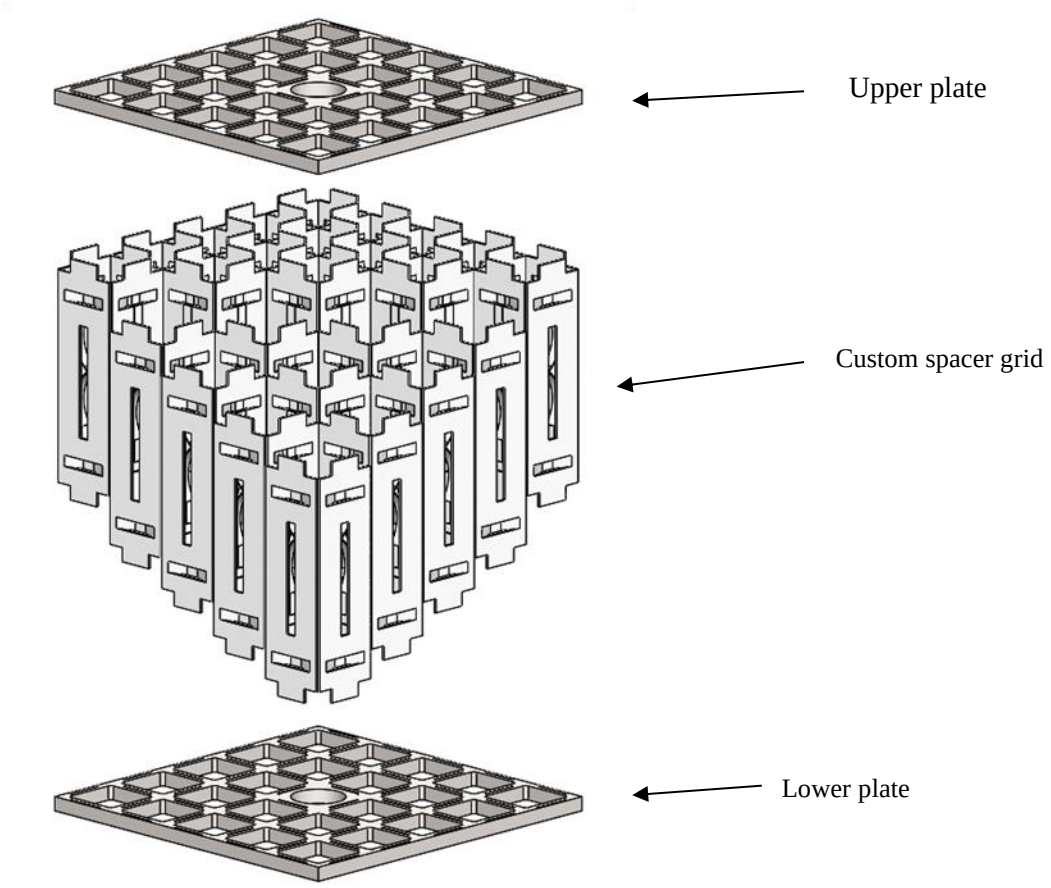

Figure 26. Exploded View of the Custom Spacer Grid Assembly.

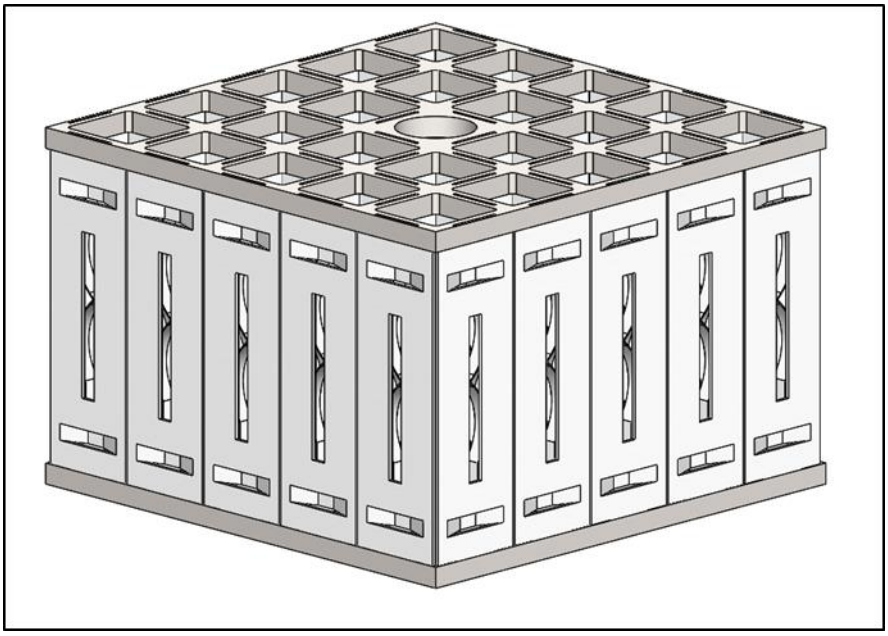

Figure 27. Fully Assembled Custom Modular Grid.

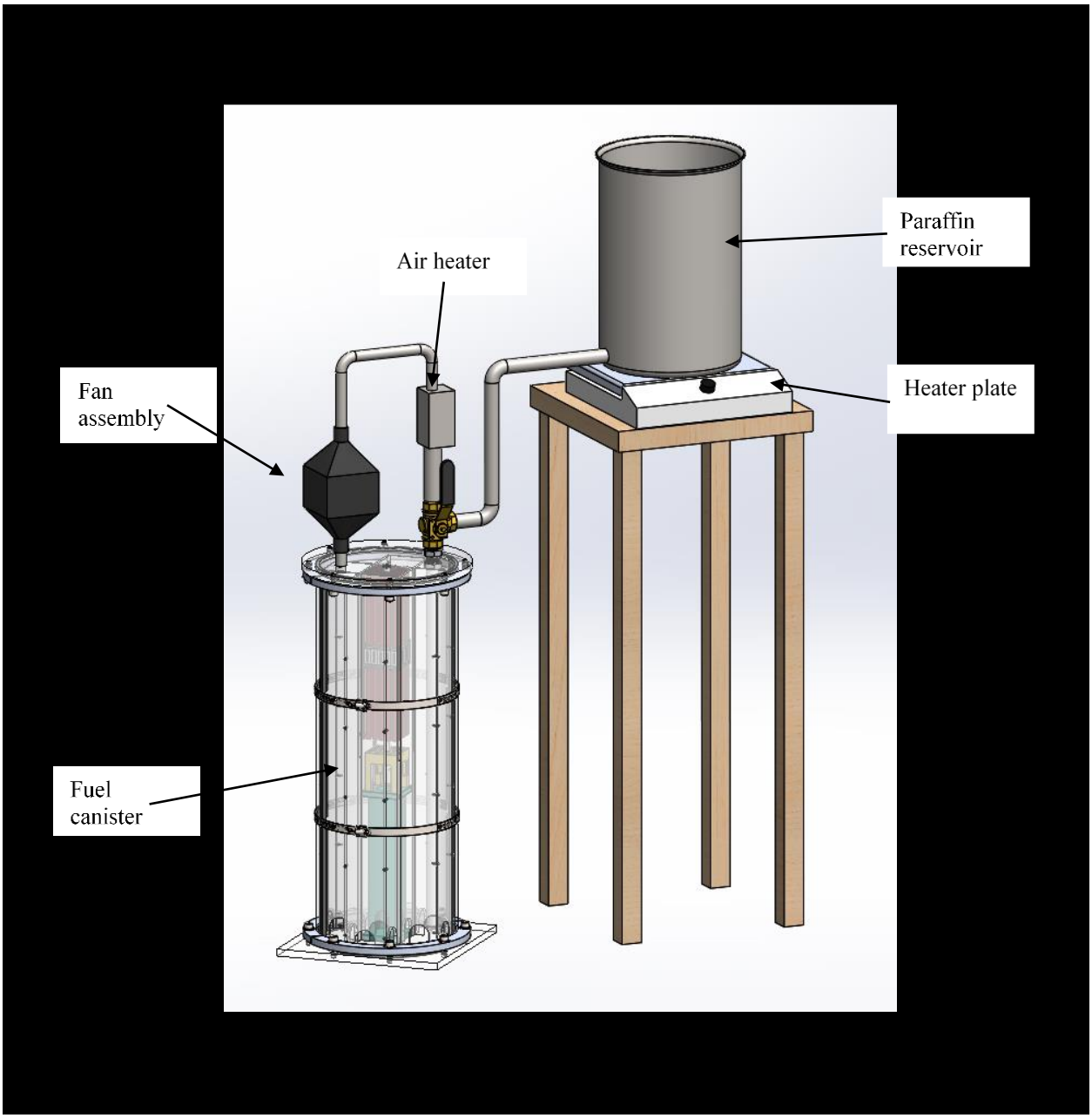

Figure 28. Set-Up for the Paraffin Experiment.

The experimental set-up shown in Figure 28 consists of a split canister assembly, an air heater, a paraffin reservoir, and a three-way valve. Initially, the three-way valve will be positioned toward the air heater tubing. The inline air heater will heat the air being circulated through the heater by the fan connected to the vent hole of the canister. A thermocouple inside the canister will register the air temperature. Once the temperature inside the canister has reached 60°C, it will be ready to be filled with paraffin. A small relief valve will also be installed on top of the upper flange to allow the air to escape as it is being displaced by the paraffin filling the canister.

Turning the three-way valve toward the paraffin reservoir will cause the paraffin to start flowing into the canister. Another valve next to the paraffin reservoir (not shown) will be used to control the paraffin flow rate. To ensure that the paraffin does not solidify before it has completely filled the canister, heat tape will be wrapped around the canister, piping, and valves. The temperature setting on the heat tape will ensure that the paraffin is maintained at 60°C. Multiple thermocouple readings will be used to ensure uniform heating during the filling experiment. Power to the heat tape, heating plate, and the air heater will have logic to ensure that components are not overheated while also ensuring that adequate temperature of the air and paraffin are maintained.

All drawings (Table 3-A) were finalized and forwarded to machine shops for fabrication. Additional information may be found in Appendix A.

Table 3. Drawing Part Number and Quantities Being Fabricated.

DWG	ITEM	Quantity
284-DPC-1110 (Assembly)	Panel weldment (with dimple)	25
284-DPC-1111 (Part)	Panel with dimple	37
284-DPC-1112 (Part)	Spring	37
284-DPC-1120 (Assembly)	Panel weldment (without dimple)	12
284-DPC-1121 (Part)	Panel without dimple	12

Table 4. Parts List.

Item	Specification	Cost	Vendor Info
Fan	1053-1116-ND	$100	Digikey
Heater	AHPF-061	$345	Omega Engineering (not used)
Plate heater (for paraffin wax)	0°C–300°C, hot plate	$115	3118K52, McMaster Carr
Paraffin wax*	Nature Wax C-1	$118	General Wax and Candles
SS-container with temperature gauge and shut-off valve	½-in. NPT Connection	$218.90	10 Gal BrewBuilt Kettle
Metal braided hoses	½-in. ID (up to 177°C)	$315	McMaster Carr
3-way ON/OFF valve	½-in. ID	$100	McMaster Carr
High precision flow valve	¼-in. tube	$380	McMaster Carr
Flexible heating tape	½-in. wide	$1,500	BriskHeat
Thermocouple and reader	--	--	Already have them

3.3 Experiment 3: Molten Metal Flow through the Drainpipe, Mousehole, and Lower Fuel Assembly (Tin)

Following the previous work to demonstrate filling of small-scale DPC geometries with water, paraffin, and glycerin, it was determined that a demonstration using a molten metal casting would be beneficial. Inundation of a small-scale, representative geometry was chosen for this first experiment with molten

metals. Without being exhaustive, the selection of metal includes the following criteria: (1) low melting point, (2) low viscosity, (3) low toxicity, (4) low density, (5) low cost, (6) low freezing range, (7) castability, i.e., without significant casting defects during solidification, and (8) corrosion resistance. Many eutectics of tin, zinc, cadmium, bismuth, copper, and lead are all potentially good candidates, given these criteria. Lead is not a good candidate because of its toxicity and density, and cadmium is not suitable because of its toxicity. Bismuth is costly, and with copper eutectics, its melting temperatures are greater than 475°C. (The maximum allowable temperature for DPC filling will be determined based on thermo-economics; higher filling temperatures are expected to accrue higher the mold heating costs.) To-date, the preliminary screening indicates that zinc and tin are the promising candidate materials for unit testing, and tin was chosen for its low melting temperature (232°C), minimal heath hazards, relative availabily, and low cost. Appendix D provides a more extensive discussion of the tin pour experiment.

This test includes fuel pins and a grid section of the fuel bundle, as well as one of the mouse hole regions and the fill pipe geometry that is accurately sized for the full-scale pipe. The experimental setup is relatively small and can be arranged on a normal sized lab tabletop. The mold and internal components were designed and fabricated by ORNL, as well as the stand and plumbing used for joining the two melting pots. The mold is a stainless-steel container with ½ in. walls on all sides and the bottom, and it is open on the top. The cavity of the mold is approximately 3 in. wide, 5 in. long, and 6 in. tall. The initial CAD model with labels indicating the major experiment components is shown in Figure 29. The target geometry for filling, pretest, is shown in Figure 30.

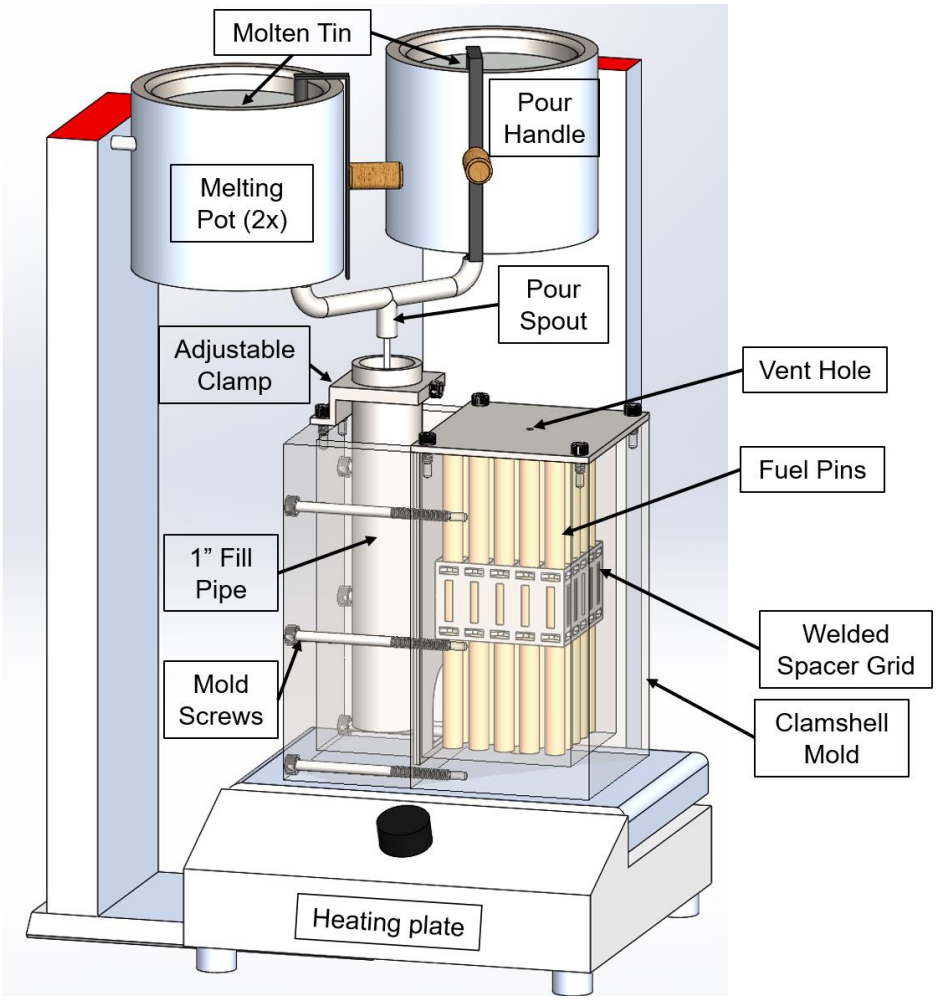

Figure 29. CAD representation of tin pour experimental setup.

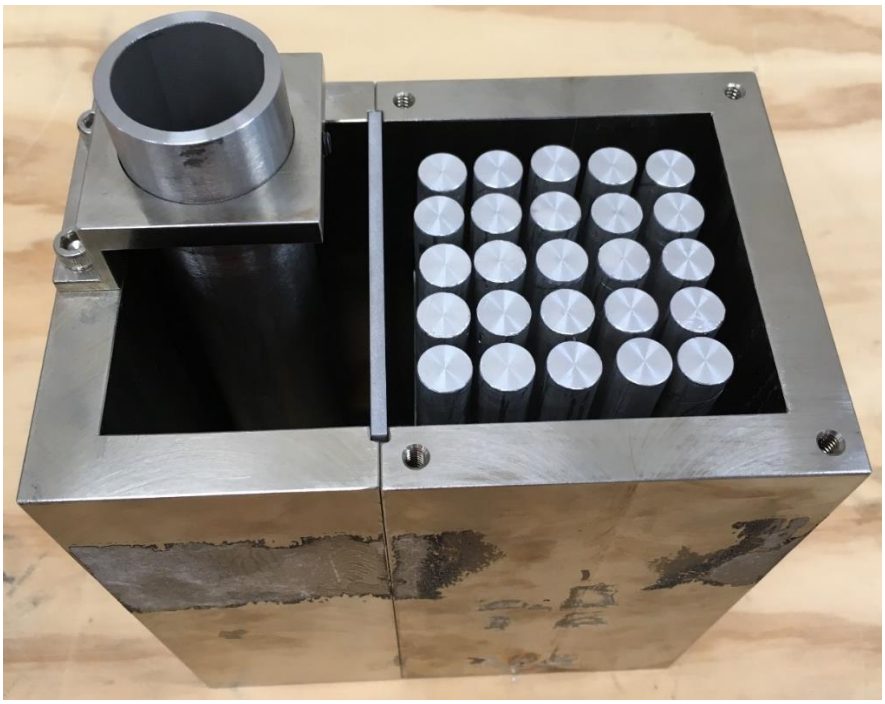

Figure 30. Mold assembly with fill pipe, mouse hole plate, and grid assembly installed.

Eight thermocouples were strategically located in the mold body, and two more were located in the casting volume at the bottom of the fill pipe and at the center of the mouse hole region. Additional thermocouples were also used at the pour spout and in the melting pots to record the tin temperature at the time of pouring.

The casting experiment focused on achieving a continuous pour into the mold assembly to completely fill the void space inside the mold. Thermocouples were placed at various locations in the mold body, with additional thermocouples being placed at the bottom of the fill pipe and the mouse hole region. Other thermocouples were used to measure the temperatures of the melting pots, heat tape, and pour spout.

The mold was filled to the top of the mold face. Since the aluminum rods were very close to this plane, they were not fully covered by the molten tin during pouring because it was not worth the risk of spilling tin over the side of the mold. This precaution did not cause an issue, because the focus of this experiment was to observe the behavior of void formation during casting mainly in the grid region, which was completely encompassed by molten tin. Figure 31 shows the mold assembly immediately after the pour was stopped and the tin was still in a liquid state.

Figure 31. Mold assembly after pour with tin in molten state.

Analysis of the data shows that the tin had a brief period in the solidification process prior to the first data gap. This is easily observed by the constant temperature at approximately 232°C across all thermocouple readings, representing the phase change from liquid to solid. Some thermocouples read a bit lower than this value because of natural thermal gradients present in this system. Thermocouples in or nearer the tin naturally read higher temperatures than thermocouples embedded in the mold wall or near the edges or corners of the molds.

The temperature data were captured for the initial cooldown, the beginning of the phase change region, and at various times during the secondary cooldown, so the gaps in the data were filled easily based on the cooldown rates. Each of the 10 thermocouples' recorded data were maintained, and data in the gaps were calculated using the data in the secondary cooldown region (which occurred place after the solidification process) and using a third-order polynomial to best fit the recorded data through all three regions of recorded data. Figure 32 shows the data from thermocouple 1, representing the regions of collected and calculated data. The blue regions are recorded from the data acquisition system, the red regions are calculated based on a third-order polynomial fit of the recorded data, and the yellow region is the extension of the phase change region.

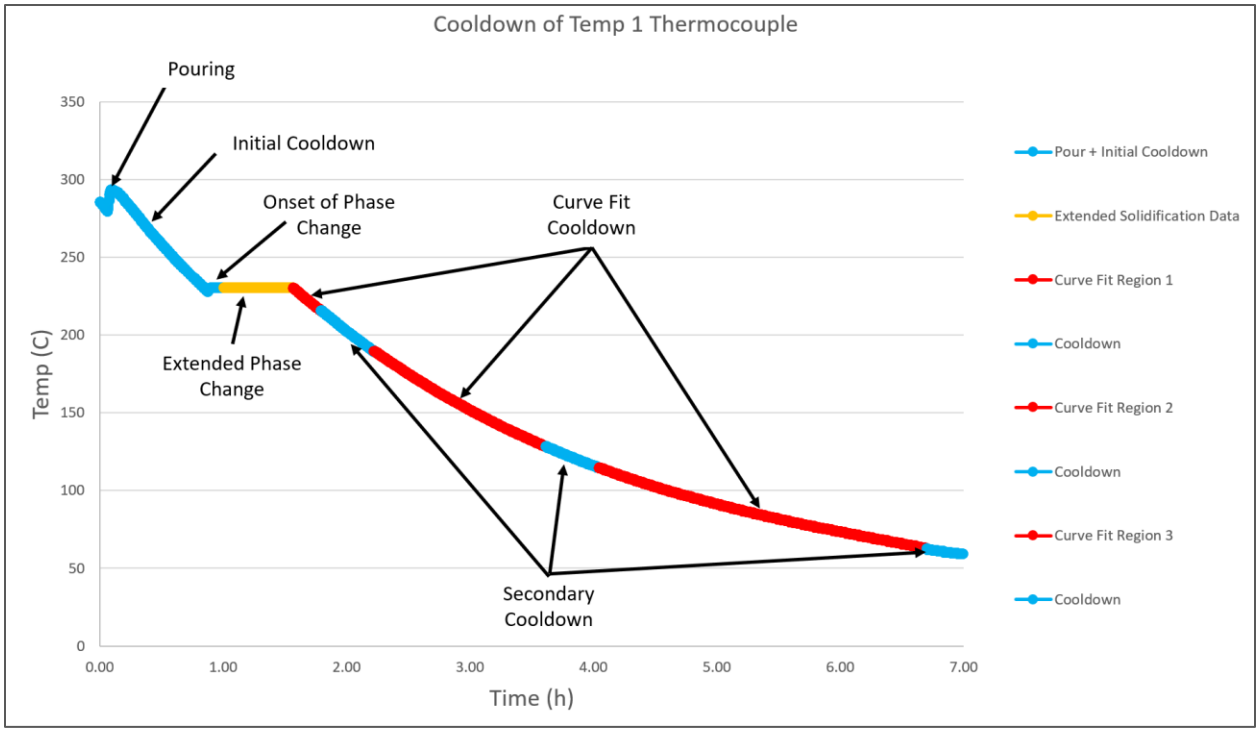

Figure 32. Thermocouple temperature data regions.

To determine the effectiveness of filling, an x-ray scan was performed on the assembly after the tin was cooled and then the assembly was subjected to a destructive inspection using EDM. The casting was imaged via two-dimensional radiography. Two image quality indicators were utilized during radiography, and sufficient source penetration through the casting to the imaging plate was confirmed. In addition, a 0.5 in. diameter steel ball placed on the casting surface produced a reference length. This ball, which was labeled "0.500 in," can be seen in the image on the right in Figure 33.

Figure 33. An image of the tin casting (left) and the associated radiographic image (right).

Destructive analysis of the casting around the area of the drainpipe further characterized this region of suspected porosity. A horizontal bandsaw was used to produce two cross-sectional cuts through the 3 in. face of the casting, positioned as shown in Figure 34. "A1" in the figure is the approximate distance from the casting's edge to the first cut (2 cm) and "A2" is the approximate distance from the casting's edge to the second cut (4.3 cm). The second cross-sectional cut served specifically to evaluate the area of defect identified via the radiograph. Mostly smooth macroporosity is evident and some macroporosity penetrates to the mouse hole's stainless-steel wall. Figure 35 shows the large shrinkage pore indicated in the radiography and revealed in the destructive examination. The exact cause of this behavior is not obvious, though its size would suggest an underfed region of the casting resulting in shrinkage porosity [25].

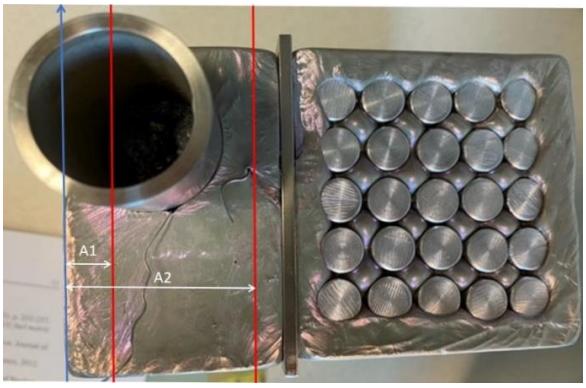

Figure 34. Cross-sectional cuts of the tin casting. The blue line is a reference representing the far edge of the casting and each red line reflects a cut.

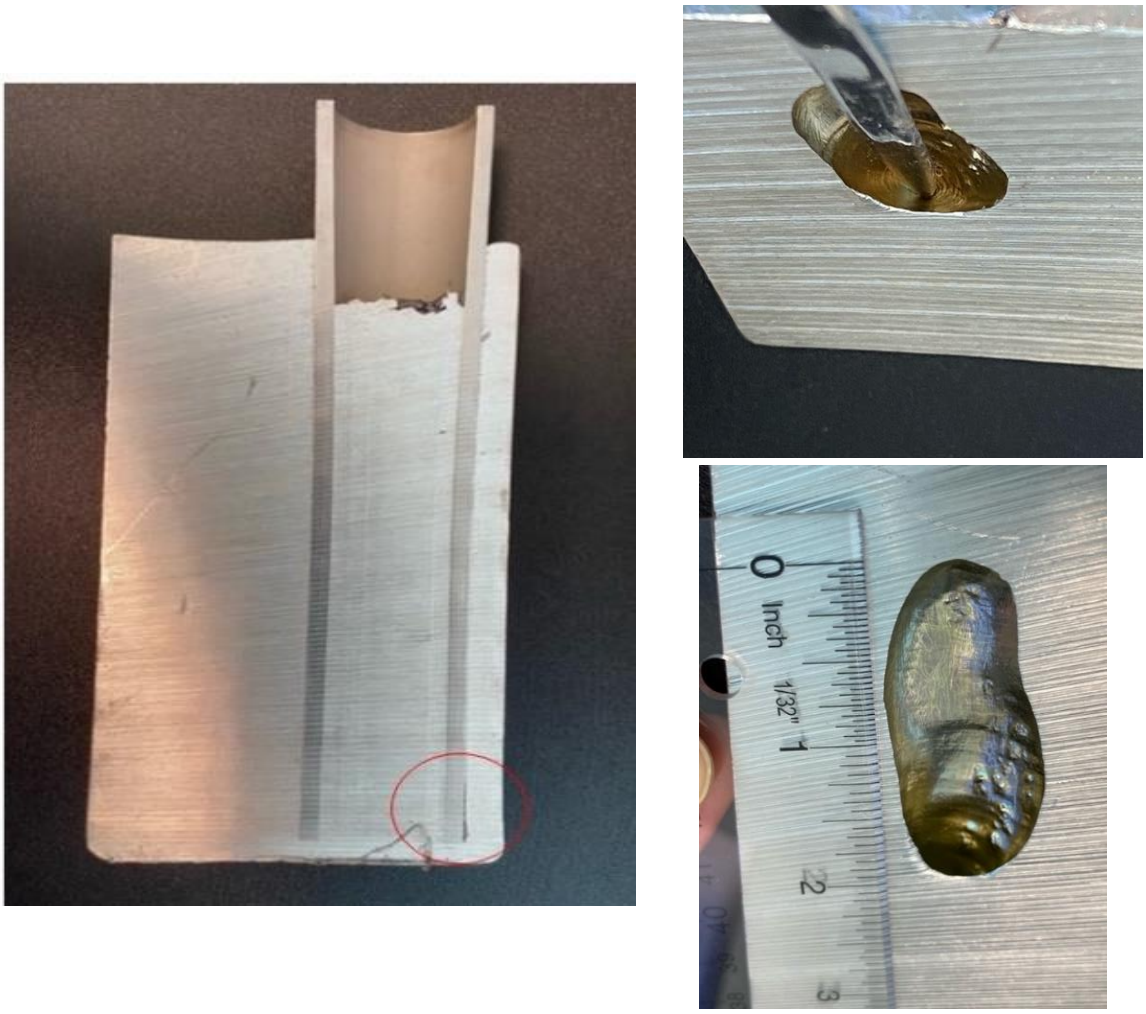

Figure 35. Identified casting flaws further revealed in the destructive examination include (a) a small area of suspected porosity along the bottom edge of the drainpipe (circled in red) and (b and c) a void at the A2 location approximately 2”x1”x1” likely developed due to shrinkage during cooling.

Further destructive analysis of the casting’s rod array is planned in FY2022 to further confirm the results of NDE, namely that no significant defects are located in this important area. Additionally, in FY2022, all characterization data will be used to support further development and benchmarking of a ProCAST simulation. Given that some defect behavior should be expected in any casting [25], development of simulations that can successfully predict the behavior will allow the development of casting conditions that will minimize defects (including surface connected defects) and optimize filler performance.

The tin pour allowed important steps towards the final DPC application:

1. Data acquisition procedures for monitoring filling and casting solidification were developed.
2. Thermocouple placement procedures were developed to assist in casting monitoring and process development.
3. The coupled multiphysics analysis capability offered by metal casting software (e.g., ProCAST) will provide a high-fidelity modeling capability for the full-scale DPC model casting, which is needed for development of the DPC filling process.

4. The computed results from the ProCAST software that are critical to the DPC filling process include total shrinkage porosity, Niyama criterion for assessing the propensity to porosity formation, effective stress, effective strain, and deformation.
5. Filling DPCs can be optimized based on combined experimental and computational study.

The following accomplishments relevant to the final DPC application were attained:

1. Casting procedures were developed by a multidisciplinary team comprising mechanical engineers, nuclear engineers, and materials scientists.
2. Procedures for obtaining boundary conditions required for DPC were developed.
3. Tin was successfully cast on a mock-up model mold that included grid and fuel inserts.
4. Filling and solidification metal casting simulations were conducted for the complex mock-up grid and fuel insert geometry.
5. The solidification model provides useful data on thermocouple placement (i.e., avoiding regions of large thermal gradients).
6. Tin has demonstrated materials compatibility with the cask grid, with no large voids detected.

3.4 Experiment 4: Planned Drainpipe Flow Experiment (Mercury)

The Target Test Facility shown in Figure 36 is a full-scale Spallation Neutron Source prototypical mercury loop that was recently modified to accommodate a smaller test section using a reduced flow rate. The facility has an inventory of ~19,000 Kg of liquid mercury, and it can drive a maximum of 547 gpm using a variable frequency driver to control the loop's pump. The typical discharge shutoff pressure is 180 psig. The facility is enclosed in an isolated room that provides independent ventilation and a filter system that is able to remove mercury vapors and maintain safety levels inside the enclosure. This facility counts with mercury vapor monitors and alarms that monitor mercury vapor levels inside the enclosure and its surroundings. A team of trained personnel with extensive experience in mercury handling operates the loop.

A simple extension of the mercury loop configuration can be designed and built to experiment with a vertical pipe of the same size as the DPC drainpipe (4 m, 1.25-in. ID). It will require some small modifications of the existing configuration and procurement of the necessary instrumentation. The existing data acquisition system can be used. This investment will be minimal compared to the initial investment in the existing mercury loop. Appendix D provides additional discussion on preparation for the mercury pour experiment.

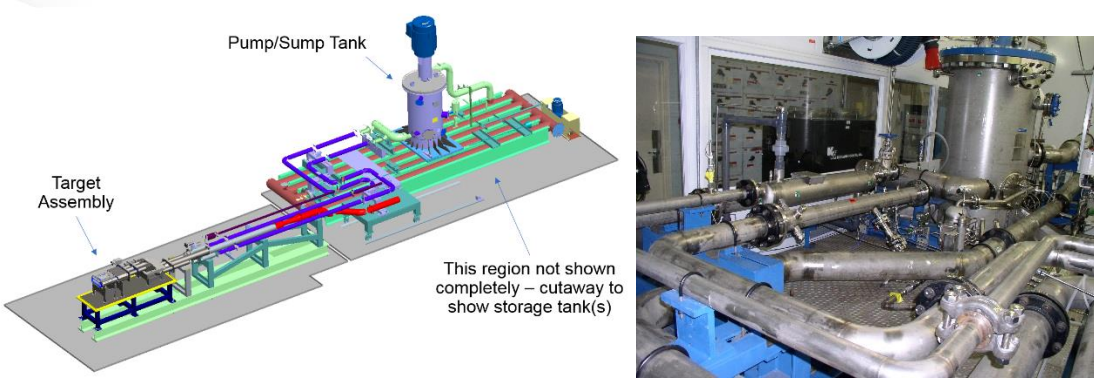

Figure 36. Target Test Facility Mercury Loop.

.

4. DISCUSSION

Two initial experimental setups were designed for liquid and paraffin experiments. Data collected from these experiments are being used to validate the filling simulation described in Section 2. The Hg experiments were not completed in FY21 and are planned for FY22. The paraffin experiments required external heating like any molten metal–based fillers and provided valuable experience which informed the full-fledged tin pour experiment. The results of the tin pour experiment provided results which will inform the development of the DPC experiments planned for the future.

This page is intentionally left blank.

5. CONCLUSIONS

A multi-phase approach as described in the joint workplan [4] culminating to a full-scale demonstration and a fully validated multiphysics simulation/prediction capability are being pursued to support direct disposal of DPCs. An acceptable filler should establish that the probability of criticality in DPCs during the disposal time frame is below the probability threshold for inclusion in a repository performance assessment. As discussed in the introduction, the filler option to support direct disposal of DPCs is being investigated in parallel with the other options such as criticality consequence assessment [17, 18, 19]. This report describes the initial single physics CFD model developed to simulate the filling process and the planned experimental setups to validate the CFD simulation and the results of those experiments which have been completed to date. The initial filling simulations of the lower region (mouse holes) of a prototypic DPC show successful removal of the inner space voids and smooth (even) liquid level progression. The filling through the drainpipe was investigated as a decoupled process due to complexity of modeling flow in a narrow long pipe. A flow experiment through a pipe to understand any issue related to filling a DPC using drainpipe is also discussed in this report. Finally, a tin pour experiment was conducted along with NDE and destructive examination of the casting.

Future efforts include the setup and execution of the Hg experiment, continuation of the simulation validation, the development of acceptance criteria for filler systems and identification of the screening criteria of candidate fillers.

Relevance to final application

The following important steps were made towards the final DPC application:

1. Data acquisition procedures for monitoring filling and casting solidification were developed.
2. Thermocouple placement procedures were developed to assist in casting monitoring and process development.
3. The coupled multiphysics analysis capability offered by metal casting software (e.g., ProCAST) will provide a high-fidelity modeling capability for the full-scale DPC model casting, which is needed for development of the DPC filling process.
4. The computed results from the ProCAST software that are critical to the DPC filling process include total shrinkage porosity, Niyama criterion for assessing the propensity to porosity formation, effective stress, effective strain, and deformation.
5. Filling DPCs can be optimized based on combined experimental and computational study.

The following accomplishments relevant to the final DPC application were attained:

1. Several screening criteria were identified. To date, the selection of metal fillers includes the following criteria: (1) low melting point, (2) low viscosity, (3) low toxicity, (4) low density, (5) low cost, (6) low freezing range, (7) castability, i.e., without significant casting defects during solidification, and (8) corrosion resistance.
2. Casting procedures were developed by a multidisciplinary team comprising mechanical engineers, nuclear engineers, and materials scientists.
3. Procedures for obtaining boundary conditions required for DPC were developed.
4. Tin was successfully cast on a mock-up model mold that included grid and fuel inserts.
5. Filling and solidification metal casting simulations were conducted for the complex mock-up grid and fuel insert geometry.
6. The solidification model provides useful data on thermocouple placement (i.e., avoiding regions of large thermal gradients).
7. Tin has demonstrated materials compatibility with the cask grid, with no large voids detected in the grid area.
8. Micropore defect, which is well known to occur in the last regions to solidify, is isolated and not connected with any other cracking or long void defect, such as interdendritic porosity, that would lead to any water intrusion.

This page is intentionally left blank.

6. REFERENCES

1. StoreFuel and Decommissioning Report, Ux Consulting Company, LLC, Vol. 20, No. 238, (2018).
2. E. Hardin et al., *Investigation of Dual-Purpose Canister Direct Disposal Feasibility (FY14)*, FCRD-UFD-2014-000069 Rev.1, (2014).
3. J. B. Clarity, K. Banerjee, H. K. Liljenfeldt, and W. J. Marshall, "As-Loaded Criticality Margin Assessment of Dual-Purpose Canisters Using UNF-ST&DARDS," *Nuclear Technology,* 199(3), 245–275 (2017).
4. *Joint Workplan on Filler Investigations for DPCs*, Sandia National Laboratory, SFWD-SFWST-2018-000481, Rev.0, (2017).
5. Holtec International, *Final Safety Analyses Report for the HI-STORM 100 Cask System*, 2010.
6. CD-Adapco, *STAR-CCM+ 13.02 Theory Guide*, (2015).
7. https://mdx.plm.automation.siemens.com/star-ccm-plus.
8. I. Zadrazil and C. Markides, "An experimental characterization of liquid films in downwards co-current gas-liquid annular flow by particle image and tracking velocimetry," *Int. J. of Multiphase Flow* 67, (2014).
9. A. Padmanaban, *Film Thickness Measurements in Falling Annular Films*, Thesis McS, University of Saskatchewan, (2006).
10. P. Kapitza, Wave flow of thin layers of a viscous fluid, Collected papers of Kapitza, Pergamon Press, (1965).
11. S. V. Paras and A. J. Karabelas, "Properties of the liquid layer in horizontal annular flow," *Int. J. Multiphase Flow* 17 (4), 439–454 (1991).
12. L. B. Fore and A. E. Dukler, "Droplet deposition and momentum transfer in annular flow," *AIChE J.* 41 (9), 2040–2046 (1995).
13. H. M. Prasser, A. Boettger, and J. Zschau, "A new electrode-mesh tomograph for gas–liquid flows," *Flow Measure. Instrum*. 9, 111–119 (1998).
14. N. A. Weichselbaum et al., *Surrogate Spacer Grid Design for Fluid-Structure Interactions Studies in Fuel Bundles*, The George Washington University, Washington, DC.
15. A. Rubin et al., *Volume I: Experimental Database and Final Problem Specification, OECD/NRC Benchmark Based on NUPEC PWR Subchannel and Bundle Tests (PSBT)*, (2010).
16. J. B. Clarity et al., *Dual Purpose Canister Reactivity and Groundwater Absorption Analysis*, M3SF-20OR010305015, US Department of Energy, Spent Fuel and Waste Disposition, June 2020
17. Gregory G. Davidson, et al., *Initial Neutronic and Thermal-Hydraulic coupling for Spent Nuclear Fuel Canister*, ORNL/SPR-2019/1144, Oak Ridge National Laboratory, 2019.
18. L. L. Price et al., *Preliminary Analysis of Postclosure DPC Criticality Consequences*, M2SF-20SN010305061, Sandia National Laboratories, 2019.
19. L.L. Price et al, *Status Report: Progress in Developing a Repository-Scale Performance Assessment Model*, M4SF-20SN010305064, Sandia National Laboratories, 2020.

This page is intentionally left blank.

Appendix A FY2019 MID-YEAR STATUS

This appendix documents work performed supporting the US Department of Energy (DOE) Nuclear Energy Spent Fuel and Waste Disposition, Spent Fuel and Waste Science and Technology, under work breakdown structure element 1.08.01.03.05, "Direct Disposal of Dual Purpose Canisters." In particular, this appendix fulfills the M3 milestone, M3SF-19OR0103050115, "Initial validation of CFD filling simulation," as Revision 2 to M4SF-18OR010305017, "Unit test plan for filler demonstration," within work package SF-19OR01030501, "Direct Disposal of Dual Purpose Canisters–ORNL."

This appendix presents (1) the CFD filling simulation of the spacer grid region of the assemblies using the model described in the main body of the report, and (2) data collected in a laboratory experiment using surrogate fillers for validating the simulation results. In summary, this appendix presents the current simulation and experimental validation status of the DPC filler project. This report will be revised periodically to document step-by-step development of a fully validated multiphysics tool that can be used for simulating the DPC filling process using various filler materials. This multiphysics tool is also envisioned to be used to select a small set of filler materials for further laboratory testing (e.g., corrosion properties, radiation damage).

A-1 Simulation Progress

A-1.1 Bottom Nozzle Filling Simulation

The main body of this report primarily presents the CFD filling simulation of the mouse hole region and the progress made to simulate the lower grid region. Since the time of report release, the following progress is made: the lower grid simulations were finalized, and the spacer grid region was fully simulated. The results are briefly presented below. This completes the initial scope of filling simulations for model validation. The simulations will continue with modeling of real canister systems for numerical filling evaluation.

The lower assembly grid region occupies the area of the lower tie grid and the upper section of the assembly stand. A part of the geometry is skipped (shortened) to save computing time by transposing the lower tie grid to fit over the mouse holes region. The rationale assumes that the flow topology (level velocity and liquid fraction) at the entrance of the lower grid is the same as the flow topology at the exit of mouse holes. Technically, this simulation is accomplished by mapping data between nonconformal domains.

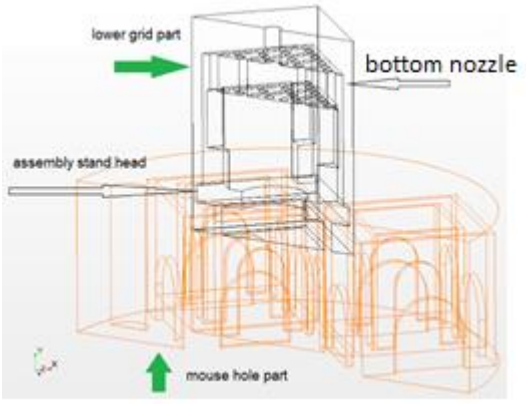

Figure A-1. Lower Tie Grid Position Relative to Mouse Holes Region with All Important Features Indicated.

The components and their relative positioning are shown in Figure A-1. The mouse hole region is shown in orange to distinguish the components. The lower grid section has an overall height of 113 mm and is set to overlap the mouse hole region, with 15 mm to allow for data mapping. The lower grid section is meshed with about 100,000 elements. The large number of elements is due to the holes in the lower assembly grid.

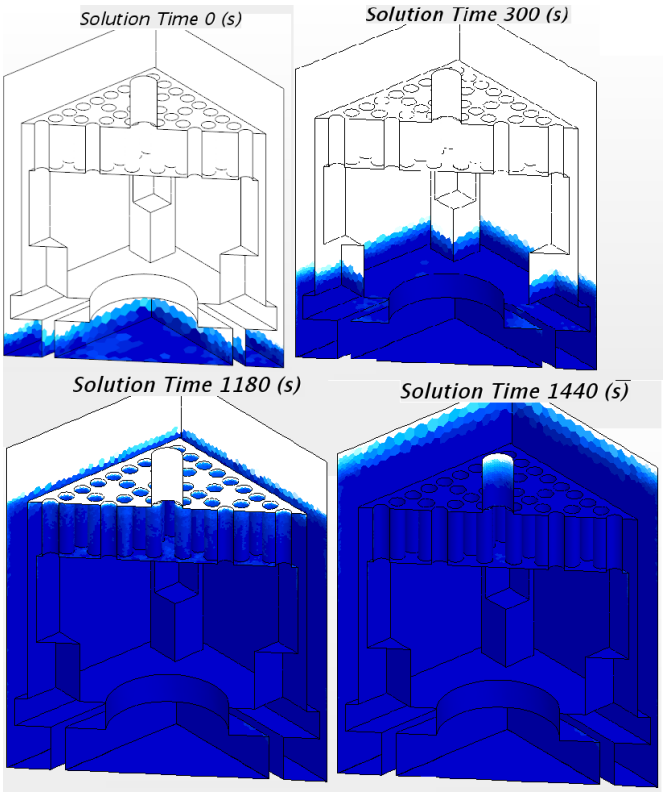

Figure A-2. Filling Simulation of the Lower Assembly Bottom Nozzle Showing Four Instances of the Filling Process. Geometry is Clearly Visible. Liquid Volume is Blue and Shows a Smooth and Continuous Level Progression.

The runs for water, glycerin and silicon oil were successfully performed and showed no trapped voids. They were executed on 96 cores (three nodes × 32 cores each). The total computed physical time was 1,440 s. The level progressed smoothly, as in the previous DPC section (mouse holes), without any anomalies. Four snapshots of the entire lower grid section showing the level advancement are plotted in Figure A-2.

Because the lower grid region simulates only one part of one fuel assembly, to properly set up the inlet flow, the filling rate is recalculated based on the total volume of this region and the volume of the entire canister mock-up section with the same height. This results in an equivalent filling rate of 0.138 cc/s.

To allow for axial tracking of the filing process and identification of eventual voids, several cross sections of the domain were plotted as shown in Figure A-3. The cross sections are taken in the symmetry plane (midsection) and at the 45-, 90-, and 135-degree sections. The information from these plots demonstrates even level progression and in all parts of the region. The most critical area for void formation is the tie grid, but the solution shows successful filling.

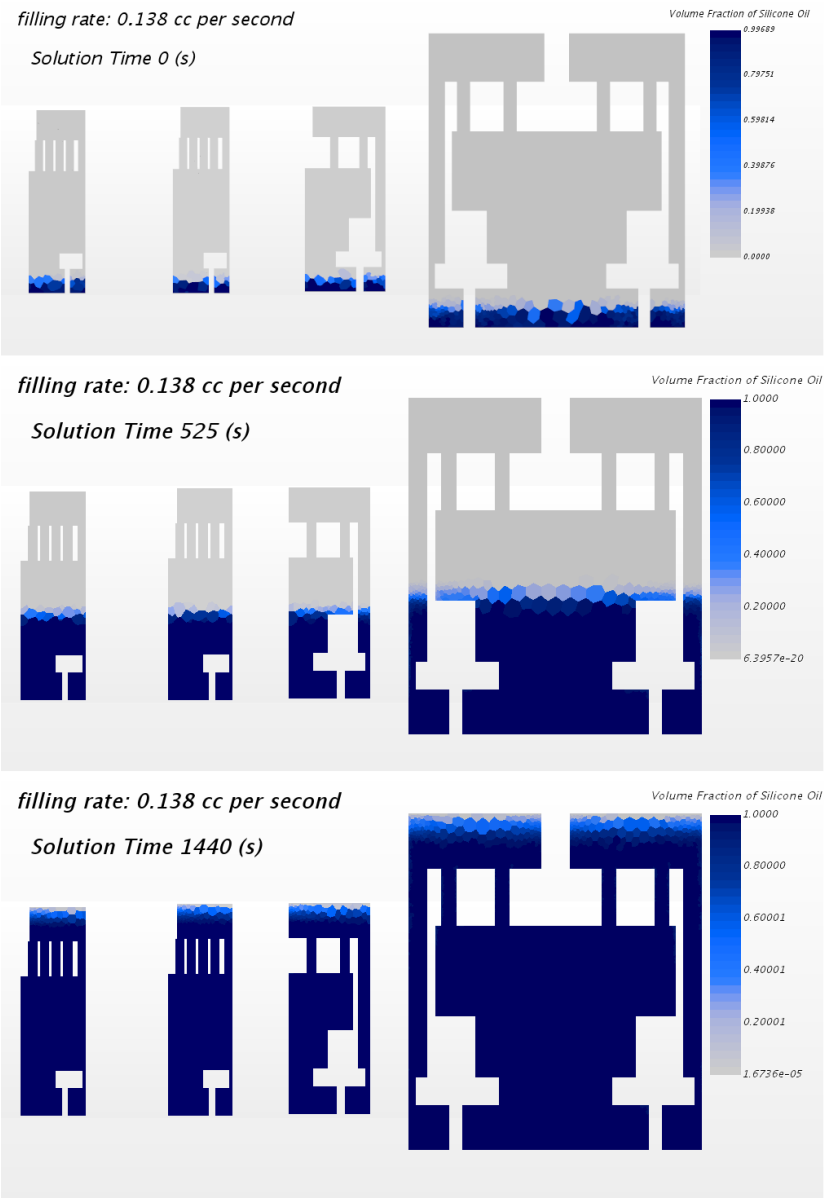

Figure A-3. Domain Sections Tracking the Level in the Lower Grid Region. Three Instances of Time Are Plotted at the Beginning, Near the Middle, and at the End of the Process.

A-1.2 Spacer Grid Filling Simulation

The spacer grid region of the domain includes the first rod spacer grid with some of its features (vanes) simplified. Since all grids are the same for the test assembly being modeled, simulating only one is acceptable to prove the filling of voids. In this case, no domain transposition was applied, and the data mapping is continuous from the bottom nozzle region. Instead of removing a section between the two regions, part of the domain occupied with rods is shortened to save computing time. In the real geometry, the spacer is located further up in the rod bundle, but in the simulation, the spacer was translated down almost immediately after the rods start.

Another change is made in the simulation to save compute time. The filling rate is increased five times, from 0.138 to 0.69 cc/s. This was done because if the filling is successful at a higher rate, it should be successful at any lower rate.

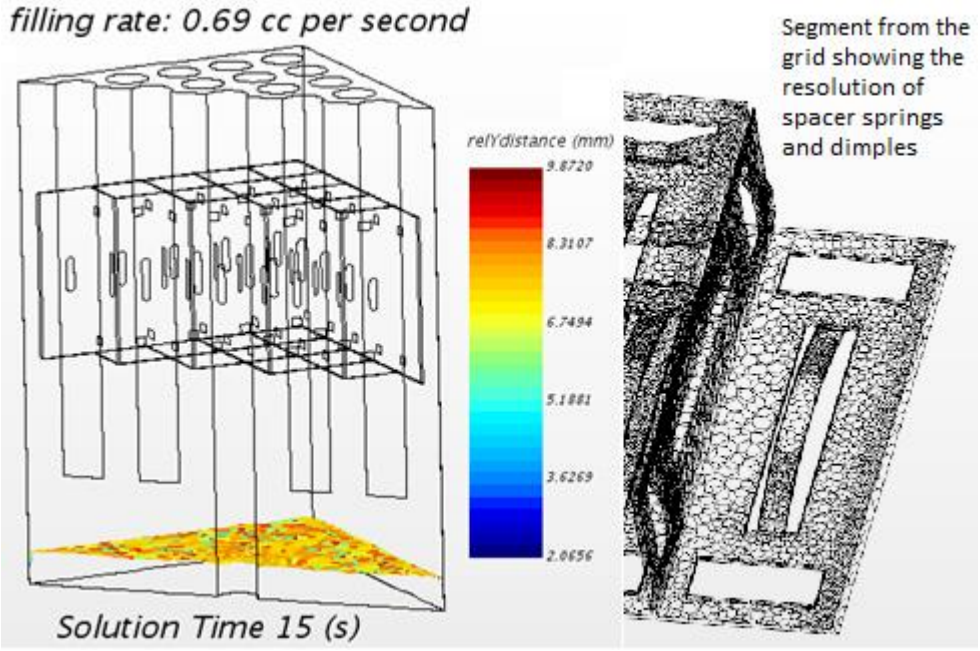

Figure A-4. Spacer Grid Region, Including Rods. The Outline Shows the Location of the Spacer Grid and Level 15 s after Filling Started. The Level Is Measured from the Floor of This Region.

The spacer grid region is shown in Figure A-4 along with a newly implemented function to compute the liquid level relative to the region floor. The function captured the level unevenness by giving the distance to the floor of any fluid elements that have more than 70% liquid content. The scale shows that the computed level varies between around 6 and 10 mm for the plotted time instance. This indicates a 4 mm level accuracy, mainly due to the resolution of domain discretization.

The overall filling of the region is shown in Figure A-5. As in all previously discussed regions, the liquid front progressed without any anomaly. The first graph on the left in Figure A-5 shows the initial state after the level has been mapped from the lower grid region. The middle graph displays the filling at the location of rods, and the graph on the right shows the filling in the spacer grid.

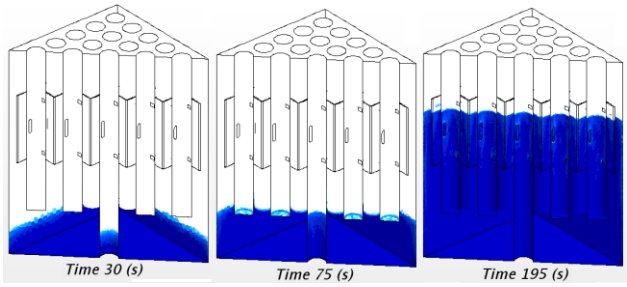

Figure A-5. Filling of Spacer Grid Region. Three Instances of the Process Are Shown: the Beginning after Mapping, at the Position of Rods, and at the Spacer.

Work continues with implementation of more controls that would allow for evaluation of the uncertainty in level determination. The concept of level tracking is being used to determine if any voids have formed, and it provides a quantitative measure of the detectable void size.

A-2 Filling Demonstration Progress

The objective of the initial filing demonstrations was to gain confidence in the computational simulations. ORNL developed a prototypical DPC mockup to investigate the injectability of liquids through the drainpipe and to provide insight for the filing operation by collecting validation data for the initial CFD simulations. Once the computational models are validated, they can be used to narrow down the candidate fillers to eliminate excessive testing and demonstration.

A-2.1 Experimental System and Configuration

The ORNL team designed and built two experimental setups to be used for the initial demonstrations. The first setup, a liquid-test apparatus, is being used to practice using fillers with different densities and viscosities and to collect validation data for the simulations. This apparatus was designed to employ nonhazardous liquids. The second experimental setup is intended to provide insight into the formation of voids in intricate geometries, such as the small and irregular spaces between the fuel rods and the springs and dimples in spacer grids. This setup will use a filler material with a low melting point, such as the paraffin wax, which melts at 64°C. This will allow for visual inspection of the filled volume, particularly to understand coalescence of multiple smaller void formations into larger voids.

The liquid-test apparatus is a mockup of the DPC [1], and it includes most of its real features. The DPC-filling apparatuses are scaled down models to expedite testing and minimize cost. The system is composed of an outer housing tube, an inner basket, a drain tube, support stands, lower assembly stands, assembly spacer grids, and fuel rods representing a portion of MPC32 DPC. The outer canister material is made out of acrylic to enable visual observation of the filling process. The outer housing is a 1.27 cm thick wall tube with a 25.4 cm outer diameter. The overall height is 70 cm. The canister is enclosed with a polycarbonate 1.27 cm thick bottom and top flanges. Flanges have three plugged holes at the bottom to allow for draining after testing.

The inner basket is designed to accommodate a 5 × 5 fuel bundle. The initial demonstration focuses on validation of the computational models for the lower 70 mm of the system, where the region of interest is the arched openings at the bottom of the basket. This region is referred to as the *mouse holes* in earlier simulation work. The mouse hole region is chosen to be the first test region due to its proximity to the drain tube. It is the first feature with which any type of filler will interact and through which it will propagate. The mouse hole openings were modeled at 3.81 cm wide and 3.81 cm long. The basket was fabricated from polycarbonate panels that were machined with upper and lower cut-outs to be assembled by interpenetration, as shown in Figure A-6.

Figure A-6. Basket Fabrication.

The second challenging path that any type of filler will traverse is through the inner mouse holes at the bottom of the support stands placed in the basket segments. The support bottom spacer is 27.31 cm long. The inner mouse hole openings are slightly higher at 4.45 cm long and 2.54 cm wide. These parts were fabricated from 304L stainless steel, and the lower assembly stands are welded on top. Figure A-7. shows the fabricated bottom spacers.

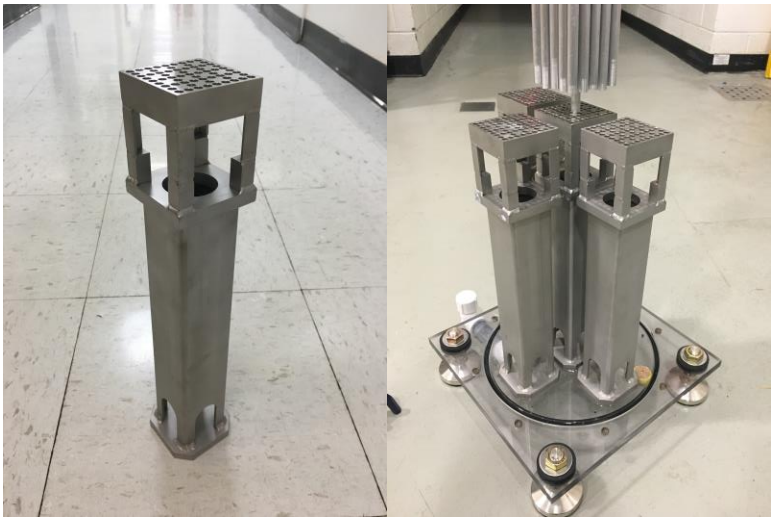

Figure A-7. Bottom Spacers.

Custom-made spacer grids (Figure A-8.) were fabricated through a subcontract with Professor Philippe Bardet from George Washington University, who has experience fabricating surrogate spacer grids with realistic features. These grids allow for capturing the phenomena of interest in that region for various research topics [2]. In this case, springs and dimples are anticipated to have a profound effect during the filling process. Understanding how small spaces between the fuel rods and the spacer grid features impact bubble formation is essential for establishing a sound technical basis when down selecting filler candidates for the program.

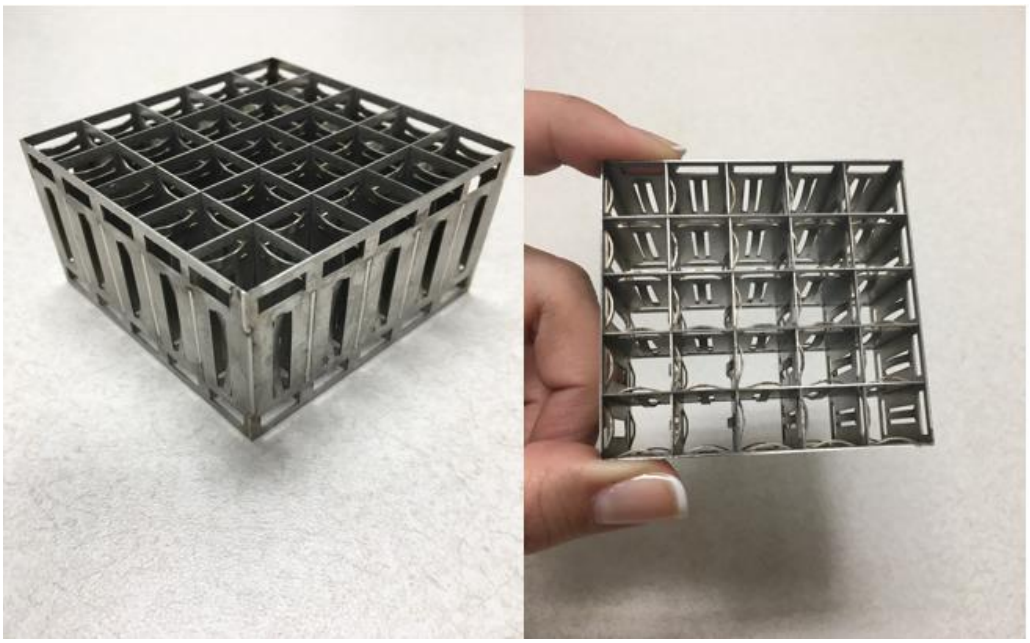

Figure A-8. Welded Spacer Grids for the Liquid Apparatus.

The complete setup is shown in Figure A-9. Measurements are taken using two level sensors inserted at different positions inside the canister. The whole canister assembly is placed on a weigh scale to collect the weigh data, and the level data is collected simultaneously by the level sensors. All output is recorded in a laptop through a data acquisition system.

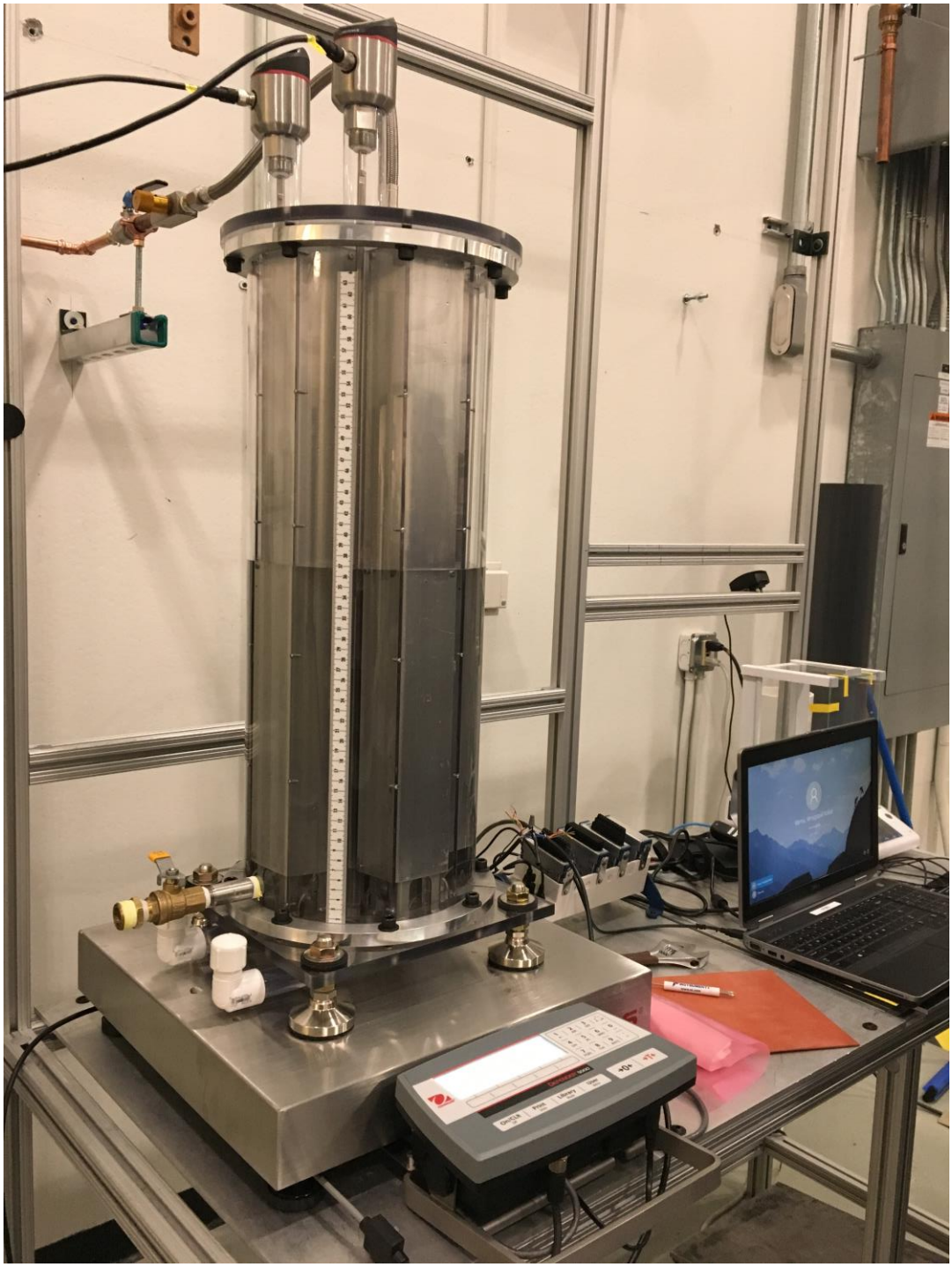

Figure A-9. Experimental Setup for Liquid Measurements.

A-2.2 Instrumentation and Measurement Methodology

Level measurement methods were investigated to acquire real-time data during the filling process. The sensors surveyed included (1) float type level sensors, (2) conductivity-based level sensors, (3) ultrasonic level sensors, (4) capacitance-based level sensors, and (5) electrical pulse echo level sensors. Float-type

sensors may present challenges, as the float takes up some space in the flow channel, thus affecting flow characteristics. Additionally, the float may potentially get stuck. The conductivity-based sensing method works on the principle of detecting changes in the conductivity of surrounding fluid and thus determining the position of the liquid-gas interface. However, this method is affected by metals in close proximity to the sensing line. This sensor type is also incompatible with nonconductive and highly viscous liquids. Ultrasonic-type level probes were also explored to assess whether they would meet the accuracy and sensitivity requirements. This method works on the principle of reflection of ultrasonic waves resulting from a sudden change of impedance along the axis of propagation—in this case the gas-liquid interface. However, since the sound waves tend to spread even with a focusing horn, the spot diameter may grow more than 70 mm at a range of 700 mm. Therefore, detection will be averaged by the ultrasonic signal reflected from other nearby objects. This method could have worked in an open tank, but this experimental setup does not meet the environmental requirements. As the spot size was found out to be larger than the free space available for detection, this sensor was eliminated from consideration. Capacitance-type level-sensing probes monitor the capacitance generated between the liquid and the tank wall. The accuracy of this sensor was found to be greater than 1.5 mm. Other sensors like radar also had similar accuracy problems (>1.5 mm), although they supported the needed range of the experiment. Finally, a reliable level sensing probe was identified that met the constraints of the experimental setup. The sensing guide pulse level sensor [3] launches a fast electrical pulse for detecting the gas-liquid interface. This approach allows for monitoring a wide range of liquids. The transmitter generates a 4–20 mA linear output. The specifications of this sensor are summarized in Table A-1.

Table A-1. Specifications for the Guide Pulse Sensor Model FL-001

MODEL FL-001 Specifications		
Measurement range		100–2,000 mm
Resolution		1 mm
Linearity		±3 mm
Temperature characteristics		0.1 mm /°C
Undetectable area	From the top end	25 mm
	From the bottom end	10 mm
Response time to comparator output		0.4s minimum
Connection bore diameter		G3/4
Analog output		4–20 mA, maximum load resistance: 350Ω
Analog output accuracy	Resolution	1 mm
	Zero accuracy	±0.1 mA (Zero point = 4 mA)
	Full scale accuracy	±0.2 mA (Full scale = 20 mA)
Current consumption		300 mA max. (at 10V) / 120 mA max. (at 30V)
Power supply voltage		10–30 VDC

The basic detection principle of the guide pulse method is that the sensor transmits a pulse signal to the liquid along the guide probe. It then receives the pulse signal reflected off of the liquid surface and determines the distance (level) from the time between the transmission and reception of the pulse signal. The detection distance L is determined by using the formula

$$L = \frac{1}{2}\, c\, t, \tag{17}$$

where *t* is the time between the transmission and reception, and *c* is the speed of the pulse. The principle of operation is illustrated in Figure A-10.

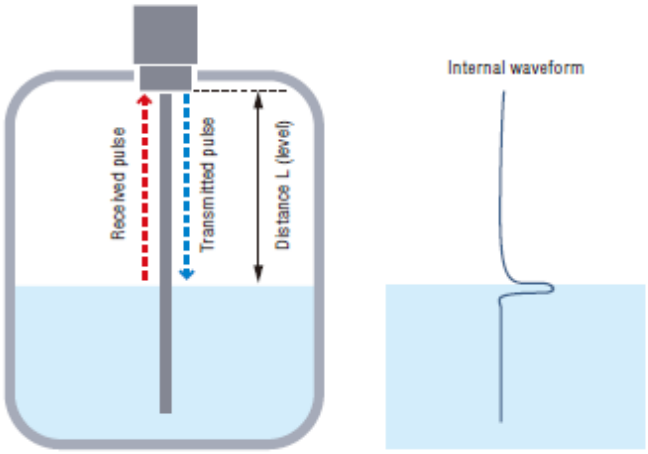

Figure A-10. Detection Principle of the Sensing Guide Pulse Method.

The model FL-001 is suitable for detecting level of water, oils, coolants, and noncorrosive liquids. It is also suitable for detecting levels of liquids containing solid particles and viscous liquids. The resolution is 1 mm, and the response time is 0.4 s.

To minimize interference, the sensor probe should be positioned away from surfaces like walls and other obstacles. Another important point is regarding the undetectable areas along the probe. The probe chosen for this experiment is 800 mm long; of that length, 25 mm from the top end and 10 mm from the bottom end are undetectable areas. To eliminate false detection and to accommodate the difference, two plastic tubes were added into the holes at the bottom flange as shown in Figure A-11. The probes are placed into those holes (centered and not touching), and the offset is considered during calibration to obtain a zero level at the bottom of the canister.

Identical units were used in two different locations for measurement redundancy.

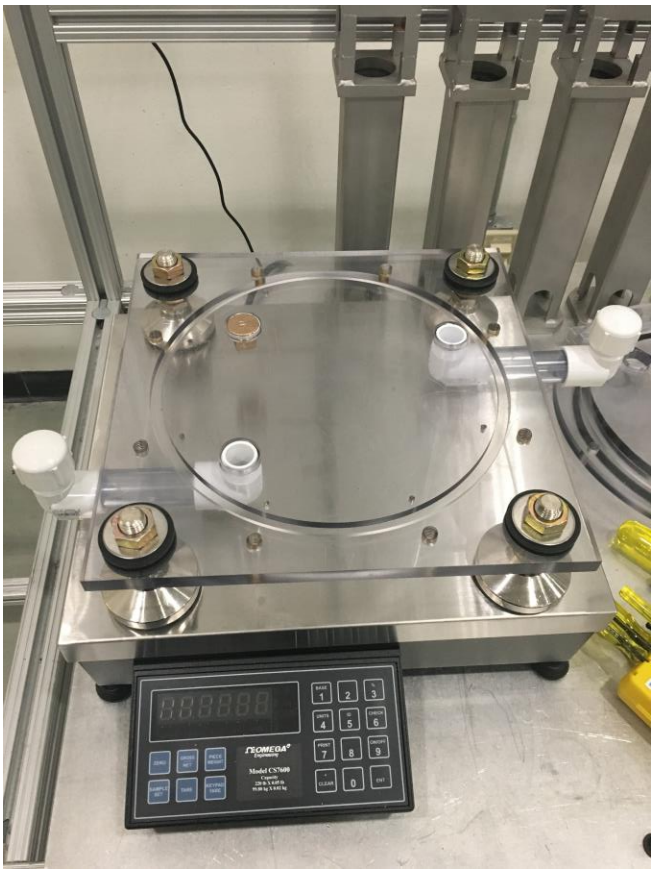

Figure A-11. Bottom Flange Modified to Accommodate the Bottom Offset of the Probe's Undetectability.

The weight of the experimental setup was measured during the filling process. This was is accomplished by placing the system on top of a digital scale and continuously monitoring the assembly's change of weight during the filling process. This method allows for verifying the flow rate, and it also provides an alternative way to infer the liquid level.

The OHAUS D52P125RQL5 Defender 5000 Low-Profile Bench Scale was chosen. This model includes a digital output port that enables real-time data acquisition. The scale's maximum capacity is 125kg ±5g

National Instruments (NI) cDAQ 9178 was used as the data acquisition (DAQ) system. Both the weight and the level measurements were converted to a 4–20 mA current signal to minimize the effect of cable lengths. A linear scaling was used to convert the current signals to weight and level readings.

The graphical user interface (GUI) used a 500 ms cycle time to acquire the data. The time stamp of the computer was used to acquire the absolute time during data acquisition. This resulted in a very accurate record of the weight measurement and level reading as a function of time.

The FL-001 pulse level sensor was observed to have stability issues in the lower levels. These issues were thought to have resulted from the metal rings that were used to clamp the canisters to the bottom flange.

Finally, the level was observed visually. A tape measure was attached to the outside of the polycarbonate canister, and a small flash light was placed underneath the canister to help illuminate the rising water level. The filling process was recorded with a camera with its own internal timer. The data were then generated by visually reading the rise of the level over the elapsed time at every 1 mm rise in fluid level.

A-3 Experiments and Results Discussion

A-3.1 Water Experiment

A bypass pipeline was installed on the main water supply to provide the water for initial calibration and testing of the experiment system. A backflow preventer, a pressure regulator, a ball valve, and a flow control metering valve were installed. A flexible hose was attached at the end to allow for easy connection to the treaded drainpipe extension.

A-3.1.1 Experimental Procedure

As described in Section 2.1, CFD simulations adopted a flow rate of 1.26 cc/sec for a half-symmetry geometry. The same filling rate was used for the liquid apparatus, but it was later found that this rate was too low for the geometry. More viscous liquids may create even more problems and may promote generation of bubbles due to surface tension forces between the wall of the pipe and the liquid flowing through. The main difference is because the experimental setup uses a drainpipe for filling, while the simulation assumes that the water flow is from the outlet of the drainpipe. The computational models do not simulate the entry of the liquid from the inlet of the drainpipe.

To remedy that problem, the flow rate was increased. A 12.6 cc/sec flow rate was set for the initial tests with the liquid test experimental setup. The desired flow rate was then set by adjusting the metering valve and collecting water in a beaker and measuring its weight. This procedure was repeated until a repeatable result was achieved. Then, the stainless steel flex hose was connected to the assembly and the measurements were taken.

A-3.1.2 Overall Data

Four test runs were made with water. The level sensor data and volume data acquired during the experiment are shown in Figure A-12. The volume was calculated based on the reading of the digital scale.

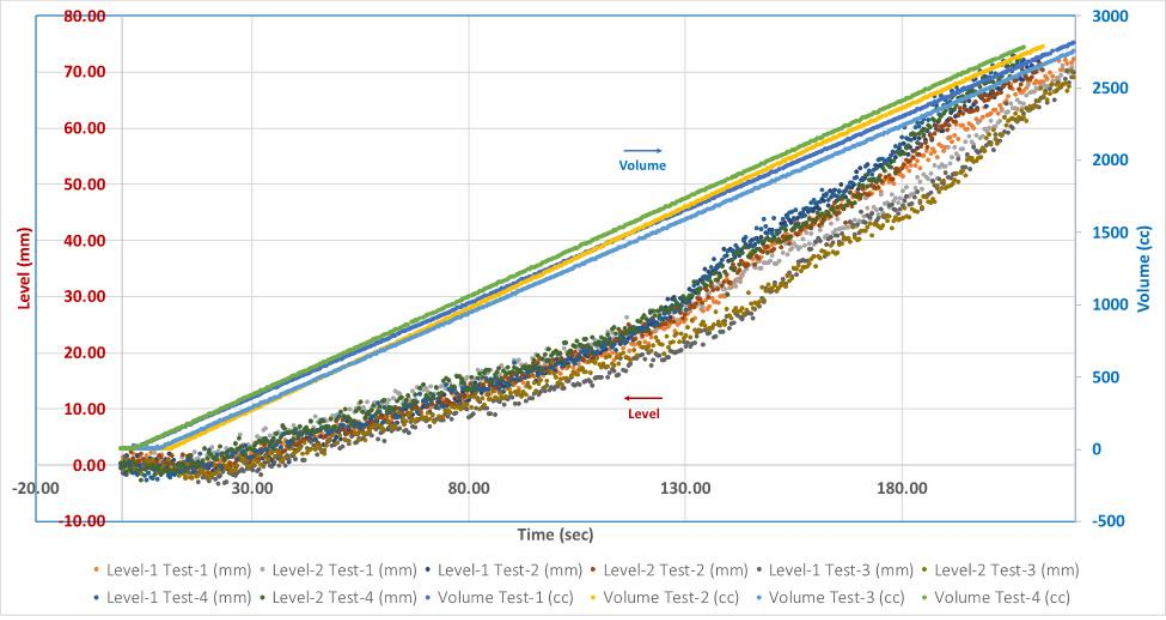

Figure A-12. Raw Experimental Data for Water Filling.

The level sensor data exhibited unexpected anomalies which are discussed in further detail below. The weight measurement was found to be highly reliable, although it also exhibited fluctuations about the measurement point during the filling process. A detailed measurement uncertainty quantification has not yet been conducted.

Uncertainties arise from the limitations of the experimental setup. One example is the onset of the filling process: the timer of the data acquisition (DAQ) system is started synchronously with the opening of the valve manually. However, there is currently no means in the experimental setup to consider the transport delay of the fluid in the flexible hose and the drainpipe. Therefore, these shortcomings inevitably create measurement uncertainties, and they are difficult to quantify. Attempts were made to alleviate these shortcomings through repeat experiments and by comparison of redundant and diverse sensor readings.

A-3.1.3 Volumetric Fill

Water volume was calculated based on the weight change. This section only discusses data from one of the test runs. The time-series data of the calculated water volume from Test #1 is shown in Figure A-13.

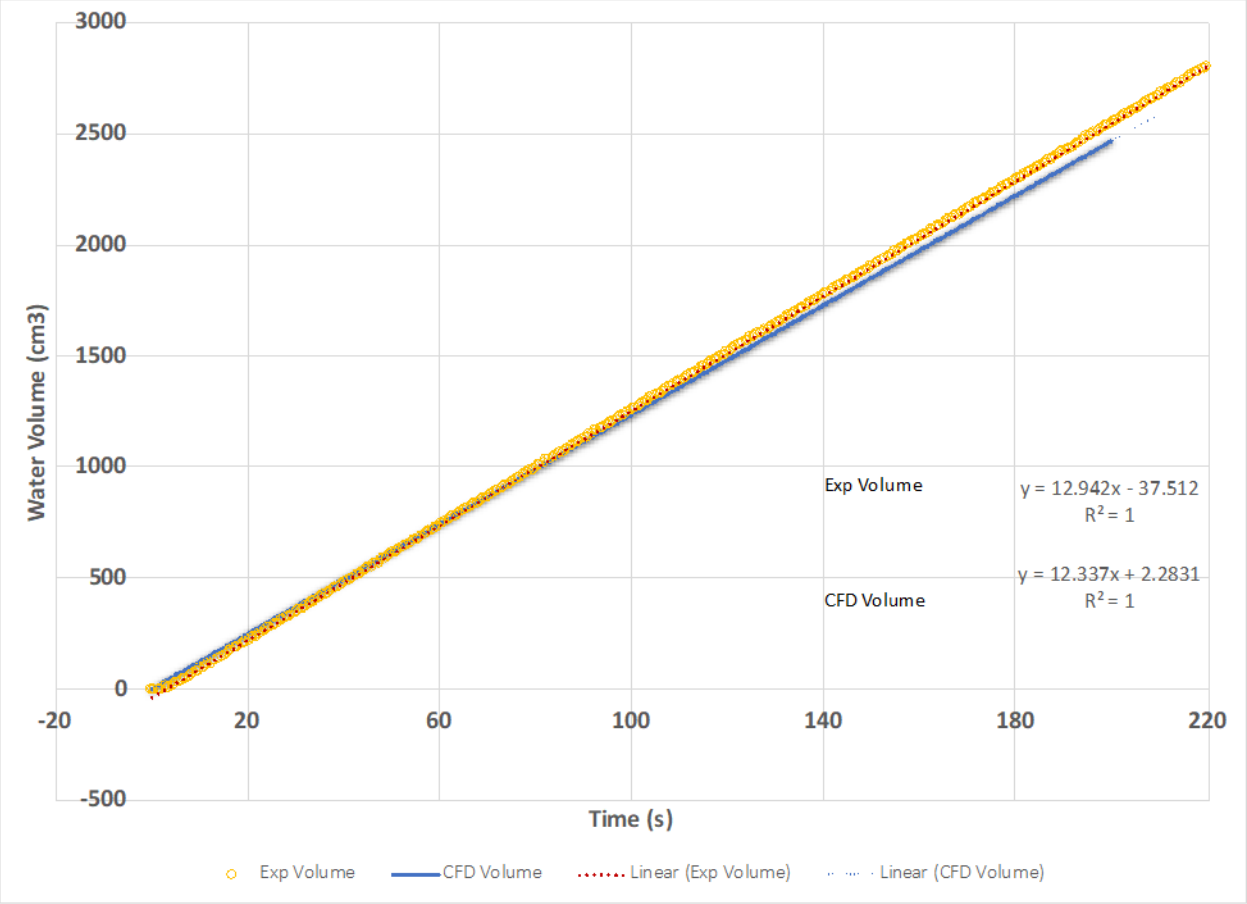

Figure A-13. Volumetric Fill Data as a Function of Time.

The linear regression to the experimental data yielded the following expression:

$$V = 12.942\, t - 37.512, \tag{18}$$

where t is time in sec, and V is the volume in cm^3. The slope of this equation yields the volumetric fill rate, which is q=12.942 cm^3/s.

The best way to observe the noise in the volume data is to look at the time differential of the time-series data as shown in Figure A-14. As the volumetric flow rate never changes during the fill process, this should ideally be a flat signal. However, as seen in the Figure A-14, the raw differential signal exhibits too much fluctuation. To reduce the noise level in the data, moving average filters of various orders have been tested. Ideally, this signal should be a flat line (i.e., a zero slope), and the constant value should be identical to the volumetric fill rate of q=12.942 cm^3/s.

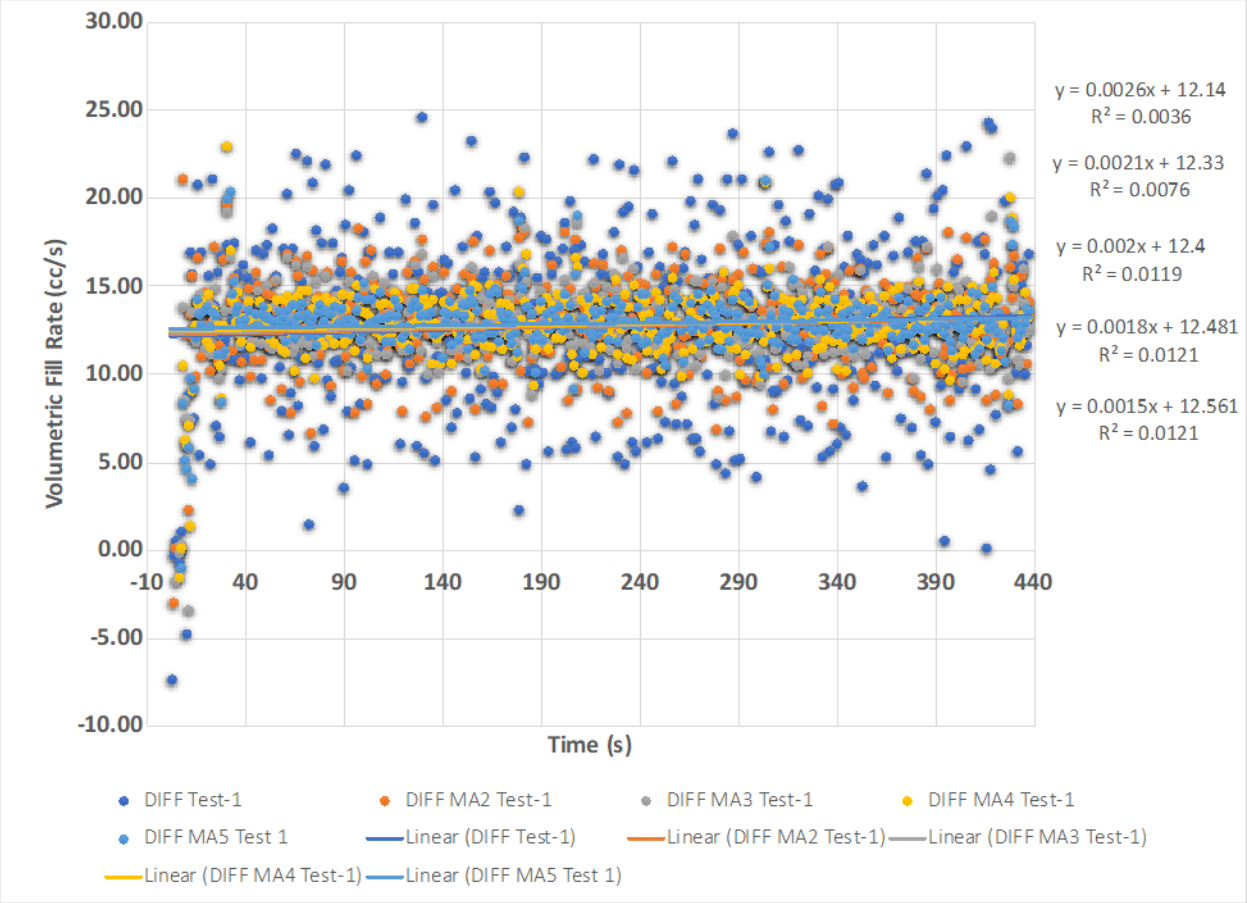

Figure A-14. Volumetric Fill Rate as a Function of Time.

The time differential of the raw signal yields a volumetric fill rate of 12.14 cm^3/s, which is significantly lower than the nominal fill rate. A moving average filter of the 5^{th} order, on the other hand, yields the following expression:

$$q = 0.0015t + 12.561 \tag{19}$$

with a correlation coefficient of $R^2 = 0.0121$, which is still quite low, and which is an indication of highly uncorrelated noise content. No higher order moving-average filter was created, but this shortcoming of the scale was noted.

There may be a number of root causes to this observation:

1. The scale is placed on top of a low-mass table; most likely the table weighs less than the experimental setup. Therefore, it does not dampen the ground disturbances.
2. The height of the experimental setup potentially amplifies the impact of ground disturbances.

These observations and the experimental shortcomings will be addressed in the later phases of the project.

A-3.1.4 Level

As described earlier in the report, the experimental setup employs two level sensors. The raw data from Test #1 are shown in Figure A-15. The discrepancy between two sensors is notable.

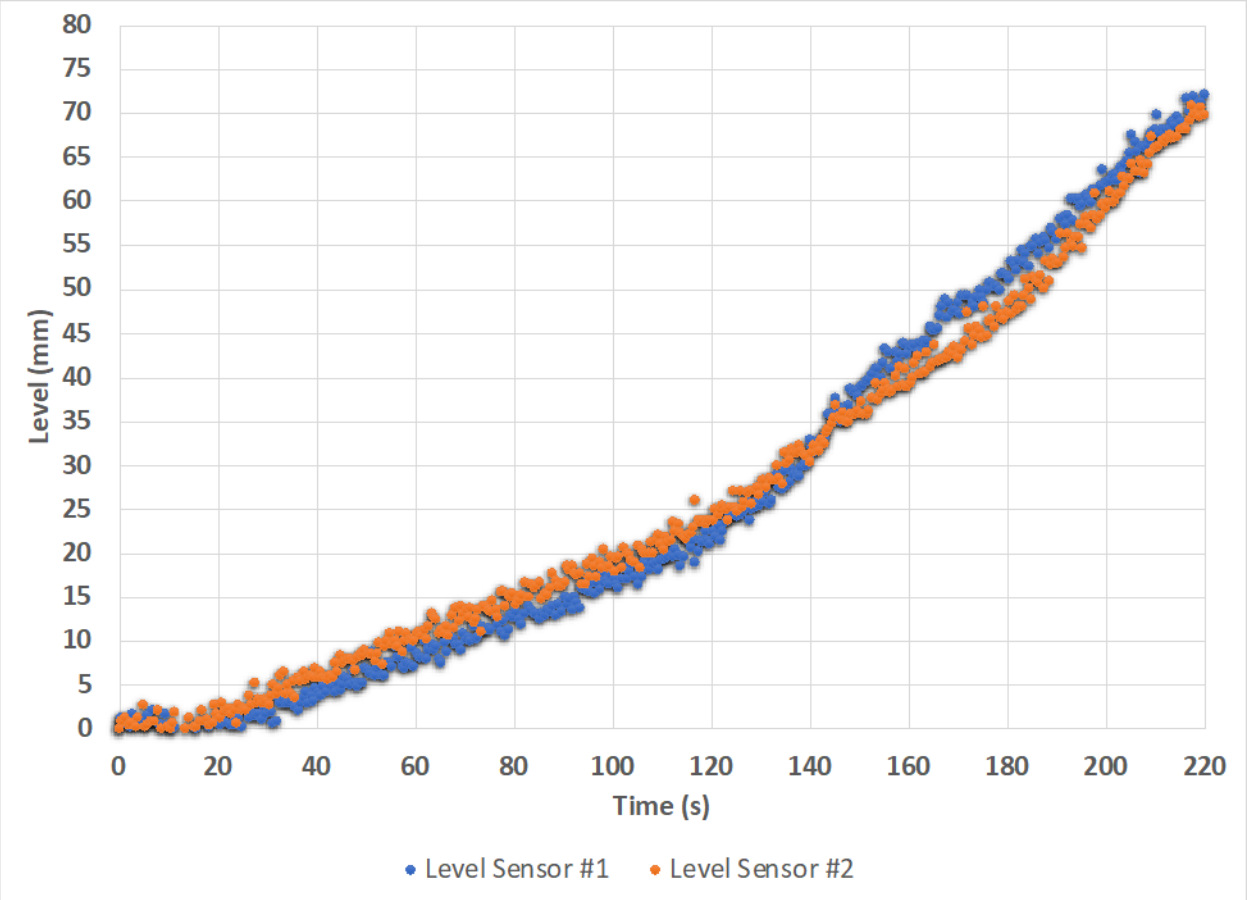

Figure A-15. Water-Level Data from the Two Redundant Level Sensors.

The time differential of the level sensor time-series data is shown in Figure A-16. Clearly, sensor #2 has significant noise content. As this observation was made, readings from this sensor were not considered reliable.

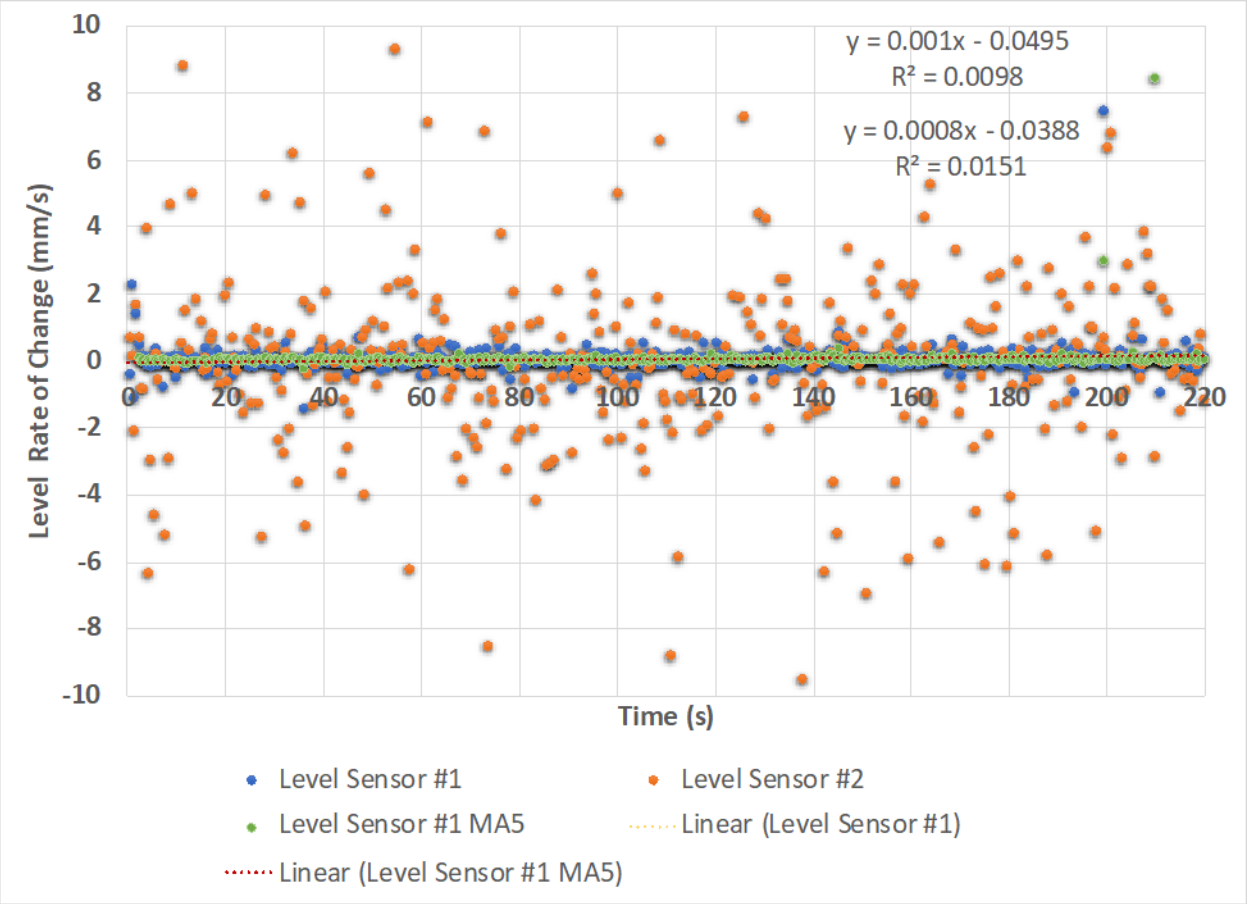

Figure A-16. Time Differential of the Raw Level Sensor Data.

A linear regression on level sensor #1 yields the following expression:

$$\dot{h} = 0.001\, t - 0.0495, \tag{20}$$

where $\dot{h}$ stands for rate of change in water level. Based on this expression, the fill rate is 0.0495 mm/s. The rate of the change in the level is a function of the geometric features of the experimental setup. Therefore, assigning a nominal rate would not be reasonable. However, the linear regression of the sensor data should have yielded the time average fill rate, i.e., as 70 mm was filled in 220 sec, the average nominal level fill rate should be

$$\langle \dot{h} \rangle = 0.32\ \frac{mm}{s}. \tag{21}$$

Even a fifth-order moving average filter was unable to improve the necessary signal quality.

Both sensors may have been affected by interference from the nearby metal walls. These observations were noted and are being investigated and addressed by the experiment team.

A-3.1.5 Comparison with CFD Data

The simulated and experimentally measured water levels are shown in Figure A-17. While the volume time-series data in Figure A-17 show a good agreement between the simulated and measured data, the level data between the two datasets are not consistent.

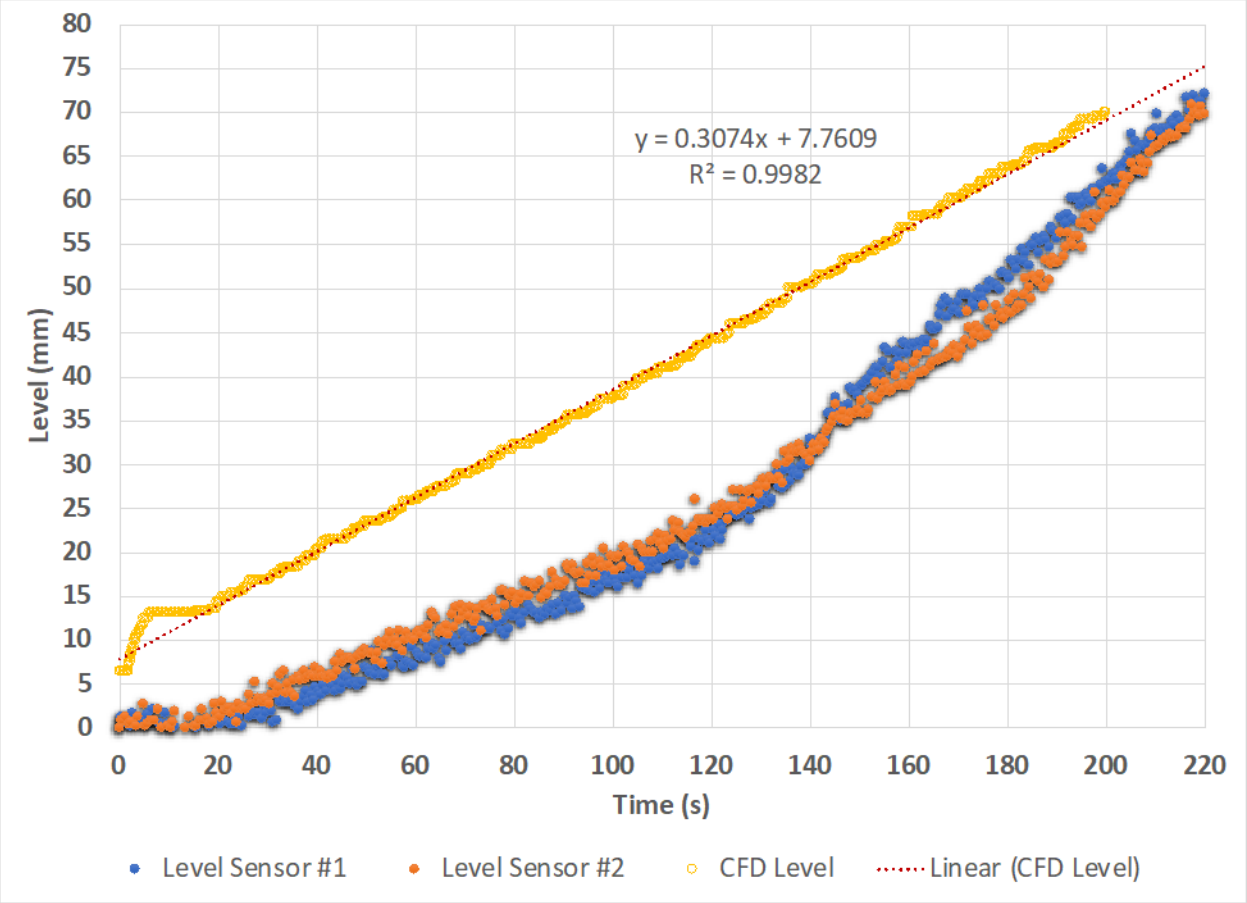

Figure A-17. Comparison of Measured and Simulated Water Levels as a Function of Time.

The level sensor stability is considered to be questionable: this issue is being investigated.

A-4 Water Experiment with Blockage

After completion of the initial testing with water, the mouse holes by the drainpipe were closed to represent a blockage scenario. Figure A-18. shows the blocked mouse holes by the drainpipe. Weight data are collected in real time through the data acquisition system, where the level rise was recorded by two separate cameras—one by the drainpipe, and the other placed 180° across from the drainpipe.

Figure A-18. View of the Blocked Mouse Holes by the Drainpipe.

Figure A-19 shows a snapshot view of the filling recorded with a camera positioned across from the drainpipe. The elapsed time is recorded for every 1 mm rise inside the canister from the video recorded.

Figure A-19. Snapshot of the Filling Camera Recording Positioned 180° across from the Drainpipe.

The raw data collected from both the open channel filling and the blocked channel filling are shown in Figure A-20. through Figure A-22. Figure A-20 shows the first 110 seconds of the filling process. The measurements indicate that it takes longer to fill in the open channel experiment than in the blocked channel experiment.

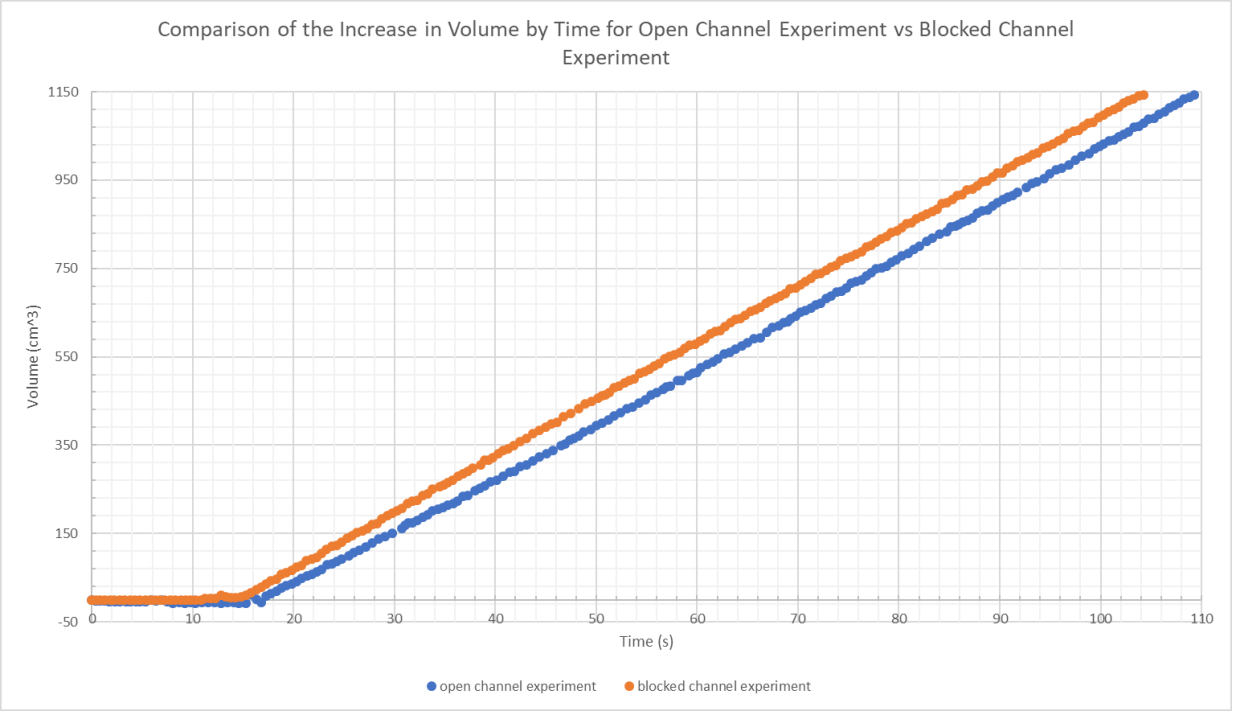

Figure A-20. Comparison of the Water Filling Time.

The raw level progression data also show that the level increase takes slightly longer in the open channel experiment than in the blocked channel experiment since there is slightly more volume to be filled in the open channel experiment. A practical use of this data would be understanding if there is a blockage in the real filling application out in the field. Currently, the data collected from those preliminary measurements are under evaluation. Further findings will be reported in the future.

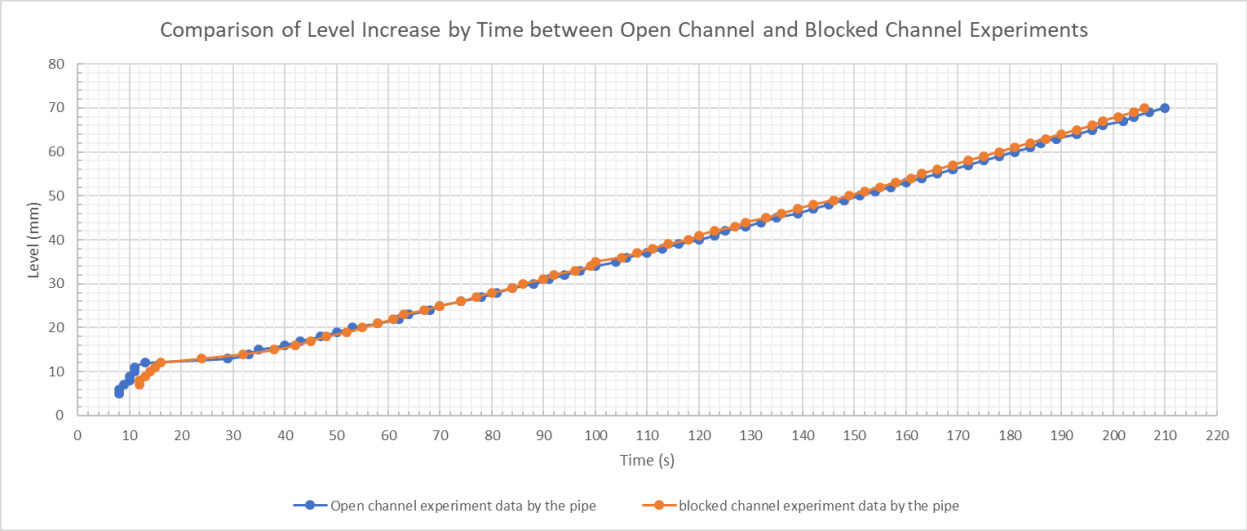

Figure A-21. Comparison of the Level Increase as a Function of Time Monitored by the Pipe.

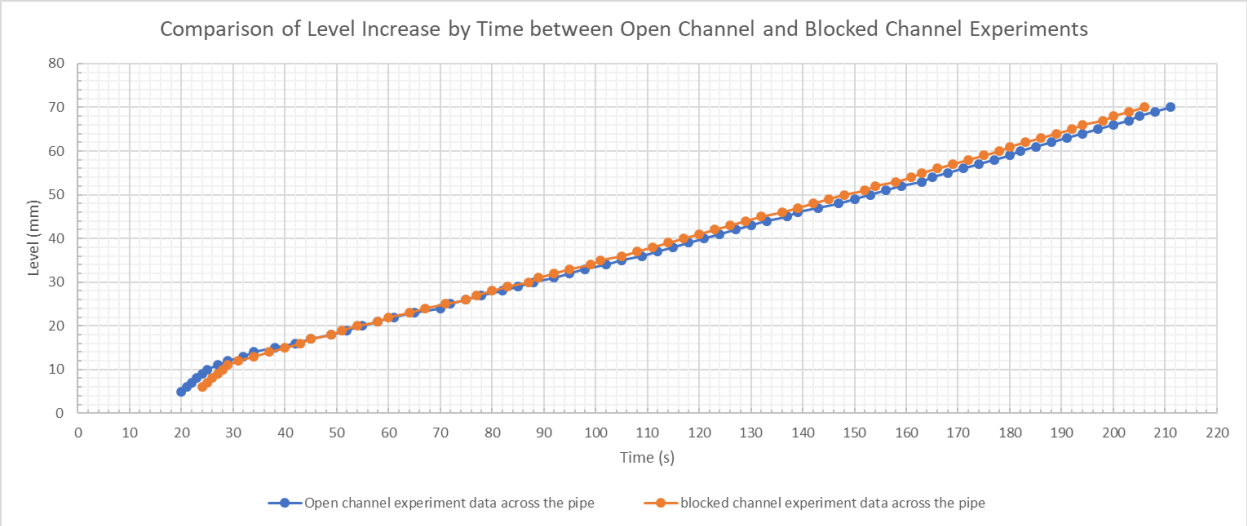

Figure A-22. Comparison of the Level Increase as a Function of Time Monitored across the Pipe.

A-5 Glycerin Experiment

Using 5 gal of glycerin, the prior experiment described above was repeated using the highly viscous fluid. The density of glycerin is 1.26 g/cc, and the dynamic viscosity is 1.412 Pa-s at around room temperatures. The experimental setup was modified for injecting the glycerin at a constant flow rate. The glycerin was held inside a bladder reservoir which was contained inside a large container. Plate weights were applied to the bladder (22.5 kg) to apply a head pressure to the glycerin bladder. The spout on the bladder was connected to the outlet of the reservoir with a valve to eliminate back flow and to allow for adjustment of the desired flow rate of glycerin out of the container. The glycerin test system is shown in Figure A-23. For the initial testing, two cameras at opposite angles were used to record and measure the glycerin level as it fills. As in the water experiment, the mass/volumetric flow of glycerin into the DPC apparatus was measured in real time using LabView software to record the increasing weight of the apparatus as it filled with glycerin.

The guide pulse sensor will be used in future testing after the stability issue is addressed by modifying the obstacles in the proximity of the detection zone.

Figure A-23. Glycerin Test System Setup.

Figure A-24 and Figure A-25 display the data collected from the initial test for filling the liquid test system with glycerin. Figure A-24 shows the filling volume increase by time. The flow rate was calibrated to 11.77 cc/sec by adjusting the metering valve at the spout of the reservoir. After the weight data was collected using the scale, the volume was calculated at each time interval. The linear trendline was fit, and the flow rate was found to be 5.18 cc/sec. Since the glycerin is much more viscous than water, it is clear that the friction inside the flex hose and the drainpipe reduced the flow rate during the filling. Data collection started before the main valve was opened to start filling process. Therefore, the initial volume values do not start from zero, so those values can be neglected.

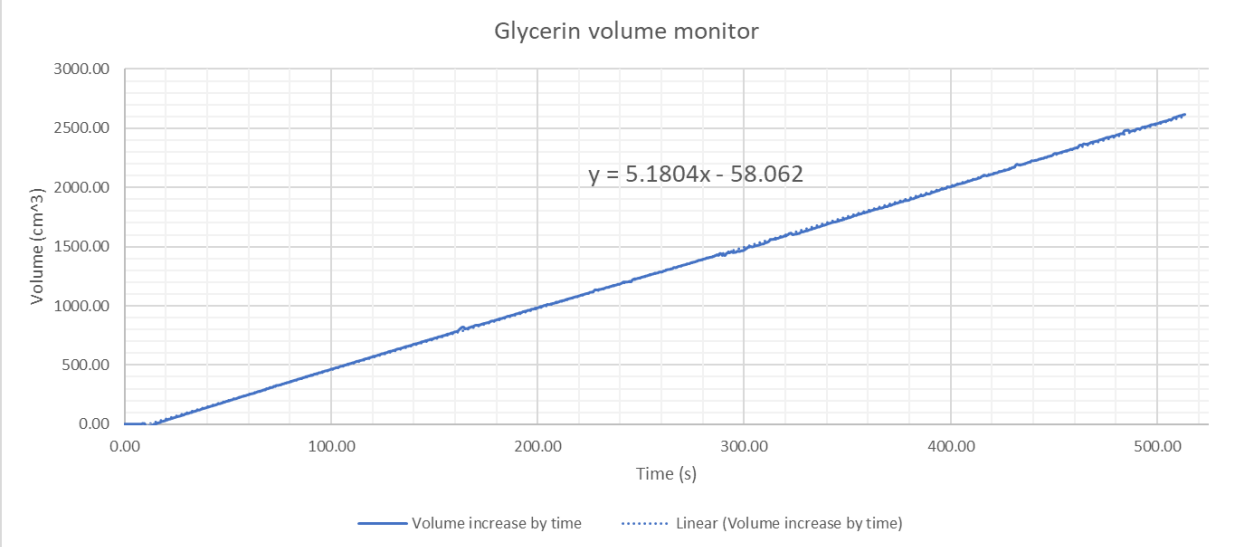

Figure A-24. Glycerin Filling Volume as a Function of Time.

Figure A-25 shows the level increase during filling as taken by two cameras. One camera was placed to monitor the filling by the pipe, and another camera was placed to monitor the level at 180° across from the pipe. The time difference between the rise of the level at the two locations is clearly different as expected due to the glycerin's higher viscosity.

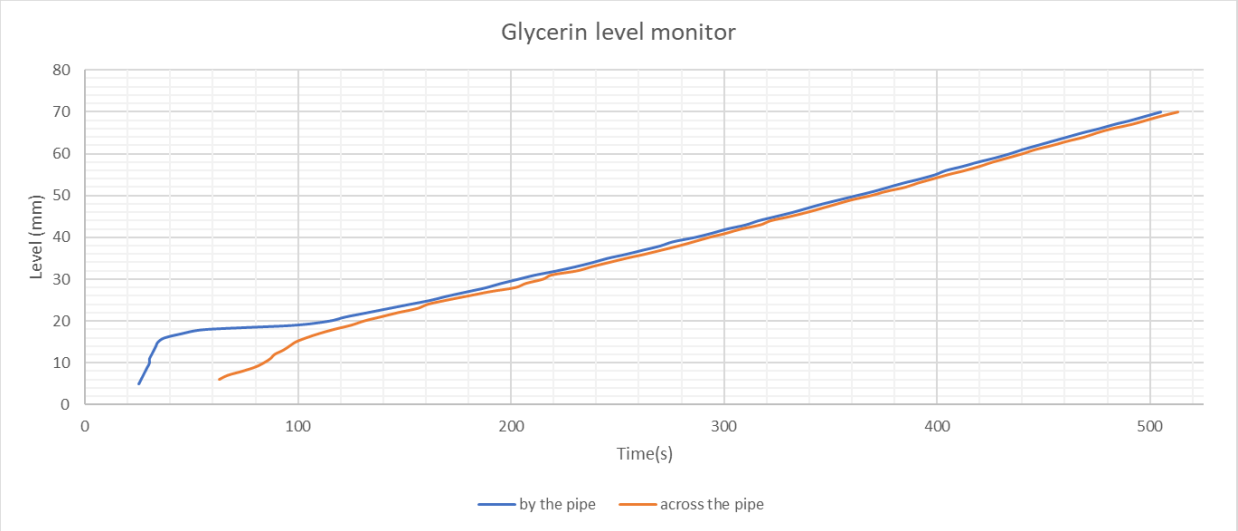

Figure A-25. Glycerin Filling Level Increase by Time.

A-6 Paraffin Experiment (In Progress)

The experimental setup of the paraffin experiment is similar in structure to the previously completed water and glycerin experiments. Figure A-26 shows the setup. However, this apparatus must incorporate a source of heat to keep the paraffin in a liquid state during the entirety of the filling process. Solid paraffin is first heated inside a large stainless steel reservoir beyond the melting point.

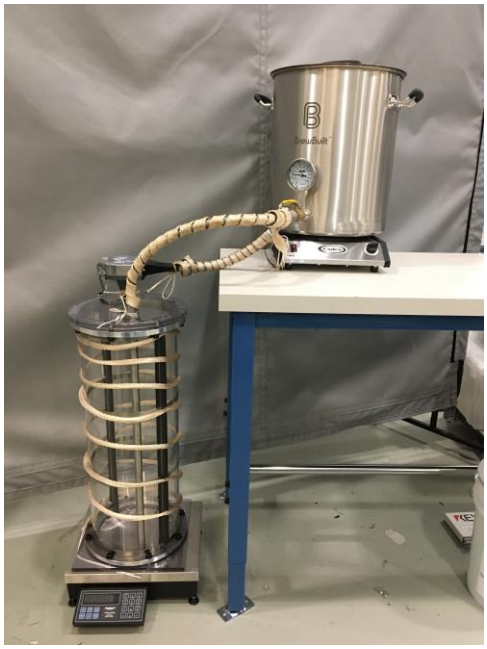

Figure A-26. Paraffin Experiment Setup.

While this paraffin heating process is taking place, the DPC canister will also be heated using heat tape and a recirculation blower. The heat tape will warm the braided tubing as shown in Figure A-27. below, which will be recalculated through the three-way valve and directed back into the DPC canister. This constant heating and air circulation will heat the canister and its internal components in excess of the

melting point of paraffin to prevent premature solidification of the paraffin once the filling process begins.

Once the paraffin is in its liquid state and the canister is preheated, the three-way valve will be adjusted to turn off the recirculation of air and to allow the inflow of liquid paraffin through the drain tube and into the canister. The paraffin will be allowed to completely fill the canister before the heat tape is turned off and the paraffin allowed to cool and solidify.

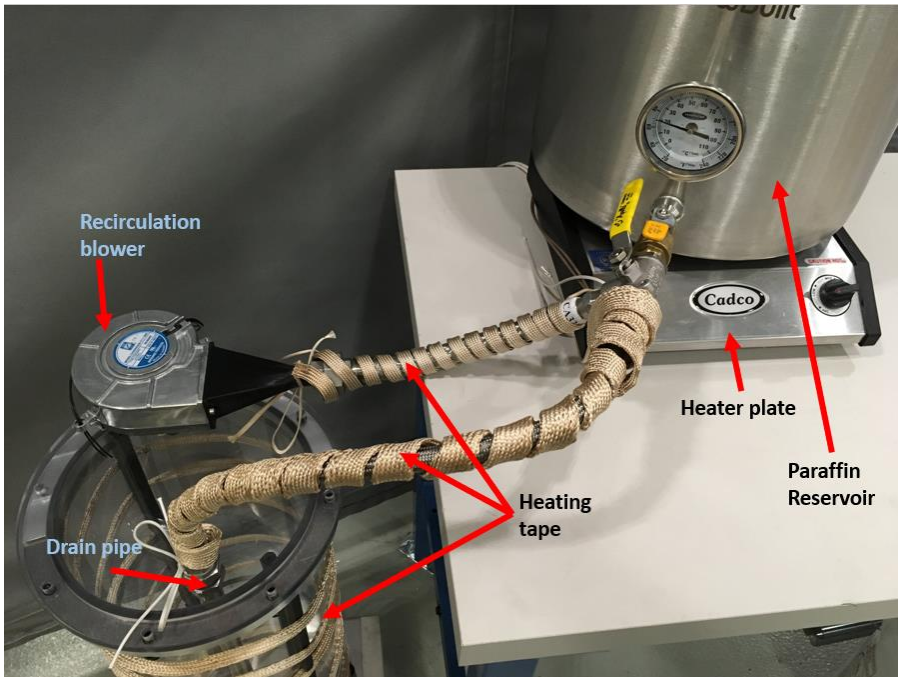

Figure A-27. Paraffin Experiment Parts.

Once the paraffin is completely solidified, the outer canister will be disassembled, and then the inner components, including the modular spacer grid shown in Figure A-28, can be disassembled and checked for filling efficiency and any voids that may be present. The grids are shown assembled using 3D printed plastic top and bottom plates. Metal plates that will essentially be used for assembly are still in fabrication.

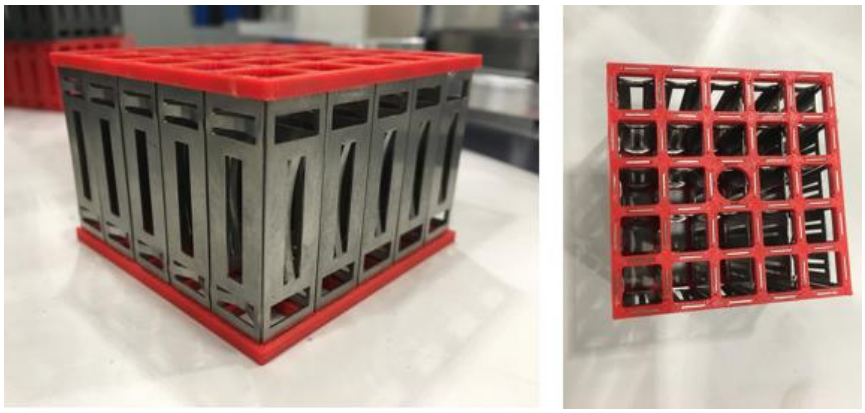

Figure A-28. Modular Spacer Grids.

A-7 Conclusions

Experiments with water and glycerin are ongoing. Necessary test system modifications have been identified and in progress. Analysis of the data in hand is ongoing. The planned future experiments are grouped into two categories: (1) the experiments that deal mainly with the filling process (flow)—water, glycerin, honey, mineral oil, etc., and (2) experiments that provide information about the thermal effects— paraffin, liquid metal, etc. The flow characteristics are being explored through modeling and experiments, while the thermal effects are yet to be characterized by modeling. The thermal experiments will be performed to address the solidification process, void spaces during filling and cooling, cracking due to nonuniform cooling, surface tension, etc. After the paraffin experiments have identified potential areas where there could be void spaces in the filling process, the same experiments will be performed with liquid metal. A nontoxic, low melting point metal such as tin, which has a melting point of 231.9°C, will be used to understand the solidification process using the actual spacer grid but with a reduced length of the fuel rods. Once the test sample is externally heated using heating tape and recirculating hot gas to establish a constant temperature, melted tin will be poured in. The temperature of the blanket will be reduced in a slow and controlled manner to reduce the possibility of cracking from differential temperature over the region. Once the experiment is complete, the sample will be analyzed in detail by sectioning it along various axes.

A-8 References

1. Holtec International, *Final Safety Analyses Report for the HI-STORM 100 Cask System*, (2010).
2. N. A. Weichselbaum et al., *Surrogate Spacer Grid Design for Fluid-Structure Interactions Studies in Fuel Bundles*, The George Washington University, Washington, DC (2015).
3. Keyence Corporation Sensing Guide Pulse Level Sensor https://www.keyence.com/products/process/level/fl/index.jsp.

Appendix B END OF FY2019 STATUS

B-1. Introduction

This appendix documents work performed supporting the US Department of Energy (DOE) Nuclear Energy Spent Fuel and Waste Disposition, Spent Fuel and Waste Science and Technology, under work breakdown structure element 1.08.01.03.05, "Direct Disposal of Dual Purpose Canisters." In particular, this appendix fulfills the M3 milestone, M3SF-19OR0103050117, "DPC filler simulation and demonstration progress report," as Revision 3 to M3SF-19OR0103050115, "Initial validation of CFD filling simulation," within work package SF-19OR01030501, "Direct Disposal of Dual Purpose Canisters–ORNL."

This appendix presents (1) the updated validation results of the CFD filling simulation using water and glycerin as surrogate filler materials, (2) information about the paraffin wax experiment conducted to gain insight into the phase change effects and the formation of voids in complicated geometries (e.g., grid spacers), (3) computerized tomography (CT) of the solidified paraffin wax that can be used to determine void fraction after solidification, (4) results of preliminary simulation to evaluate DPC preheating/preconditioning by blowing hot gas (needed for uninterrupted filling of DPCs using metallic or cementitious fillers), and (5) updates of the series of pipe experiments being planned/executed to determine the feasibility of filling a DPC using the existing drainpipe.

B-2. Status Update on the Development of Fully Validated Multiphysics Filling Simulation Tool

This section is a continuation of the work described in the main body and in Appendix A. This section provides updated validation results obtained using liquid (surrogate) fillers, as well as new experimental data from the paraffin wax experiment described in Appendix A.

B-2.1. Updated Validation Experiment Results with Liquid (Surrogate) Filler

As discussed in the main body and in Appendix A, a multiphysics simulation/prediction capability is under development to narrow the options for the filler materials. Experiments are being designed with geometries similar to those used in the simulations. The objectives of the initial tests are to validate the numerical simulation and to understand various aspects of the filling process.

The option of filling a loaded DPC through its existing drainpipe is currently being investigated. This would eliminate the need for modifying the canisters by drilling holes to perform the filling. However, the challenges associated with introducing the considered fillers through a drainpipe and filling a DPC from the bottom need to be evaluated. During injection, the flow should have a clear path to propagate through the openings, or *mouse holes*, at the bottom of the basket. The second challenging path that any type of filler will encounter is to get through the inner mouse holes at the bottom of the lower spacers. These spacers are used to place fuel assemblies inside a DPC.

The initial filling simulations of the lower region (mouse holes) of a prototypic DPC showed successful filling of the inner space voids, as well as smooth, even liquid level progression (see main body for detail). The initial demonstration of the filling process was performed using surrogate fillers (water, glycerin) that are typically used in computational fluid dynamics (CFD) simulations. The objectives of the demonstration were to collect validation data, to gain insight for injectability through the drainpipe, to identify a sustainable filling rate, and to determine the resulting filling time.

The CFD simulations were carried out applying a 180° symmetry and were set to introduce a constant flow rate of 6.3 cc/sec from the pipe outlet. The test system is constructed with a configuration composed of an outer housing tube, a 5 × 5 cell inner basket, a drain tube, bottom spacers, bottom nozzles, a spacer grid, and fuel rods representing a portion of an MPC-32 DPC (see main body and Appendix A for more details). A constant flow rate of 12.6 cc/sec was maintained by using a peristaltic pump to inject the surrogate fillers. The initial demonstration focused on validation of the computational models for the lower 70 mm of the system, or the mouse hole region. This region was chosen due to its proximity to the drain tube outlet. Two level sensors were inserted at different positions inside the canister to track the level progression. The whole test assembly was placed on a weigh scale to continuously monitor the assembly's change of weight during the filling process. The acquired real-time data from the scale and the 2 level sensors were simultaneously collected through a data acquisition system.

The measured water level progression as a function of time is compared with computed results from the CFD simulation shown in Figure B-1. Two transport properties are important for the filling evaluation: density and dynamic viscosity. Glycerin is also being considered for testing in the CFD simulations due to its higher viscosity. The density of glycerin is 1.26 g/cc, and the dynamic viscosity is 1.412 Pa-s at around room temperature. The runs for glycerin were successfully simulated and showed no trapped voids. The same fill rate of 12.6 cc/sec was maintained during in the simulation and the experiment. The results showed good agreement on the level propagation. Figure B-2 presents a comparison of the data for glycerin.

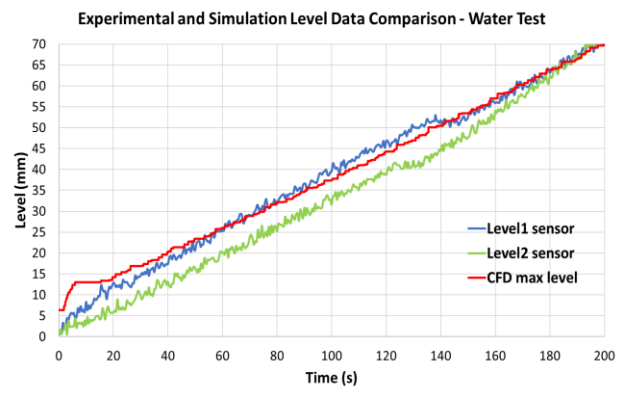

Figure B-1. Experimental- and Simulation-Level Data Comparison for the Water Test.

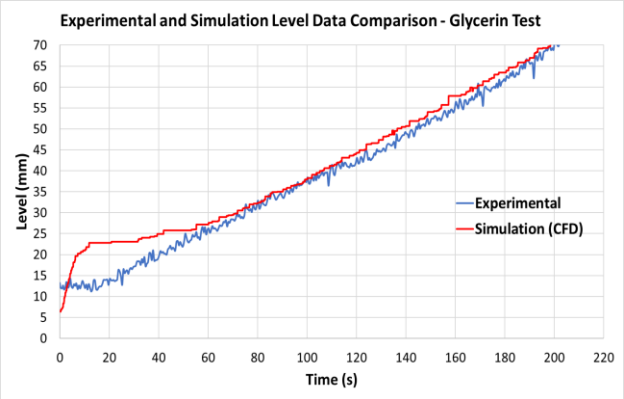

Figure B-2. Simulation and Experimental Data Comparison for the Glycerin Fill Test.

B-2.2. Solidification Experiments

The objective of the initial solidification experiment using paraffin wax as surrogate filler was to gain insight into the phase change effects and the formation of voids in complicated geometries such as the small and irregular spaces between the fuel rods and the springs and dimples in the spacer grids. To capture that complex geometry, a generic spacer grid was fabricated (see main body and Appendix A for detail). The spacer grids are made of individual panels so they can be removed individually to observe the filled volume.

The setup of the paraffin wax experiment was built using a similar in structure to the water and glycerin experiments, except this setup incorporated a source of heat to keep the wax in a liquid state during the filling process. The test DPC was heated using heat tape to maintain constant heating. Air circulation was achieved using a recirculation blower to heat the canister and its internal components close to 64°C, the melting point of paraffin, to prevent premature solidification of the paraffin during the filling process. Paraffin wax was melted completely using a heat plate.

Multiple thermocouples were installed at various location inside the canister to monitor the temperatures during filling and cooling. Table B-1 summarizes the location of the thermocouples.

Table B-1. Temperature Sensor Positions

Sensor ID	*Position*
TC-0	Canister center middle
TC-1	Canister side top
TC-2	Canister side bottom
TC-3	Spacer grid
TC-4	Pipe bottom
TC-5	Pipe middle
TC-6	Pipe top
TC-7	Wax reservoir spout
TC-8	Ambient

Before the filling operation was initiated, the canister was heated with heat tapes for about two hours. An insulator was wrapped around and under the canister and the piping to minimize heat loss. The average overall temperature measured inside the canister was ~55°C, and the minimum temperature reached inside the canister was 43°C. The temperature of the molten wax, which was monitored separately, was ~75°C. Once the paraffin was in its liquid state and the canister was preheated, a three-way valve was adjusted to turn off recirculation of air and to allow the liquid paraffin to flow through the drain tube and into the canister.

Additionally, a high spatial resolution temperature probe was used to capture temperature distribution along the axial direction of the fuel bundle assembly during wax filling and solidification. The probe can allocate ~ 511 temperature sensors with a spatial resolution of 0.65 mm along 355 mm of optical fiber length. The probe was fabricated by a commercial company using a fiberoptic embedded into a 316 stainless steel capillary tube, as shown in Fig B-3 [1].

The probe was inserted in lieu of a fuel rod in the fuel bundle and was extended from the nozzle to the top of the bundle, as shown in Fig B-3. The filling process was recorded with a high-speed camera, focusing specifically to discern the propagation of the initial spurt once the filler comes out of the pipe.

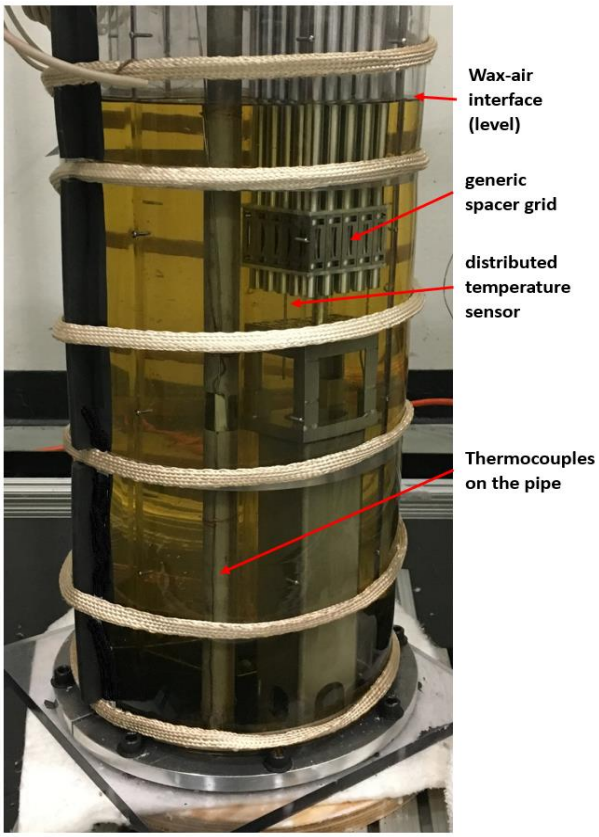

Figure B-3. Canister with Molten Wax and Positions of Various Internal Sensors.

Three thermocouples were installed on the bottom, middle, and top of the fill pipe. Evaluating the temperature gradient along the pipe is important for understanding the solidification effects. Clogging of the pipe outlet during pouring is one risk under consideration for the real application.

Various data sets were acquired during the filling and cooling process (solidification) with a time resolution that ranged from 0.016 to 60 sec. The temperature profiles of the 511 sensors were plotted as a function of distance from the probe's tip at discrete time intervals. Figure B-4 shows the time evolution of temperature profiles during the filling process. The abrupt temperature changes, including a significant temperature gradient at the liquid-gas interface, were captured accurately by the probe. Tracking this space-resolved feature could provide complementary information that can be used to calculate the filling process rate using known geometry parameters such as local volume. Local filling rates were corroborated using the video imaging data.

Transient filling and cooling data are plotted in Figure B-5. The phase change can be seen from the plots at each location where temperatures are measured. The temperature at the center of the canister increased to ~70°C during the filling process. The side of the canister and the spacer grid close to the side were at slightly lower temperatures.

In the paraffin filling experimental setup, the guide tube, fuel rods, and spacer grids were coated with mold release for easy removal of the interior pieces that came in contact with paraffin. The modular construction of the test setup and its ability to be easily disassembled allows for visual inspection of the filled volume. After the canister was filled with liquid paraffin wax, the system was allowed to cool down

to its solidus temperature. The experimental plan includes opening of the canister's clam to expose the solid paraffin. Once the inner fuel assembly is accessed, the guide tube will be removed, followed by the fuel pins. Working from the outer regions, individual spacer grid plates will be removed to ultimately expose the paraffin. Sections of these regions can then be screened under x-ray CT scan to gain an understanding of the coalescence of multiple smaller void formations into larger voids.

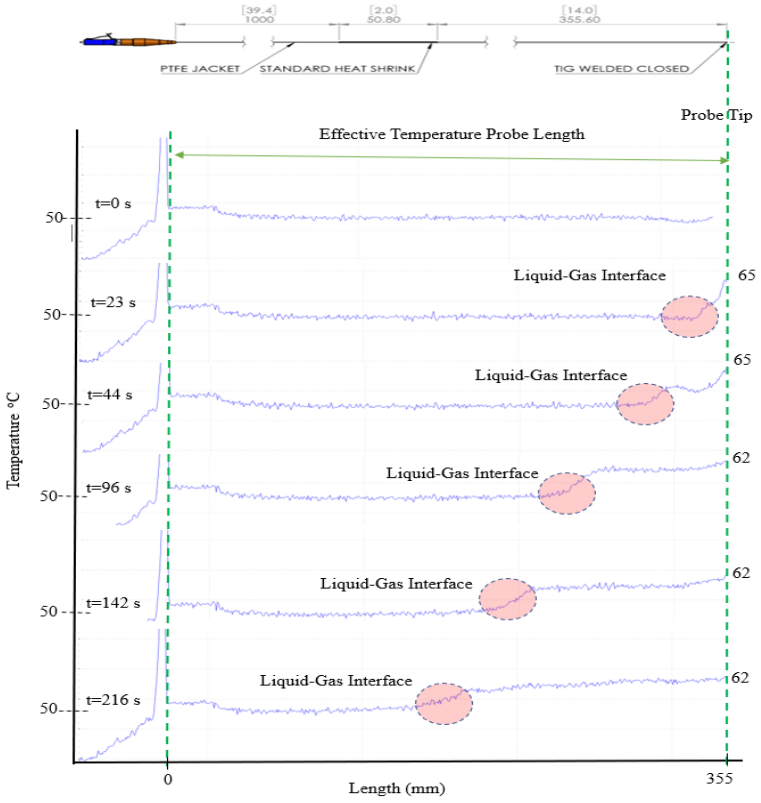

Figure B-4. Temperature Data from Fiberoptic Distributed Sensor.

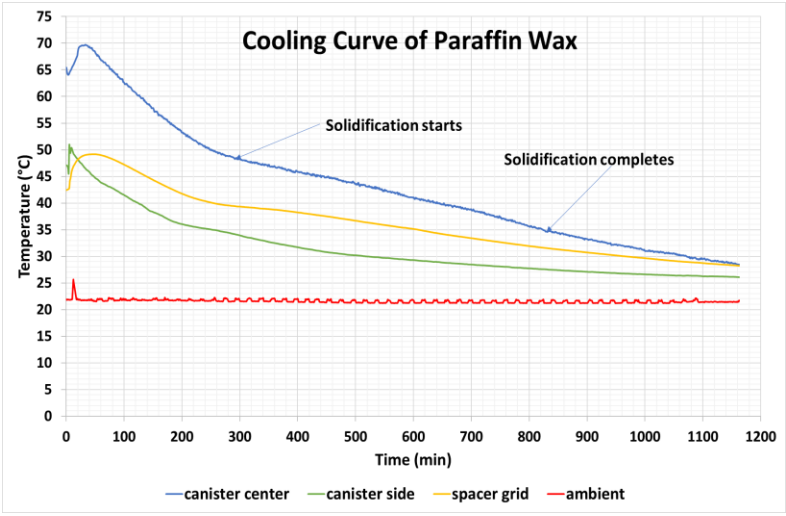

Figure B-5. Cooling Curve of Paraffin Wax.

B-2.2.1. Computerized Tomography (CT) Scan of Solidified Paraffin

Originally, the paraffin experimental apparatus was designed to be easily disassembled (as described above) in order to allow hands-on determination of void spaces present in the solidified paraffin. This method would have been crude and would have lacked the level of accuracy desired for these measurements and for future model validation. Therefore, x-ray technology with a CT scanner was used to accurately analyze the solidified paraffin for voids. Figures B-6 and B-7 present the CT scans of the canister showing void spaces in the solidified paraffin.

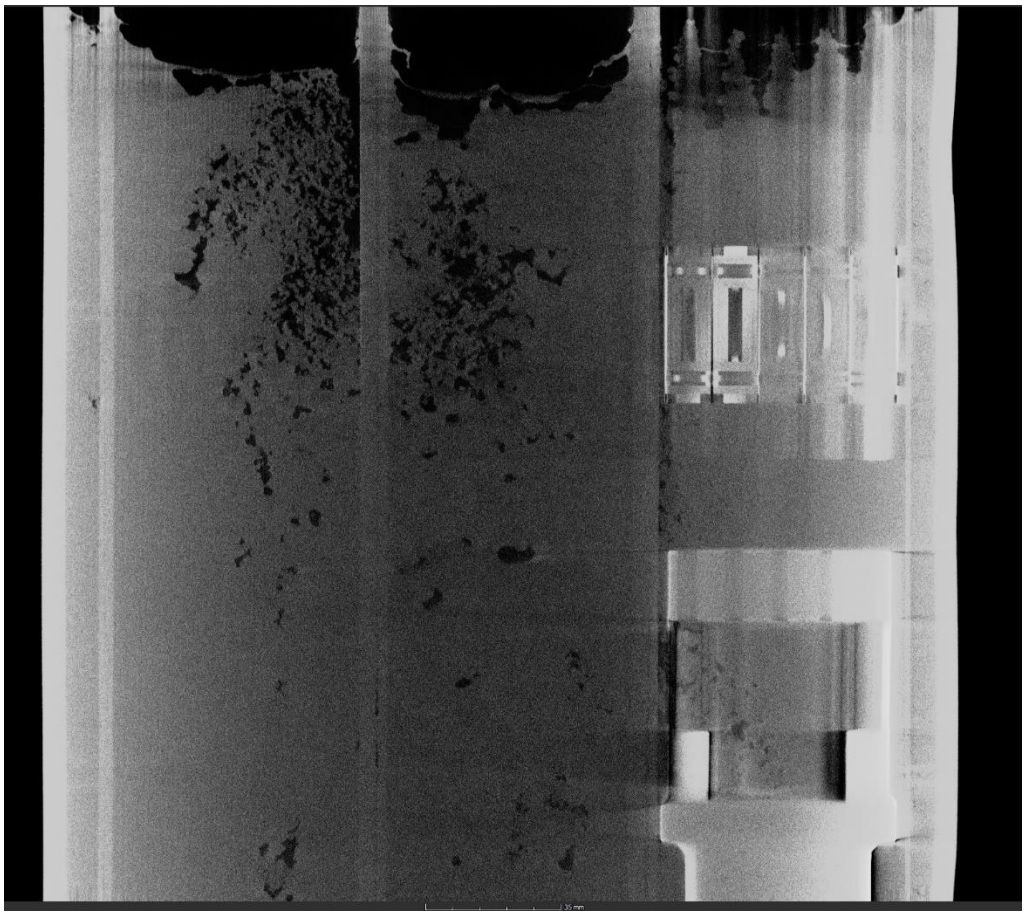

Figure B-6. Side View of Solidified Paraffin Apparatus with Surrogate Fuel Spacer, Nozzle, and Spacer Grid on the Right-Most Column.

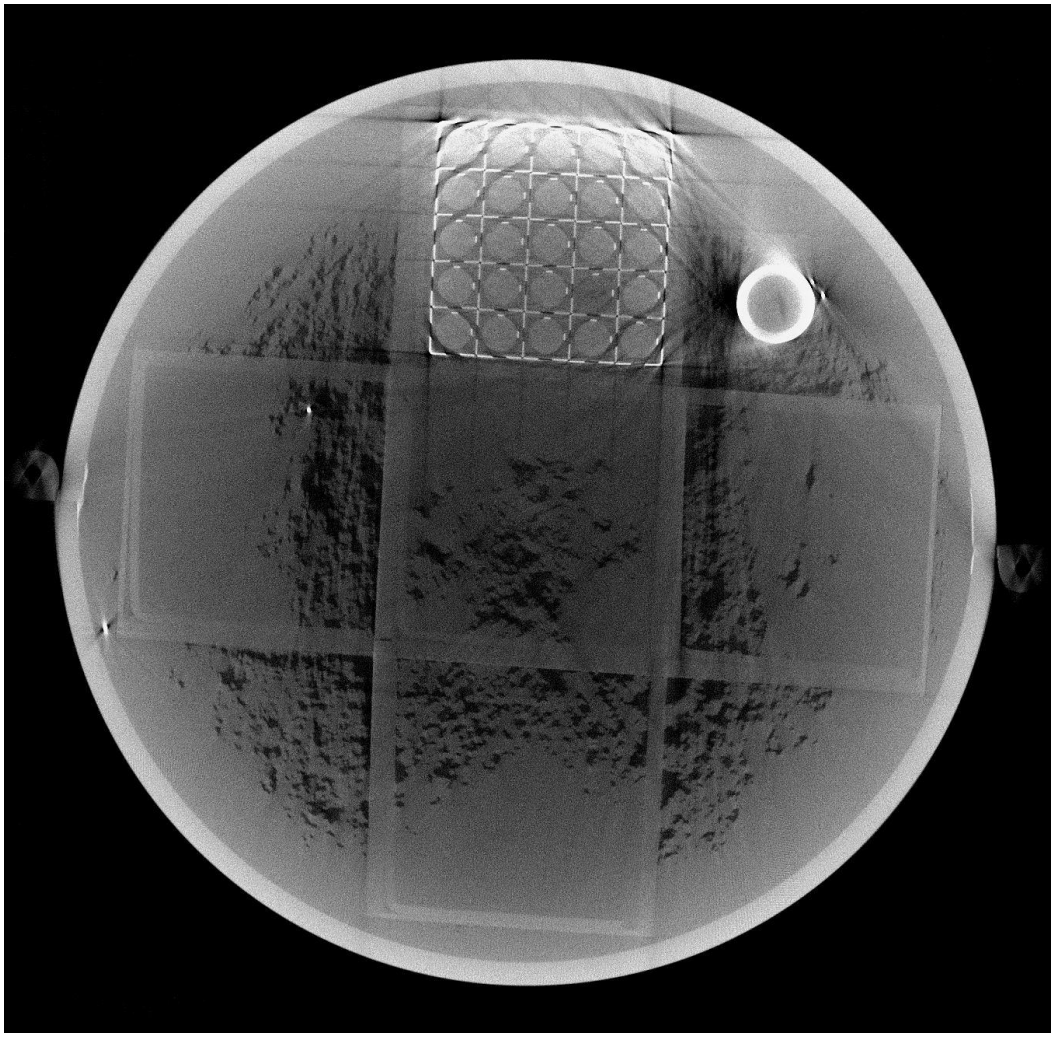

Figure B-7. Top-Down View of Solidified Paraffin Apparatus with the Fuel Spacer Grid in the Upper Column and the Fill Pipe in the Adjacent Space.

The CT scanner can create a 3D model of the scanned experiment by taking scans while the canister is rotated on a turntable to its new orientation and reconstructing the 2D x-ray images from multiple angles into a composite 3D image. The 3D image allows detailed analysis of the scanned experiment. For example, the location, size, and shape of a void inside the paraffin are all computable by the analysis software, as shown in the Figure B-7 and Figure B-8.

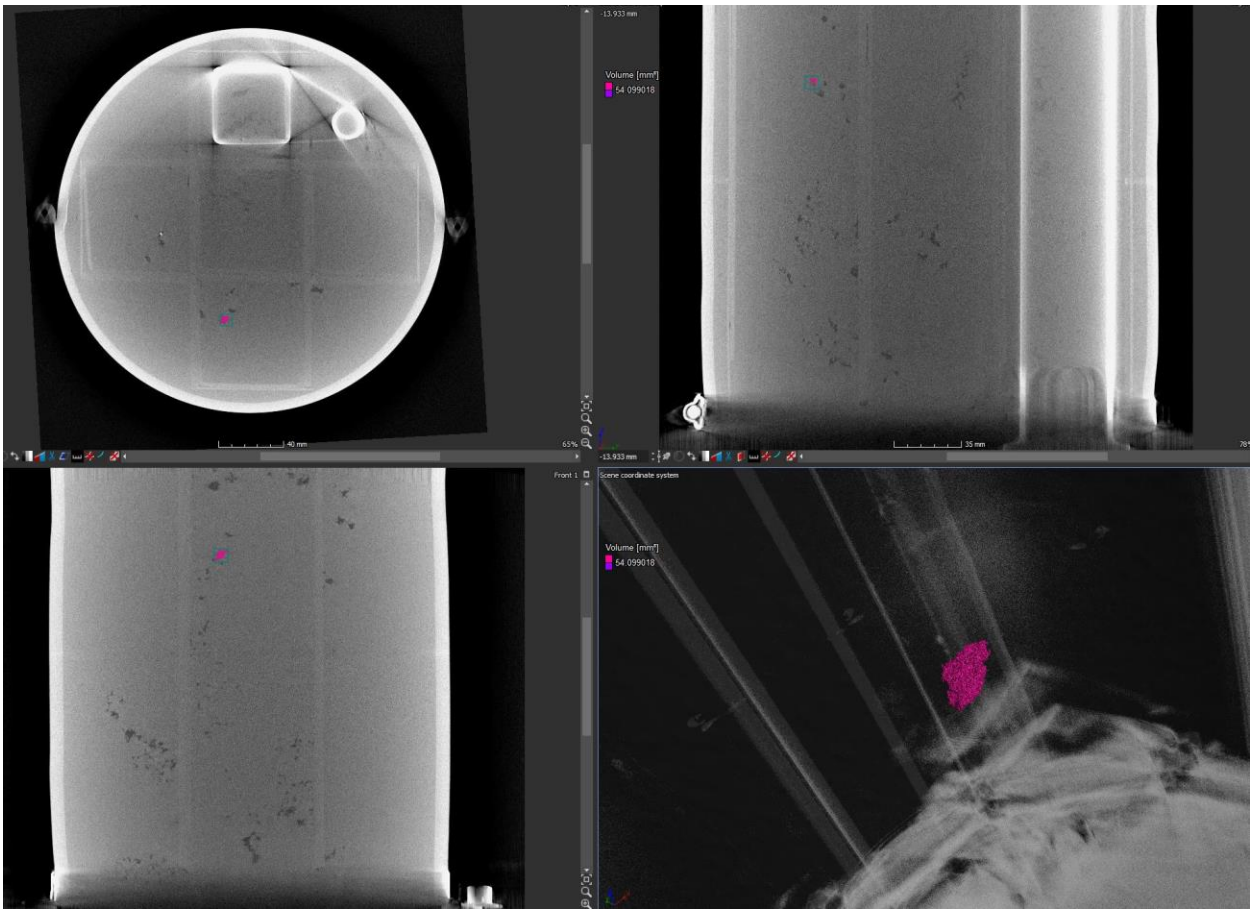

Figure B-8. Chosen Void (Magenta) Captured from Different Angles and Analyzed for Total Volume (mm^3).

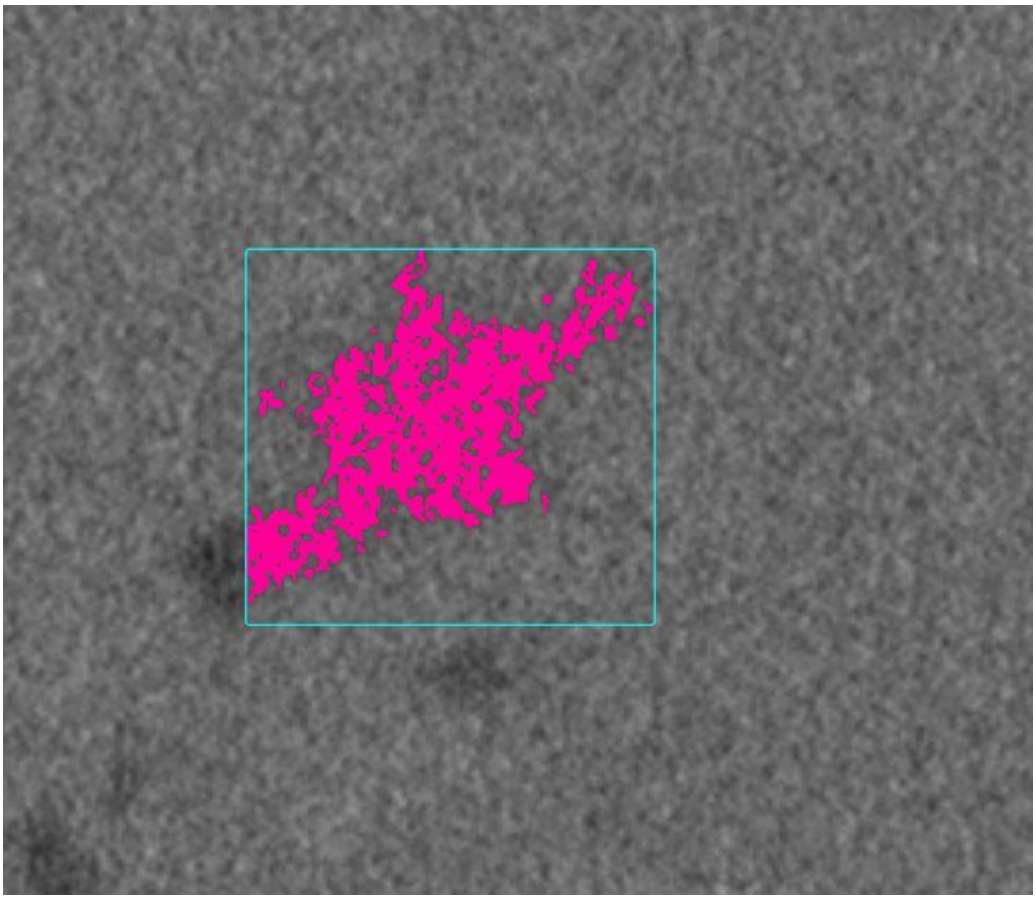

Figure B-9. Detail of Chosen Void.

As shown in Figures B-8 and B-9, the chosen void was calculated to be approximately 54.1 mm^3. The analytical capabilities also allow the user to specify a minimum void diameter, and the program will identify all voids above that specified minimum. Initially, voids greater than 0.5 mm in diameter will be identified. The data can then be used to identify large interconnected voids and can also be used to compute the total void fraction in the solidified paraffin. In the future, during metal filling of canisters, CT scan may be used identify voids.

B-3. Dual-Purpose Canister Preheating Simulation

Thermal preconditioning or preheating is required for casting/solidification of liquid fillers. One option for preheating the DPC is to use hot gas that can be circulated through the existing DPC ports. This work is a preliminary evaluation of the viability of such an option. COBRA-SFS (Spent Fuel Storage; CSFS), a well-known thermal analysis tool, was selected to perform the simulations, and an existing canister model of the TN-24P spent fuel cask is used as a prototype. The simulation is the first of its kind, and this section provides an overview of the progress made to date. A Transnuclear, Inc. TN-24P cask is used as a representative cask for this simulation. A drawing of the TN-24P is presented in Figure B-10 below.

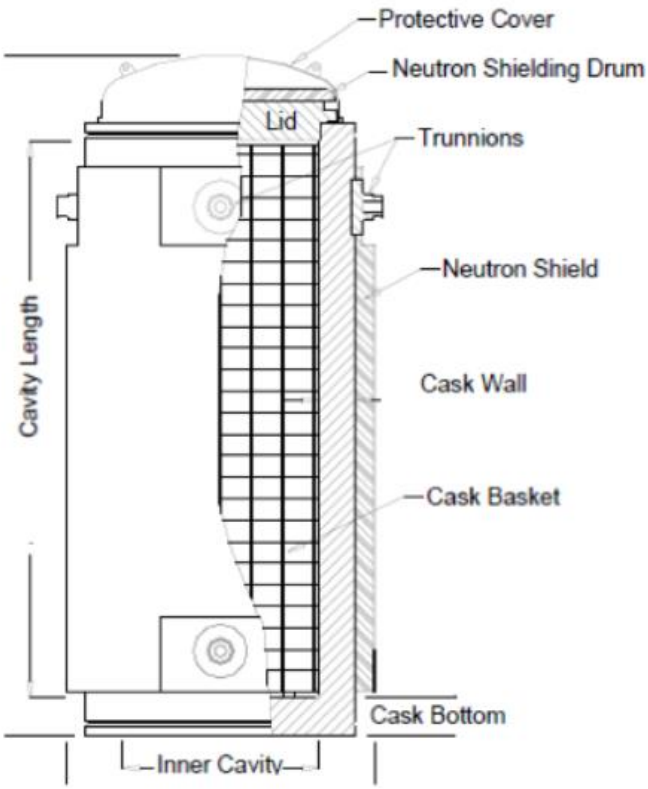

Figure B-10. Schematics of TN-24P Spent Fuel Storage Cask [3].

B-3.1. TN-24P Canister

The TN-24P consists of a cylindrical forged steel body surrounded by a resin layer for neutron shielding (Figure B-10). The internal basket structure consists of thin plates of borated aluminum arranged in rectangular cells to accommodate 24 fuel assemblies. The total decay heat load of the cask is 8 kW with a power density of about 4 kW/m^3.

As part of the CSFS validation, experiments with the TN-24P cask were simulated [3]. A model was developed and tested by Michener et al. [2] and is used for the heating evaluations in this study. The performed CSFS validation assessment showed good results, matching well the experimental data and thus providing the main rationale for selecting this prototype canister model.

B-3.2. COBRA-SFS Model of TN-24P Canister

The cask and its components are represented with rod and assembly models of the 24 fuel bundles. The basket, supports, the metal of the cask container, and the layers of the neutron shields are modeled with a network of radially and azimuthally connected slab nodes. The cask base and the region above the basket, including the various layers of structures, are modeled with a lower and an upper plenum. Figure B-11 is a cross section diagram of the model, showing the assembly and radial heat slab numbering and presenting an overall view of the model. Each assembly is modeled with 225 rods (15 × 15) and 256 subchannels.

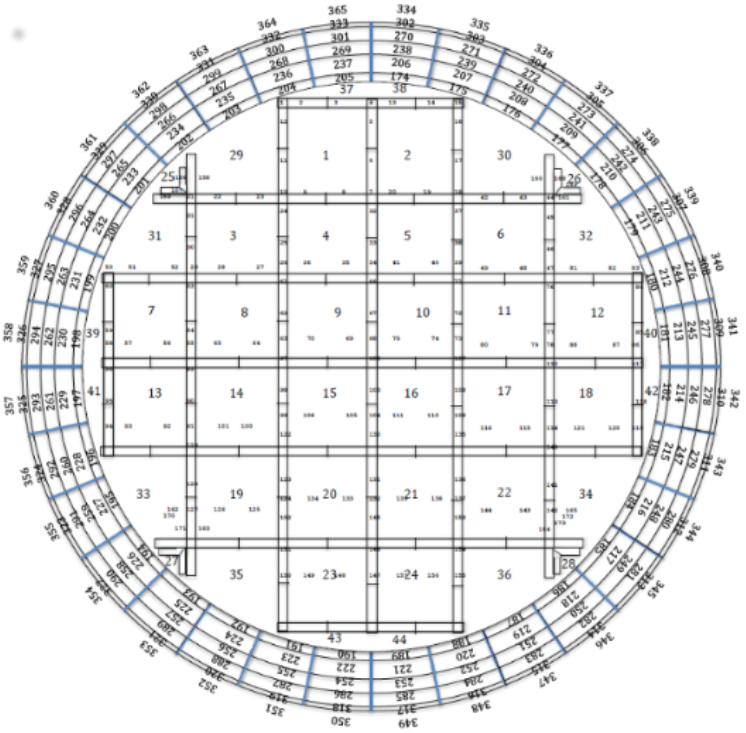

Figure B-11. CSFS Noding Diagram of TN-24P Canister [2].

The model was developed for CSFS validation and is not suitable for heating analysis. Therefore, several modifications have been made, most of which focus on capturing the following two processes:

- Injection of the heating gas into one of the existing basket sections
- Forced gas circulation through the active (fueled) and the inactive assemblies (space between the basket and the shell).

To accomplish the modifications, the lower plenum was removed, and assembly 28 was chosen as the inlet port. The intent is to model a hot gas injection through the drainpipe. A flow path formed, so the gas redistributes in the upper plenum to the assembly outlets. The flow in the assemblies is from the top down. This flow configuration is dictated to a great extent by the modeling functionality of CSFS, in which the upper plenum model does not allow inlet boundary conditions. In reality, if the drainpipe is used for gas injection, then the flow would enter at the bottom and leave at the top through the vent port. While other configurations are possible, the one described above was selected as a starting point.

Individual assemblies operate in flow regime mode, in which the inlet mass flux is distributed among each assembly, and pressure drops are calculated. The normalization to the assembly flow area requires the inlet gas assembly to have a recalculated mass flux fraction. The fraction is defined as shown below, assuming equity of the incoming and outgoing mass flows:

$$\dot{m}_{in} = \dot{m}_{out} = Gin \sum N_i A_i, \quad (1),$$

where

$\dot{m}_{in} = inlet\ mass\ flow$, kg/s,

$\dot{m}_{out} = outlet\ mass\ flow, kg/s,$

$Gin = total\ inlet\ mass\ flux, kg/sm^2,$

$A_i = assembly\ flow\ area, m^2,$ and

$N_i = number\ of\ assemblies\ type\ 'i'$

The inlet assembly fraction *FRin* is:

$$FR_{in} = \frac{\sum N_i A_i}{A_i^{in}}, \quad (2)$$

where

$A_i^{in} = the\ inlet\ gas\ assembly\ flow\ area, m^2$

The inlet hot gas, heat load, and outside boundary conditions for the performed simulations are summarized in Table B-2.

Table B-2. Inlet and Boundary Conditions for TN-24P Cask Heating Simulations

Heating gas	*Nitrogen*
Inlet assembly	28 (basket corner)
Outside temperature	21°C
Inlet mass flow rate	0.021 kg/s
Inlet gas temperature	425°C
Fuel decay heat	8 kW

B-3.3. Results from the Original Model Modified for Gas Injection

There are four assembly types in TN-24P. Type 1 includes the fuel assemblies, and types 2–4 are assemblies modeling the space between the basket and the wall. Initially, the canister was assumed to not be thermally insulated on the outside surface. An open boundary natural convection heat transfer coefficient was applied to all external canister surfaces to simulate the ambient air cooling the canister.

The entire heating gas flow was injected into the basket periphery in the corner slot corresponding to the position of the pipe used for drainage (drainpipe). This area was modeled with assembly type 2 (assembly 28), as shown in Figure B-11. The thermal and fluid results for assembly 28 are plotted in Figure B-12.

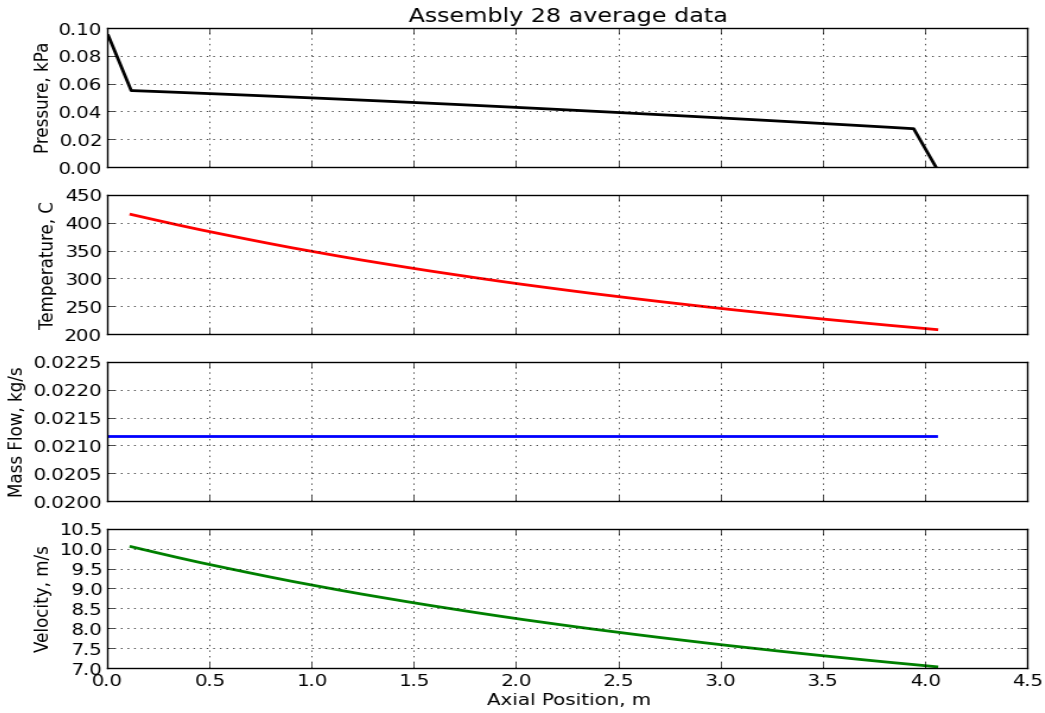

Figure B-12. Assembly 28 Average Results: Pressure Drop, Temperature, Mass Flow, and Velocity.

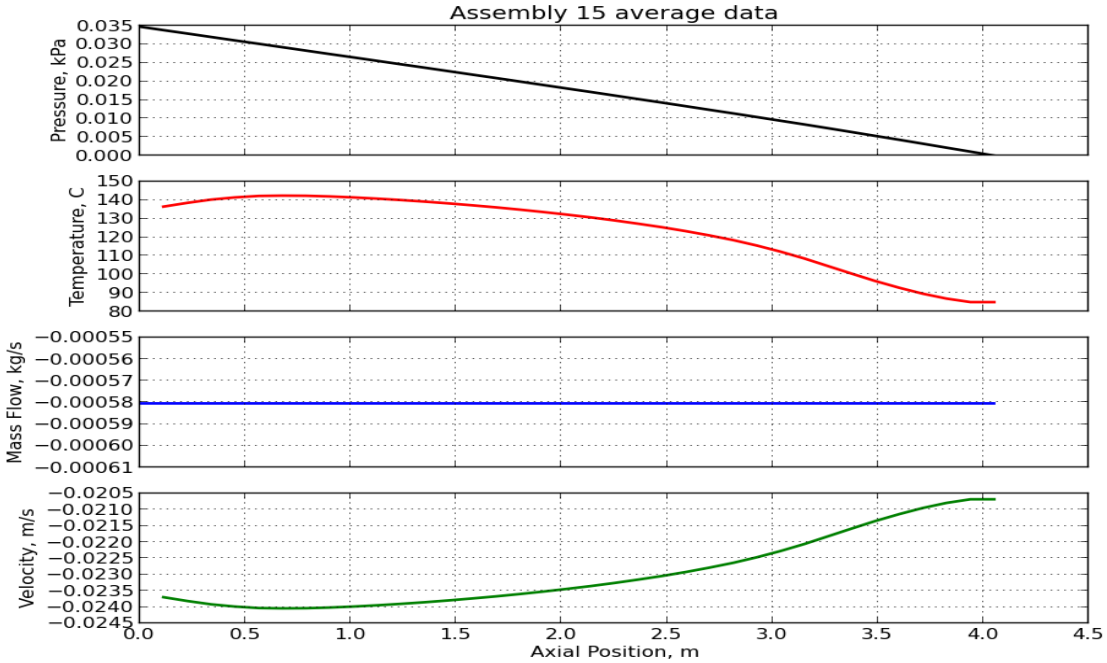

Figure B-13. Average Results for a Centrally Positioned, Mid-Canister Fuel Assembly.

The gas enters at a temperature of 425°C, which is assumed to be the maximum possible for some of the canister materials. As the gas flows upward, it transfers heat to the canister structures and reaches a temperature of around 200°C when entering the upper plenum. The gas flow rate is defined by the assumed maximum velocity of 10 m/sec.

The flow direction in the remainder of the assemblies is from the top down, resulting in a negative mass flow and velocity. Results for a representative, centrally positioned fuel assembly are shown in Figure B-13. The fuel assembly entry temperature is only 85°C. The temperature further increases as the gas flows down due to heating from the fuel rods, reaching around 135°C at the assembly exit. Due to heat losses to the environment, the temperature experiences an inflation.

The thermal conditions in the space between the basket and the wall are calculated in assemblies 30 (type 3) and 38 (type 4). The results are similar and are plotted in Figure B-14. In the basket corners (assembly 38), some heat is transferred from the fueled part of the canister, and the temperature recovers. The lowest temperature is around 65°C.

The calculations suggest that without thermal insulation on the outside or without other means of keeping the canister off thermal contact with environment, it will not be possible to achieve the temperatures needed for casting. Depending on the filler material, the target temperatures are expected to be in the range of 250–300°C.

The upper plenum has a relatively large volume, and the velocity of the injected gas significantly decreases. When combined with the intensive heat transfer, this leads to a noticeable gas cooling and causes a temperature inflation as seen in Figures B-13 and B-14. Within the plenum alone, the temperature drops at least 120°C. This result led to a revision of the original upper plenum modeling which is carried out below.

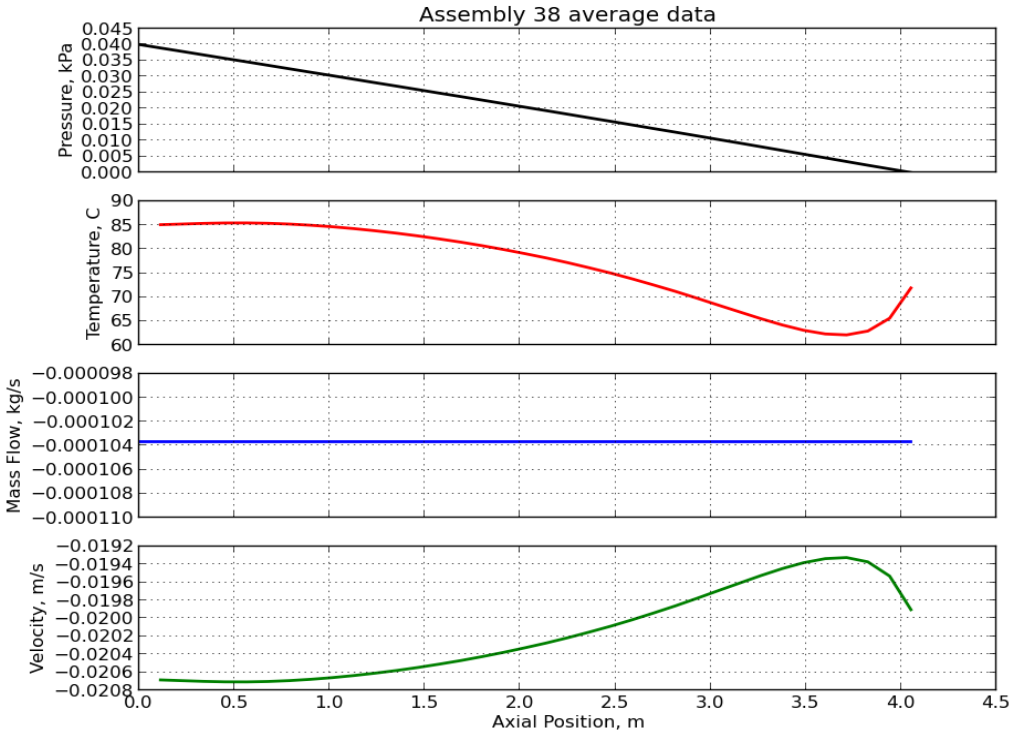

(a)

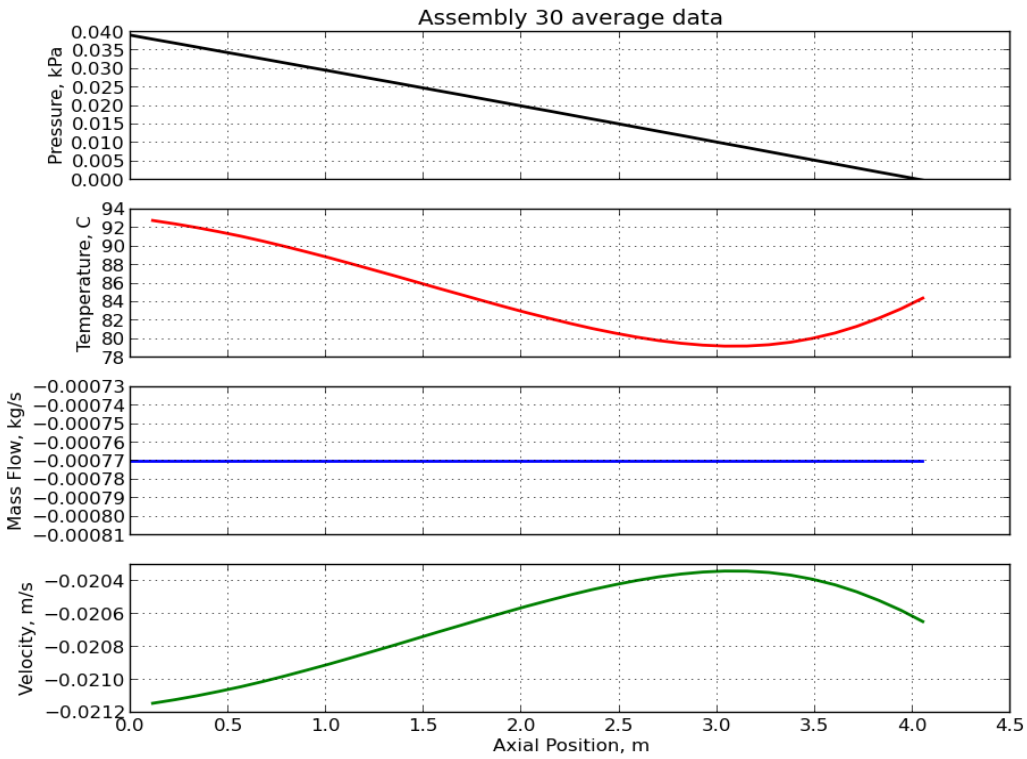

(b)

Figure B-14. Results for Basket Sides (Space between Basket and Canister Wall) with Two Characteristic Assembly Types: (a) Assembly 38, with a Narrow Space on Each Side of the Basket in Proximity to the Canister's Wall, and (b) Assembly 30, with a Wide Space in the Basket Corners.

B-3.4. Revision of the Upper Plenum Model

The upper plenum model in CSFS is a lumped parameter model. The model computes only a thermal solution in which a heat balance is taken on the incoming and outgoing fluxes, including fluxes to the outside. The model has three axial and three radial nodes. The first two nodes model solid material conduction, while the third node (both axially and radially) models a convective heat transfer boundary to the environment. The upper plenum contains the TN24P lid, shown in Figure B-15. The noding configuration is colored with green in axial direction, and with brown in the radial direction. The nodes represent different materials that are as close as possible to reality in view of the geometry complexity and the modeling limitations.

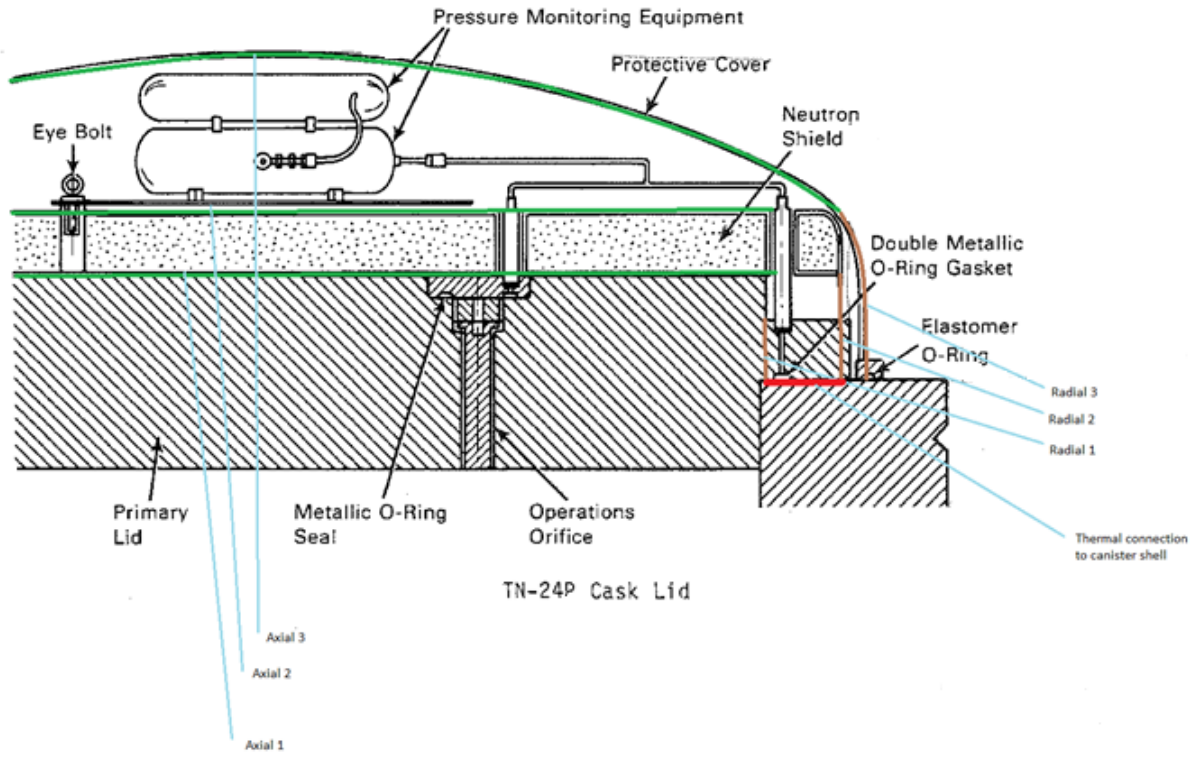

Figure B-15. A Schematics of TN24P Canister Lid and Assumed Noding in Axial and Radial Direction [3].

To estimate the convective heat transfer to outside, the following correlations for the Nusselt (Nu) number on isothermal vertical and horizontal surfaces are used based on the Rayleigh number (Ra):

Horizontal: $Nu = 0.15\, Ra^{1/3}\ for\ 10^7 < Ra < 10^{11}$

Vertical: $Nu = 0.1\, Ra^{1/3}\ for\ 10^9 < Ra < 10^{13}$

CSFS models the heat flux by a generalized equation in which the surface areas of each node are given, together with three coefficients: C1, C2, and C3. The meaning of the coefficients is defined in the CSFS input description [2]. In Table B-3, the original upper plenum data are compared with evaluations of the same quantities using the assumptions presented above. There are several areas of large discrepancies: (1) in the radial node surfaces, nodes 2 and 3 heat transfer areas are about three times larger than the estimated surface, and (2) in the coefficients C1 and C2 for both the axial and the radial nodes. One of these coefficients is to note C2 for the third radial node, which has a value of 1 in the original model. The estimated value is nine orders of magnitudes higher. Changes were introduced to the upper plenum model to account for the new values, and the simulation was rerun.

Table B-3. Assessment of the Upper Plenum Heat Transfer Areas and Coefficients.

Region	*Heat Transfer Area*		*Thickness or convective length (L)*	*Region thermal conductivity*	*Heat transfer coefficients C1 - Btu/s-in2-F; C2 – 1/F, C3 – n/a*	
	In model	Estimate	Estimate	Material based	In model	Estimate
Radial 1 steel 2 mix 50/50 (steel+prop) 3 convective	411in^2 (0.26 m^2) 4650 in^2 (3.0 m^2) 6373 in^2 (4.1m^2)	666 in^2 (0.43 m^2) 1194 in^2 (0.77m^2) 2187 in^2 (1.41m^2)	ΔX=0.73 m ΔX=0.14 m L = 4 m	Carbon Steel 24 Btu/h-ft-F 41.5 w/m-K Propylene 0.09 Btu/h-ft-F 0.15 w/m-K Air at 35°C 0.015 Btu/h-ft-F 0.027 w/m-K (ν=1.65-5 m^2/s) (β=3.25-3 1/K)	C1=1.89-6 C1=3.26-5 C1=1.09-6 C2=1 C3=0.33	C1 = 1.93-5 C1 = 5.06-5 C1 = 2.3-10 C2=2.91+9 C3=0.33
Axial 1 steel 2 propylene 3 convective	2599 in^2 (1.67 m^2) 2599 in^2 (1.67 m^2) 2599 in^2 (1.67 m^2)	2577 in^2 (1.66 m^2) 2577 in^2 (1.66 m^2) 3923 in^2 (2.53 m^2) (spherical cap)	ΔX=0.28 m ΔX=0.11 m L = A/P = 2.53/5.4=0.5m		C1=4.73-5 C1=4.60-5 C1=5.30-9 C2=7.74+7 C3=0.33	C1 = 5.04-5 C1 = 4.64-7 C1=2.75-9 C2=5.69+6 C3=0.33

Results for temperature variation in selected assemblies are compared in Figure B-16. The assemblies shown are assembly 16 (fueled bundle), assembly 33 (large space/gap), and assembly 39 (narrow gap). The temperature gain after remodeling the upper plenum is between 40 and 50°C. The remodeling helps to keep the temperatures in the entire canister above 100°C, except in the narrow gap, where the cooling by the shell has a larger impact. Apparently this area will be limiting for the heating process. The temperature trend changed from increasing to declining in the large space area, and a more even distribution is seen in the fueled part. The overall effect is positive, but it is insufficient to provide enough margin to allow for filler material casting. Further evaluation of the side boundary convective cooling will be performed in order to analyze the origin of the temperature inflation seen in the fuel bundles and in the narrow gap.

Another view of the temperature distribution in the canister can be obtained by plotting all assemblies together on a map plot. The map plot gives a distribution of temperatures in a plane passing at a specified axial position in the canister. Views are taken at the entrance, at the mid plane, and at the exit. The exit (top, level 36) plane is shown in Figure B-17, which provides a good representation for the temperatures in the upper plenum. The effect of modifying the heat exchange areas and the free boundary heat transfer coefficients is clearly seen. The temperatures are significantly higher in the revised upper plenum model. The gas injection assembly, seen in the lower right corner, is the hottest. All assemblies on the map have equal areas, but in reality, the injection assembly (#28) models a very small space in the corner of the basket (the drainpipe). If a larger port for gas injection is identified, then the gas flow can be increased and the heating improved. In this analysis, the gas flow is limited by the assumed maximum gas velocity of 10 m/s.

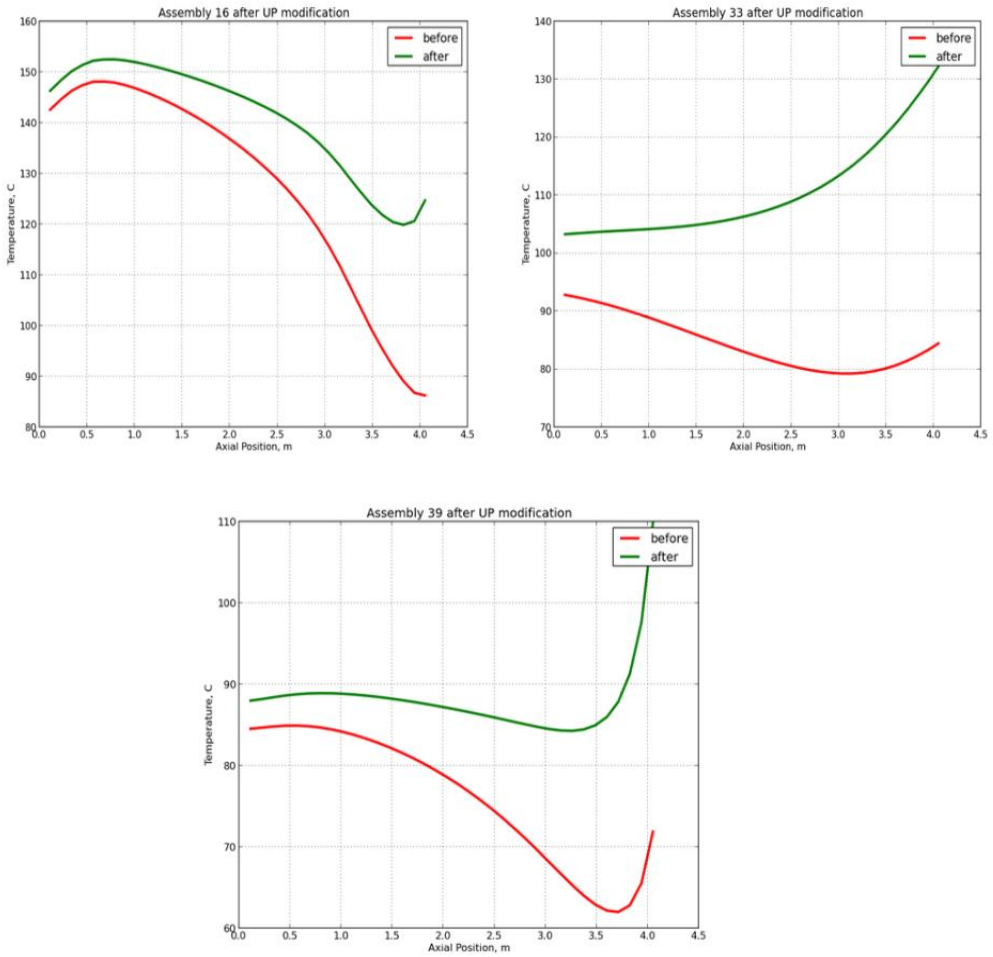

Figure B-16. Comparison of Temperature Evolution in Three Selected Assemblies from the Fueled, Large Space, and Narrow Gap Regions between Basket and Shell for the State Before and After Modification of the Upper Plenum Model.

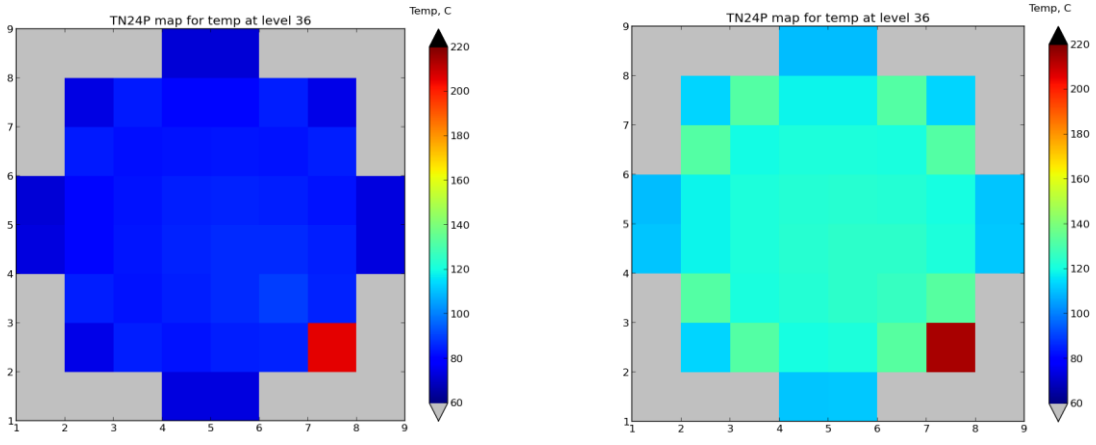

Figure B-17. Map of Temperature at the Exit (Level 36) of the Canister. Left (Before) and Right (After) the Upper Plenum Modification. The Gas Injection Assembly with the Highest Temperature is Seen in the Lower Right Corner.

The effect of upper plenum modification weakens with decreasing axial height. In the mid-canister plane (Figure B-18), the temperature gain is significantly lower. Only a slight increase of temperature is seen around the gas injection assembly (marked with black). The canister periphery areas (wide and narrow gaps) are much cooler and are of main concern for the heating, because they experience the most cooling from the shell.

At the bottom of canister, the temperature map has not changed after the modifications (Figure B-19). The dissipation through the sides (canister shell) has a significant impact on the axial cooling, and the temperatures have remained almost the same. Only the assembly in close proximity to the injection assembly stays relatively hot (yellow colored, assembly 22, temperature around 160°C). The heating occurs mostly due to radial conduction, because assembly 22 is in direct contact with the hot heating gas. The contribution of the convective gas flow coming from the upper plenum is small. This figure demonstrates the ability of CSFS to capture and correctly interpret different heat trasfer mechanisms occurring in the canister.

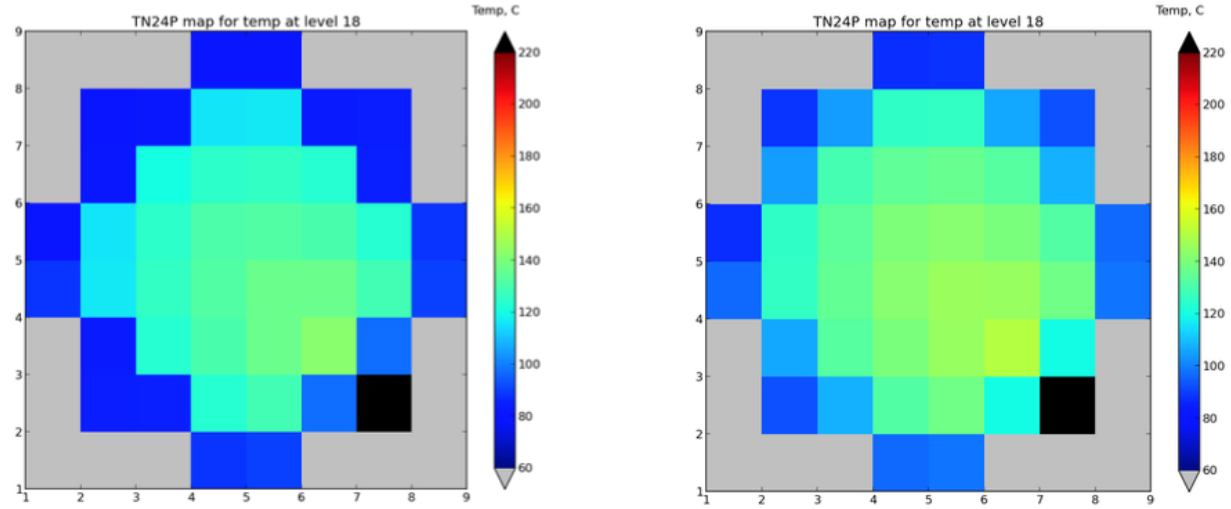

Figure B-18. Temperature Map at the Mid Canister Plane –Before (Left) and After (Right) the Upper Plenum Modification. (Gas Injection Assembly Shown with Black to Allow for a Narrower Scale).

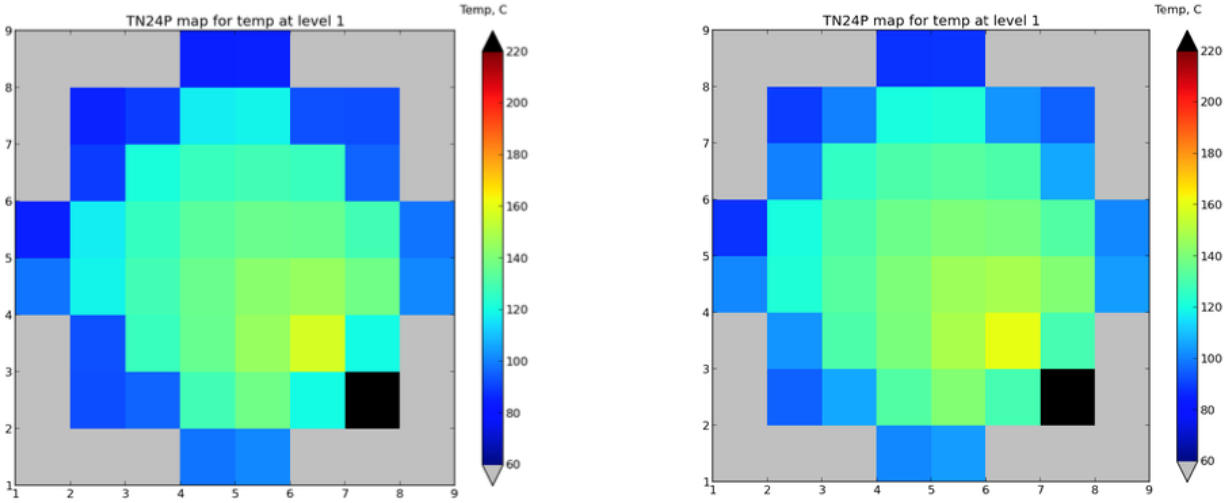

Figure B-19. Assembly Temperature Map at the Canister Bottom Before (Left) and After (Right) the Upper Plenum Update. Gas Injection Temperature (Black Assembly) is 425°C.

B-4. Drainpipe Experiment

As described in [5], the pipe experiments were divided into two phases to provide a separate effects approach to the problem and to allow for development of system scalability. The first phase included taking strain measurements in a short length pipe, as well as measurements of flow-induced vibration. The second phase consists of the design and construction of a separated mercury flow loop capable of hosting exchangeable test sections and more localized instrumentation. These experiments are being used to determine the feasibility of filling DPCs using the existing drainpipe. The Phase I experiment was performed and reported in [5]. This section provides the data reduction and data analysis of the Phase I experiment, as well as the status of the Phase II experiment.

B-4.1. Data Reduction and Analysis of Phase I Experiment

A distributed fiber sensor with a design based on the use of fiber optics with fiber Bragg gratings (FBGs) was installed to characterize the strain distribution along the vertical pipe and at the bottom external surface of the elbow. Dedicated fibers with a diameter of 0.150 mm were attached to the surface of the vertical pipe and at the bottom external wall of the 45° elbow using bonding epoxy to characterize strain measurements, as shown in Figure B-20.

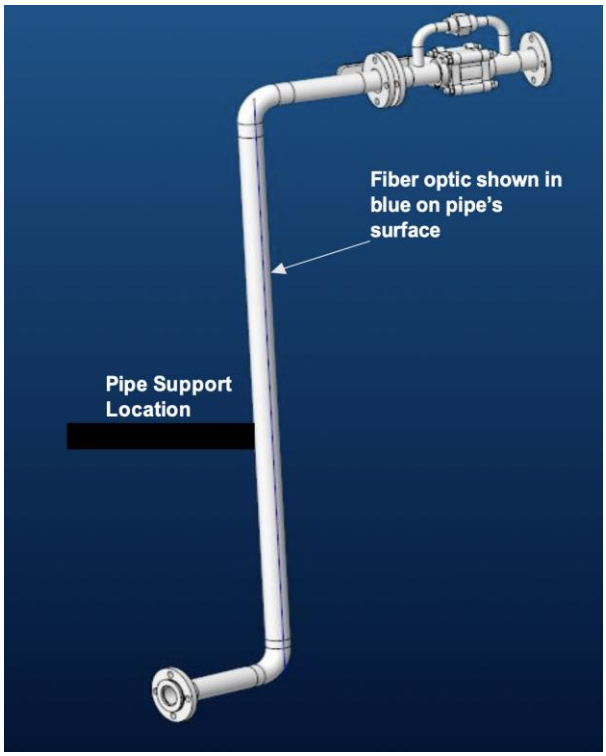

Figure B-20. Vertical Pipe with Distributed Fiber Optic Sensor for Strain Measurements.

Raw data obtained from the distributed optical sensor were processed using commercial software frequency spectrum analysis tools. The raw data are exported as a comma-separated value (csv) file format so that it can be used as an input deck for external software. Typical raw data obtained from the distributed optical system are showed in Figure B-21. The data were normalized using a moving average function. The x-axis shows sensor location along the pipe, in which sensors 1–20 are located at the bottom of the vertical pipe with a space resolution of 1 mm. Sensors 21–60 are processed as sensors with a constant distance between them of 25.5 mm. It should be noted that all sensors are located on the same physical fiber, which has fiber Bragg gratings along its length, with constant spacing. Data are detrended by subtracting a cubic fit, as shown in Figure B-22.

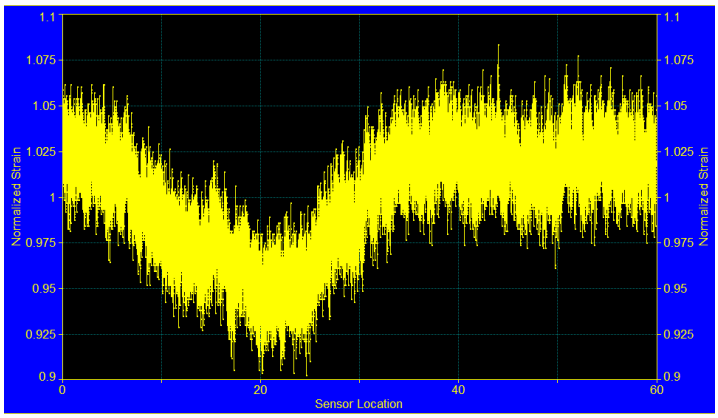

Figure B-21. Typical Normalized Raw Data Obtained from Distributed Optical Sensor.

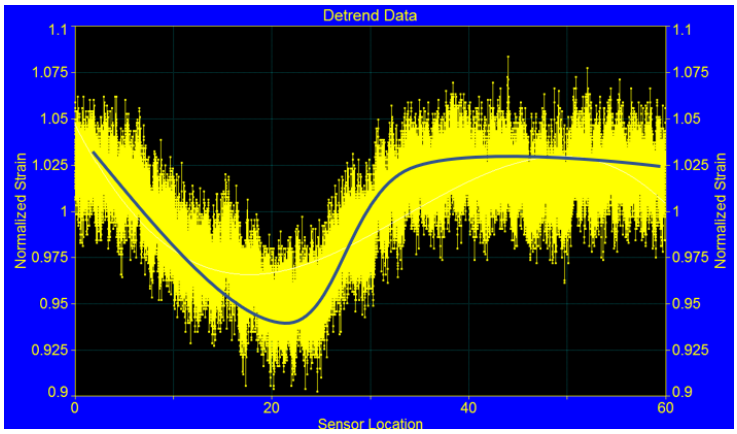

Figure B-22. Typical Detrend Data Obtained from Distributed Optical Sensor.

A continuous wavelet transform (CWT) was performed on each data signal to obtain vibration frequencies along the pipe, as shown in Figure B-23. Characteristic frequencies can be related to time gaps by the use of CWT. For all analyzed cases, a Morlet mother wavelet was used to process the signals.

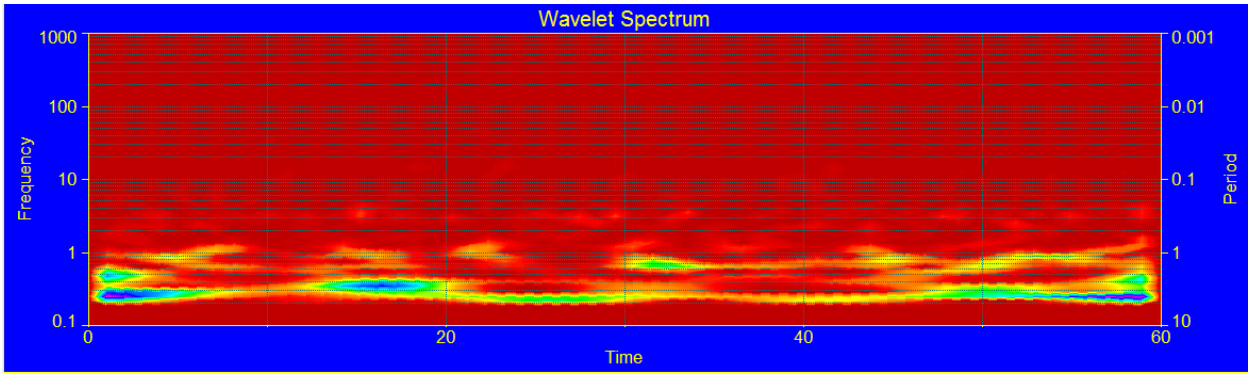

Figure B-23. Typical Continuous Wavelet Spectrogram Data Obtained from Distributed Optical Sensor.

The vibration frequencies for each tested case were obtained using information provided by the CWT, along with the average strain rates along the length of the pipe, as shown in Table B-4. Visual vibration confirmation obtained during operation was observed for the two highest flow rates tested.

Table B-4. Measured Pipe Vibration Frequencies as a Function of Flow Rate.

Flow rate (kg/s)	Main measured frequency (Hz)	Observed pipe vibration	Maximum average strain along pipe (μs)
25.5	7.5	Yes	520
17	4.2	Yes	460
8.5	3.6	No	304
4.25	4	No	350

B-4.2. Status of the Phase II Test Loop

Phase 2 of the experimental program addresses the design of an independent low volume mercury loop that will share the current test facility's environmental enclosure. The design and construction of this secondary liquid metal loop will provide a more versatile way to place exchangeable test sections and will provide more realistic flow conditions as expected during the DPC drainpipe filling operation.

The test design of all loop components was finalized. A parts list was generated, and a test stand design has been finalized. The test section has been specified as an exchangeable standard stainless steel pipe with a coaxial transparent PVC pipe. The test section is contained in a secondary vessel made of schedule 40 PVC transparent pipe, as shown in Figure B-24.

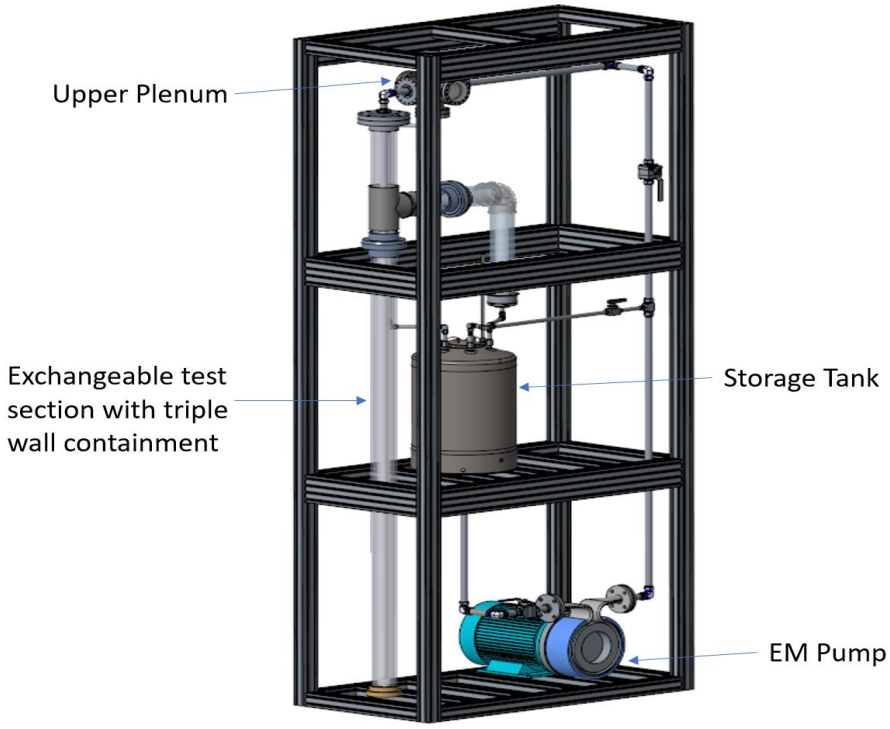

Figure B-24. Designed Liquid Metal Flow Loop with Induction Electromagnetic Pump and Test Section.

B-5. Ongoing and Future Activities

Ongoing activities include casting/solidification simulation and planning for an experiment with molten metal. Work will also continue to identify viable options for preheating a DPC to support the filling process. ProCast casting simulation software [4] has been selected for the purpose of casting simulation. ProCast has the capability to model shrinkage-related casting defects and void nucleation. Initial modeling efforts include simulation of a drainpipe that is 14 feet long to determine the threshold length for blockage or to discern whether solidification on the walls will drastically reduce the pressure drop. Unit tests will also be performed to validate casting simulation.

As described above, initial solidification experiment using wax as surrogate filler has been performed to study the flow and the void formation characteristics in a DPC mockup. Wax was considered due to its

low density and high viscosity compared to liquid metals. Therefore, problems faced using wax can be considered as the worst-case scenario for filling, thus establishing a lower bound for the filling process. The only aspect of wax that is better than liquid metal is its thermal capacity due to its high specific heat compared to that of metal:2.5 J/g °C (wax) to 0.1-0.25 J/g °C (liquid metals). Experiments with candidate metallic fillers are currently being planned to collect data and broaden knowledge and experience with various aspects of metallic fillers.

Selection of metal: The selection of metal must satisfy certain criteria: (1) a low melting point, (2) low viscosity, (3) low toxicity, (4) low density, and (5) low cost. Many eutectics of tin, zinc, cadmium, bismuth, copper, and lead are all good candidates. However, lead may not be a good candidate due to its toxicity and density, and cadmium may not be suitable due to its toxicity. Bismuth is costly, and with copper eutectics, temperatures are still greater than 475°C. Therefore, zinc and tin are the best candidate materials for unit testing. Tin does not have any known toxicity and is the material chosen for these initial tests with metal filler in a laboratory environment.

Testing Configuration: With a melting point of only 232°C, tin (Sn) is an ideal candidate for filler material. This test will only consider the fuel pins and grid section of the fuel bundle. Tin will be melted in a lead melting pot of the appropriate size and placed above the fuel grid. The fuel assembly will be placed in a sectioned box for easy disassembly (see Figure B-25). Once the tin is melted, the lever will be pulled, and the molten tin will pour into a pipe which will fill the mold with tin from the bottom, similar to the DPC filling setup. The box will be preheated with a heating tape to raise its temperature to about 120°C to avoid instant solidification of tin when it comes in contact with the metal box. The box will be placed on an insulated surface to reduce convective loss of heat during pouring of molten tin.

Post examination: A CT scan will be performed on the assembly to determine the effectiveness of filling after the tin has cooled. By adjusting for the energy level of the x-ray, it is anticipated that the void that may have formed at the tin /stainless steel grid interface can be determined.

After the x-ray is performed, a destructive inspection of the assembly will be performed using electro-discharge machining (EDM). By examining the various areas of the grid, effectiveness of the filling process and its adhesion to the stainless-steel surfaces can be ascertained.

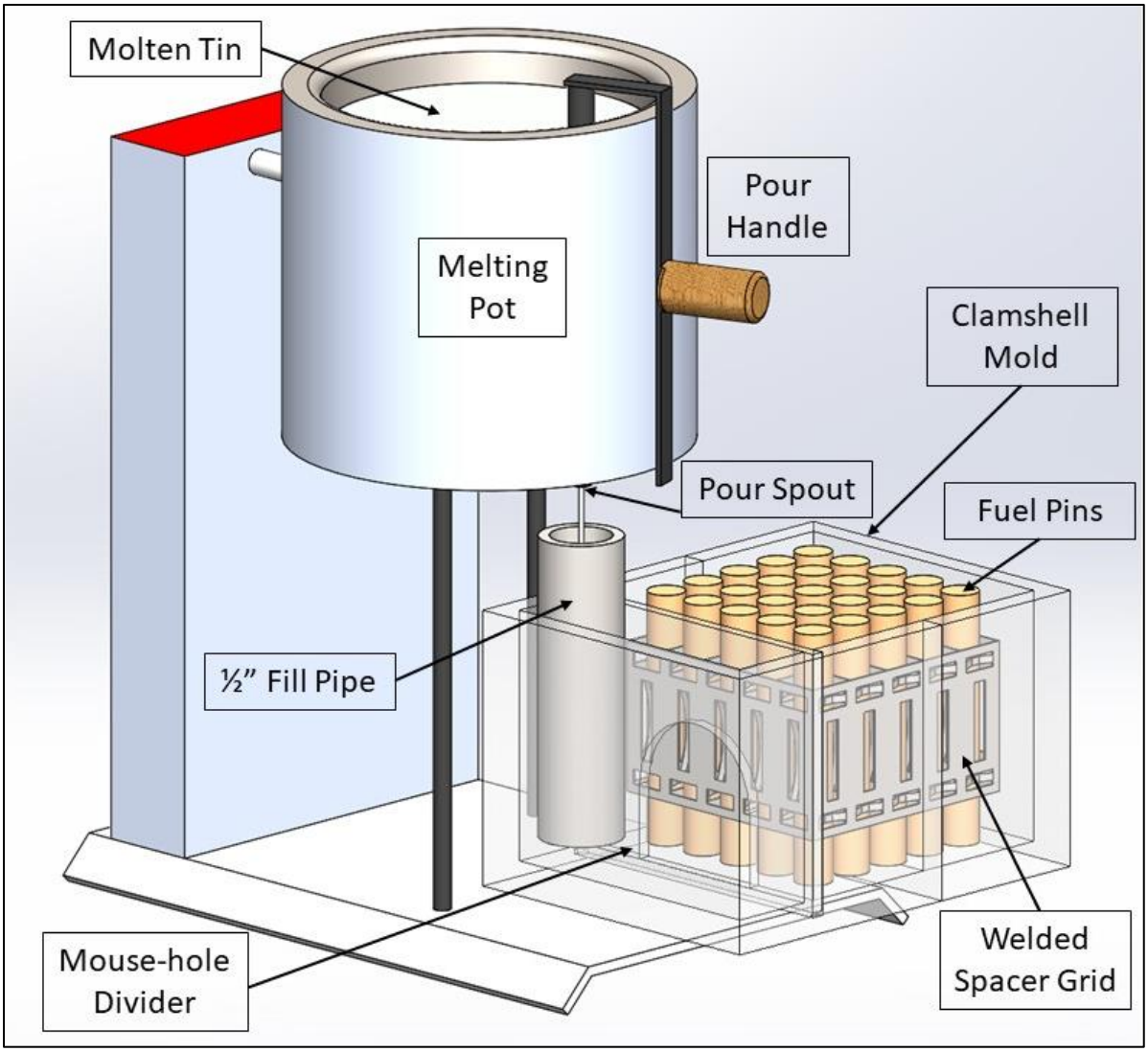

Figure B-25. Experimental Molten Canister Fill-Up Set-Up.

B-6. Discussion

A single physics CFD model was developed to simulate the filling process, and the simulations of the lower region (mouse holes) of a prototypic DPC showed successful removal of the inner void spaces and smooth, even liquid-level progression. Several experiments were performed to validate the numerical simulations. The results from the experiments with water and glycerin showed good agreement with the simulation results.

Another experiment was conducted to investigate the thermal effects associated with the cooling process and to evaluate the void formation inside the restricted geometries. Paraffin wax was used as a surrogate filler to demonstrate the solidification process. A computational casting model is under development to simulate the wax experiment and to help identify issues due to thermal expansion, shrinkage, and cracking due to nonuniform cooling.

After completion of the initial filling demonstrations, the same experiments will be performed with liquid metal. A nontoxic, low melting point metal such as tin, which has a melting point of 231.9°C, will be

tested for further investigations to understand the various foreseen and unforeseen issues related to filling the DPCs in support of direct disposal.

The DPC preheating simulation results demonstrate the modeling capability of CSFS to simulate gas induced canister heating. These initial simulations provide a good basis for further analyses and confirm the applicability of this approach. The selected model seems adequate and suitable for numerical experiments during the search for an optimal and feasible canister heating process. Work will continue with assessments of other gas heating options, as well as thermal conditioning of the outer canister surface. The model developed for CSFS, based on the TN-24P cask, provides a good starting point for these thermal analyses.

B-7. References

1. Luna Innovation Incorporated Fiber Optic Sensors Resource Library (https://lunainc.com/documenttype/tech-notes)
2. T. E. Michener, D. R. Rector, J. M. Cuta, and H. E. Adkins, COBRA-SFS, A Thermal-Hydraulic Analysis Code for Spent Fuel Storage and Transportation Casks Cycle 4a, PNNL-24841 (2017).
3. T. E. Michener, D. R. Rector, and J. M. Cuta (2017) Validation of COBRA-SFS with Measured Temperature Data from Spent-Fuel Storage Casks, Nuclear Technology, 199:3, 350-368, DOI: 10.1080/00295450.2017.1327253.
4. ProCAST / QuikCAST - Casting Processes Simulation Software, https://www.esi-group.com/software-solutions/virtual-manufacturing/casting/procast-quikcast-casting-processes-simulation-software.
5. E. Dominguez-Ontiveros, *Demonstration and Feasibility Analyses of Using the Dual-Purpose Canister Drainpipe to Support the Filling Process*, M4SF-19OR0103050116, ORNL/SPR-2019/1130, March 2019
6.
7. .

Appendix C FY2020 STATUS REPORT

C-1. Introduction

This appendix documents work performed supporting the US Department of Energy (DOE) Nuclear Energy Spent Fuel and Waste Disposition, Spent Fuel and Waste Science and Technology, under work breakdown structure element 1.08.01.03.05, "Direct Disposal of Dual-Purpose Canisters." In particular, this appendix fulfills the M3 milestone, M3SF-20OR010305017, "DPC filler simulation and demonstration progress report," within work package SF-20OR01030501, "Direct Disposal of Dual Purpose Canisters–ORNL."

This appendix presents (1) findings about the paraffin wax experiment conducted to gain insight into the phase change effects and the formation of voids in complicated geometries (e.g., grid spacers), (2) a computed tomography (CT) analysis of the solidified paraffin wax that can be used to determine void fraction after solidification (3) results of the casting simulation, (4) preparations of first casting experiment, (5) benchmarking experiment to verify CFD results, (6) updates of the series of pipe experiments being planned/executed to determine the feasibility of filling a dual-purpose canister (DPC) using the existing drainpipe, and (7) results of preliminary simulations to evaluate DPC preheating/preconditioning (needed for uninterrupted filling of DPCs using metallic or cementitious fillers).

C-2. Examination of Solidified Paraffin and Characterization of Void Distribution using X-Ray CT

The experimental setup designed as the DPC mockup, which used paraffin wax as the filler material, is described in Section B-2.2.

Key objectives of this experimental setup were to gain insight on the formation and distribution of voids during the filling and the subsequent solidification process due primarily to the following:

1. the effect of fluid thermophysical properties such as laten heat of crystallization, specific heat, and liquidus and solidus temperatures;
2. the effect of complex geometries including miscellaneous cavities, holes connecting the cavities, and assembly rod bundles; and
3. the effect of complex physical phenomena between internal structure surfaces and the filler fluid such as contact angle for surface wetting and filler shrinkage upon casting or post solidification cooling, causing voids to open up.

The DPC mockup experimental setup is shown in Figure C-1 with the onset of solidification in the bottom shown on the left, and the fully solidified paraffin wax shown on the right. This simple experimental setup provides opportunities to validate various simulation tools described later in this section. Once a particular filling and solidification model that adequately represents the bounding conditions of the experimental setup is validated, the model can then be used to assess the impact of variations of thermophysical properties on the formation of voids and air gaps. Of particular interest is the connectedness of these internal void and gap clusters, and their communication with the external boundary. The primary driver of this concern is the likelihood of water ingress into a large cluster of void, potentially leading to a re-criticality incident.

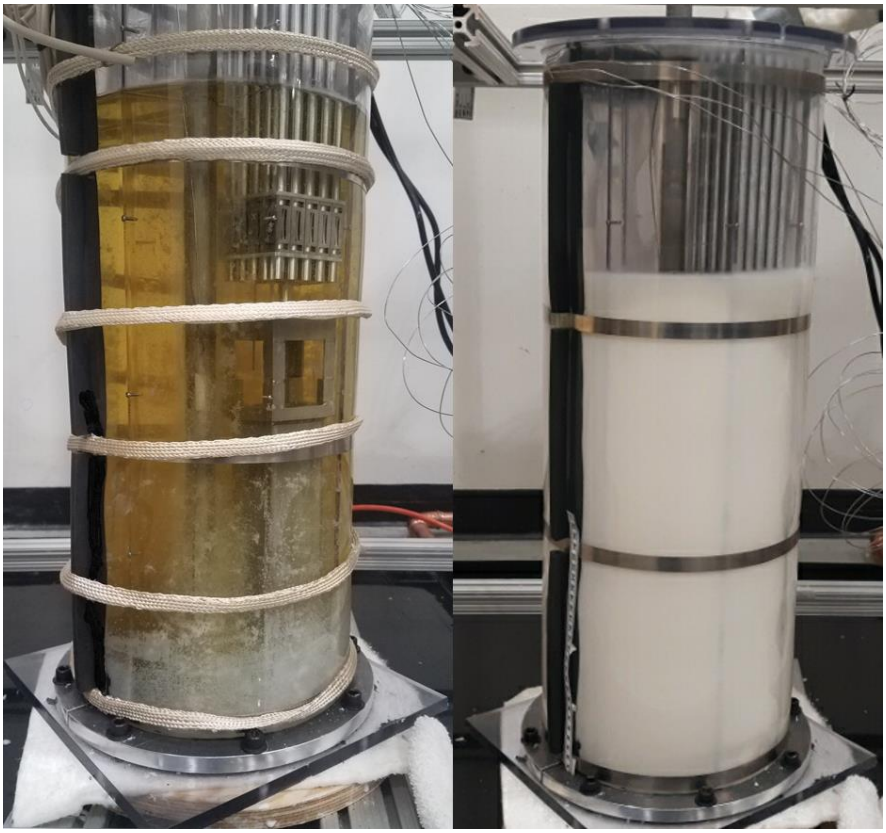

Figure C-1. Experimental Setup for Demonstration of Solidification Process: (left) Onset of Solidification of Paraffin Wax; (right) Fully Solidified Wax.

Numerous experiments and data collection were performed with the paraffin wax using the DPC mockup during the filling, solidification, and after solidification. The fully solidified wax from the first experiment was physically cut and sliced into pieces, as shown in Figure C-2, to obtain visual confirmation of the whereabouts of voids and air gaps.

Figure C-2. Cross Sections from Solidified Wax Samples with Different Concentration of Voids.

The use of paraffin wax offers a number of advantages in the investigation of the filling process. First, the paraffin wax melts at reasonably low temperature of approximately 64°C, facilitiating the design and construction of an experimental setup. Moreover, it provides a conservative case for the formation of voids within the solidified material because of its rapid change of specific volume. The parrafin wax possesses a relatively large specific volume difference between the liquid and the solid states—approximately 12%—which drives the shrinkage process. As a comparison, the change in the specific volume between the liquid and solid states for tin is approximately 3%. Moreover, as will be described later in this section, the paraffin wax enables the use of x-ray CT for quantitative assessment of void volumes and distribution in a large volume, but yielding an acceptable contrast and signal-to-noise ratio between the solid regions and voids. The authors recognize the vast differences in thermophysical properties between the paraffin wax and the potential candidate filler materials, particularly thermal conductivity and diffusivity, latent heat of fusion, specific heat capacity, and the density/specific volume difference between the liquid and solid states. However, the goal of this work is to provide reasonable assurance that casting simulations for DPC filler work for supporting design decisions in the pre-prototype phase of a system. Validating the simulations against a surragate material such as parafin is a fast and inexpensive way to accomplish this goal.

A visual analysis of the sliced pieces of paraffin wax can identify void accumulation with dendritic and inter dendritic structures [1]. The authors observed that void density is significantly larger in bulk sections with a large separation from the walls. This observation further supports that the void formation, at least in this particular arrangement, is primarily driven by unequal volumetric cooling rates and the subsequent non-homogeneity in changes in specific volume of the phase-changing material.

The destructive analysis briefly explained previously provided qualitative evidence on the void formation and distribution, however this destructive investigation lacks the quantitative information—a key experimental objective. This capability is important for numerous reasons: a quantitative analysis is critical to establish a process of validation for the casting models (discussed later in this appendix) and the simulation tool; and a quantitative metric will allow comparison of shrinkage performance of candidate filler materials over a predetermined quantities of interest or an integrated figure of merit.

To enable quantitative characterization of void formation, another test run was conducted with the paraffin wax using the DPC mockup. Once the paraffin wax fully solidified, the DPC mockup was

carefully transported to Pinnacle X-Ray Solutions, Inc. in Atlanta, Georgia, a company that provides industrial x-ray CT services. An x-ray CT scan was performed to examine the solidified wax to gain insight into phase change and the formation and distribution of voids. DPC mockup was scanned in two sections, top and bottom, to enable detailed analysis.

The 3D model was created by reconstructing the 2D x-ray images collected at various orientations by rotating the turntable that holds the canister. These individual images were then used to create a 3D composite image that provided details on the interior, as shown in Figure C-3.

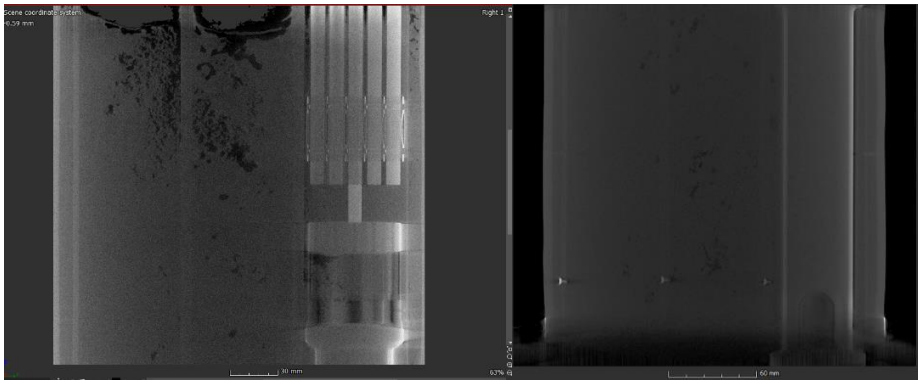

Figure C-3. Side View Showing (left) the Top and (right) Bottom Sections of the Basket, One with the Assembly and Two Empty Cells.

The raw data collected at the Pinnacle X-Ray Solutions, Inc. facility were analyzed with the Volume Graphics Studio Max software package to generate quantitative information about the size and distribution of interior voids. These capabilities were previously reported.

As shown in Figures C-4 through C-5, the Volume Graphics software package offers extensive analysis and metrology capabilities to characterize the voids distributed throughout the interior of the solidified material. Figure C-4, for instance, shows cross sectional details that can be obtained at a plane right at the nozzle but below the assembly level on the 3D model. The nozzle was filled smoothly with no problem. Likewise, Figure C-5 provides a cross sectional view at the first spacer grid mid-plane where excessive accumulation of voids in the basket's empty cell is visible. The void formed inside the pipe was also noticeable at that level on the cut plane.

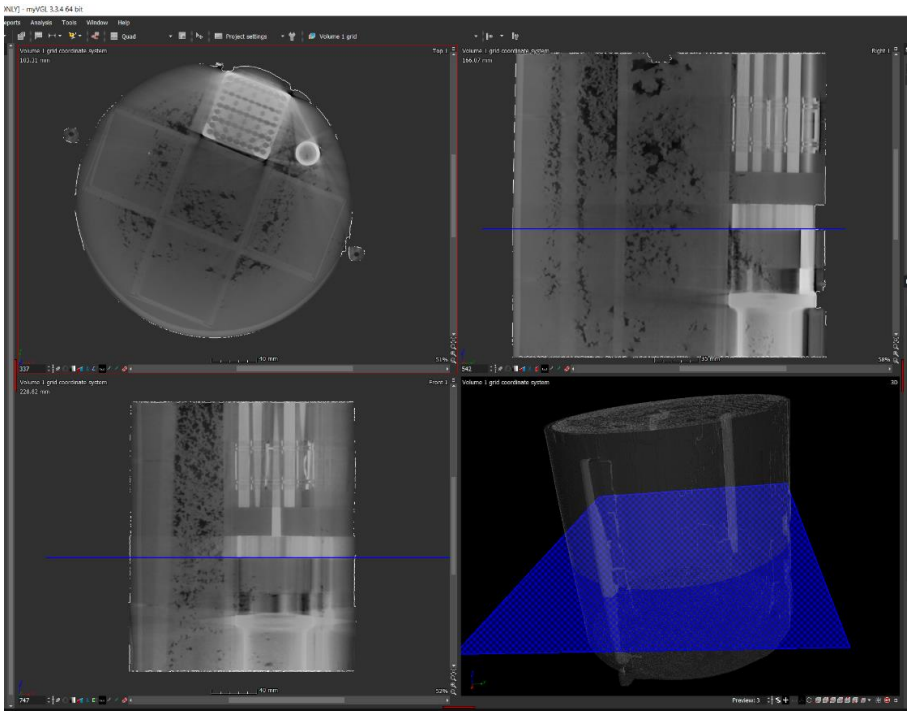

Figure C-4. Cross Sectional Cut Plane Showing across the Nozzle from the Top, Side, and Front Views.

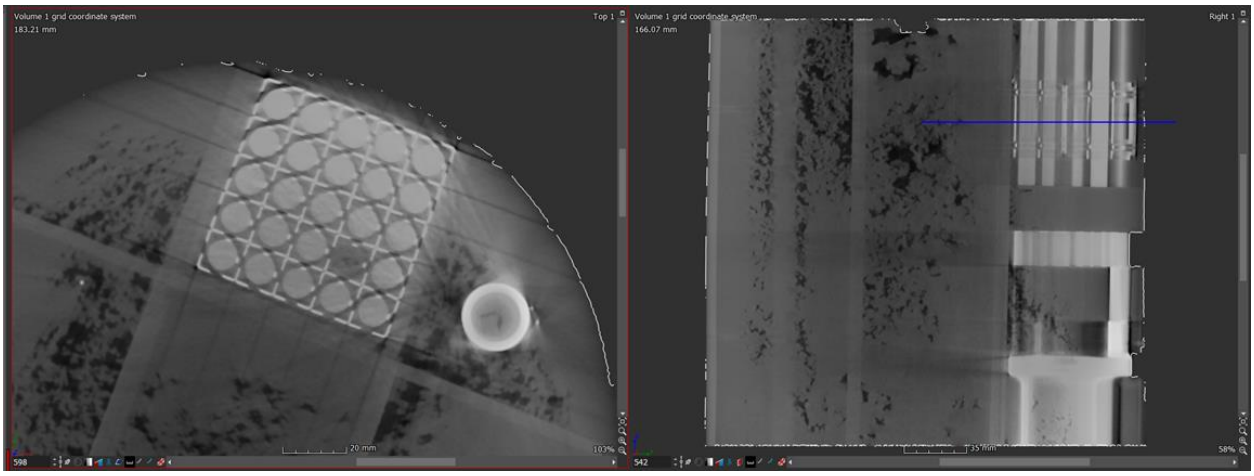

Figure C-5. View of the CT Scan of the Top and Side Cut across the Spacer Grid.

The void formation was more prevalent in the empty cells of the basket, but not as widespread in the cell where the fuel assembly was present. This was expected because the presence of fuel pins provides a conduction path (predominantly axial) leading to a more uniform temperature distribution during the solidification process.

Another important capability of the CT data processing software package is the ability to calculate the volume and diameter of the voids, as shown in Figure C-6 and Figure C-7.

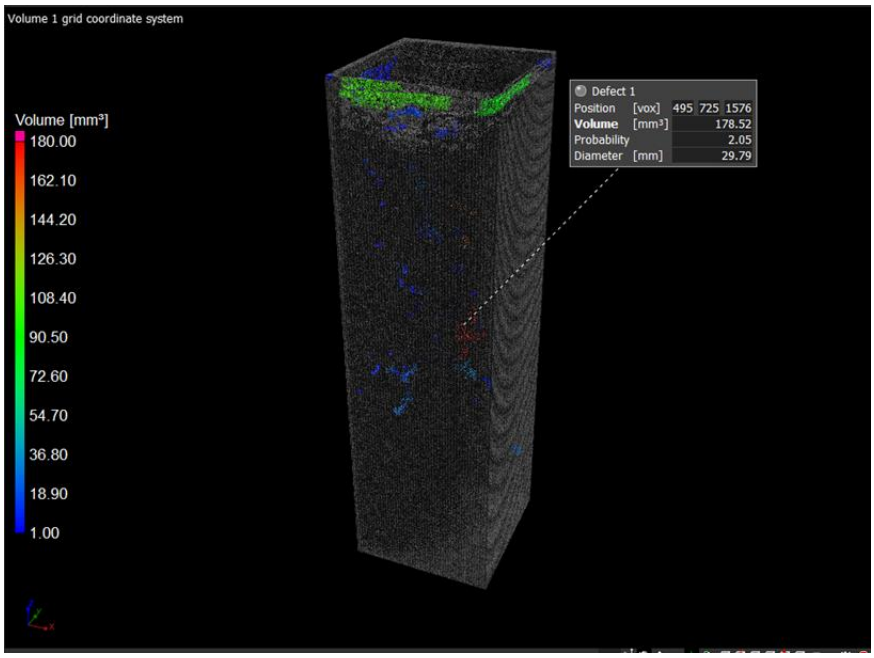

Figure C-6. Analysis Showing the Largest Defect at One of the Cells of the 5 × 5 Basket.

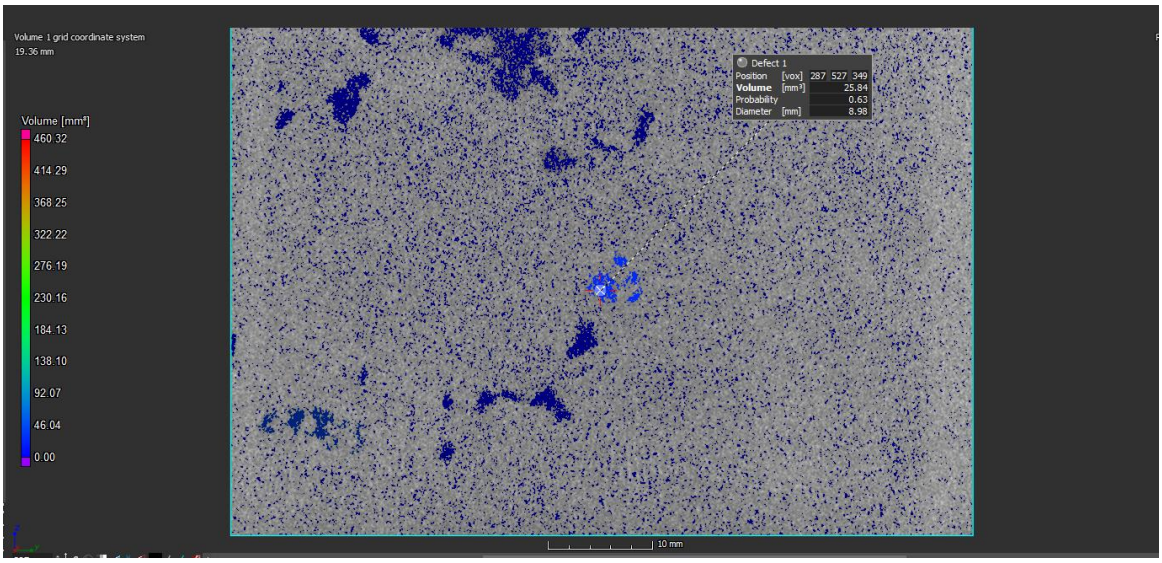

Figure C-7. Defect with 8.98 mm Diameter at the Bottom Section in the Cell on the Right of the Assembly.

CT scan analysis results provided the ability to locate the connected voids. Figure C-8 shows are connected voids inside the solidified wax at the center cell of the bottom section of the DPC mock-up.

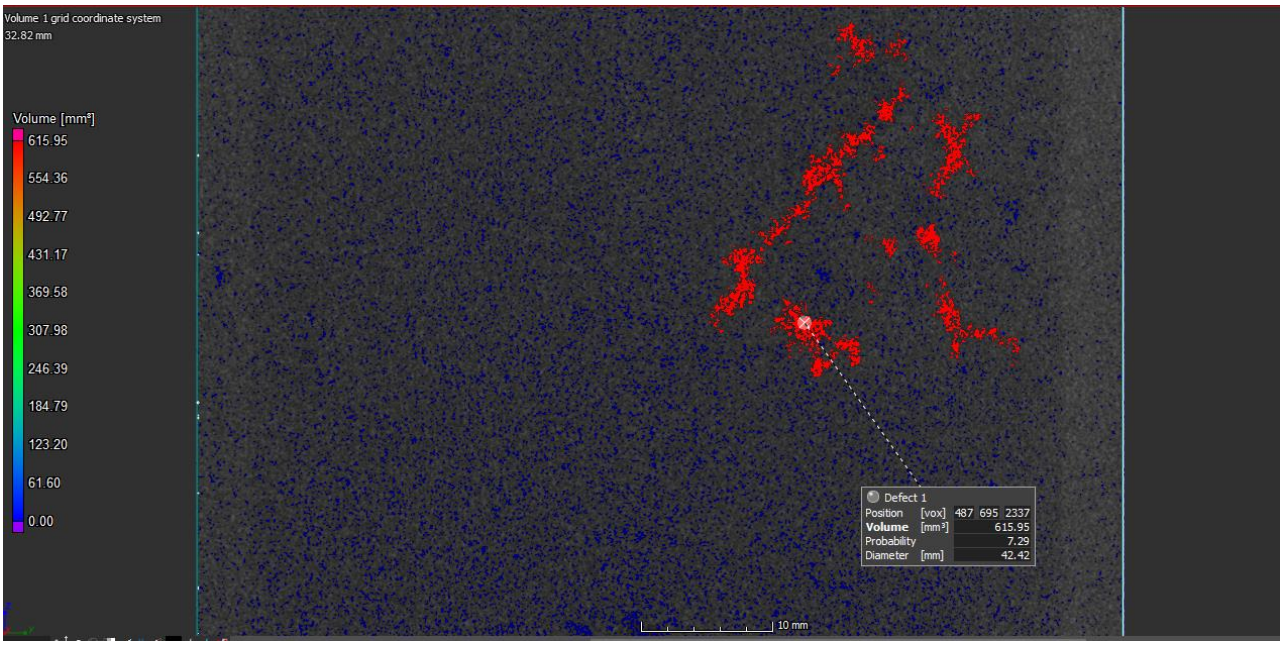

Figure C- 8. Connected Voids at the Bottom Section in the Center Cell of the Basket.

Before examining the solidified wax destructively, a simple experiment was performed to estimate the external connected void fraction. A wax canister was filled with water up to the level of the wax surface. Weight difference with and without water was recorded. 0.0013 m^3 (1,332,083 mm^3) of external connected void fraction was calculated. Total inner defects (voids) were detected from the analysis of the CT scan data and calculated as 50,389 mm^3. The large volume fraction of the external voids agreed with the separation of the cooled wax from the inner walls of the basket and the outer shell. As mentioned earlier, the paraffin wax experiment represents a conservative upper boundary of formation of porosity in solidification.

C-3. Casting Simulations

Step-by-step casting simulations are being developed to enable screening candidate fillers. ProCAST casting simulation software was selected to simulate both metal and composites candidates. ProCAST uses the finite element method to model flow, thermal, and stress behavior in casting. Thermal results include temperature, fraction solid, total shrinkage porosity, and Niyama criterion. Velocity, pressure, and void fraction are results for flow analysis. ProCAST offers the capability to visualize effective stress, effective strain, and displacement. This coupled multiphysics analysis capability will provide a high-fidelity modeling capability once the scaled simulations evolve into full-scale DPC model casting.

C-3.1 Partial Paraffin Solidification Experiment Simulation

The first model used for casting was a section of the DPC mock-up filled with paraffin wax. A quarter symmetry was used for the dummy fuel bundle attached to the bottom nozzle shown in Figure C-9. Spacer grids were not used this time to eliminate the complications from the mesh. Since the model did not include a fill pipe, filling started from the bottom of the assembly and progressed upward through the nozzle holes and among the dummy fuel bundle. Initial temperature for the solid parts were set to 45°C and 65°C for the paraffin wax (Figure C-10) same as measured in the experiments. Liquidus temperature of paraffin wax is 43°C and solidus temperature is 33°C and is important for casting simulation to determine the solidification behavior.

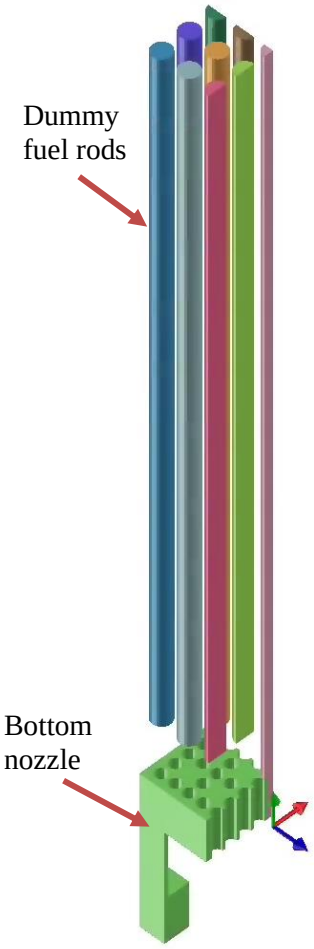

Figure C-9. Fuel Assembly Attached to the Bottom Nozzle (90° symmetry)

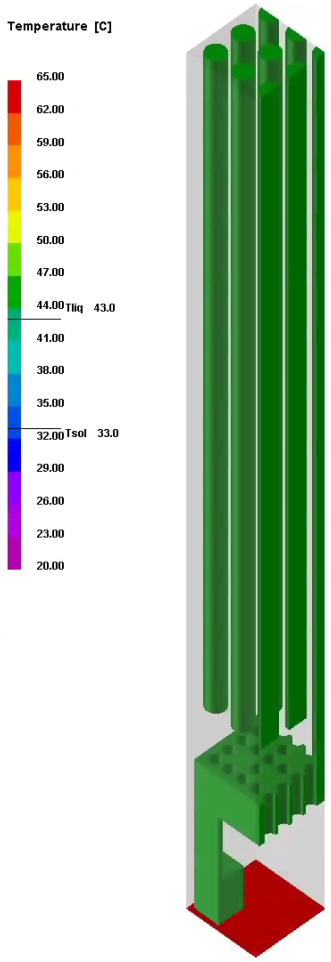

Figure C-10. Initial Temperature Profile at the Onset of Filling.

A pressure boundary condition with 1.5 atm pressure was applied to the bottom of the fluid domain to initiate the filling from the bottom. 1,785,445 tetragonal, hexagonal, and wedge solid elements were used for the mesh. This fine mesh was required to compute the fluid level propagation around very small spaces between the parts.

Figures C-11 through C-13 display the temperature profile and progression of filling. No issues were observed during filling when the internal temperatures were maintained at a level higher than the liquidus temperature of the paraffin wax. This was achieved by using an insulator blanket and heat tapes wrapped around the DPC mock-up canister. Also, the wax was melted in a pot heated on a heat plate. The temperature of the molten wax was also around 65°C. The authors observed that the temperatures were slightly different at different locations inside the basket in the DPC mock-up. At the fuel assembly section, all the solid structures were heated up to 45°C.

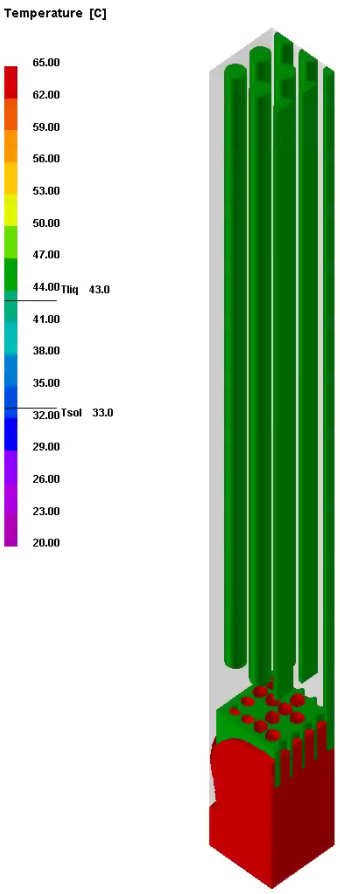

Figure C-11. Temperature Profile during Filling through the Nozzle Holes.

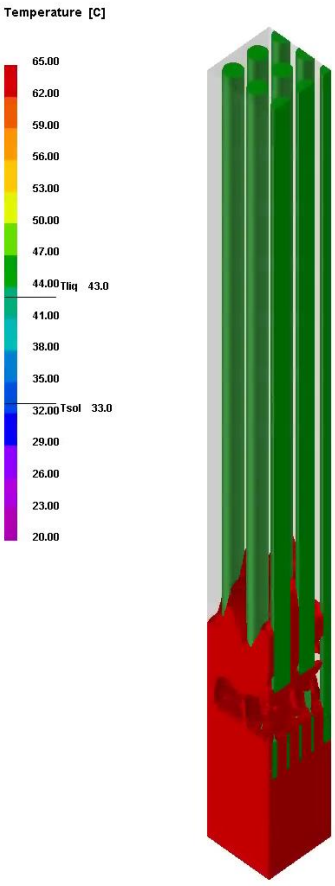

Figure C-12. Temperature Profile during Wax Rising Up among the Dummy Fuel Bundle.

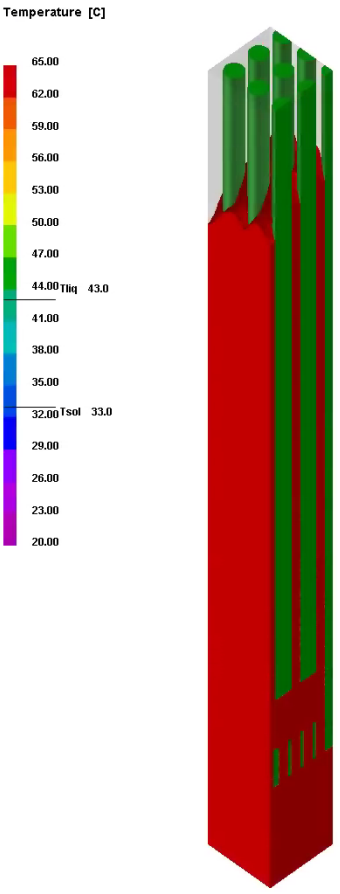

Figure C-13. Temperature Profile at Higher Levels of the Fuel Bundle.

Figure C-14 through C-16 show the temperature profile of the assembly section after the filling completed and cooling started. The temperature contour plots demonstrate the cooling at 5, 30, and 130 s after filling completed.

Solidification is shown in Figures C-17 and C-18 at two different stages during cooling with 28.5% and 61.5% solid fraction. Solidification began from the external faces and progressed toward the internal regions. In the figures, gray contour represents 100% solidification. Some regions remained at higher temperature than others inside the entire model. In Figure C-18, the highest fraction of the liquid phase is shown at the bottom of the nozzle. The reason for that region still being in liquid state is that there was a large void space under the nozzle. The regions surrounded with solid parts have more paths for the heat transfer to take place. Figure C-19 shows the hot spot under the nozzle with a cross sectional cut through the XY plane. Figure C-20 displays the defects caused by shrinkage after solidification completes.

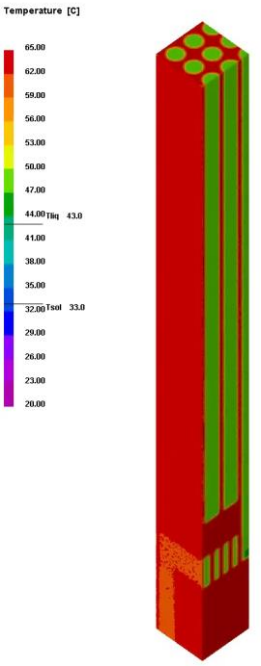

Figure C-14. Temperature Profile at the End of Filling at 5 s.

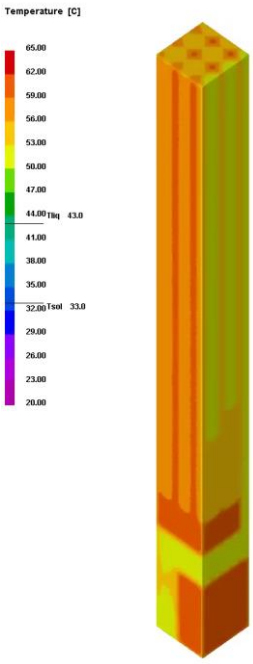

Figure C-15. Temperature Profile of Cooling at 30 s.

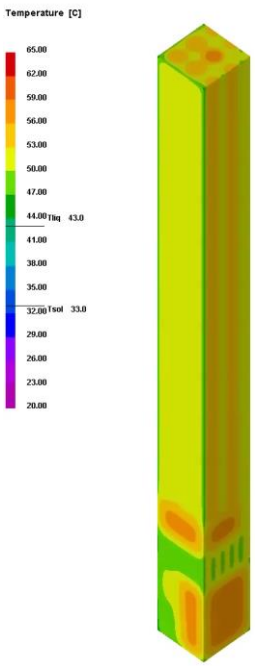

Figure C-16. Temperature Profile of Cooling at 130 s.

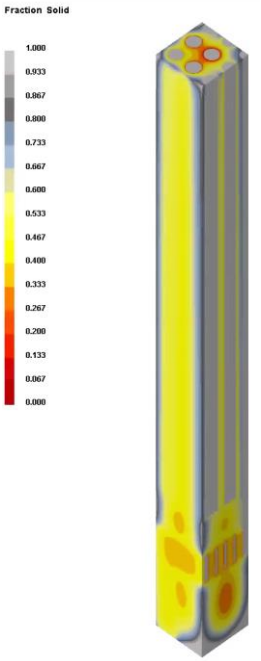

Figure C-17. Fraction Solid 28.5%.

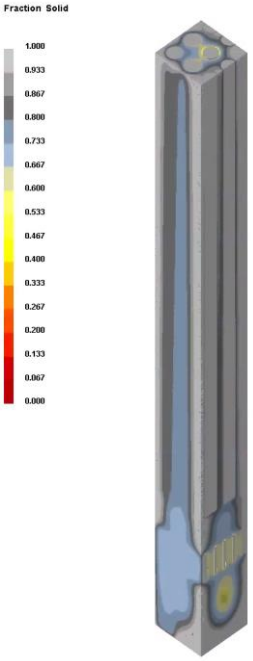

Figure C-18. Fraction Solid 61.5%.

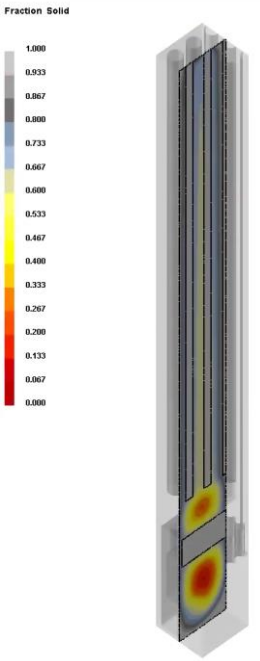

Figure C-19. Cross Sectional View Cut through the XY Plane.

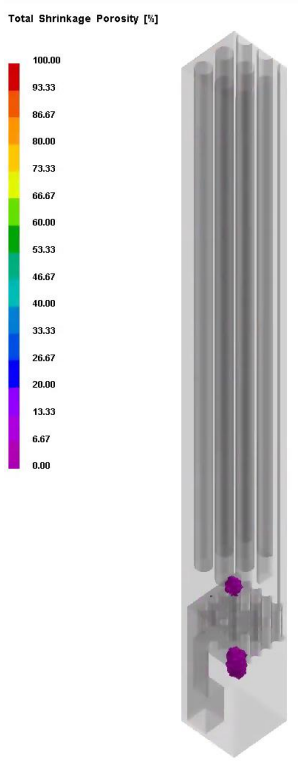

Figure C-20. Total Shrinkage Porosity.

C-3.2 Pipe Simulation

In preparation for the first metal casting experiments, simulations efforts continued by examining the fill pipe itself. The existing drainpipe inside the DPCs was under consideration for filling. The drainpipe length and diameter vary from system to system. For this simulation, a drainpipe 4.26 m (14 ft) long and the inner diameter is 3.175 cm (1.25 in.) was modeled. For the casting simulation, the pipe was modeled using 90° symmetry. The top of the fluid domain is defined as the inlet as shown in Figure C-21. Since the first metal casting experiment is planned to use tin alloy as the filler, simulations adjusted to use suitable properties to represent the same conditions. Liquidus temperature was set to 236.85°C and solidus temperature was set to 231.85°C.

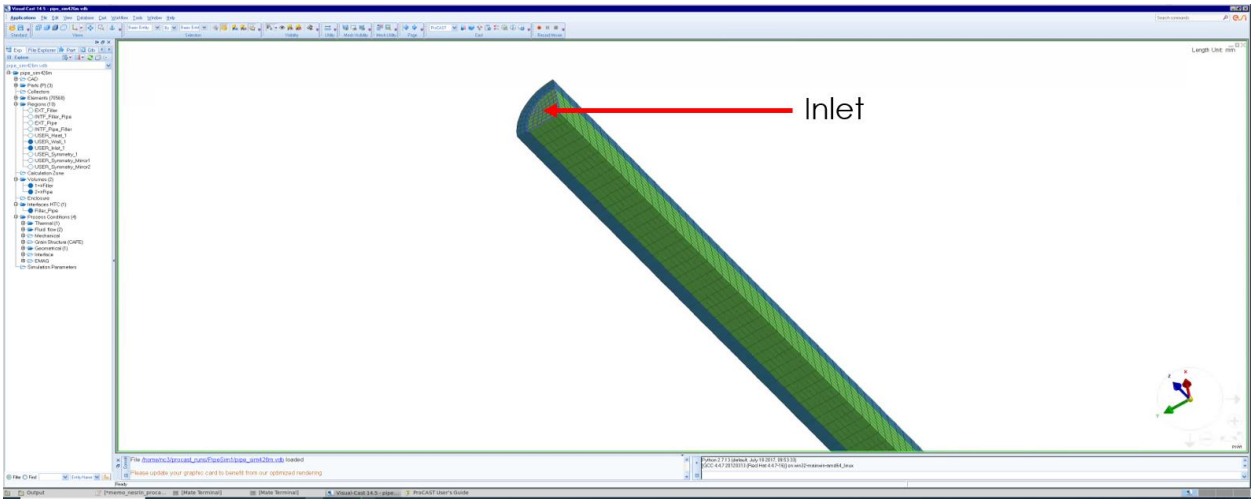

Figure C-21. Simulation Model Setup.

Temperature-dependent thermal and fluid properties for tin are shown in Figure C-22.

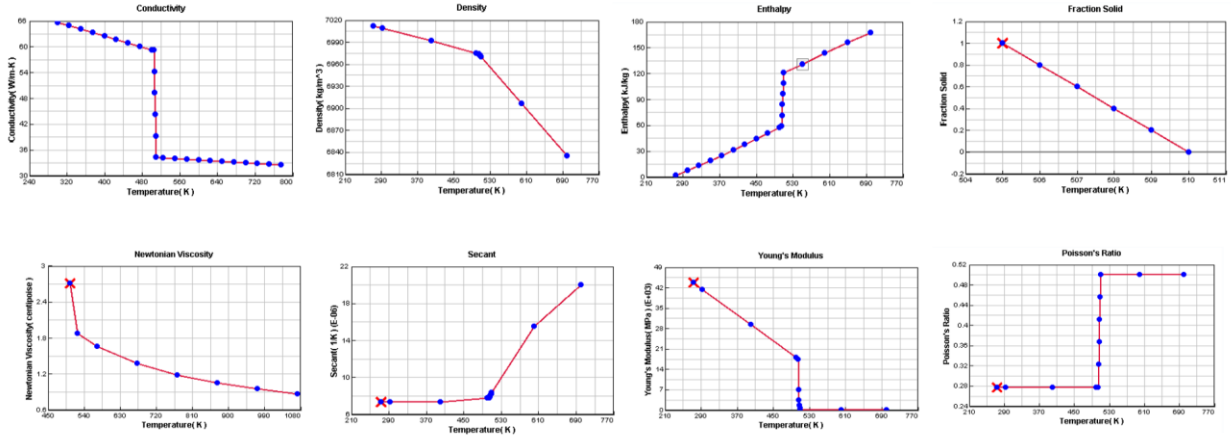

Figure C-22. Tin Properties for Casting.

The temperature plot in Figure C-23 shows the temperature of metal at any given point of time. Filling started with the molten tin at temperature 350°C. Once it cooled to temperature below the solidus temperature, it solidified (Figure C-24), and defects can be observed. Figure C-25 displays the void inside the solidified metal inside the pipe.

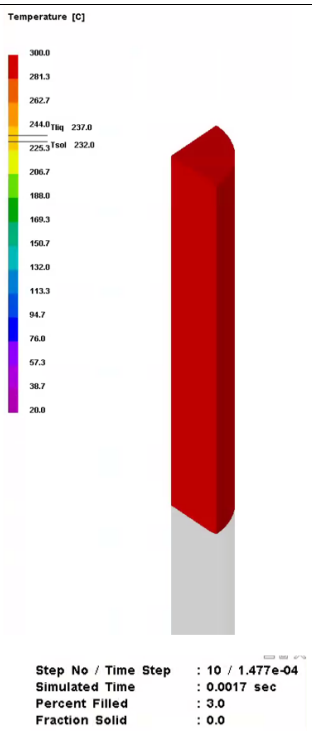

Figure C-23. Temperature Contour Plot at 3% Fill.

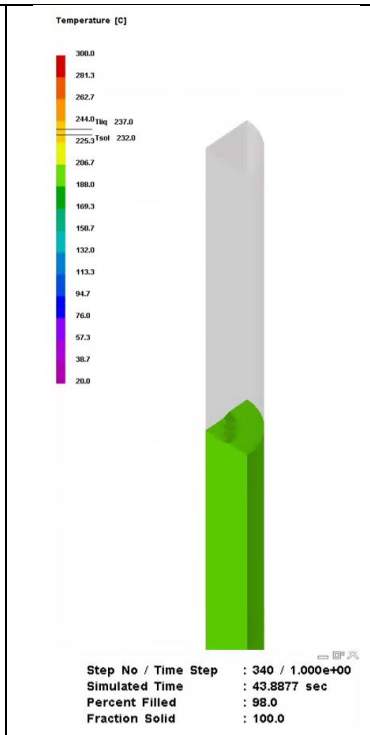

Figure C-24. Temperature Contour Plot at the End of the Simulation, 100% Solidified.

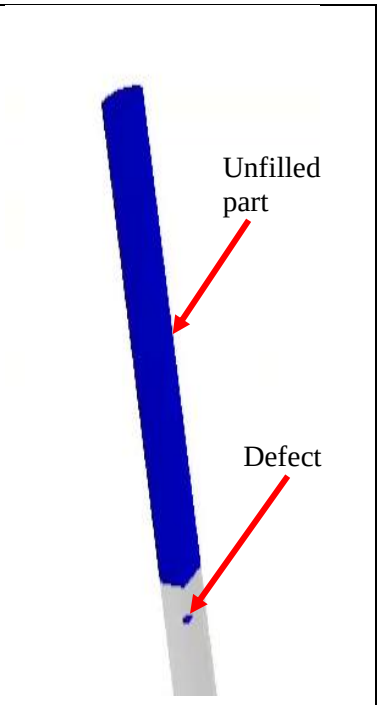

Figure C-25. (top part unfilled) Voids and (bottom) the Defect Inside the Solidified Material.

C-3.3 Tin Experiment Simulation

A filling experiment is being designed to demonstrate the solidification process with molten metal. Before embarking on an extensive experimental testing, a casting simulation model was developed. This simulation capability is primarily intended to properly set up the boundary conditions of the experiment and identify potential challenges during the filling process.

The simulation used the CAD drawing of the tin experiment. The experiment was designed in a small scale focusing on the fuel bundle and spacer grids area. The fixture was 6 in. tall. The drainpipe had an inner diameter 1.06 in. and a wall thickness 0.0034 in. The divided panel represented the lower mouse hole in the basket. The drainpipe and the bottom of the mold had a 50.8 mm (2 inches) clearance. The objective of the experiment was to examine the molten metal flow through the pipe and propagation from the spout with that small clearance, and the level rise of the molten metal fill through the dummy fuel bundle and spacer grid region.

The mold will be heated in the planned experiment. Simulations were used to determine the amount of heat that needed to be applied to the external walls to avoid blockage during the filling process due to premature solidification. The model parts are shown in Figure C-26. A tetrahedral mesh was used on overall model using ProCAST mesher as shown in Figure C-27. An inlet boundary condition was applied (shown in Figure C-28) and a heat flux boundary condition was applied to the external wall of the mold. The temperature of the molten metal was set to 350°C, and the mold temperature was set to 100°C in the initial simulation.

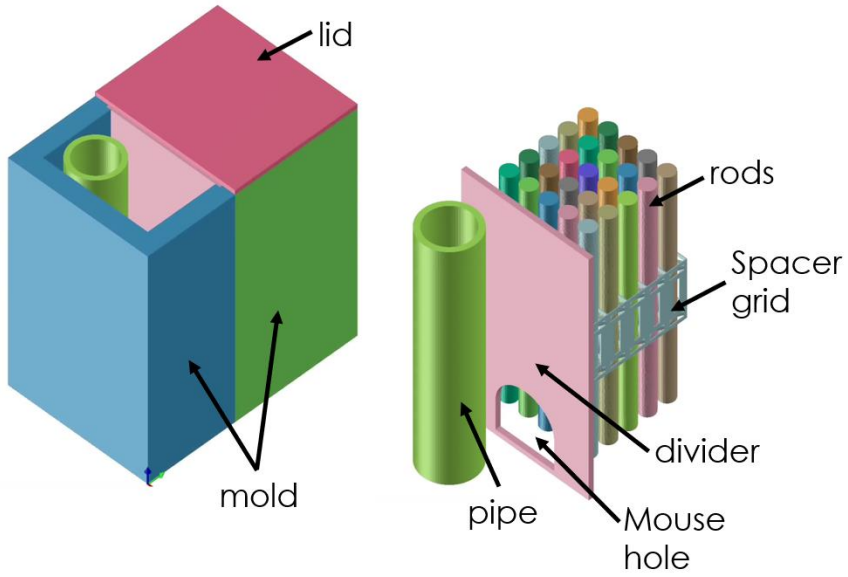

Figure C-26. Tin Experiment Model Parts.

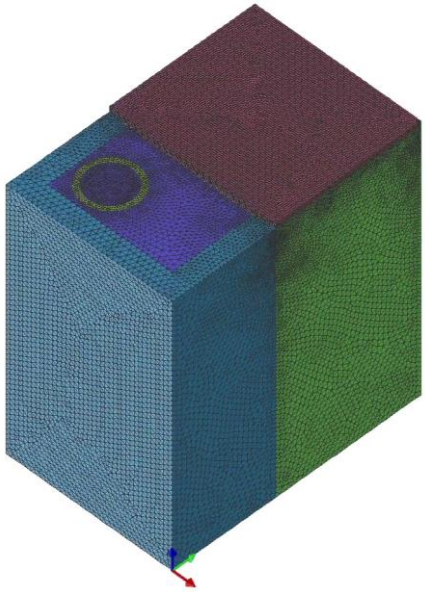

Figure C-27. Tetrahedral Mesh of the Model.

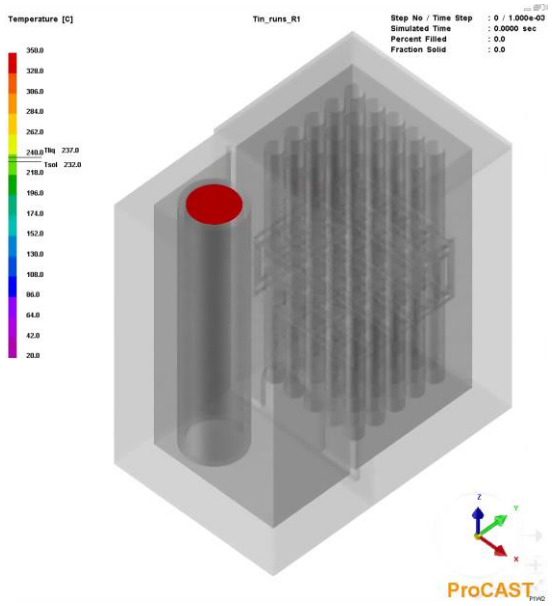

Figure C-28. Inlet Defined at the Top of the Pipe Tin at 350°C.

Initial simulation conditions were set to identify the anomalies. The gravity filling was set as the process condition. Figure C-29 shows the temperature at the time when the fluid contacted the bottom of the mold. Figure C-30 shows the velocity of the fluid at the time when the molten tin dropped to the bottom of the mold. The velocity reached a value of 1.546 m/s before hitting the bottom.

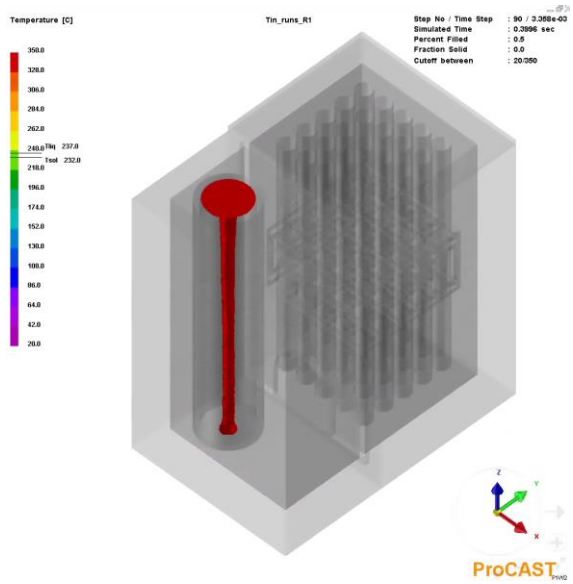

Figure C-29. Temperature Contour Plot at the Time Tin Contacted the Bottom of the Mold.

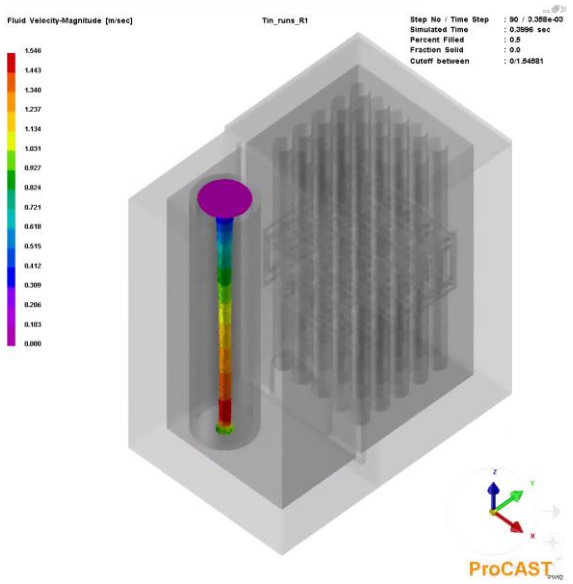

Figure C-30. Velocity Profile Plot at the Time Tin Contacted the Bottom of the Mold.

Figures C-31 through C-36 show the filling process. Each plot shows the temperature contour at different time steps. The filling was successfully simulated coupled with thermal analysis. The propagation of the fluid was observed as expected, going down the fill pipe, splashing to the walls of the mold, slowly making its way through the mouse holes, filling the bottom of the mold completely, and then rising upward. As the level rises, the filling among the dummy fuel rods and spacer grids can be observed.

From initial settings, the authors determined that the temperature of the mold was not enough to maintain the liquid phase as the authors observed onset of solidification during filling. When the fluid reached corners of the walls, as seen in Figure C-33, the temperature of the fluid quickly dropped to the solidification temperature. Figure C-34 through C-36 clearly show the temperature distribution at different time steps during filling. On the corner away from the fill pipe the fluid starts to cool down at a higher pace, resulting in partial solidification around hot spots that remain liquid. Hot spots are sections of casting that have cooled more slowly than the surrounding material because of a higher volume than their surroundings. This causes abnormal shrinkage in this region, which typically leads to more excessive void formation and cracks. For a successful casting, this must be avoided. When the spot solidifies, contraction can lead to generation of voids due to the inability of the fluids and solid in the hot spot to change volume to compensate for the solidification or thermal shrinkage. This creates isolated hot spots, and partial solidification may result in contraction and lead to generation of voids.

Shrinkage porosity is a type of defect that forms within the casting. Porosity can be gas porosity or trapped air. Isolated pools of liquid form inside solidified metal, which are called hot spots. The shrinkage defect usually forms at the top of the hot spots.

Figure C-37 shows the temperature contour plot at the time when filling is completed, and cooling started. Figure C-38 shows the solid fraction at the same time just after filling finished. The gray represents the solidified region. Figure C-39 displays only the solidified portion at the same time step. This simulation confirmed that the initial boundary conditions are not favorable for an acceptable cooling process.

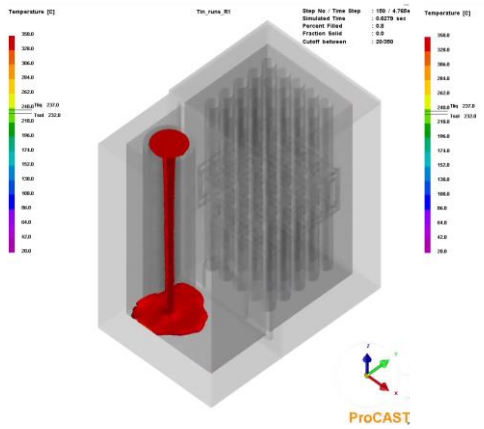

Figure C-31. Temperature Contour Plot at Step No. 150.

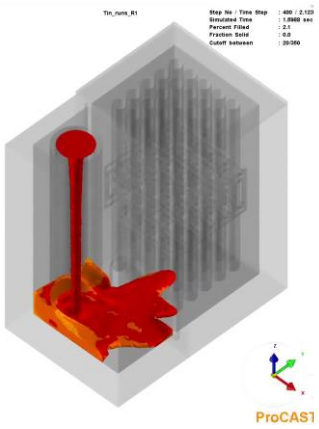

Figure C-32. Temperature Contour Plot at Step No. 400.

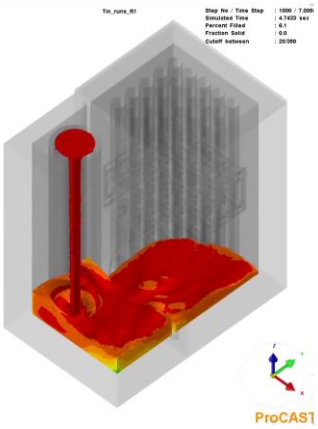

Figure C-33. Temperature Contour Plot at Step No. 1,000.

Figure C-40 shows the temperature profile at the end when tin is completely solidified. A 100% solid fraction is shown in Figure C-41. Figure C-42 shows the time to solidus in each region of the fluid.

For the follow-on simulation, the molten tin temperature was set to 350°C and the mold temperature was set to 250°C. Additionally, the inlet diameter was made smaller to match the pouring container spout size. The analysis is still ongoing but preliminary results show no indication of solidification during the filling process. These conditions were chosen to perform the first molten metal casting experiment using tin.

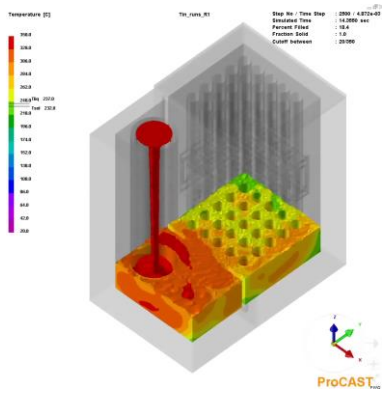

Figure C-34. Temperature Contour Plot at Step No. 2,500.

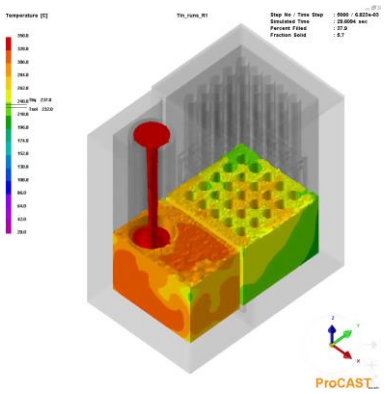

Figure C-35. Temperature Contour Plot at Step No. 5,000.

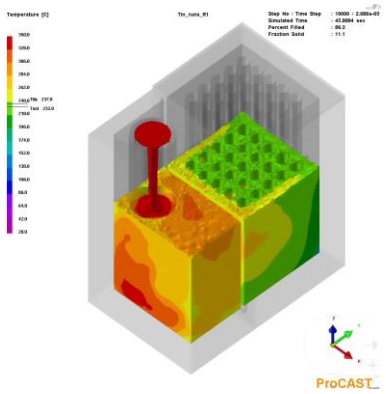

Figure C-36. Temperature Contour Plot at Step No. 10,000.

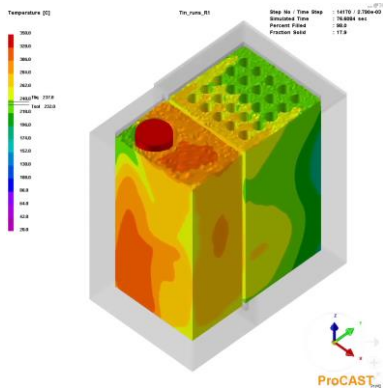

Figure C-37. Temperature Contour Plot at Step No. 14,170.

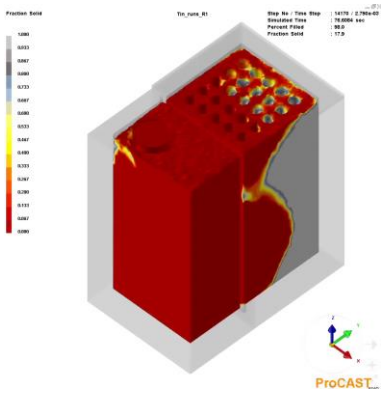

Figure C-38. Fraction solid Contour Plot at Step No. 14,170.

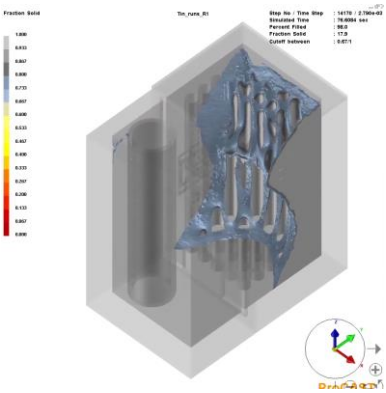

Figure C-39. Fraction Solid Cut of below 0.67%.

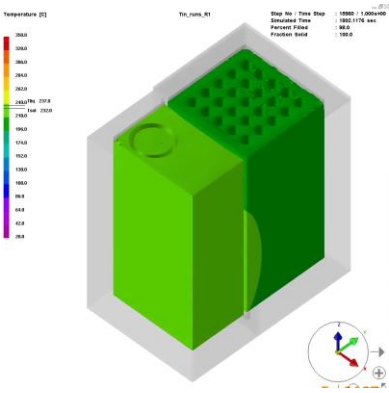

Figure C-40. Temperature Contour Plot after 100% Solidified.

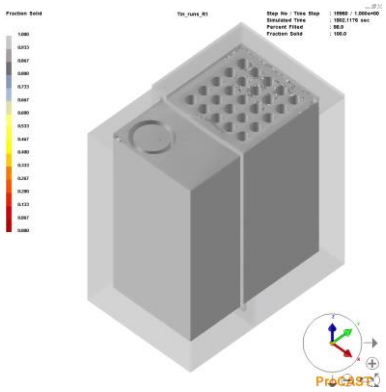

Figure C-41. Fraction Solid Plot after 100% Solidification.

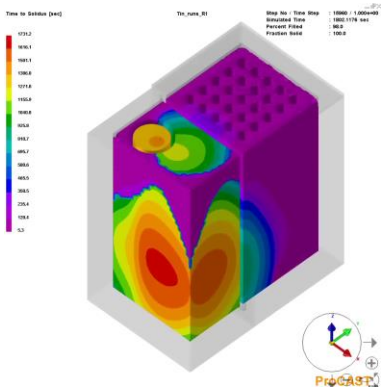

Figure C-42. Time to Solidus Temperature across the Filler.

C-4. First Casting Experiment Preparation

The preparations for the first casting experiment are ongoing. The experimental setup is described in the Appendix B (Figure B-25). All the parts are being fabricated. This experiment is planned to be performed in the 7603 Highbay multiuser facility at Oak Ridge National Laboratory. The Highbay facility has 50 ft high ceiling and sufficient space available to accommodate large experiments that cannot be accommodated elsewhere.

According to the simulations results, the preheating of the tin mold box was increased from 120°C to 250°C. Temperature will be monitored with thermocouples installed various locations outside of the mold and placed inside the mold wall. Additionally, fiber optic sensors are planned to be used to as strain gauges. After solidification completes, the mold will similarly be scanned by x-ray CT. The inside of the solidified tin will be examined for porosity and solidification defects.

C-5. Final Benchmarking CFD Simulations

This experiment is to conclude the verification and validation of the CFD model (Section 2-1). Similar to the previous liquid experimental setups used to evaluate water, glycerin, and liquid paraffin, this scaled experiment represents the bottom most 100 mm of volume of the scaled experimental setup. In order to better mimic the geometry of the one used in the CFD model; an exact replica of this geometry was 3D printed using a clear plastic material (SOMOS water clear ultra) as a single, seamless part. The part is applied and outside finish and a surface treatment to obtain maximum transparency. The geometry has allocations for level sensors in each major cavity, and when not in use they are plugged, as shown in Figure C-43.

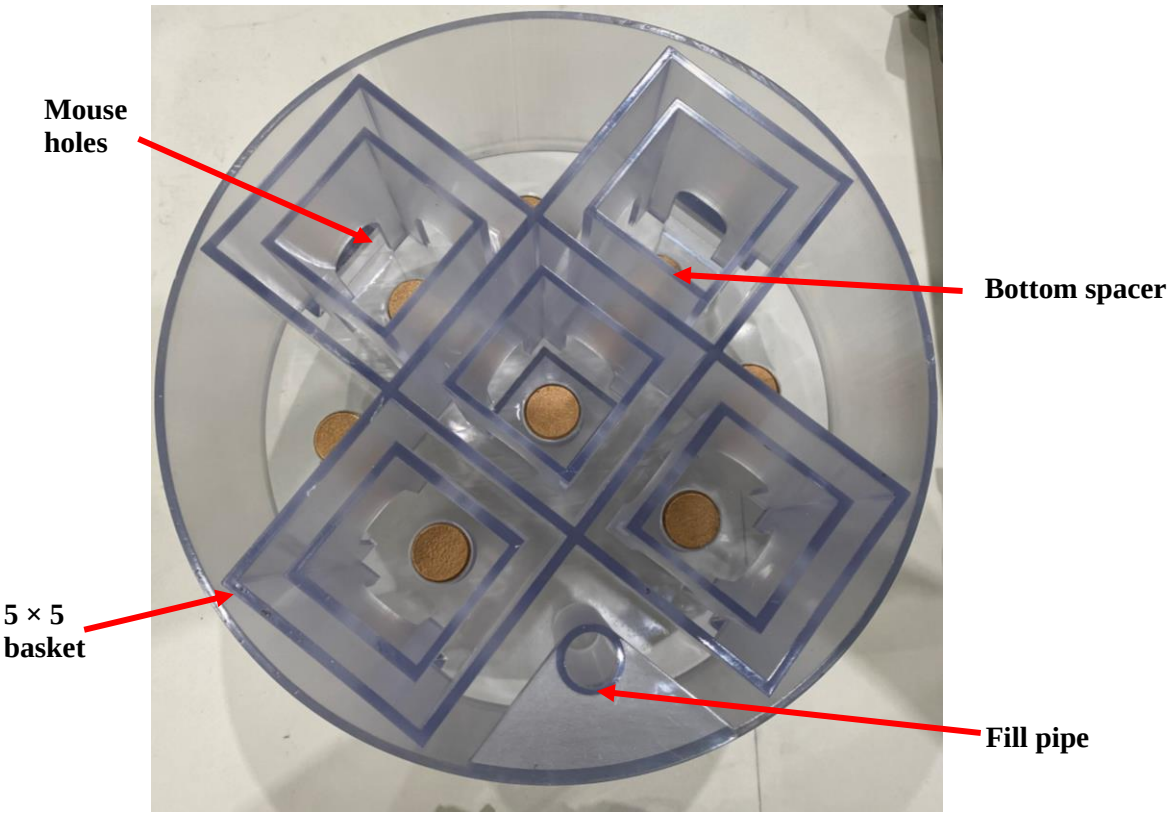

Figure C-43. 3D Printed Fixture for Surrogate Filling Experiments.

The integral legs raise the unit above the tabletop sufficiently to use the same level of sensor penetration plumbing as used in the original experiment, effectively locating the probe's "dead band" below the bottom plane of the experimental setup to help eliminate measurement inaccuracies. The level sensors are supported by a plate attached to four 80/20 legs. These locate the level sensors above the desired locations and hold them at the proper level. A sketch of the setup is shown in Figure C-44.

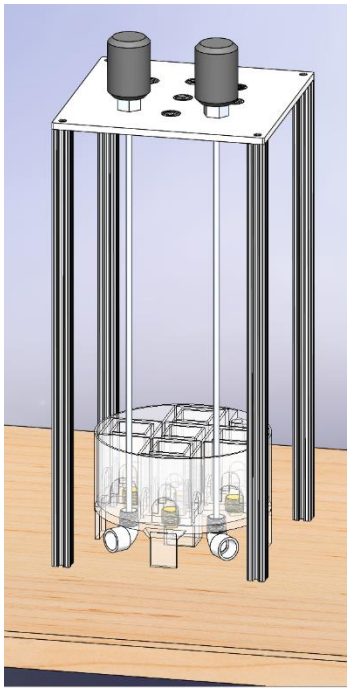

Figure C-44. Sketch of the Experimental Setup.

During the experiment, a peristaltic pump was used to supply precision flow into the fill pipe of the test unit. This rate was set and verified prior to the experimental runs with each filling liquid. The unit was placed on a scale to record real-time weight data to verify mass flow rate, and two independent level sensors measured the real-time fluid level (Figure C-45).

Figure C-45. Lab Setup.

At least two cameras were used to record the progress of the filling: one perpendicular to the unit recorded the vertical filling of the unit and one above the unit, located on the level sensor stand, recorded the propagation of the filling liquid radially from the filling pipe.

This experiment will be repeated with water, glycerin and, for the first time, silicon oil. Different viscosities of silicon oil will be used to capture the viscosity dependent behavior and verify the modeling of the viscosity-driven fluid propagation in the CFD model.

The initial propagation of the fluid after entry through the pipe will be compared with CFD results using a high-speed camera.

A Basler acA640-750uc USB 3.0 with a frame rate of 751 fps and external trigger capability will be used for level measurements. To compare the CFD simulation of the level of the surrogate fillers with the experiments, the flow level sensors will be connected to the external trigger mechanism of the high-speed camera. The captured images with respect to time will be compared with CFD simulations to check for agreement and the frame rate will be adjusted to match the simulation.

C-6. Drainpipe Experiment Status Update

The design of an independent low-volume mercury loop is addressed through the Phase II test loop experiment and will utilize the current mercury containment of the Spallation Neutron Source Target Test Facility. The development of the phase II test loop will enable the testing of exchangeable test sections and will provide capabilities to simulate realistic flow conditions during the DPC drainpipe filling process. For several filler materials, annular flow is likely, and instability could introduce bubbles. This test shows when that might occur or will show slug flow is unlikely. The test loop has been updated with reinforcement plates at the electromagnetic (EM) motor level and the tank level as shown in Figure C-46.

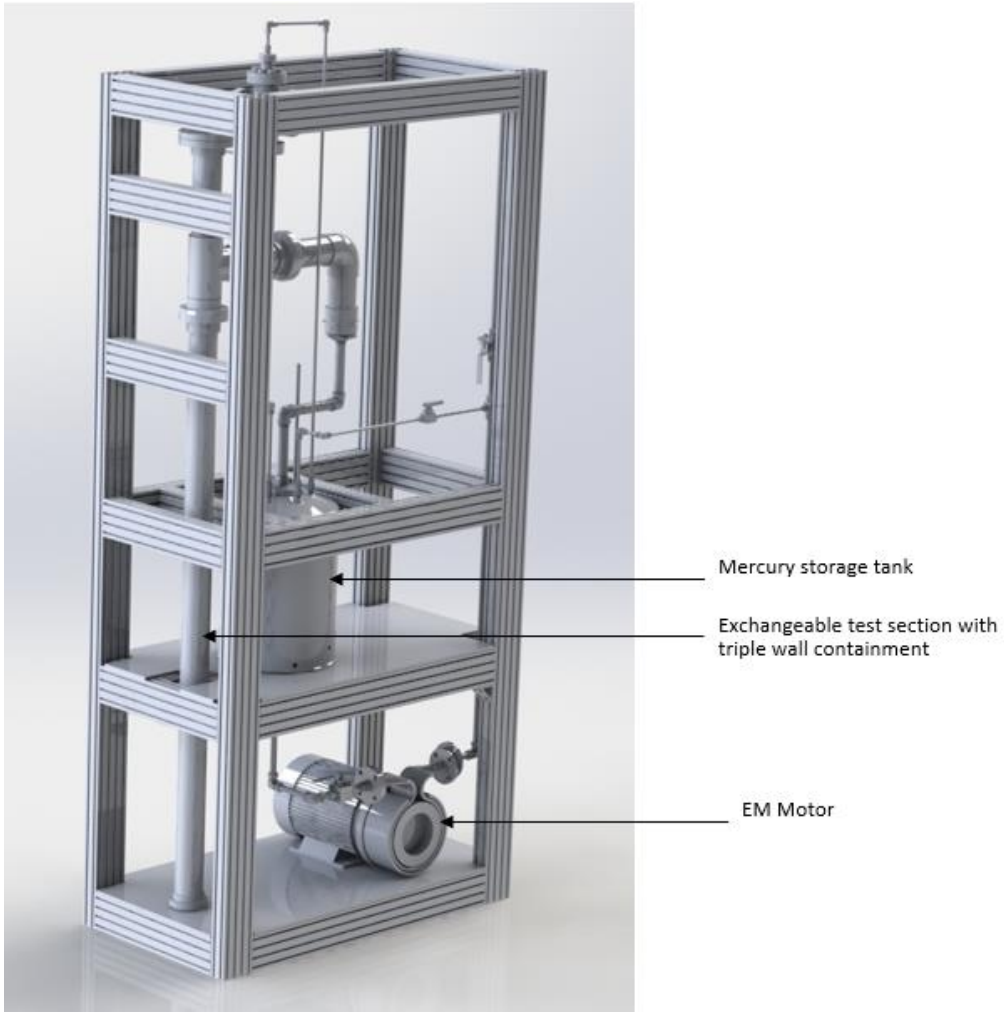

Figure C-46. Updated Phase II Flow Loop.

The test section is an exchangeable standardized stainless steel pipe with coaxial transparent PVC and is contained in a 40 PVC transparent pipe. The main components of the test setup have been ordered. The authors will use an EM pump, and the motor coupler is currently being designed. The experiment zone for the test section to be placed inside the Spallation Neutron Source Target Test Facility mercury containment zone must be cleared of existing components, which will be moved to a separate facility. The clearing of existing components and moving to a separate mercury containment facility is planned in the next few months with coordination with safety personnel. The tank and support structure of the test loop will be pressure tested and structural simulations will be performed. The pressure loop is estimated to require 14 gal of mercury and the tank will be safely tested for 21 gal of mercury. The current system was identified as safe without a pressure test because it is made of 316 stainless steel and no additional pressure tests are required since the tank will not be pressurized. The effect of mercury on 316 stainless steel for the duration of the experiment will be investigated.

The updated test loop system will be reinforced with plates beneath the tank and the motor and was analyzed for stresses and deflection. A new coupler is being designed to connect the motor to the tube.

One concern for the experiment is the effect on the weight of mercury inside the tank, which would induce stresses on the support structure of the test loop. To remove the ambiguity surrounding the level of stresses experienced on the structure, a structural simulation was performed assuming the mercury

volume inside the tank to be 25 gal. Figure C-47 shows the contour plots of total displacement and von Mises stresses. The structural simulation confirmed that the stresses generated by the 25 gal of mercury in the tank can be sustained by the structure from the updated design of the test loop. The total deflection and stresses are also not significant to cause damage to the test loop support structure during recurring cycles of experiments.

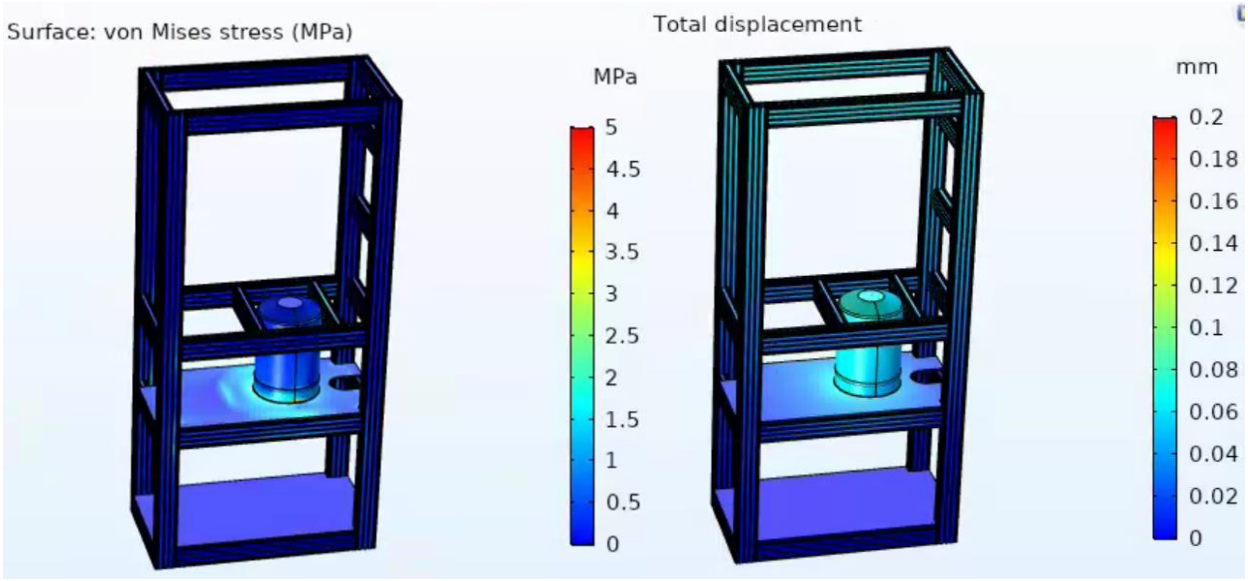

Figure C-47. Structural Analysis—Contour Plot of Displacement and von Mises Stress for 25 gal of Mercury in Tank Performed by Sunday Aduloju, Remote Systems Group, Fusion Energy Division.

C-7. Dual-Purpose Canister Preheating Simulation Update

The thermal analysis of spent fuel canisters continued this year. The past year's focus was on analyzing hot gas injection methods to preheat the canister, and the corresponding analytical models were developed. This year, the emphasis was on using the fuel residual heat in combination with adding thermal insulation to the outside surface. In the course of study, the canister, being a very thermally inertial structure, was found to be susceptible to the outside thermal conditions, which affected its response during the preheating process. Models and methods were used to analyze the transient canister thermal behavior as it was processed from the dry storage to the site for filling and ultimately disposition. Details on these analyses are discussed below.

C-7.1 Thermal Analysis of Spent Fuel Canisters

Fillers can be cast into the DPCs prior to disposal to fill the void and block the ingress of primarily water (or other material) that can act as moderator. The casting may require the canister to be preheated. In previous work [3], preheating methods were examined. Because of the large canister mass, the thermal history of the canister is important. This report further shows that the canister takes several days to reach steady temperatures. The existing temperature distribution in the canister is of importance for the preheating process and ultimately determines the feasibility of one or another preheating method. To perform the casting of fillers, presumably the canister needs to be removed from the storage overpack and

transported in a transportation overpack to a casting site. These actions, depending on their duration and thermal conditions, affect the canister temperature. Tracking the thermal history becomes necessary.

C-7.2 Modeling Method and Computer Code Used

COBRA-SFS (Spent Fuel Storage; CSFS), a well-known spent fuel analysis tool, was selected to perform the simulations, and an existing model of the TN-24P spent fuel cask was used as a test case [3]. The simulation is the first of its kind, and this section provides an overview of the progress made to date.

The TN-24P cask was manufactured by Transnuclear, Inc. and consists of a cylindrical forged steel body surrounded by a resin layer for neutron shielding. The assembly is enclosed in an annular tank formed by the other surface of the cask and a thin carbon steel outer liner [3]. The internal basket structure consists of thin plates of borated aluminum arranged in rectangular cells (crates) to accommodate 24 fuel assemblies. The total decay heat load assumed for this analysis was 10 kW with a power density of 15 kW/m^3. As part of the CSFS validation, experiments with the TN-24P cask were simulated [4]. A model was developed and tested by Michener et al. [3]. The performed CSFS assessment showed good results, matching well the experimental data and providing the main rationale for selecting the prototype canister model. The same model was used as a baseline and was further modified in this study. Typical DPC shell wall is made of ~0.5” thick stainless steel. Starting with the existing TN-24P cask model a representative DPC model was developed by thinning out the cask shell and modifying some other components.

C-7.3 Modification of the TN-24P Canister Model for Thermal History Analysis

A typical canister thermal history sequence, defining the initial temperatures for the preheating and casting operations, may consist of the following major stages:

1. Long-term dry storage at a specific site Figure C-48 (left): The canister is placed in a radiation shield (overpack) that represents a specific thermal boundary, including convective heat transfer. Usually, the canister reaches a steady temperature profile in the overpack.
2. The canister is removed from the storage overpack and placed in a transport overpack as shown in Figure C-48 (right), which acts as a different thermal boundary. Depending on the shipping time and the changing environmental conditions, the canister may reach steady temperatures, which will be different from those in the storage.
3. Delivery at the casting site and removal from the transport container: This stage is still undefined and may consist of several operational steps.
4. Installation in the heating mold and carrying out the preheating process: Maintaining the target temperature for a certain time period.

Figure C-48. Illustration of the Different Thermal Conditions that a Canister may Exhibit (left) in a Storage Concrete Shield, (right) in a Transportation Cask.

Developed for CSFS validation, the existing TN-24P model was not suitable for the described thermal history simulation. Therefore, several modifications were made, with the main ones focusing on the following processes:

1. Fast and accurate transient calculations with time steps large enough to allow for computing of physical process times of up to five days
2. Functionality that would permit the canister thermal structures (slabs) to be modified at a calculation restart thus modeling the interchangeable outer thermal boundary
3. Functionality to allow modeling of different thermal layers at the upper and lower canister boundaries (plena)
4. Ability to perform multiple restarts while preserving continuous and smooth transition in the energy solution

To accomplish the modifications, a spreadsheet calculation was developed (Figure C-49) for calculating the required CSFS input data. It also verifies the existing TN-24P cask data by performing estimates of input parameters such as thermal resistances. The data was grouped in six categories:

1. Material thermal properties (conductivity, heat capacity, and density) necessary for the time-dependent solution
2. Geometry of the interchangeable boundary, thickness, axial areas, and number of nodes
3. Fluid to solid heat transfer defined as a connection geometry factor (GF):

   GF = W/L (see Figure C-50)

4. Lateral solid slab connections defined as thermal resistances (LTR), Figure C-41:

   LTR = W/L/k
   where k is the material conductivity (Btu/s-ft-F)

5. Radial solid slab connection defined similarly to the previous as thermal resistances (RTR):

$$RTR = (W_{low}.k_{low} + W_{high}.k_{high})/L$$

6. Outer liner environmental boundary conditions modeling the outside temperature and convective heat transfer, including the outer boundary length scale

Thermal connections for thin shell with insulation

- No change of number of slabs in model: 5 layers 32 lateral slabs = 160 slabs
- Slabs 174 - 205 steel shell, one layer, 0.5" thick
- Slabs 206 - 301 insulation, three layers, 24" thick (3 x 8")
- Slabs 302 – 333 steel liner 10 mm
- Upper plenum model modified, three axial and three radial regions:
  - Region 1 – axial: lid 9.5"; radial: shell 0.5"
  - Region 2 – insulation
  - Region 3 – liner
  - Connections UP-shell wall removed due to thin shell

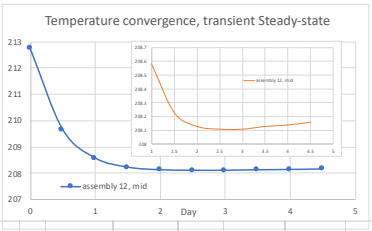

UPPER PLENUM							lid thickness, inch =	9.5																
IN MODEL: AXIAL				ESTIMATE for verification			lid thicker than shell insulation instead of shield			IN MODEL: RADIAL				ESTIMATE for verification			thin shell canister insulation instead of shield		
		sq. inch	m2		m2							sq. inch	m2		m2				m2	sq.inch
nominal heat transfer		2599	1.68		1.66					nominal heat transfer		411.2	0.27		1.23				0.06	89.98
area				Nu=0.15Ra^0.33, 10e+5 < Ra < 10e+11						area				Nu=0.1Ra^0.33, 10e+9 < Ra < 10e+13			fix slab connections to wall		
				Ra = Gr.Pr and defines C2 = Pr.g.β.L³/n²=Ra/delta										L (height), m	4.00				
		multiplier		where: g – gravity, m/s²,								multiplier					region	multiplier	
region 1		1	1.68	β - air thermal expansion, 1/K,		3.25E-03				region 1	27cm shell	1	0.27	1.00	1.23		shell	1.00	0.058
region 2		1	1.68	n - air kinematic viscosity, m2/s,		1.65E-05				region 2	14.3cm shield	11.31	3.00	1.37	1.69		insulation	1.02	0.059
region 3		1	1.68	Pr		0.71				region 3	1cm liner	15.5	4.11	1.57	1.93		liner	1.86	0.108
				L		1.46													
boundary connections				air conductivity, w/m-K		0.027				boundary connections									
		C1		C2		C1, w/m2-K	C2, 1/F		C1, w/m-K	C1, Btu/s-in2-F			C1		C2			C1, w/m-K	C2, 1/F		C1, w/m-K	C1, Btu/s-in2-F
number		Btu/s-in2-F	w/m2-K	1/F							number		Btu/s-in2-F	w/m2-K	1/F							
region 1	2	4.73E-05	139.11	-	27cm lid	153.85	-	9.5" lid	172.15	5.85E-05	region 1	5	1.89E-06	5.56	-	27cm shell	same as in G17		shell	3270.93	1.11E-03
region 2	4	4.60E-05	135.29	-	14.3cm shield	129.37	-	insulation	0.07	2.23E-08	region 2	6	3.26E-05	95.88	-	14.3cm shield	same as in G18		insulation	0.07	2.23E-08
region 3	4	5.30E-09	0.02	7.74E+07	1cm liner	0.003	1.44E+08	outer BC	invariant (same to on left)		region 3	7	1.09E-06	3.21	1	1cm liner	0.001	2.96E+09	outer BC	invariant (same to on left)	
						9.43207E-10											2.2951E-10					
LOWER PLENUM																						
model axial regions: 4											model radial regions: 7											
		sq. inch	m2										sq. inch	m2								
nominal heat transfer		2578	1.66								nominal heat tansfer area		248.4	0.16								
											region 1											

Figure C-49. Spreadsheet for Calculating the Thermal Properties of Slab Structures and Plena. Compatibility with Existing in the Model Factors [3], Demonstrating their Relevance to the Simulated Sequence of Thermal Events; was Verified.

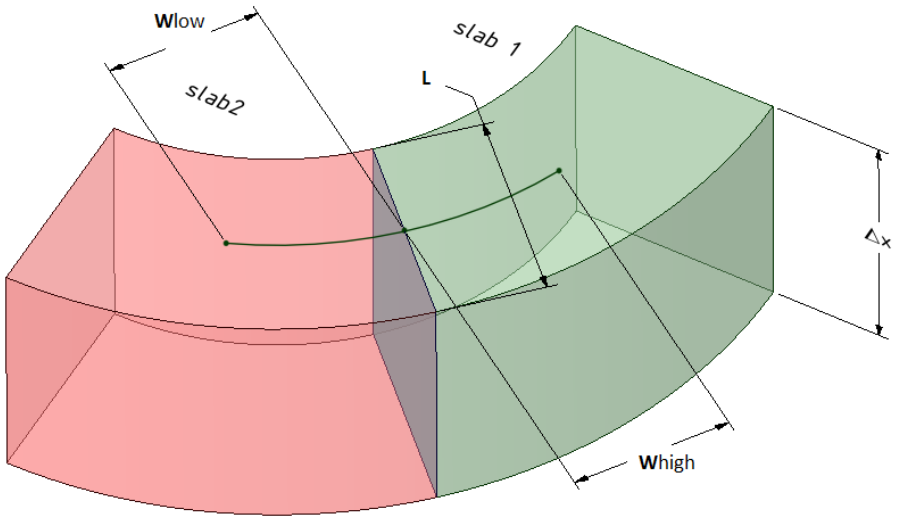

Figure C-50. CSFS Nomenclature in Modeling of Network of Interconnected Thermal Structures. Example of Radial Connection: L = with, W = length.

The implemented approach permits performing long transient runs with a series of restarts for modeling of varying canister enclosing materials and changing environmental conditions. Credible thermal history scenarios will be developed and analyzed in conjunction with canister preheating to confirm the feasibility of the entire engineering filling process.

C-7.4 Results for Heating by Residual Heat

To demonstrate the thermal history calculation algorithm, a relatively simple scenario was considered. The canister was assumed to be at an open-air yard for indefinite time with no additional thermal layers (e.g. radiation shields or other) around the outer shell. After reaching thermal steady conditions, the canister was wrapped with a thermal insulation of a known thickness. Only the fuel residual heat was used for heating, and the time needed to reach a specified temperature at a selected location inside the canister was computed. This simulation verified the feasibility of using the SNF residual heat to preheat the canister before casting fillers. The initial and boundary conditions and other important data for the simulation are summarized in Table C-1.

Table C-1. Initial and Boundary Conditions and Material Configurations for TN-24P Canister Thermal History Tracking Simulations.

Backfill gas	Helium
Canister shell thickness	0.5 in.
Target temperature	250°C
Outside temperature	18°C
Insulation thickness	24”
Insulation material	Glass wool
Fuel decay heat	10kW

Initially, the canister was assumed not to be thermally insulated on the outside surface. An open-boundary natural convection heat transfer coefficient was applied to all external canister surfaces to simulate the ambient air cooling. To verify the calculation algorithm, a steady state calculation was carried out. Then, the same calculation was performed in transient mode with multiple restarts to confirm that the restart method with interchanging CSFS heat structures (slabs) does not affect the solution accuracy. The temperature difference between the steady and transient solutions is plotted in Figure C-51.

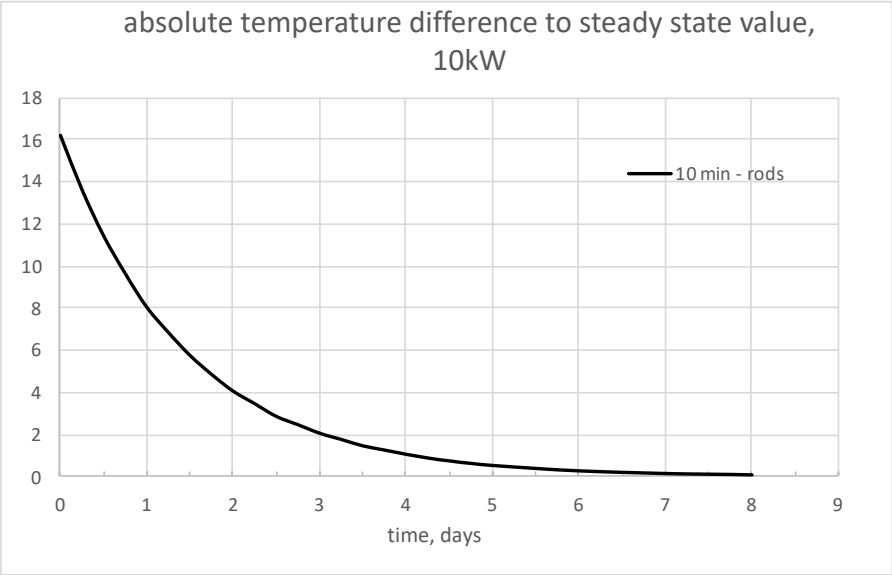

Figure C-51. Temperature Difference between Steady and Transient-Steady Solutions with Slab Structure Restarts.

The long duration of the transition to steady temperature, shown to be eight days (Figure C-51), is due to the accuracy in setting up the initial canister temperature distribution in the transient run. The multiple restarts did not affect the solution and it proceeded with smooth transitions. There is no residual difference between the steady and the transient final temperatures. This calculation was also used to select the time step, which after some sensitivity analysis was chosen to be 10 min. 20 inner iterations were sufficient to reduce the residuals below 0.0001, demonstrating a good convergence rate. The computing takes a couple of hours clock time to complete a 5–8-day actual run.

After performing this initial verification step, the selected thermal history scenario was executed under the conditions described in Table C-1. Temperature profiles in the canister radial direction (normalized) and assembly temperature maps are plotted in Figure C-52 through C-54. They include average data for the fuel assemblies and data for the thermal structures (e.g., crates, absorbers). The outer canister wall was at position 0.55; the rest was insulation. In the steady state plot (initial, black line), the insulation part showed no temperature change because it was still not present. After the insulation was placed, the temperatures inside the canister began to rise. Because the radial plots show only a centered temperature profile, two map plots were added under each graph to demonstrate the full radial distribution at the beginning and end of heating.

The temperature distribution in the lower canister region is shown in Figure 52. The maximum attained temperature was about 180°C, well below the target. This appears to be the region with higher thermal losses that would require longer time for heating. The initial temperature distribution was within a narrow band of 20°C. This temperature band widened during the heating process and was about 32°C at the end of heating. Although relatively small to pose any problems to the canister structure, the temperature gradient was the largest in the canister, likely because of an elevated radial heat transport. The fuel assemblies, as they were placed in the canister, had relatively long stands (stilts) that separated them from the canister bottom. This stilt region was not heated (like the assemblies) and was an area with larger heat dissipation. Also, in this simulation, the heat transfer to the ground was not modeled; instead, the canister was assumed to have an ambient boundary condition at the lower surface. This approximation led to elevated loses from the bottom surface. In the future, a proper model for the ground heat transfer will be developed and implemented in the model, which may improve the temperature distribution in the lower canister region.

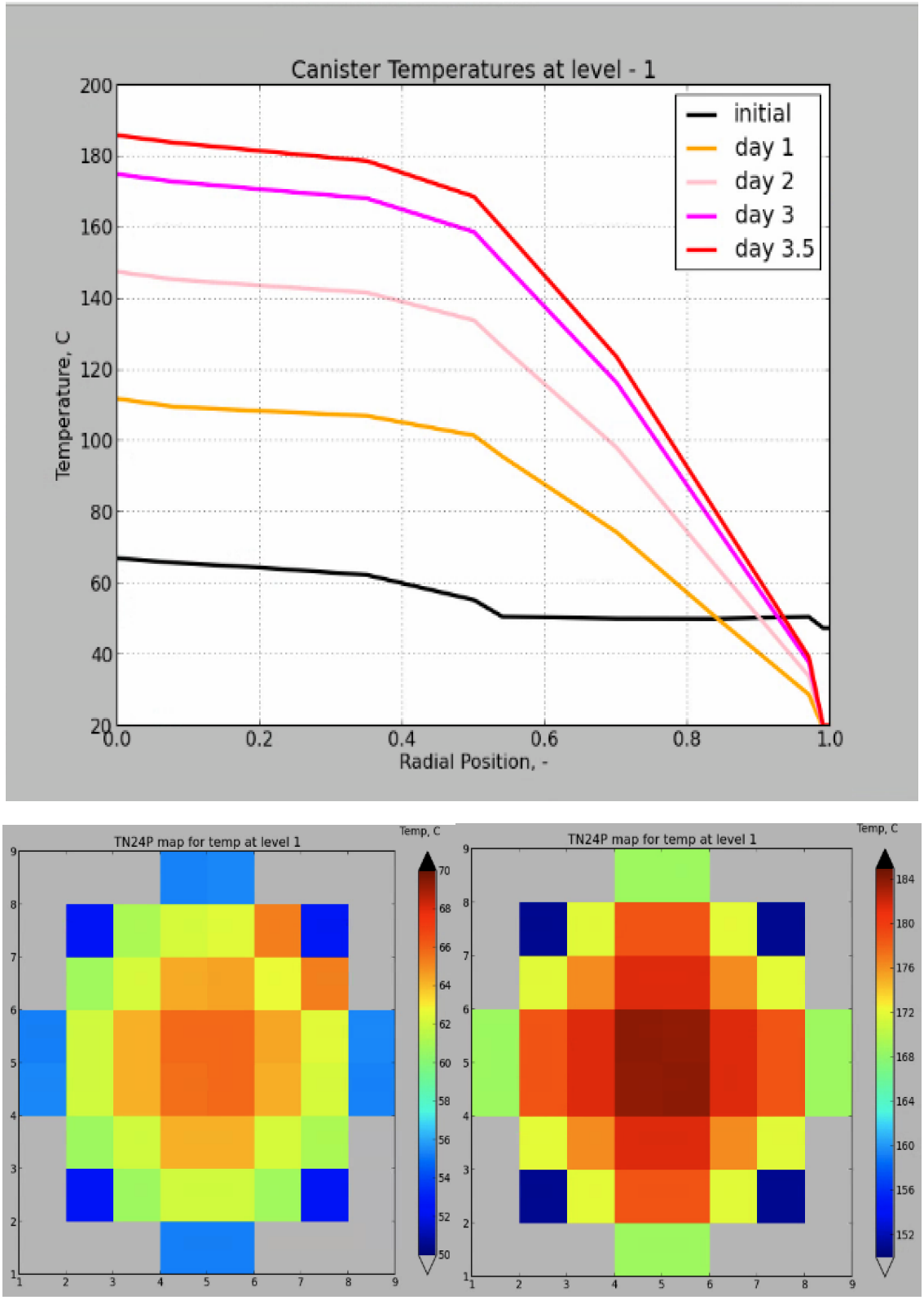

Figure C-52. Heating of Canister by Residual Heat, Lower Canister Region Temperature Distribution. (top plot) Radial Canister Temperatures Evolution in Time; (lower plots) Assembly Temperature Maps, (left) Initial Temperature and (right) at the End of the Heating Process.

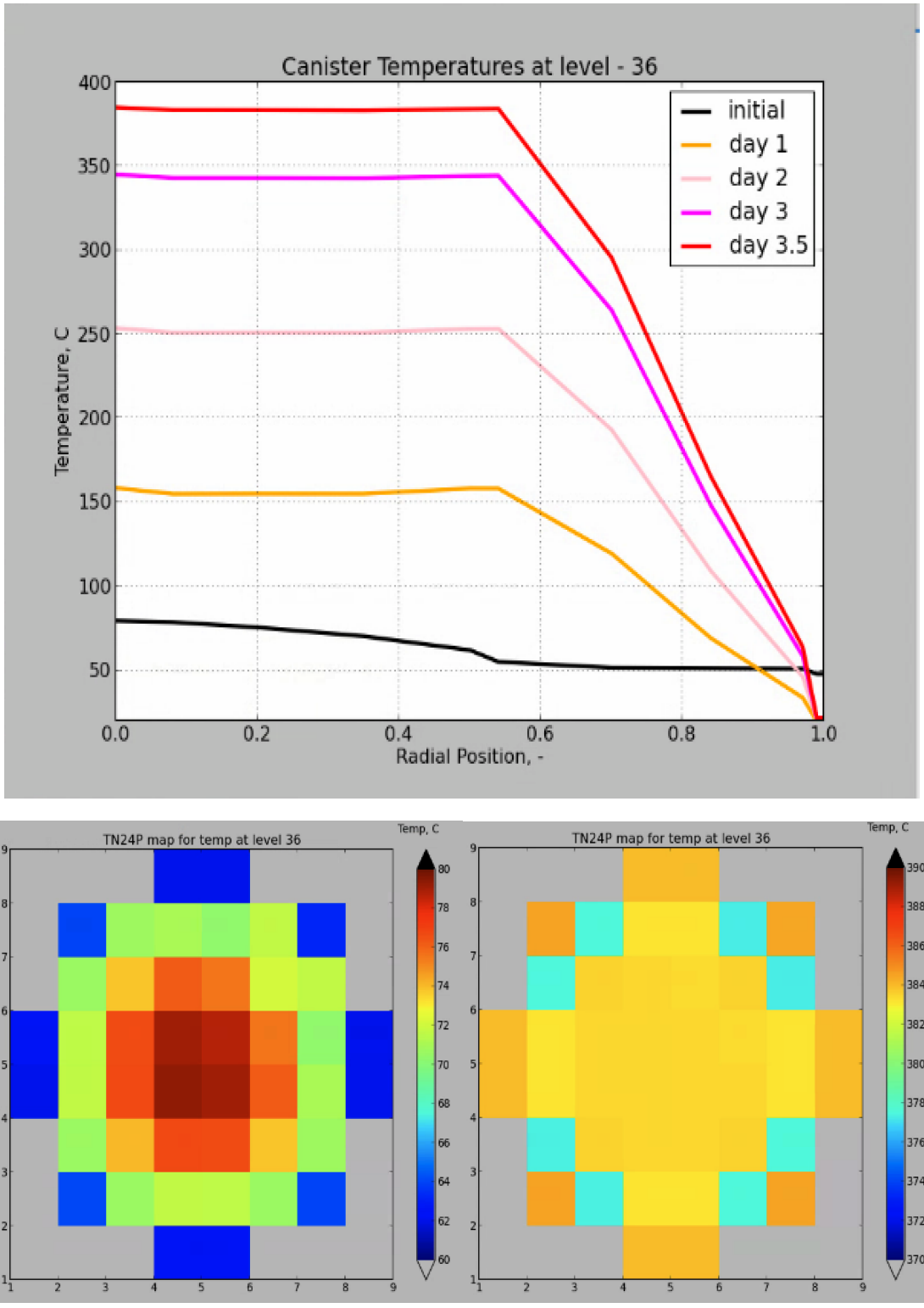

Figure C-53. Heating of Canister by Residual Heat, Upper Canister Region Temperature Distribution. (top plot) Radial Canister Temperatures Evolution in Time; (lower plots) Assembly Temperature Maps, (left) Initial Temperature and (right) at the End of the Heating Process.

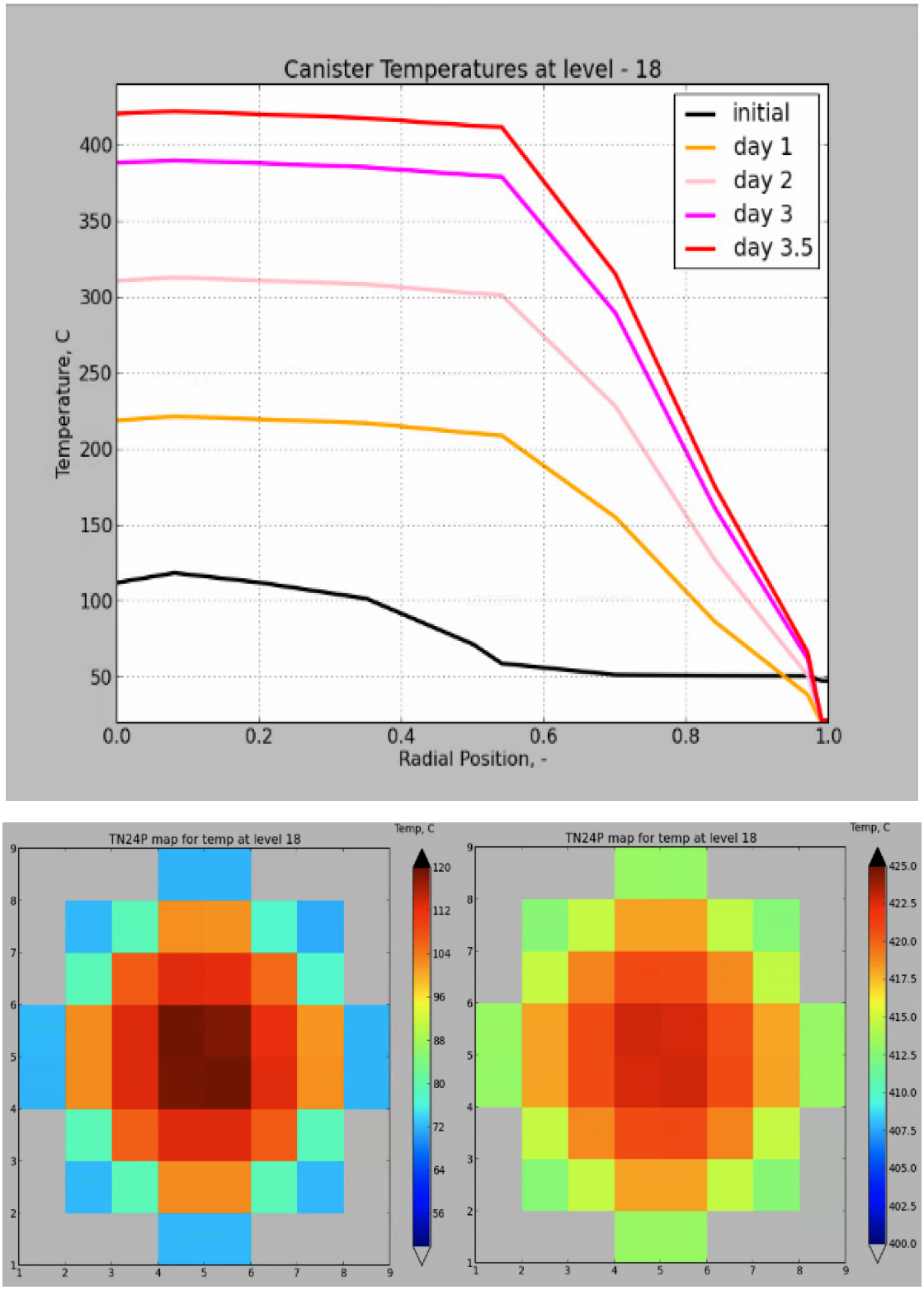

Figure C-54. Heating of Canister by Residual Heat, Middle Canister Region Temperature Distribution. (top plot) Radial Canister Temperatures Evolution in Time; (lower plots) Assembly Temperature Maps, (left) Initial Temperature and (right) at the End of the Heating Process.

Temperatures in the upper canister region (Figure C-53) showed a significant improvement after adding the insulation. The target temperature of 250°C was reached in two days. Moreover, the radial distribution was very flat (map on lower row, right) with only a 20°C difference between the hottest and coldest assemblies. This result is promising in that it indicates that the residual heat alone could be sufficient to preheat the canister for casting fillers without any additional source of heating. The two-day heating time could be further reduced by the added heat of the molten filler material. The casting simulations performed in parallel to these analyses will determine the minimum temperature requirement and will set the target temperature for the preheating phase. The 250°C used in this simulation was based on an average liquidus temperature of the molten filler, but in reality, that temperature might be lower since a significant heat is introduced by the filler material itself. Experiments with real canisters are also planned for next year that will allow the current models to be validated and the obtained results to be verified.

The mid-plane (center) canister temperatures are shown in Figure C-54. This plane with the largest initial radial temperature deviation. It was more than 70°C because of the residual heat axial profile. The fuel heat generation had a cosine-like axial distribution that was additionally complemented with different heat generation in each individual assembly. The resultant effect is that the temperature in the central part of canister varies largely in the radial direction. However, during the heating process, this radial temperature profile tended to flatten out, reaching a delta of about 25°C at the end of heating. In this plane, the target temperature was reached for less than 2 days. This result further affirms that by using residual heat, it would be possible to precondition the canister for casting fillers in reasonable time frame. More analyses will be carried out to confirm this finding, which will substantially facilitate the entire casting procedure. Even the opposite problem of cooling the canister after casting may become more actual because it may take more time than the preheating. A method to analyze this phase is part of the planned activity for the next phase of studies.

The temperature gradient in the axial direction was still significant, demonstrating substantial thermal losses through the lower boundary, as indicated previously. This gradient was about 50°C in the upper canister half and more than 200°C across the entire canister. The question will be addressed in the follow-up analyses because it poses problem of properly modeling the heat transfer to the ground and through the canister side boundary in the stilts region. It will also depend on the facility setup used to heat the canister.

C-8. Conclusions

The CT scan analysis provided significant detail throughout the wax experiment solidification behavior. This data was useful to have the capability to distinguish the type of voids, either separation from the walls or connected in the inner regions. Several voids detected throughout this experiment due to the solidification properties of the wax. Based on that observation, voids expected due to shrinkage was also detected in the simulation, in the lower parts of the assembly region. The wax experiment provided extensive insight into the solidification process. It had been observed that in the empty cells of the basket, separation of the wax from the walls and onset of voids due to shrinkage effects were more significant than the basket cell full of the assembly and the bottom nozzle and bottom stand. That showed that the filling and solidification was successfully performed around those intrinsic geometries.

The casting simulations are progressing step by step by establishing a ground for testing and down selecting the candidate filler materials Casting simulations defined the initial conditions for a successful molten tin experiment. The pre-heating conditions are determined using the results of the simulation. The tin experiment simulations, there were no shrinkage defects observed. The experiment will be performed based on those conditions.

The canister thermal history significantly affects the process of casting liquid fillers in preparation for permanent canister disposal. An approach to model the thermal histories associated with the removal from

storage, transportation, and preheating was presented. CSFS computational software was used for the analysis in a non-trivial mode with interchangeable thermal structures. An algorithm was developed that allowed transients of several days to be analyzed with varying thermal conditions, both structural (insulation, variety of shields) and environmental.

A thermal scenario was evaluated, and the results showed that about two days would be necessary to preheat the canister if fuel residual heat was only used for heating. This positive result gives an expectation that no additional heating would be needed in the preconditioning process, which is a finding that may largely simplify the entire canister handling procedure and may reduce the filling process cost.

Planned future works include (1) completion of the first casting validation experiment; (2) gradual development of the casting simulation for various full-scale DPC models with step-by-step validation; (3) performance of casting simulations with various cementitious materials, metals, and alloys; (4) completion of the initial pipe testing and planning for future investigations based on the initial findings; and (5) completion of the DPC preheating simulation.

C-9. References

1. Campbell, J., *Castings*, 2nd ed., Elsevier (2003).
2. "Store Fuel and Decommissioning Report," Ux Consulting Company, LLC, **20**, 238 (2018).
3. E. Popov, K. Banerjee, "Dual Purpose Canister Heating Evaluation for Casting of High Temperature Fillers," ANS Winter Meeting, Washington DC, 2019
4. T. E. Michener, D. R. Rector, J. M. Cuta, and H. E. Adkins, "COBRA-SFS, A thermal-hydraulic analysis code for spent fuel storage and transportation casks Cycle 4a," PNNL-24841 (2017).
5. J. M. Creer et al., "Castor-V/21 PWR Spent Fuel Storage Cask Testing and Analyses," EPRI NP-4887 (1986).
6. E. Hardin et al., "Investigation of Dual-Purpose Canister Direct Disposal Feasibility (FY14)," FCRD-UFD.
7. Nesrin O. Cetiner, et al., "Dual-Purpose Canister Filling Demonstration," Trans. of the American Nuclear Society, Vol. 121, pp. 283-286, Washington DC, (Nov. 2019)

This page is intentionally blank

Appendix D FY2021 STATUS REPORT

This appendix documents work performed supporting the US Department of Energy (DOE) Nuclear Energy Spent Fuel and Waste Disposition, Spent Fuel and Waste Science and Technology, under work breakdown structure element 1.08.01.03.05, "Direct Disposal of Dual-Purpose Canisters." In particular, this appendix fulfills the M3 milestone, M3SF-21OR010305019, "DPC filler simulation and demonstration progress report," within work package SF-20OR01030501, "Direct Disposal of Dual Purpose Canisters–ORNL."

This appendix presents (1) demonstration of the feasibility of molten metal fillers to completely fill the spent fuel inside the DPCs, (2) metal casting simulations using ProCAST software, (3) fabrication of DPC fill pipe flow experiment, (4) modeling the filling of DPC with water and validating the flow model with experimental results, and (5) acquisition of a full-scale DPC for future studies.

D-1. Molten Metal (Tin) Experiment

Following the previous work to demonstrate filling of small-scale DPC geometries with water, paraffin, and glycerin, as well as work to create and verify a CFD model of these experiments for use on full-scale models, it was determined that a demonstration using a molten metal casting would be beneficial. Inundation of a small-scale, representative geometry was chosen for this first experiment with molten metals.

Without being exhaustive, the selection of metal includes the following criteria: (1) low melting point, (2) low viscosity, (3) low toxicity, (4) low density, (5) low cost, (6) low freezing range, (7) castability, i.e., without significant casting defects during solidification, and (8) corrosion resistance. Many alloys of tin, zinc, cadmium, bismuth, copper, and lead are potentially good candidates. Lead was eliminated as a candidate because of its toxicity and density, and cadmium was eliminated because of its toxicity. Bismuth is costly and its copper alloys have melting points greater than 475°C. The maximum allowable filling temperature for a full DPC will be determined based on thermo-economics, among other criteria, and higher temperatures will result in higher filling costs. This preliminary screening indicated that zinc and tin are promising candidate materials for unit testing, and tin was chosen for this initial experiment due to its low melting temperature (232°C), minimal heath hazards, relative availabily, and low cost.

The demonstration involved melting pure tin in melting pots and pouring the liquid tin into a pre-heated mold (representing the canister walls) containing a full-diameter drain pipe, basket wall with mousehole, and 9 surrogate fuel rods in a surrogate spacer grid. The geometry is described in Section D-3. The temperature of the mold and tin-filled region were recorded during the pour and cooldown. Defects in the casting were characterized using destructive and non-destructive means following solidification to identify and quantify any significant voids in the solidified filler material.

A virtual model of the molten tin experiment was performed using ProCAST software.

D-1.1 Experiment Design and Setup

This test includes geometry representing 9 fuel pins and 1 spacer grid section of the fuel bundle, as well as one of the mouse hole regions, and geometry that is accurately sized for the full-scale canister drainpipe. The experimental setup is relatively small and can be arranged on a normal sized lab tabletop. The major components of the setup are the mold assembly, the hot plate, the melting pot assembly, and the computer with the data acquisition system.

The equipment used for this experiment includes:

- 2× Lee Precision 20 lb. melting pots – 120V AC
- Laboratory Hot Plate – 120V AC
- 20 in. × 24 in. × 3 in. stainless steel catch pan
- Mold assembly with grid region
- 30 lb. tin wire cuttings (melting point 450°F)
- Thermal insulation
- Temperature probes / data acquisition system / LabView software
- Briskheat® heat tape / controller

To reduce design and fabrication costs, most components used in the experimental setup are commercially available. The mold and internal components were designed and fabricated by ORNL, as well as the stand and plumbing used for joining the two melting pots. The outer wall of the geometry is a stainless-steel container with ½ in. walls on all sides and the bottom, and it is open on the top. The cavity of the geometry is approximately 3 in. wide, 5 in. long, and 6 in. tall. For convenience in reporting, the assembled geometry to be filled with the molten metal is refered to as a "mold."

Because the mold volume was more than the volume capacity of one of the melting pots, and a melting pot of larger capacity was not readily available, it was decided to join the pour spouts of two individual melting pots with stainless-steel tubing to ensure sufficient volume of molten tin for a continuous pour. The initial CAD model with labels indicating the major experiment components is shown in Figure D-1.

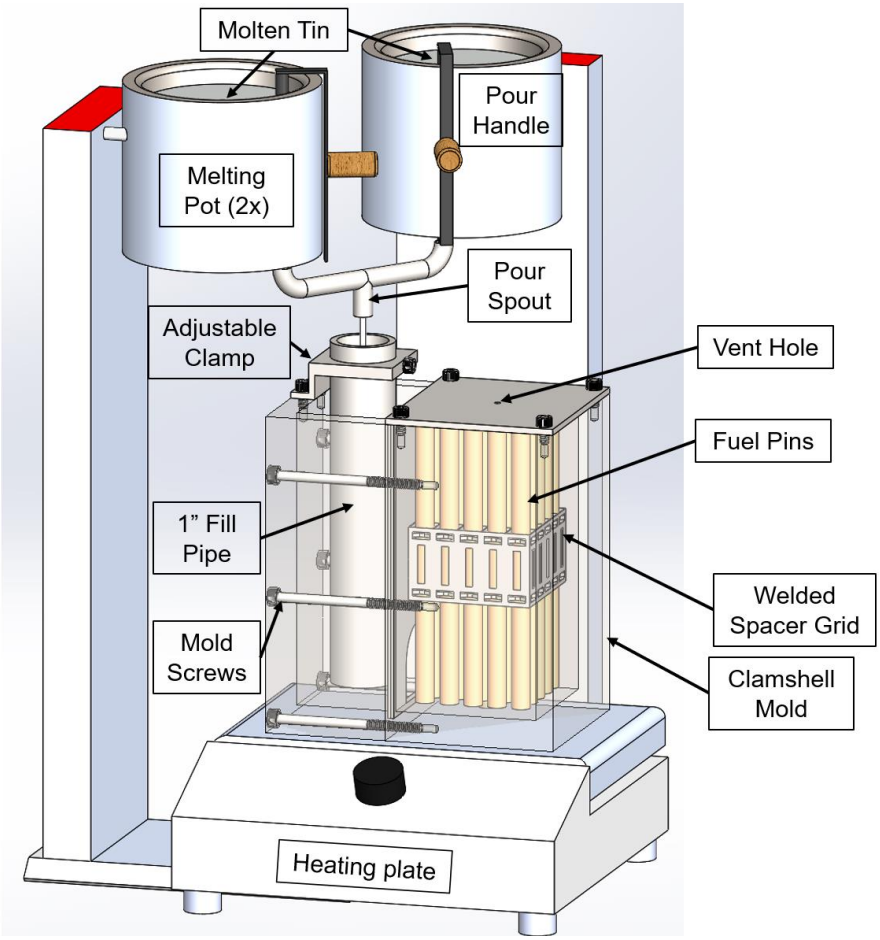

Figure D-1. CAD representation of tin pour experimental setup.

A reduced size 5×5 stainless-steel grid was fabricated with welded components.The same geometry was used in the previous filling experiments which used paraffin and water. The fill pipe is 1 in. schedule 80 stainless pipe, which is representitive of the actual pipe size and material in the full-scale DPC. The mouse hole region is represented as a stainless-steel plate which divides the fill and grid cavities of the mold. These components are shown in Figure D-2.

Figure D-2. 5×5 grid (left) and fill pipe and mouse hole divider (right).

Solid aluminum rods 7⁄16 in. in diameter were used to represent the fuel rods and were installed into the grid. The central rod was slightly longer than the 24 surrounding rods. This rod interfaced with a shallow hole in the bottom of the mold to center and support the grid and rod assembly. This assembly is shown in Figure D-3. The mold assembly consisted of two main halves which were held together by 6 socket head cap screws. This allowed the mold to be taken apart to extract the solidified casting. The grid and rod assemby, pipe, and mouse hole divider were installed into the mold as shown in Figure D-4. .

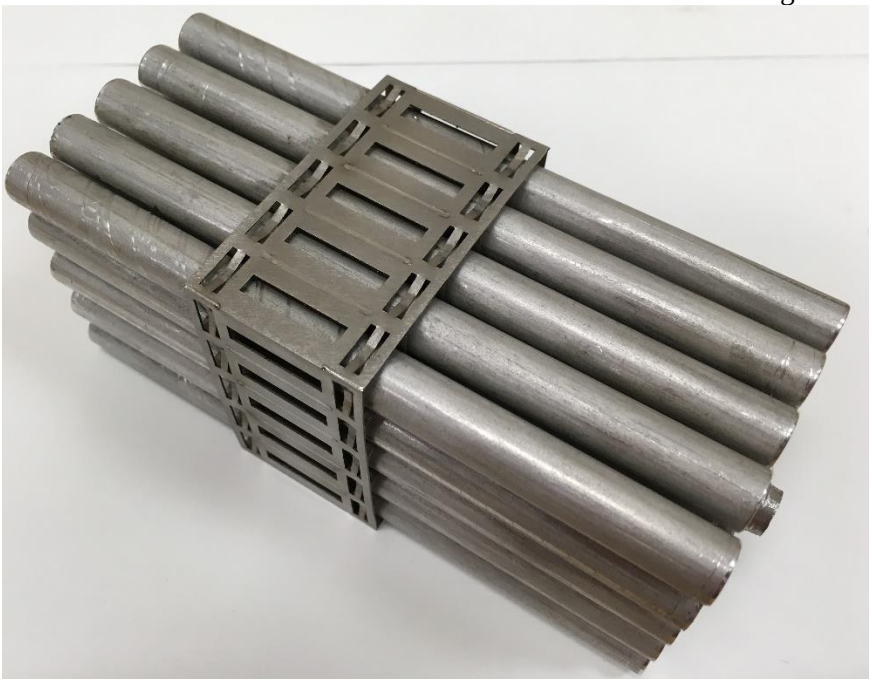

Figure D-3. Assembled grid and aluminum rods.

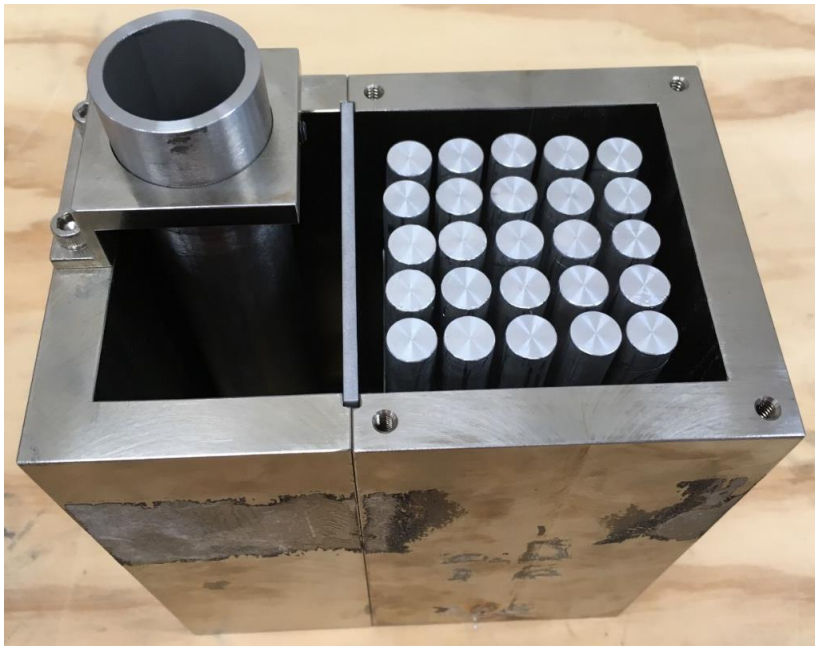

Figure D-4. Mold assembly with fill pipe, mouse hole plate, and grid assembly installed.

The melting pots and insulation were placed on a large stainless-steel pan to contain any accidental spilling of molten metal from leaks in the system or any other malfunction during filling. Although the insulation was not needed to achieve the target temperatures above the melting point of tin, it helped to reduce the temperature variations in the mold during heatup and cooldown, which is more representative of the full-scale DPC. Heat tape was added to the small-diameter piping connecting the melting pots to prevent freezing of the tin during pouring. The arrangement of the main experimental components is shown in Figure D-5. and Figure D-6. .

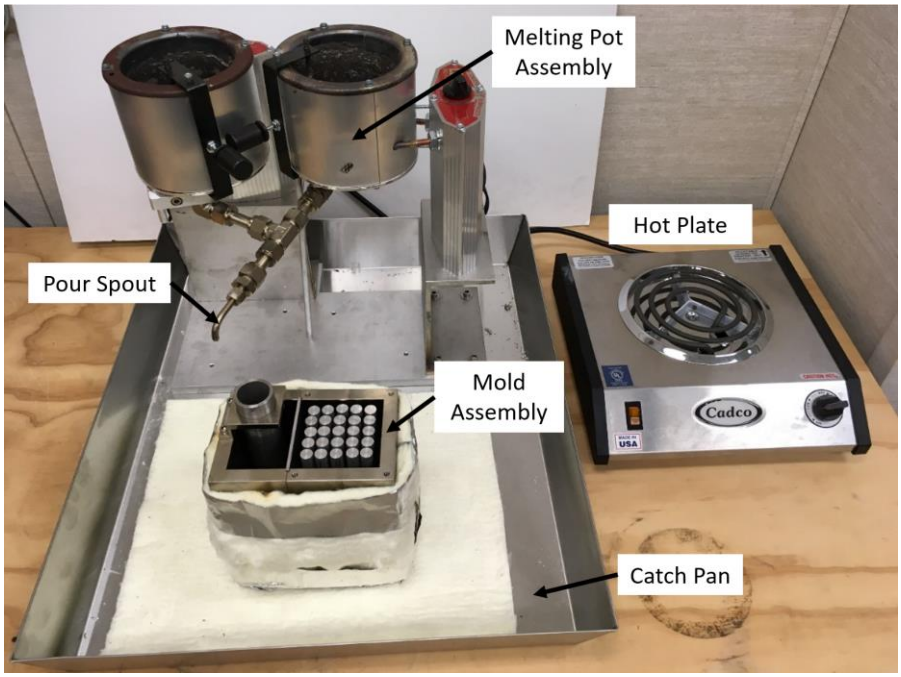

Figure D-5. Major components of the tin pour experiment, including mold assembly, melting pot assembly, hot plate, and catch pan.

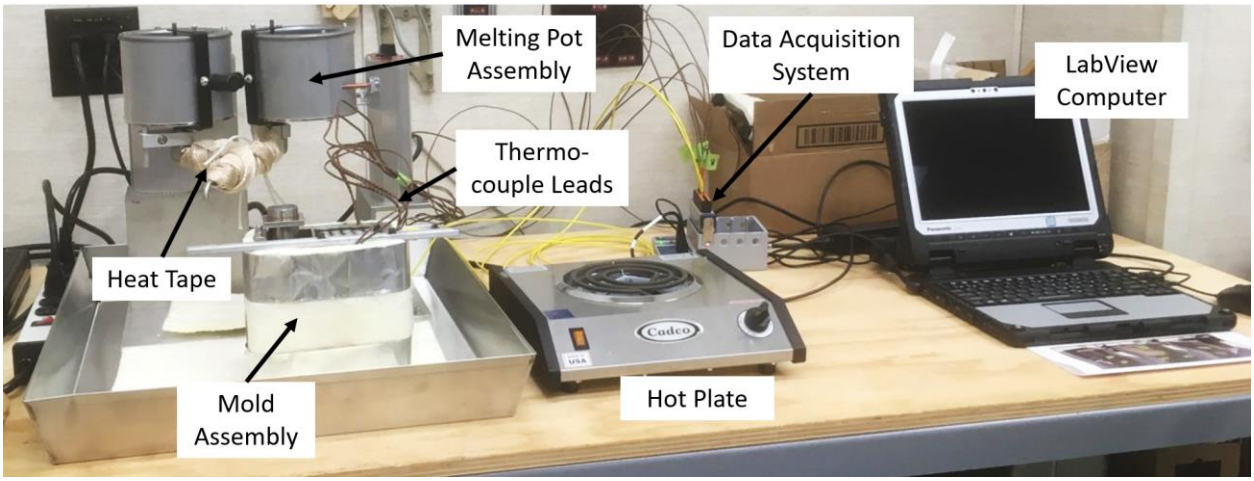

Figure D-6. Full experimental setup with LabView laptop, thermocouples, and heat tape added to connective pipe.

Eight thermocouples were strategically located in the mold body, and two more were located in the casting volume at the bottom of the fill pipe and at the center of the mouse hole region. Additional thermocouples were also used at the pour spout and in the melting pots to record the tin temperature at the time of pouring. Figure D-7. shows the relative placement of the temperature probes in the mold body. These were drilled into the mold body ¼ in. deep and affixed with aluminum tape.

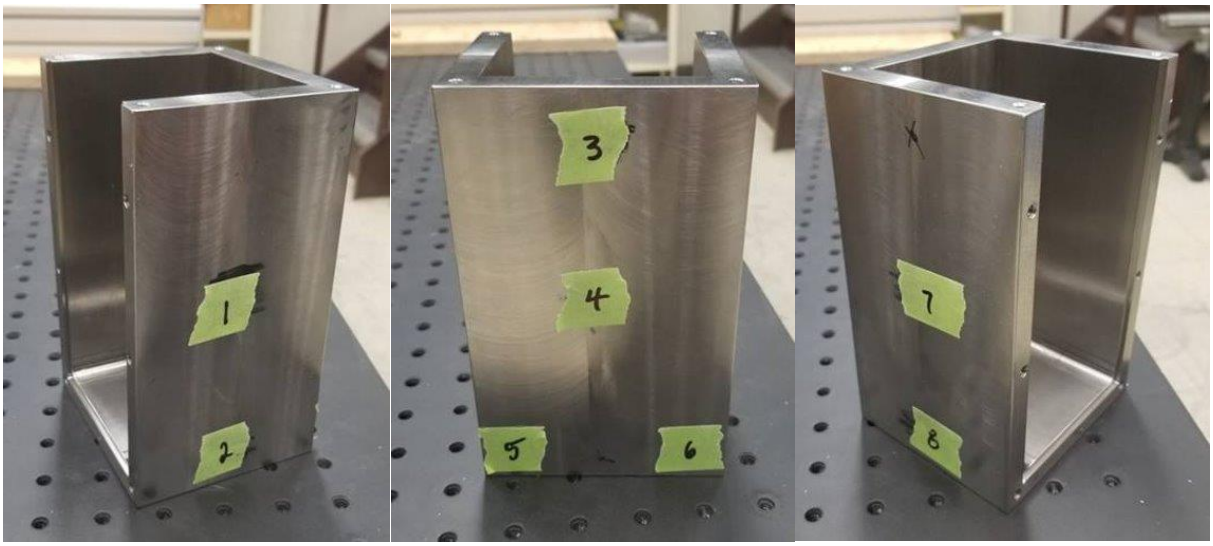

Figure D-7. Thermocouple locations in the mold body.

D-1.2 Experiment Procedure

Preliminary functional and calibration tests were conducted prior to the casting experiment to verify the seamless function of the equipment and measurement of the flow rate achieved by the merged melting pots. The measured flow-rate data provided critical input data to be used in the ProCAST simulation of filling, cooling, and solidification analysis. Once this dry-run test was completed and proper equipment function was verified, the casting experiment was performed.

Flow-rate test overview

The goal of the flow rate test was to determine the average and time-dependent flow rates of tin through the combined melting pot assembly. Tin was be melted in the melting pot assembly to represent the approximate volume expected for the casting experiment. Tin was poured into an ingot mold in stages, and the pour times and pour masses were recorded. The process was repeated until the melting pots were emptied. The data were averaged to estimate the pouring rate of the tin with this experimental setup.

Flow-rate setup procedure:

1. Place melting pot assembly in stainless catch pan.
2. Wind heat tape onto connection spout and ensure that the tape does not overlap.
3. Add tin cuttings to the melting pots and turn the melting pots ON.
4. Turn the heat tape controller ON, and adjust the setpoint to 300°C.
5. When all tin is melted, proceed to the experiment procedure:

Flow-rate experiment procedure:

1. Designate one person to operate a stopwatch and another person to operate the pour levers on the melting pots.
2. Place ingot mold below the pour spout and elevate the pour spout using noncombustible materials (metal plates / rectangular tubing, etc.) to within approximately ½ in. of the top of the ingot mold.
3. The instant the levers are lifted, the lever operator shall call out "START" to allow the molten tin to flow, and the stopwatch operator shall start the stopwatch.
4. When the ingot mold is nearing full, the lever operator shall call out "STOP" the instant the levers are released, and the stopwatch operator shall stop the stopwatch.
5. Allow the remaining tin to flow out of the spout until drained for the most accurate reading.
6. Allow the mold shall then be allowed to cool until the tin has solidified in the mold. Quench the ingot in water to release it from the mold, and then weigh the ingot using a high-precision scale.
7. Record the total pour time and the ingot mass.
8. Repeat steps 2 through 7 until the melting pots are empty.
9. Turn OFF power to the melting pots and the heat tape controller.

Post flow-rate experiment procedure:

1. Add pour time / ingot mass to spreadsheet for data analysis.
2. Calculate the experimental mass flow rate vs. the duration time of the experiment.
3. Provide the flow rate for the ProCAST simulation.

Casting experiment setup procedure:

1. Assemble mold with grid, rods, fill pipe, and mouse hole divider.
2. Add the thermocouples to the mold assembly at the designated locations. Connect the thermocouple leads to the data acquisition system.
3. Wrap and affix thermal insulation to the outside surfaces of the mold assembly and secure it using aluminum tape. DO NOT insulate the bottom surface of the mold assembly.
4. Place the complete mold assembly in the center of the hotplate.
5. Place the melting pot assembly in the catch pan and place a layer of insulation on the catch pan under the pour spout to serve as the bottom insulation of the mold during filling and cooldown.
6. Ensure that the heat tape is properly wrapped around the connective piping on the melting pot assembly to cover as much of the pipe as possible to prevent freezing in the pipes during the pour.
7. Fill the melting pots with the tin ingots / wire cuttings.

Casting experiment heat up procedure:

1. Ensure that the hot plate is turned to the OFF position. Turn ON the master power strip.

2. Adjust the power to approximately ***5*** on each melting pot dial, which should correspond to a steady-state temperature of 400°C.
3. Turn ON the heat tape controller and adjust the setpoint to 400°C.
4. On the LabView computer, start the data recording for the mold temperatures.
5. Ensure that the mold assembly is well positioned on the hot plate and turn the hot plate ON to HIGH.
6. Allow the mold assembly to heat up until the average temperature across the body thermocouples is approximately 300°C. (This only includes thermocouples in direct contact with the mold body.)
7. Continue adding tin ingots / wire cuttings to the melting pots as the tin is melted to ensure that they are nearly full.
8. Once all tin is melted, adjust the temperature to achieve 400°C ± 10°C. This may require different settings for each pot.
9. Once the mold has achieved an average temperature of 300°C and the melting pots are 400°C ± 10°C, proceed to the pouring procedure.

Casting experiment pouring procedure:

1. Wearing proper personal protective equipment (heat-resistant gloves, safety glasses), turn OFF the hot plate.
2. Carefully remove the mold assembly from the hot plate and place it onto the insulation in the catch pan, positioning the pour spout directly above the fill pipe of the mold assembly.
3. Ensure that no obstructions (e.g., thermocouple wires, insulation) are present between the pour spout and the fill pipe. Ensure that the data acquisition system is running and recording data.
4. Wearing heat-resistant gloves, actuate the pour handles simultaneously and fully to begin pouring the tin and filling the mold assembly.
5. Allow the mold to fill all the way to the top, but DO NOT allow the tin to spill over the side. Release the handles to stop pouring the tin.
6. Carefully shift the pour spout away from the mold pipe. Use the ingot mold to empty any remaining tin from the melting pots.
7. Once all tin has been removed from the melting pots, turn OFF the power to the melting pots and heat tape controller.
8. Allow the mold to cool down undisturbed. This could take 10 or more hours. Measure the reading on the thermocouples to ensure that the mold is cool enough to be handled safely before touching the mold without gloves.

Post casting experiment procedure:

1. Remove the thermal insulation from the mold assembly.
2. Remove the 6× mold screws holding the two halves together and remove the fill pipe bracket.
3. Carefully separate the mold halves from the tin structure.
4. Perform post casting analysis (CT scanning and / or wire EDM, bandsaw, water-jet sectioning) to determine the casting behavior in the grid region and to quantify the voids.
5. Perform data analysis on the temperature vs. the time data to verify the ProCAST simulation results.

D-1.3 Experiment Results

The following sections provide the processed data from the flow rate and casting experiments.

D-1.3.1 Mass Flow Rate Data

For the flow rate experiment, recorded and measured data include the duration of each pour as measured from the instant the pour spout is opened until the pour spout is closed. The mass of each pour was measured by weighing each ingot. The running weight denotes the cumulative total ingot weight, which

represents the total mass poured during the experiment. The pour rate is the average mass flow rate for each pour calculated by dividing the ingot weight by the pour time. The midpoint is simply the pour duration divided by 2, and the running time is the time elapsed to the midpoint of each pour. This operation was performed to place the average flow rates at the midpoints of the pour, because the true rates diminish linearly as the melting pots are emptied. As the pressure head of molten tin in the melting pots reduces, the flow rate also reduces proportionately. The data are shown below in Table D-5.

Table D-5: Mass Flow-Rate Experiment Data.

Pour	Duration (seconds)	Weight (grams)	Running weight (g)	Rate (g/s)	Midpoint (s)	Running time (s)
1	21.22	968.0	968.0	45.62	10.61	10.61
2	23.85	1034.8	2002.8	43.39	11.925	33.145
3	26.28	1056.4	3059.2	40.20	13.14	58.21
4	29.4	1090.4	4149.6	37.09	14.7	86.05
5	33.66	1097.4	5247.0	32.60	16.83	117.58
6	36.18	1085.8	6332.8	30.01	18.09	152.5
7	41.15	1032.4	7365.2	25.09	20.575	191.165
8	47.53	1027.2	8392.4	21.61	23.765	235.505
9	65.96	946.6	9339.0	14.35	32.98	292.25

The main objectives of this preliminary experiment were to verify proper equipment function and to quantify the mass flow rate of the custom melting pot arrangement. To quantify this flow rate, which varied based on the amount of molten tin contained in the melting pots, the observed flow rates for each pour were plotted against the running time of the pour. Based on the results, the flow rate at the onset of the pour was determined to be approximately 46.5 g/s, and it reduced linearly by 0.11 g/s^2. A linear correlation provides a good representation of the data (R^2 = 0.995). The data is shown in Figure D-8.

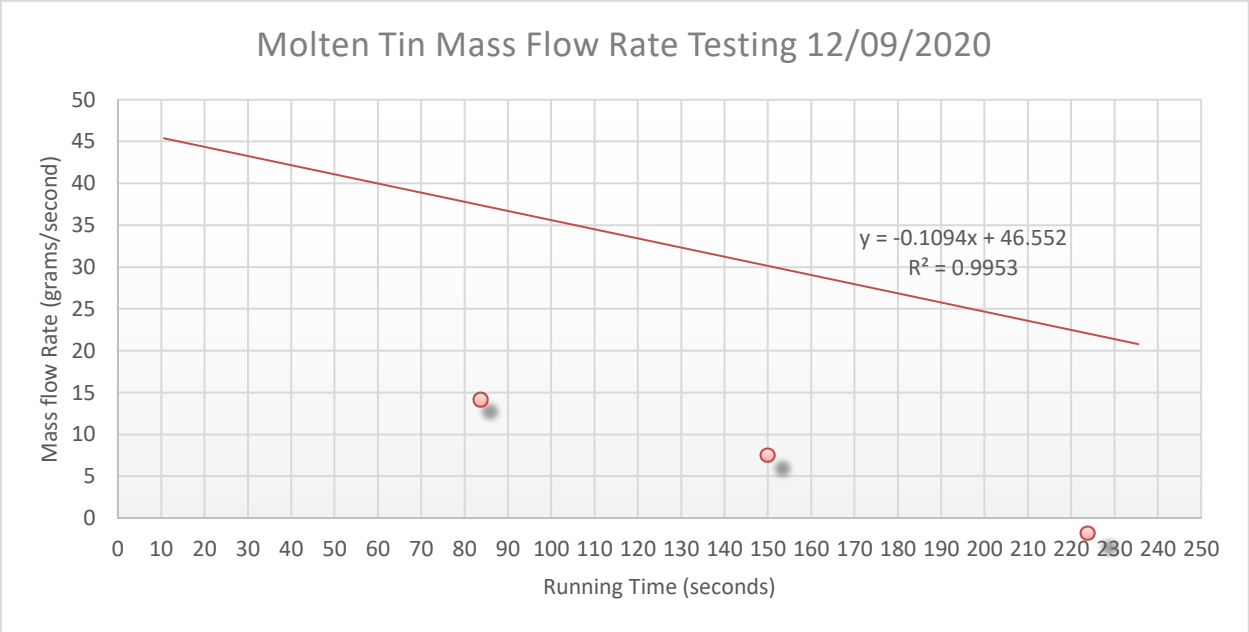

Figure D-8. Flow rate experiment mass flow vs. running time showing discrete data points and computed trendline.

D-1.3.2 Casting Temperature Data

The casting experiment focused on achieving a continuous pour into the mold assembly to completely fill the void space inside the mold. Thermocouples were placed at various locations in the mold body, with additional thermocouples placed at the bottom of the fill pipe and the mouse hole region. Other thermocouples were used to measure the temperatures of the melting pots, heat tape, and pour spout.

The mold was filled to the top of the mold face with molten metal. Since the top of the aluminum rods were very close to this plane, they were not fully covered by the molten tin during pouring to avoid spilling tin over the side of the mold. Figure D-9. shows the mold assembly immediately after the pour was stopped and the tin was still in a liquid state.

Figure D-9. Mold assembly after pour with tin in molten state.

The data acquisition system recorded the temperature data using a laptop running LabView software. Datapoints were recorded approximately every 2.5 seconds for each of the 10 thermocouples for 7 hours after the pour. Figure D-10. shows the data from thermocouple 1.

When the data were transferred from the computer to an Excel spreadsheet for data reduction, it was observed that large portions of the cooldown data were missing from the recorded dataset. This was because the computer's sleep function had not been disabled. The computer was checked three times during the cooldown process and data was recorded for approximately 30 minutes before the machine went into sleep mode again. An effort was made to fill the gaps in temperature data using curve-fitting techniques. The data shows a brief period of solidification prior to the first data gap visible as a period of constant temperature at approximately 232°C across all thermocouple readings, representing the phase change from liquid to solid. Some thermocouples read a bit lower than this value because of natural thermal gradients present in this system. Thermocouples in or nearer the tin naturally read higher temperatures than thermocouples embedded in the mold wall or near the edges or corners of the mold, because these were relatively cooler areas.

The temperature data were captured for the initial cooldown, the beginning of the phase change region, and at various times during the secondary cooldown, so the gaps in the data were filled easily based on the cooldown rates. Each of the 10 thermocouples' recorded data were maintained, and only the data in the gaps were calculated. This was accomplished by using the data in the secondary cooldown region (which occurred place after the solidification process) and using a third-order polynomial to best fit the recorded data through all three regions of recorded data. This polynomial was used to approximate the temperature vs. the time data for all data gaps for each thermocouple. For each polynomial, the temperature was set to the phase change temperature recorded to calculate the time, and the gap was filled in with the generated data up to this point. The solidification region (characterized by a very stable temperature over a long period of time) was extended to meet the cooldown curve fit data for each thermocouple, thereby completing each of the data sets. Figure D-10. shows the data from thermocouple 1, representing the regions of collected and calculated data. The blue regions are recorded from the data acquisition system, the red regions are calculated based on a third-order polynomial fit of the recorded data, and the yellow region is the extension of the phase change region.

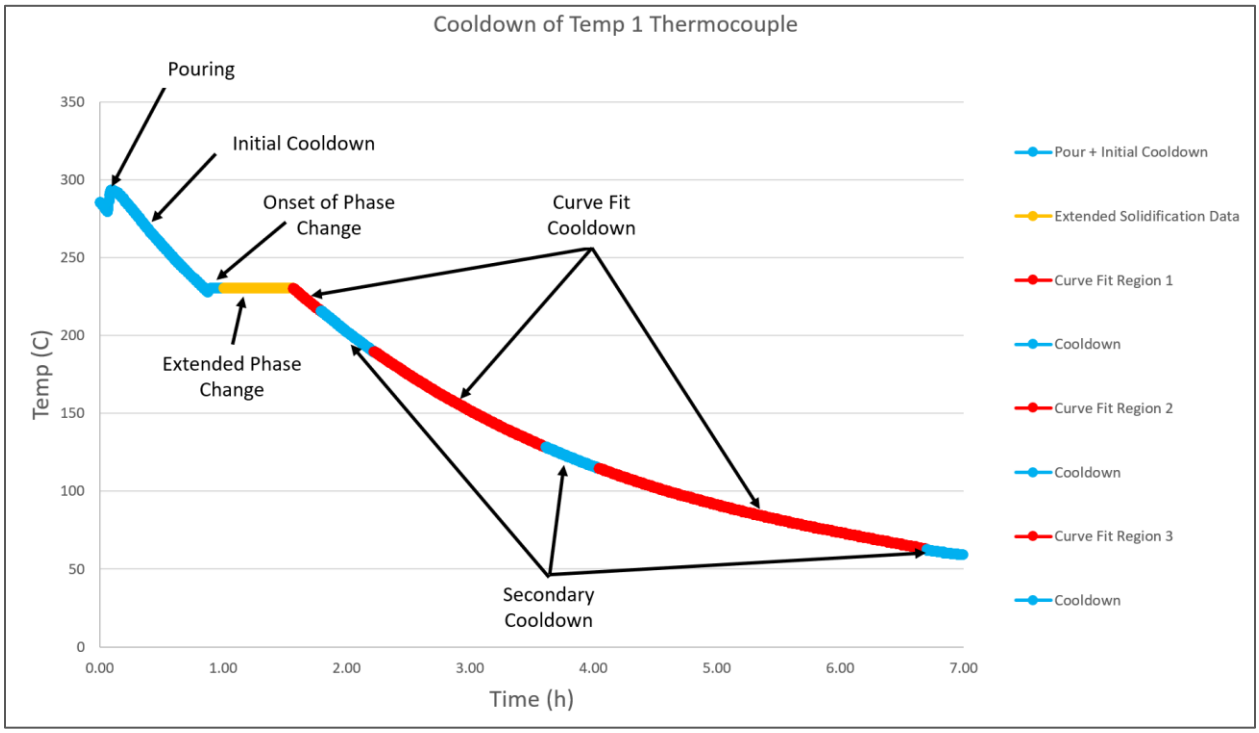

Figure D-10. Thermocouple temperature data regions.

Shortly after the pouring was completed, the mold and internal components quickly converged to a relatively uniform temperature. This is appropriate behavior for a thick-walled mold with insulated sides and bottom and good thermal conductivity between the mold and casting. As shown in the graph below, after the first couple of minutes, all thermocouple readings converge to within 4°C of each other as the cooling process begins. The graph shows temperatures of all thermocouples dipping slightly from time 0 until about 3 minutes into the data collection, which represents the slight cooling of the mold from the time the hot plate was turned off until the pour began. Temperatures from thermocouples 9 and 10 dipped more harshly than the others because they were in the interstitial air inside the mold cavity and not in the mold body, making them more sensitive to temperature fluctuations.

When the pouring began, temperatures for thermocouples 9 and 10 spiked above the rest of the readings. This is because these thermocouples came into direct contact with the molten tin as it left the melting pots

at close to 400°C. Temperatures read by the remaining thermocouples 1 through 8 were increasing more slowly because the elevated temperature must conduct through the walls of the mold, whereas the thermocouples near the top of the mold (thermocouple 3) were not detecting an increase in temperature until the end of the pouring, which occurred at almost 7 minutes into the data recording. The graph in Figure D-11. shows the thermocouple readings from the beginning of the data capture (when the hot plate was turned off) until approximately 7 minutes after the data recording (approximately when the pouring was complete). This graph shows in detail the behavior of the mold thermocouples (#1–#8) and the void space thermocouples (#9 and #10) during the pouring process.

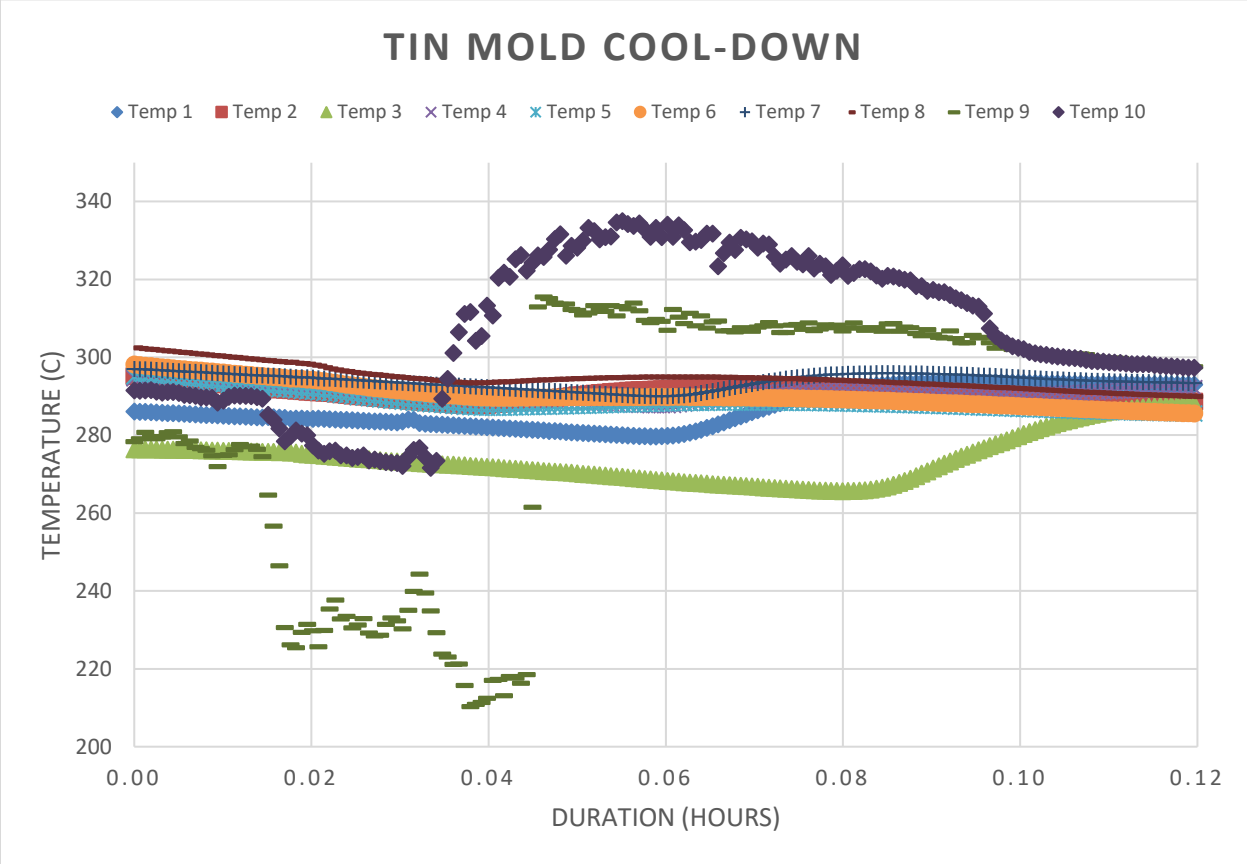

Figure D-11. Collected and calculated temperature data during the pouring process for all thermocouples.

Figure D-12. shows the temperature data for all thermocouples over the duration of the pour, solidification, and cooldown periods, illustrating the tight correlation between all thermocouples immediately after the pouring was completed. This correlation was maintained throughout the solidification and cooldown periods resulting from the good contact and thermal conductivity of the mold and casting material, as well as the thermal insulation applied to reduce convection on the outside surfaces. These conditions allowed the mold to cool down in a controlled, and uniform manner. Note that the data presented in Figure D-12. are a combination of collected and calculated data, as described above.

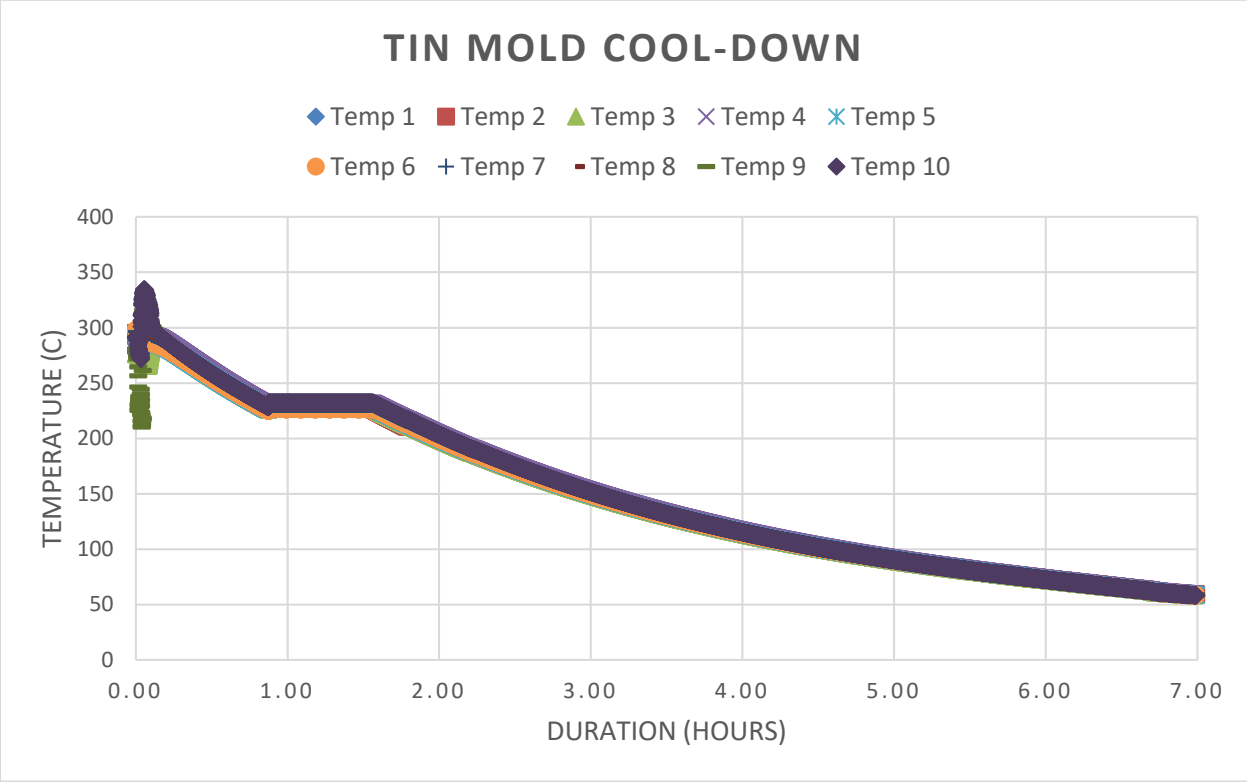

Figure D-12. Collected and calculated thermocouple temperature data collected during the entire pouring, solidification, and cooldown experiment.

D-1.3.3 Casting Void Analysis

Non-destructive evaluation (NDE) was first utilized to evaluate the tin casting for defects (Figure D-13). The casting was imaged via two-dimensional radiography; the Comet MXR-451/26 450 kV x-ray tube assembly was used at a setting of 10 mA for 5 minutes in conjunction with a 5⁄16 in. copper filter. The copper filter was used to harden the energy spectrum of the resulting beam for better penetration through the smallest 3 in. thickness of the cast. Imaging and analysis of the results were performed by personnel certified via the American Society for Nondestructive Testing Level III requirements. Two image quality indicators were utilized during radiography, and sufficient source penetration through the casting to the imaging plate was confirmed. In addition, a 0.5 in. diameter steel ball placed on the casting surface produced a reference length. This ball, which was labeled “0.500 in,” can be seen in the image on the right in Figure D-13.

The image of the tin casting is provided on the left in Figure D-13 to serve as a reference point for evaluating the associated radiography image. In addition, the drainpipe, the mouse hole divider plate, and several of the aluminum rods are identified in the radiographic image. Areas appearing white that are either to the right of the mouse hole divider or adjacent to the darker, aluminum rods represent tin fill. Note that the aluminum rods appear dark in the radiographic image as a result of the relative strength of the x-ray source used to penetrate the higher density tin.

Figure D-13. An image of the tin casting (left) and the associated radiographic image (right).

In the area of the drainpipe, a relatively uniform image suggests that there is no defect detected. Similarly, tin fill surrounding the aluminum rods in Figure D-13 appears uniform and does not immediately suggest any areas of gross concerns for casting defects. Figure D-13 does identify an area outside of the drainpipe, circled in red, that is darker than the surrounding tin material. This area most likely represents a shrinkage or entrainment defect that occurred as the casting solidified [24, 25]. Based on the reference ball included in the radiography image, the size of this defect is ~2 × 0.5 in.

Given that the radiographs produced two-dimensional images of the casting, straight beam ultrasound was used next to confirm and further locate the defect. The Olympus Epoch 600 was used in conjunction with a 0.5 in. diameter 5 MHz transducer. The casting surface scanned via ultrasound is depicted to the left in Figure D-13. Figure D-14. , below further demonstrates the scanning activity and the side of the casting scanned. By evaluating this side, the approximate depth of the defect was measured.

Figure D-14. Efforts to use ultrasound to locate defects, including a full thickness scan (left) and a scan identifying defects (right)

The picture included on the left in Figure D-14. reflects a portion of the casting through which the ultrasound penetrated the full thickness of tin, identifying no defects. The distance the signal travelled before being reflected, approximately 3 in. is indicated in the image as a reflection peak centered within the blue gate. The picture included on the right in Figure D-14. lacks a similar peak in the same location. This image depicts ultrasound measurements in the vicinity of the defect identified via radiograph. Instead, a reflection peak is located approximately 1.1–1.2 in. into the casting, suggesting the entirety of the ultrasound signal was reflected from the interface between tin and the suspect void. Ultrasonic evaluation from the opposite side of the casting also suggests that the interface between tin and defect begins at a thickness of approximately 1 in. Therefore, it is possible based on the results of ultrasonic evaluation that the area of defect extends through the middle 1 in. of the casting. This information can be added to that obtained via radiography to estimate the size of the defect as ~0.5 × 2 × 1 in.

Destructive analysis of the casting around the area of the drainpipe further characterized this region of suspected porosity. A horizontal bandsaw was used to produce two cross-sectional cuts through the 3 in. face of the casting; see Figure D-15 "A1" in the figure is the approximate distance from the casting's edge to the first cut (2 cm) and "A2" is the approximate distance from the casting's edge to the second cut (4.3 cm).

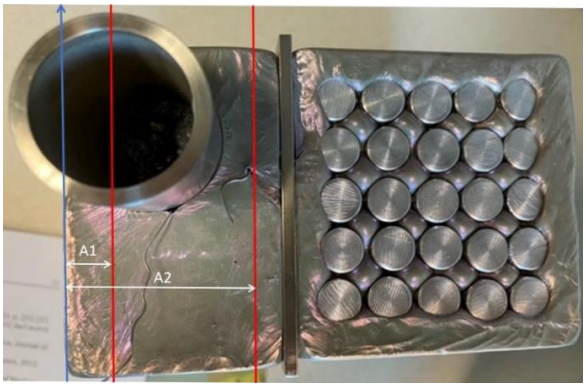

Figure D-15. Cross-sectional cuts of the tin casting. The blue line is a reference representing the far edge of the casting and each red line reflects a cut.

The first cross-sectional cut performed was intended to evaluate the approximate centerline of the drainpipe for any unexpected defects. Figure D-16 and Figure D-17 include cross-sectional images at this location. The picture on the left in Figure D-16 does not suggest any areas of macroporosity or gross defect, consistent with radiography and ultrasound results. The picture on right in Figure D-16 was taken looking down into the drainpipe and highlights a cavity of roughly conical shape that appears to penetrate the drainpipe to an indeterminate depth. This cavity is a casting defect well known as a shrinkage pipe [2], which reflects the final dip of the free-surface due to metal shrinkage in the top region to solidify. The images in Figure D-17 are also included to highlight a small area of suspected porosity along the external edge of the drainpipe.

Figure D-16. Images of the cross-sectional cut through the centerline of the drainpipe. Both the entire cross section (left) and a view down into a suspected shrinkage pipe (right) are included.

Figure D-17. Additional images of the cross-sectional cut through the centerline of the drainpipe, showing a small area of suspected porosity along the bottom edge of the drainpipe (circled in red).

The second cross-sectional cut served specifically to evaluate the area of defect identified via the NDE techniques discussed above. As expected, destructive analysis confirmed the findings associated with NDE. Specifically, mostly smooth macropore is evident from the images included in Figure D-18 and Figure D-19. The image included to the right in Figure D-18 indicates that the macropore may reach the mouse hole's stainless-steel wall. The image to the far left in Figure D-19 indicates that this macro-pore measures at least 2" in length, though the additional views of the macropore included in Figure D-19 suggest that it extends further downward into the cast. Additional measurements suggest the total macropore measures approximately 3" in length. The macropore's thickness varies but does not appear to

be more than 1" at its widest location. The formation of this macropore is a clear indication of the last region to solidify in the casting [25].

Figure D-18. Two images depicting a micropore originally identified via NDE techniques.

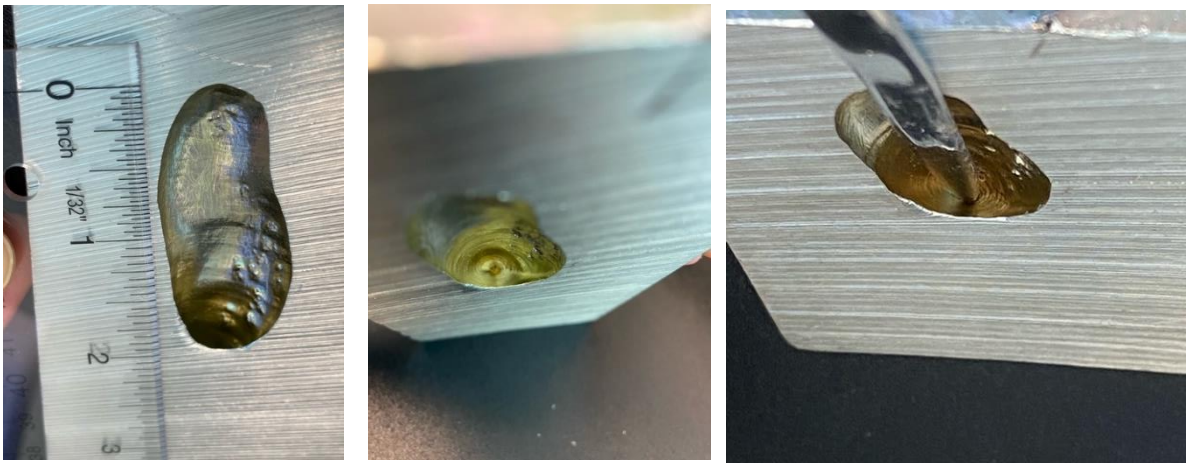

Figure D-19. Additional macropore images approximating size (right) and illustrating additional penetration into the casting (center and right).

The NDE indicates that the wetting behavior between tin and drainpipe is very good, as no continuous interfacial gaps detected along the interface between the drainpipe and tin. This is likely to limit any water intrusion into the casting. Micropore defect, which is well known to occur in the last regions to solidify, is isolated and not connected with any other cracking or long void defect, such as interdendritic porosity, that would lead to any water intrusion. Destructive analysis of the casting's rod array is planned in FY2022 to further confirm the results of NDE, namely that no significant defects are located in this important area. Additionally, in FY2022, all characterization data will be used to support further development and benchmarking of a ProCAST simulation. Given that some defects should be expected in any casting [25], development of simulations that can successfully predict the behavior will allow the development of casting conditions that will minimize defects (including surface connected defects) and optimize filler performance.

D-1.4 Experiment Conclusions

The equipment and procedure used for the tin pouring experiment worked as designed and predicted. The thermocouples and data acquisition system also worked well, and except for the missing data caused by the sleep function of the laptop, the temperature data were read and recorded successfully. With the reconstructed data using polynomial curve fitting for the missing data, a complete dataset for the cooldown and solidification regions was obtained and used in the casing simulation detailed in Section 3.

Relevance to final application

The following important steps were made towards the final DPC application:

6. Data acquisition procedures for monitoring filling and casting solidification were developed.
7. Thermocouple placement procedures were developed to assist in casting monitoring and process development.
8. The coupled multiphysics analysis capability offered by metal casting software (e.g., ProCAST) will provide a high-fidelity modeling capability for the full-scale DPC model casting, which is needed for development of the DPC filling process.
9. The computed results from the ProCAST software that are critical to the DPC filling process include total shrinkage porosity, Niyama criterion for assessing the propensity to porosity formation, effective stress, effective strain, and deformation.
10. Filling DPCs can be optimized based on combined experimental and computational study.

The following accomplishments relevant to the final DPC application were attained:

9. Casting procedures were developed by a multidisciplinary team comprising mechanical engineers, nuclear engineers, and materials scientists.
10. Procedures for obtaining boundary conditions required for DPC were developed.
11. Tin was successfully cast on a mock-up model mold that included grid and fuel inserts.
12. Filling and solidification metal casting simulations were conducted for the complex mock-up grid and fuel insert geometry.
13. The solidification model provides useful data on thermocouple placement (i.e., avoiding regions of large thermal gradients).
14. Tin has demonstrated materials compatibility with the cask grid, with no large voids detected.

This page is intentionally blank

D-2. Metal Casting Process Simulation and Process Design

ProCAST casting simulation software was selected for this project to simulate the casting filling and solidification of metal and composite candidates. ProCAST software uses the finite element method to model fluid flow, energy transport, and stress evolution during casting solidification. Without including the stress analysis, the casting simulations can predict the formation of macroporosity and microporosity defects [1, 2]. Once the cooling conditions have been modeled adequately, the final casting simulations can be conducted by including the stress analysis to predict hot-cracking defects [3].

The computed results from the ProCAST software without the stress analysis activated include temperature, fraction solid, total shrinkage porosity, and the Niyama criterion [27, 28] for assessing the propensity to porosity formation. Velocity, pressure, and void fraction are results obtained from the flow analysis. ProCAST offers the capability to visualize effective stress, effective strain, and deformation. This coupled multiphysics analysis capability will provide high-fidelity modeling once the scaled simulations evolve into full-scale DPC model casting.

D-2.1 Initial Conditions Based on Experimental Evidence

To conduct numerical simulations of the metal casting, specific input and initial conditions must be determined based on the experimental observations and data acquired. For example, data on the pouring area and the metal flow rate are required. A photograph showing the spout delivering the molten tin is provided in Figure D-20. .

The fill rate is an important parameter for the numerical simulations. The flow rate was not constant in the experiment detailed herein. Based on the results from the fill test results, the following fill rate (or mass flow rate) [g/s] was obtained as a function of pouring time (t[s]):

$$\dot{m}_p(t) = 46.552 - 0.11\ \mathrm{t[s]} \tag{1}$$

Figure D-20. Spout inlet area of the molten Sn stream.

In Figure D-14, the temperature evolutions of the following three thermocouples are shown:

- Mousehole (MH) (T9): mouse hole thermocouple
- Fill-pipe bottom (FPB) (T10): fill-pipe bottom thermocouple
- Spout (T13): spout temperature

The following pouring conditions were identified from measured temperature data (Figure D-21):

- 120 s pouring onset
- 340 s pouring ends (220 s pouring time)
- 393°C *final* pouring temperature

As a first option, a constant pouring temperature of 393°C can be estimated, thus neglecting the heat transfer in the delivery pipe. Pouring temperature is expected to be lower than pot temperature as a result of heat lost from the Sn through the delivery pipe. A close analysis of the temperature data shown in Figure D-21. (a, b) revealed that the delivery pipe was initially cold (50°C) and was heated up as the Sn started to flow. Considering that the spout temperature is the pouring temperature, the time dependence of the pouring temperature, $T_P(t)$, was obtained from Figure D-21. (b) and is shown in Table D-6.

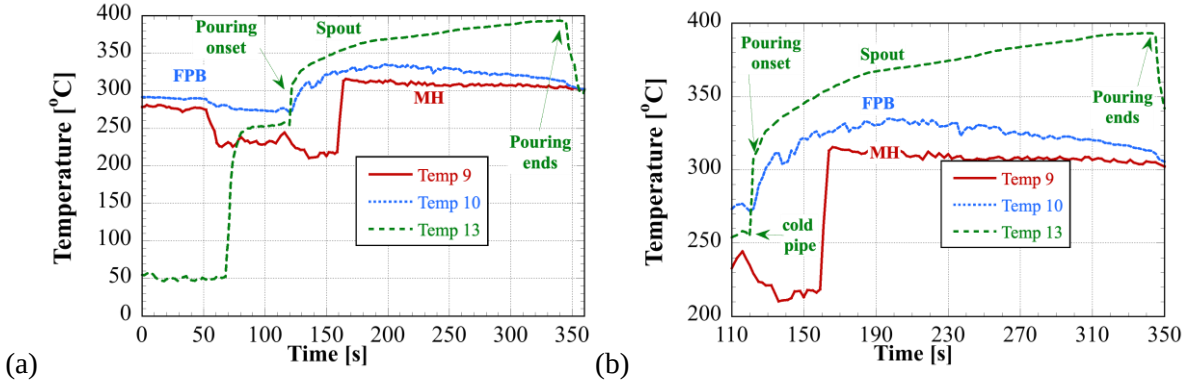

Figure D-21. Temperature evolution measured in the mouse hole (T9), fill-pipe bottom (T10), and spout (T13) for data ranges (a) 0:350 s and (b) 110:350 s.

Table D-6: Pouring temperature as a function of pouring time, $T_P(t)$, as identified from experimental data.

Time [s]	Pouring temperature [°C]
0	315
8	328
59	364
190	391
220	393

D-2.2 Identifying Cooling Conditions from Actual Experiments and Formulating Boundary Conditions for Numerical Simulations

To conduct numerical simulations of the metal casting, cooling conditions at mold surfaces and metal mold interfaces must be prescribed, and specific input and initial conditions must be determined from experimental observations and data acquired. For example, mold surfaces are cooled through ambient natural convection, which can be described as

$$q" = h_1(T - T_0), \tag{2}$$

where h_1 is a heat transfer coefficient that accounts for natural convection of the ambient air.

The thermal contact resistance at the metal–mold interface accounts for a jump between the surface temperature of the casting, T_c, and the surface temperature of the mold, T_m, as

$$q" = h_3(T_c, g_a)(T_c - T_m), \tag{3}$$

where $h_3(T_c,\ g_a)$, is a heat transfer coefficient which generally varies with the casting temperature and the air gap, g_a, that forms when the casting shrinks away from the mold during solidification [5]. The $h_3(T_c,\ g_a)$, can be cast, as

$$\frac{1}{h_3(T_c,g_a)} = \frac{1}{h_3(T_c)} + \frac{g_a}{k_a}, \tag{4}$$

where k_a is the thermal conductivity of the air at the local temperature.

For simplicity, in this study, heat transfer coefficients in various regions are identified through the heat transfer coefficient (HTC) label. In Figure D-22. the positions of several thermocouples inserted in the mold are identified. Thermocouples 2, 5, 6, and 8 were inserted 1 in. away from the bottom of the mold, in the lower sections of the mold. Thermocouples 1, 4, and 7 were inserted in the midsection of the mold, at locations just above the thermocouples inserted in the lower sections. The locations of different regions for heat transfer boundary conditions are also identified in Figure D-22. . Four different heat transfer coefficients were identified on different internal regions and surfaces (Figure D-22. ,

Table D-7).

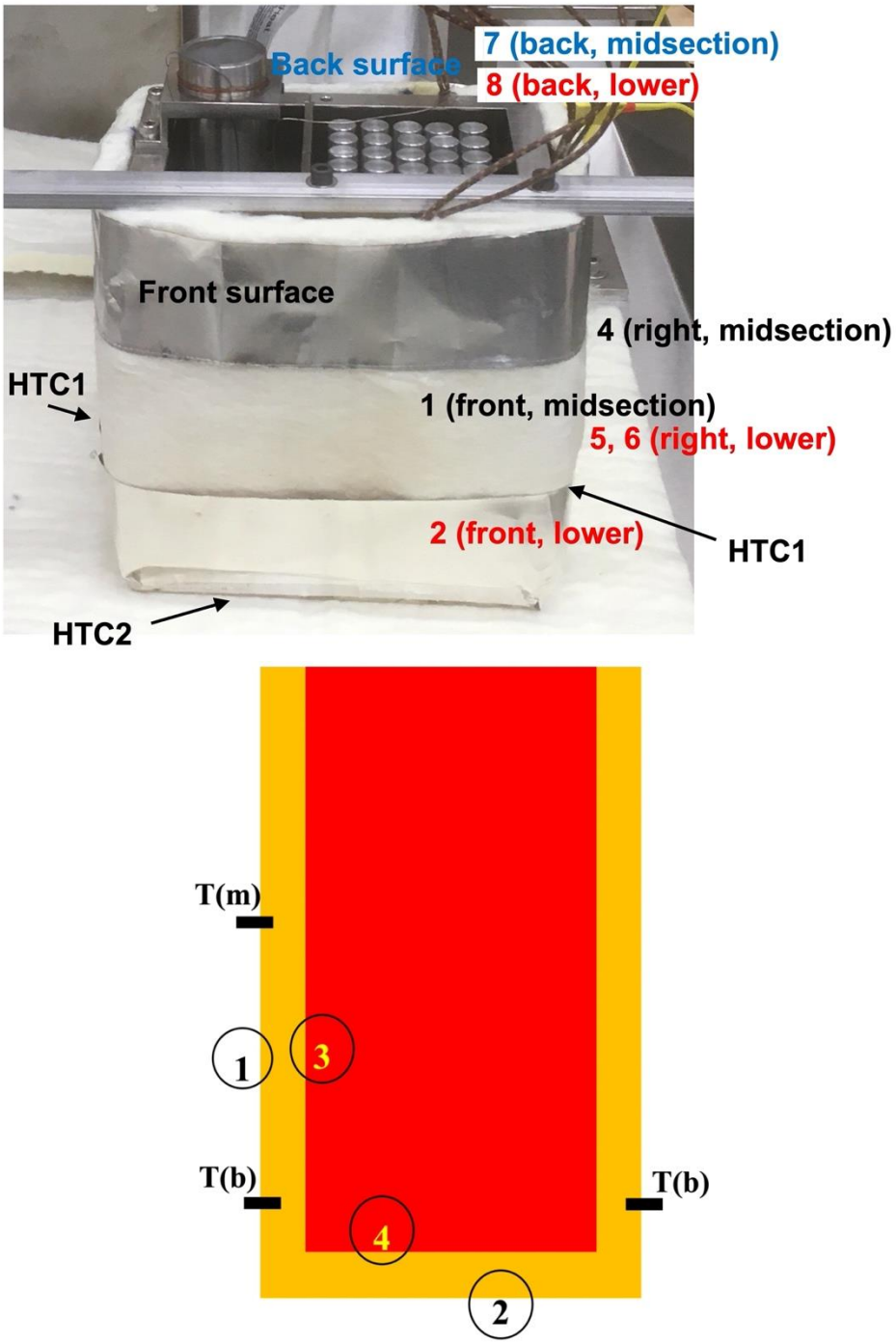

Figure D-22. Thermocouple placement and identification of cooling conditions: (top) picture with empty mold and placement of thermocouples 2, 5, 6, 8 (lower) and 1, 4, 7 (midsection), and (bottom) schematic of model setup identifying 4 types of boundary conditions and thermocouple placement in the lower region (b) or midsection (m).

Table D-7 Heat transfer coefficients (HTCs) considered in the simulation.

No.	Region	Considerations/Assumptions/Notes
HTC_1	Around the mold circumference	• HTC_1: will be determined based on the air cooling + insulation effects • HTC_1: recommended start value of 4.7 W/(m^2K)
HTC_2	Between the mold and table/tray support	• HTC_1: the contact surface is pressed by the casting weight • Insulation is compressed under the casting weight, increasing insulation thermal conductivity
HTC_3	Metal–mold interface on vertical sides	• Based on metal casting in permanent mold, a starting value of HTC_3~1,000 W/(m^2K) can be recommended
HTC_4	Metal–mold interface; at the bottom	• HTC_4 > HTC_3– as the contact pressure at this metal-mold interface is much higher than side surfaces due to the casting weight • Initial value: HTC_4~ 2 HTC_3

The measured temperatures in the mold and melting pots are shown at two consecutive data points at the onset of pouring in Table D-8. At the onset of pouring, the data show that the mold temperature, as measured by Thermocouples 1–8, varied between 283 and 294°C, with a mean temperature of ~290°C. Hence, the initial mold temperature was assumed to be 290°C in the numerical simulations, whereas the temperature measured in the melting pots was ~390°C (mean temperature of Thermocouples 11–12).

Table D-8 Measured temperature at the onset of pouring in the mold (Thermocouples 1–8) and melting pots (Thermocouples 11 and 12).

*Time [s]	Thermocouple								
	1	2	4	5	6	7	8	11	12
0	282.8	288.3	290.8	287.9	290.6	293	294.1	401.4	383.7
1	282.7	288.2	290.7	287.8	290.5	293	294	402	374

*time since onset of pouring

D-2.3 Analysis of Measured Temperature

The temperature evolution obtained from experiments is analyzed in this section in order to extract useful data that can be used to understand the metal casting process. Before presenting the temperature data, some additional information on thermocouple placement must be mentioned. The thermocouple tips were braided, their ends were beaded, and they were inserted in holes which were drilled with a 1.52 mm drill bit. Therefore, the thermocouples could not be inserted all the way into their holes, and thermocouples did not touch the mold (Table D-9). This may have affected the thermocouple reading. For the slow cooling rates, the artifacts in thermocouple contact/placement may have been minimized, but the implications of thermocouple type, construction, and placement must be investigated further to ensure the appropriate accuracy for this application.

Table D-9. Thermocouple wire length and drilled hole.

Thermocouple No.	Hole length [mm]	Length of thermocouple wire [mm]
1	7.6	4.7
2	7.3	5.8
3	7.5	5.5
4	7.6	6
5	7	5.7
6	5.4	4.7
7	8.7	7
8	8.6	6.8

In Figure D-23. , the temperature evolution for the first 1,000 seconds is shown for Thermocouples 2, 5, 6, and 8, which are located in the lower part of the mold (1 in. away from the support surface). In short notation, Thermocouples 2, 5, 6, and 8 were labeled as follows, based on their locations:

- FB2: Front face Bottom location (Thermocouple 2)
- RB5: Right face Bottom location (Thermocouple 5)
- RB6: Right face Bottom location (Thermocouple 6)
- BB8: Back face Bottom location (Thermocouple 8)

Data from thermocouple on the bottom of the mold could be used to identify the heat transfer conditions on the bottom of the mold and with the ambient air. However, since the thermocouple location was mainly close to the corner of the mold and away from the metal–mold interface, the information provided by these thermocouples for obtaining HTC1 and HTC2 may be of limited usage.

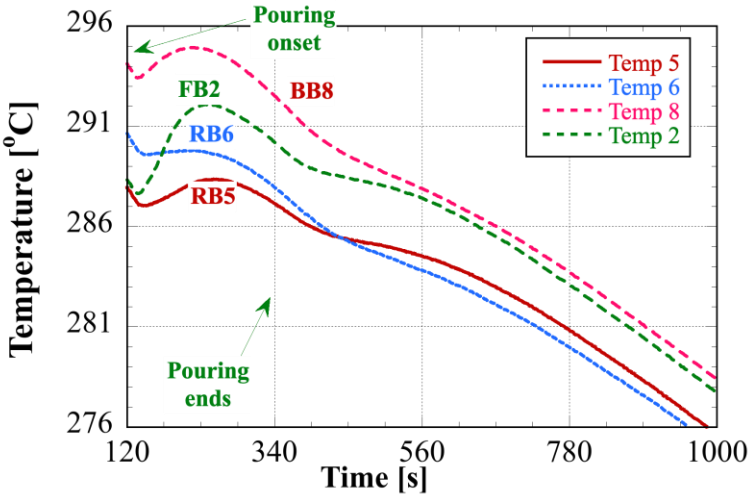

Figure D-23. Measured temperature data using Thermocouples 2 (FB2), 5 (RB5), 6 (RB6), and 8 (BB8).

In Figure D-24.(a), the temperature evolution for the first 1,000 s is shown for Thermocouples 1, 4, and 7, which are in the midsection of the mold. In short notation, Thermocouples 1, 4, and 7 were labeled as follows, based on their locations:

- 1 (FM1), 4 (RM2), and 7 (BM7).
- FM1: Front face Midsection location (Thermocouple 1)
- RM4: Right face Midsection location (Thermocouple 4)
- BM7: Back face Midsection location (Thermocouple 7)

Data from thermocouple in the midsection could be used to identify the heat transfer conditions with the ambient and metal–mold interface. However, since the thermocouples were 7 mm away from the metal–mold interface, the information provided by these thermocouples for obtaining HTC1 may be of limited usage. The plateau in the temperature profile evidenced in Figure D-24.(c) indicates that isothermal solidification occurs in the casting.

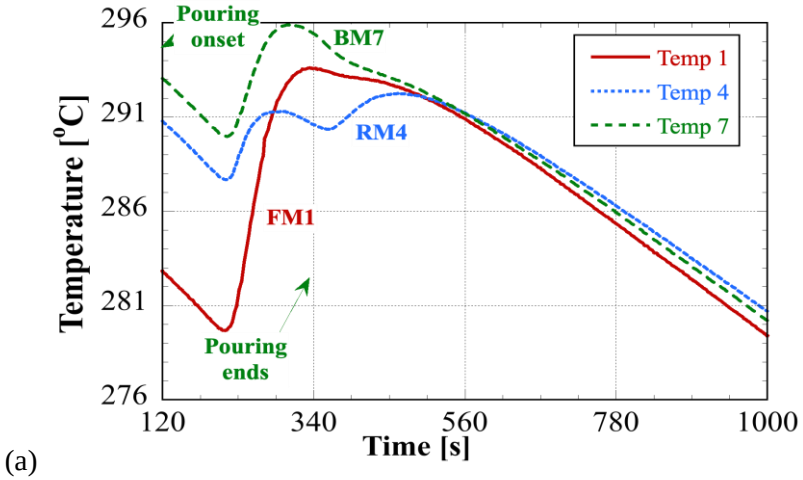

(a)

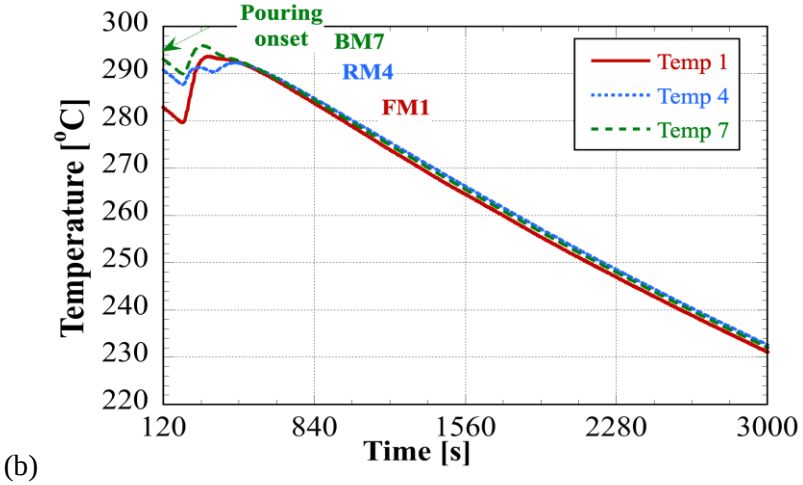

(b)

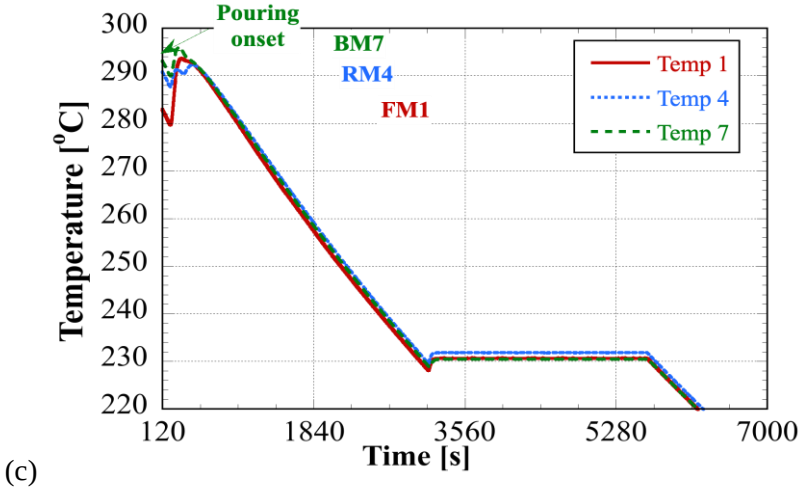

(c)

Figure D-24. Measured temperatures using thermocouples 1 (FM1), 4 (RM2), and 7 (BM7) for time ranges of: (a) 120–1,000 s, (b) 120–3,000 s, and (c) 120–7,000 s.

In Figure D-25. , the temperature is shown in the casting at Thermocouples 9, MH and 10, FPB, for the entire pouring and solidification domain. The isothermal solidification plateau is also evident.

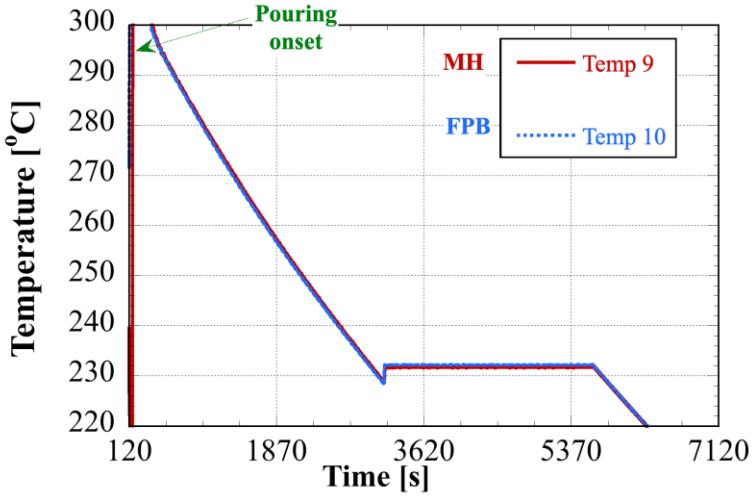

Figure D-25. Measured temperatures in the casting using Thermocouple 9 (MH) and 10 (FPB) for the entire pouring and solidification domain.

D-2.4 Numerical Simulation Cases Considered

An analysis of the heat transfer conditions for metal casting simulations is presented in Section D-3.5. The heat transfer conditions can be imposed using Heat Transfer Coefficients (HTC) at mold surfaces and/or interfaces between various materials in the mold assembly and metal-mold interface. As discussed in Heat Transfer Boundary Conditions for Numerical Simulations, the heat transfer conditions were not uniquely specified because each of the HTCs can vary over a certain range. To identify the values for all the HTCs that are appropriate for the experimental conditions considered, several simulations were conducted, as shown in Table D-10. The correct identification of the appropriate HTCs for the simulations is very important for validation of the entire simulation of the metal casting process [4, 5]. As a first step towards accurate metal casting simulations, the stress analysis model for casting solidification was not included in this study. The cooling conditions identified in Table D-10 are a starting point and are not finalized. An example of the functional definition for the HTC, namely HF1(T, Tmax, Tmin), which is used account for the temperature variation during casting solidification, is indicated in Table D-7. The data from the simulations will be analyzed to identify other possible HTC configurations that were not considered in these preliminary simulations. The results presented in this section are preliminary.

Table D-10. Cases run in ProCAST for various cooling conditions.

Case	HTC1 W/(m^{2}K)	HTC2 W/(m^{2}K)	HTC3 W/(m^{2}K)	HTC4 W/(m^{2}K)	T_{pour} [°C]
A	4.7	60	750	750	393
B	1.5	60	500	500	393
C	4.7	40	HF1(T, 500, 200)	HF1(T, 800, 200)	393
D	1.5	20	HF1(T, 500, 200)	HF1(T, 800, 200)	393
D1	1.5	20	HF1(T, 500, 200)	HF1(T, 800, 200)	$T_P(t)$
C1	4.7	40	HF1(T, 500, 200)	HF1(T, 800, 200)	$T_P(t)$

Table D-11. Definition of HF1(T, max, min) function values used to describe HTC temperature dependence from maximum (max) values at high temperature to minimum (min) values at low temperature.

Temp [°C]	Value
310	max
300	max
237	max
232	*A1
220	min
100	min

*A1=300 W/(m^2K) for function HF1

The data for case 4 are presented in the remainder of this section. Temperature-dependent thermal and fluid properties for tin were considered. Liquidus temperature was set to 236.85°C, and solidus temperature was set to 231.85°C. An example of temperature distribution during mold filling is shown in Figure D-26. The location of thermocouple placement is identified in the mold with white dots. Simulation results were obtained at the same locations where Thermocouples 2, 5, 6, and 8 were placed and are shown in Figure D-27. Compared to experimental results shown in Figure D-23. , the simulation results show higher temperatures, by 20 °C, although the variation is qualitatively the same. Simulation results at locations where temperature was measured in the midsection of the mold are shown in Figure D-28. The simulation results shown in Figure D-28. (a) indicate that higher temperatures were predicted than those shown in Figure D-23. . However, the qualitative temperature variation is in good agreement with the experimental data shown in Figure D-24.(a).

To aid the convergence of simulations of already very complex fluid flow and thermal models, the solidification interval was considered to be 5°C (~232–237°C), and the tin phase change occurs isothermally at 232°C. This solidification interval can be further decreased in the numerical simulations to reproduce a plateau like the solidification signature seen in Figure D-24.(c). Simulation results for temperature the mid-section (Figure D-37(b)) and in the casting (Figure D-29.) qualitatively reproduce the solidification signature observed experimentally in Figure D-24.(c) and Figure D-25. , respectively. Since the results are preliminary, a combined figure with experimental and simulation results was not provided. For final simulations, combined figures with both experimental and simulation results will be provided.

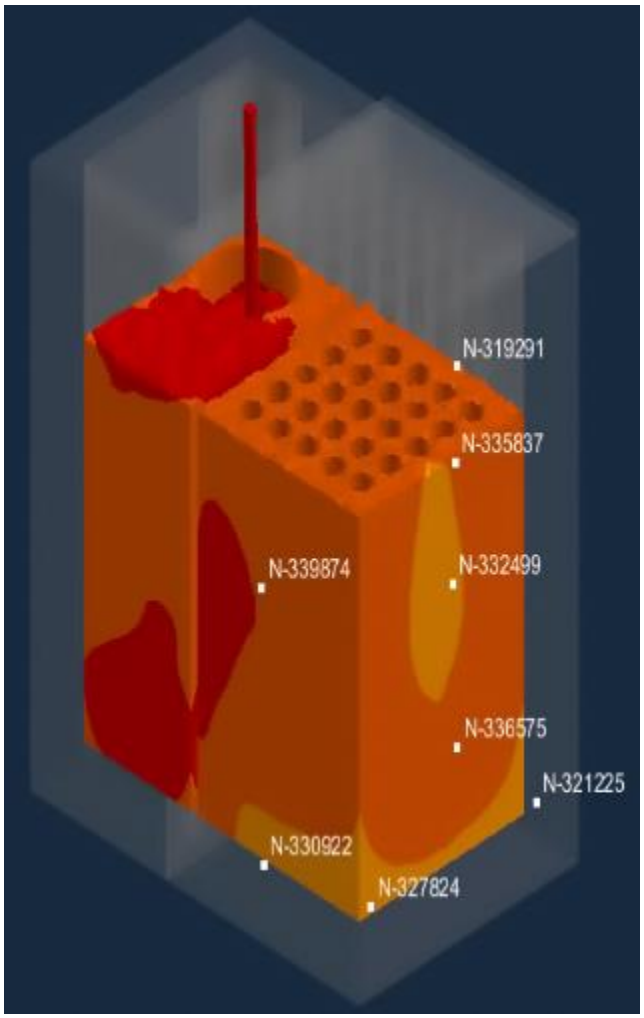

Figure D-26. Snapshot of temperature distribution during mold filling. Location of thermocouple placement is identified.

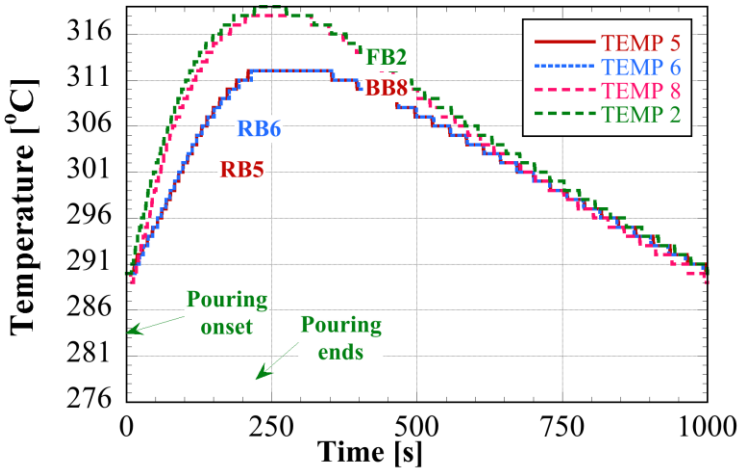

Figure D-27. Simulation results for case D lower section temperatures that qualitatively reproduce the heating and cooling observed experimentally.

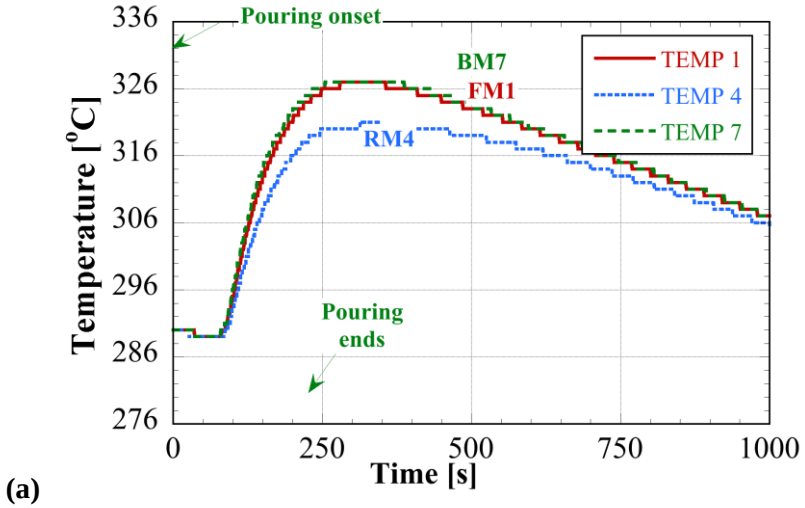

(a)

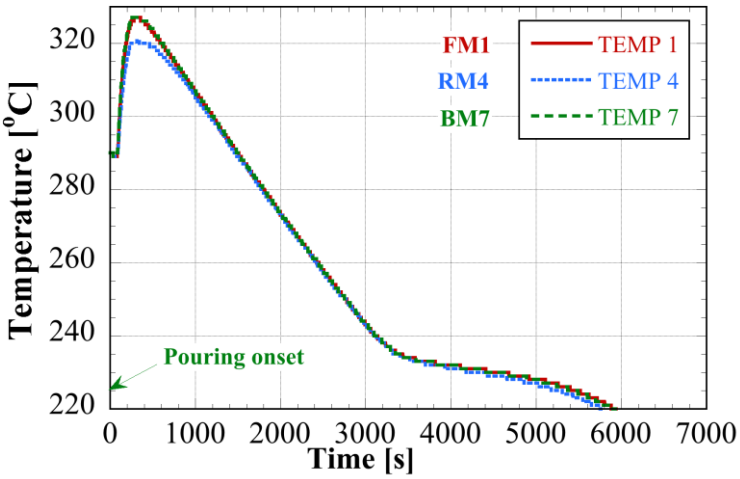

(b)

Figure D-28. Simulation results for case D at the midsection level that qualitatively reproduce the heating and cooling observed experimentally for time ranges of (a) 0:1000 s and (b) 0:7000 s.

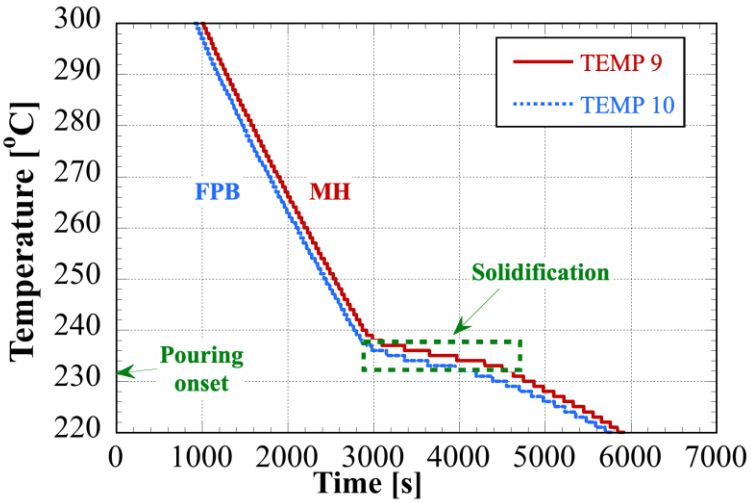

Figure D-29. Simulation results for case D in the casting at thermocouple locations 9 (MH) and 10 (FPB) for the entire pouring and solidification domain.

D-2.5 Heat Transfer Boundary Conditions for Numerical Simulations

To conduct numerical simulations of the metal casting with the cooling conditions detailed in the experimental section, the mold is wrapped in insulation to minimize the heat losses to the ambient air. The insulation keeps the mold hotter before pouring begins, attains a more uniform mold temperature, and increases the metal solidification time. The insulation effect was included in HTC1 through its thickness, x_I, and thermal conductivity, k_I, as:

$$\frac{1}{h_1} = \frac{1}{h_a} + \frac{x_I}{k_I}, \tag{5}$$

where h_a is the HTC due to natural convection in air. For room temperature, the correlations for natural convection on vertical surfaces of 6×4 in^2 indicate that h_a~5 W/(m^{2}K) [4]. The insulation used was acid-resistant silica sheet that is 0.25 in thick. As provided by the McMaster-Carr supplier, the insulation was rated with an R value of 0.3 K m^2/W, yielding a thermal conductivity of the uncompressed insulation to be k_I=0.021 W/(m^{2}K), as $k_I = \frac{x_I}{R}$. This would yield to estimate value for HTC1 ~1.7–2.4 W/(m^{2}K). Since the interface thermal contact resistance between insulation and mold was not considered in Eq. (3), in this study, HTC1 is considered to vary between 1.5 and 5 W/(m^{2}K).

Concerning the cooling conditions at the bottom of the mold (i.e., at the mold surface that is facing downward) the following considerations can be made:

- The mold is also insulated on its back surface with the same insulation that is used on its vertical sides.
- The insulation is compressed, reducing its R values from the uncompressed state.
- The insulated mold is placed on paper sheets, the paper sheets are placed on a metallic tray, and the metal tray is placed on a wooden table.

The insulation effect was included in HTC2 through its compressed thickness, $x_{c,I}$, and thermal conductivity, $k_{c,I}$, in the same manner as for HTC1. The thermal contact resistance data published in Guerin et al. (2001) for a stack of 1 to 6 sheets (from a total thickness of 0.2 to 1 mm), reported values of thermal resistance from 0.001 to 0.006 Km^2/W, respectively. These values indicate that this thermal contact resistance is negligible with respect to that of the insulation, so it was not included in this study. Thus, HTC2 can be given as

$$\frac{1}{h_2} = \frac{1}{h_{c2}} + \frac{x_{c,I}}{k_{c,I}}, \tag{6}$$

where h_{c2} is an HTC that includes thermal contact resistances between the mold and a hard surface, in absence of the insulation and paper sheets. Based on experience in permanent mold technology for metal casting, h_{c2} for metal–metal contact at low contact pressures it is considered in this study to vary between 100 and 400 W/(m^{2}K). This range can be updated later based on more experimental data. The effect of variable contact pressure through the weight of casting on h_{c2} is not considered and may need to be included. The R-value for the compressed, acid-resistant silica insulation was not available. Instead, compressed R-value charts for glass fiber insulation available from the building industry were used. Compressed R-value charts for glass fiber insulation indicate that the R-value can decrease by a factor of 0.72 when compressed to 60% of its original thickness. The ratio of the R-values between the compressed insulation, R, and uncompressed insulation, R_0, is shown in Table D-10.

Table D-12. Ratio of the R-values between the compressed insulation, R, and uncompressed insulation, R_0, as a function of compressed thickness.

Compressed thickness [%]	R/R_0
10	0.17
20	0.29
30	0.41
40	0.52
50	0.62
60	0.72
70	0.8
80	0.88
90	0.94

The HTC2 was evaluated as shown in Table D-13, considering R-value ($\frac{x_{c,I}}{k_{c,I}}$) for the compressed insulation at compressed thicknesses of 40, 20, and 10% of the original insulation thickness. HTC2 was found to weakly depend on the h_{c2}, and it strongly depended on compression of the insulation.

Table D-13. Overall HTC2 estimated at different insulation compression thicknesses.

	HTC2 (W/m^2K)		
Compressed thickness [%]	40	20	10
h_{c2} (W/m^2K)			
100	6.02	10.3	16.4
200	6.21	10.9	17.9
300	6.28	11.1	18.4
400	6.31	11.2	18.7

This page is intentionally blank

D-3. Modeling the DPC Filling and Validating the Flow Model with Experimental Results

This work follows previously performed analyses [18], [11], [12] with model validation. A more in-depth look at the computing techniques is taken, providing error quantification, phenomena identification, and a demonstration of how the approach can determine the canister residual void and the associated uncertainty. Tank filling has been studied numerically in the past, in many cases related to the automotive industry. Successful filling simulation of a car tank with hydrogen is reported by Heitsch [17] using the ANSYS-CFX code. The problem does not involve free surface, and the emphasis is on gas thermodynamics, unlike the focus of this work. The series of simulations of gasoline tank filling [20], [13] are more relevant to this work. The authors employ ANSYS-Fluent to solve the incompressible Navier-Stokes equations (NSEs), together with the VOF method, which is similar to the approach taken in this study. They show that the flow forming in the tank filling neck can be simulated with the method described above without analysis of the micro-phenomena governed by surface tension. Because the filling rates are high enough to generate turbulence, the key-epsilon (k-e) turbulence model was used.

Gasoline tank filling involves high velocities, several phases (air, liquid and gasoline vapor, mist) and interactions (evaporation). This differs from the canister filling studied in this work, in which velocities are low and phases do not interact significantly. An application of multiphase Eulerian method (separate phases) is applied to the same problem of gasoline tank filling by Greif [9]. The authors used a custom CFD software, AVL SWIFT, and solve for only two phases: air and liquid gasoline. The results demonstrate applicability of the approach with relatively low computational resources. The grid for the entire system has less than 200,000 elements, and the problem was solved using a single computing process.

The study most resembling the canister filling problem is that of Kim [19], whose study explores a little-used computing method called marker-and-cell (MAC) to track the liquid front when filling a tank from two inlets (ingates). The method of implementation results in a direct numerical simulation (DNS) on a coarse grid with explicit time advancement. The liquid kinematic viscosity was the only fluid property considered in the simulations, which seemed sufficient to model the tank filling process.

Based on this brief survey, it can be concluded that the CFD solutions of NSE, combined with the VOF method, would provide a tested computational platform and can reliably be used to simulate the canister filling process. This study validates the CFD models that have been developed and formulates approaches to quantify the error of the liquid volume calculation, which can also be used to detect an existing unfilled (void) space.

D-3.1 Mockup of the Lower Canister Region

Filling analyses were carried out on a scaled down mockup of a real canister (Figure D-30.). The mockup consisted of the following components: (1) the mouse holes region (used for validation in this work), (2) the support stands, (3) the assembly lower grids, and (4) the first spacer grid. The design used a 5×5 rod array, which is considered representative of a PWR fuel bundle. For model validation, however, only the mouse holes region of the mockup was used because it is less geometry intensive (easy to fabricate) and provides enough features to validate the computational models. It was selected as a representative geometry for the validation. To perform the experiments, this section was printed out of clear plastic by additive manufacturing.

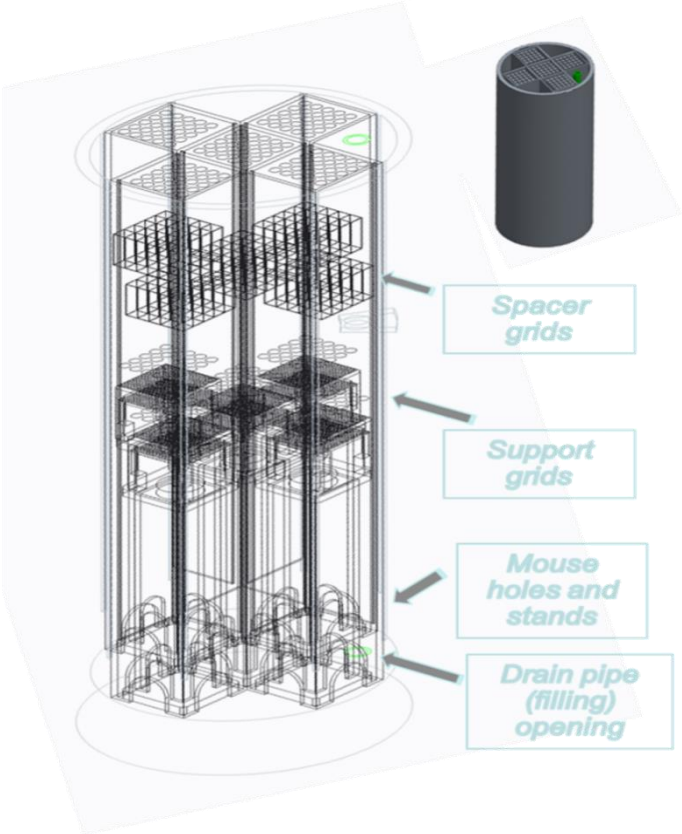

Figure D-30. Canister mockup test section, including 5 5×5 rod bundle simulators.

D-3.2 Mouse Holes Experimental Setup and Instrumentation

This portion of the canister mockup was used to perform the validation tests (Figure D-31.). It was printed from the CAD and fully matches the numerical model. The material is SOMOS water clear ultra [23], and it was printed as a single, seamless part. An outside finish and surface treatment allowed for maximum transparency. The test section instrumentation consists of a digital scale to determine the overall liquid content, two level probes, and a pump. To track the liquid line for the wetting tests, the images from a simple photograph were processed as explained below. The weight of the experimental setup was measured with OHAUS D52P125RQL5 Defender 5000 Low-Profile Bench Scale. The fixture was equipped with a digital output port that enabled real-time data acquisition. The scale's maximum capacity was 125 kg ± 5 g.

The 3D-printed fixture was placed on an elevated leg support. The horizontal position was confirmed using a digital level. A digital camera placed under the fixture looking upwards was used to take photos of the fixture bottom. Snapshots were taken at a continuous rate of 1 frame per second. Wilton food coloring was used in the water and glycerin to improve imaging contrast.

The liquids were injected with a peristaltic pump. The pump operated at ~50% speed for water testing and on full speed for glycerin. It was calibrated to produce the desired flow rate.

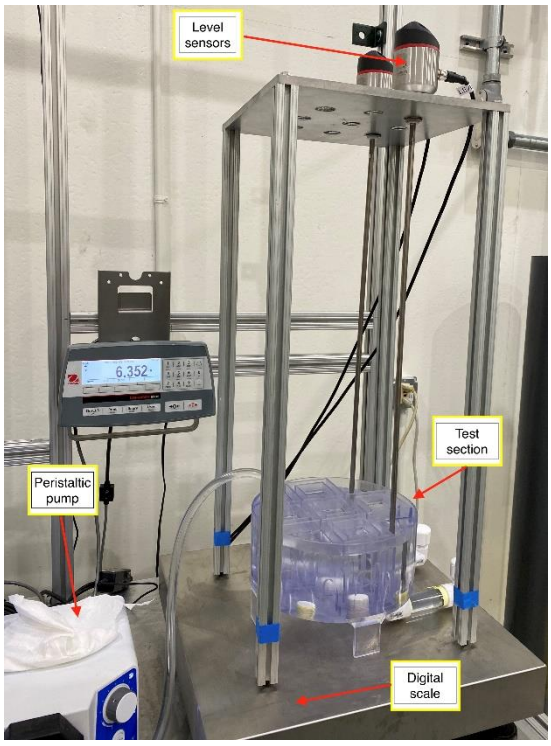

Figure D-31. Printed test fixture of the mouse holes region, a full replica of the computational model, is used to perform the wetting and level tracking experiments

Conductivity-based sensing probes (model FL-001) were used to measure the liquid level. They are suitable for detecting level of water, oils, coolants, and noncorrosive liquids. The resolution was 1 mm, and the response time was 0.4 s. The fixture's bottom plugs were removed, and extension tubes were added to accommodate the probe's dead end. The tubes were filled with liquid, the probe was set to zero, and the bottom was leveled. National Instruments cDAQ 9178 was the data acquisition system used for the level and weight readings.

D-3.3 Calibration of the Flow Rate

The peristaltic pump used in the experiments did not have a metering function, so the flow rate was determined by running a calibration test. The test fixture was weighted on a precision scale, and the result was recorded. After adjusting for water density, a linear regression of data was applied to calculate the flow rate (Figure D-32.). A rate of 11.18 cm^3/s was defined for use in the tests and simulations. Experimenting with liquids other than water required the pump flow to be recalibrated for the same flow rate. There was a bias of 3.7 cm^3, which was attributed to the regression accuracy and results in a relative error of 0.1%.

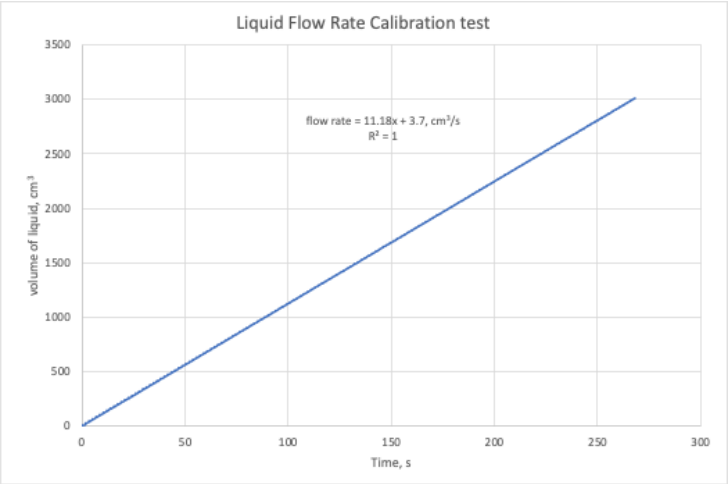

Figure D-32. Flow rate calibration test, time versus liquid volume with the resulting flow rate equation.

D-3.4 CFD Model of the Experimental Setup

The filling process was modeled as a two-phase, two-component system in isothermal conditions. The backfill gas (helium) and the filler liquid velocities were computed with a viscous flow mixture using the VOF [8] approximation. A transport equation for the liquid phase fraction, Eq. (7), was introduced, in addition to the laminar NSEs, and was solved by a segregate method. To implement this approach, the commercial software STAR-CCM+ was selected [22]:

$$\frac{d}{dt}\int_V \alpha_i dV + \int_S \alpha_i \boldsymbol{v} \cdot d\boldsymbol{a} = \int_{\boldsymbol{V}} \left(s_{\alpha_I} - \frac{\alpha_i}{\rho_i}\frac{D\rho_i}{Dt}\right) dV, \tag{7}$$

where a_i and ρ_i are the phase fraction and density, s is the phase source, n is the velocity vector, and a is the area vector.

To stabilize the solution for large time variations of phasic densities, a term was added to the right-hand side (the material derivative of the phasic density) of Eq. (7)

The liquid-gas interface was not resolved in detail because it was deemed less important for the filling of voids; therefore, the surface tension was not accounted for. This simplification allowed coarse polyhedral grids to be generated for fast computing. The calculations were performed in parallel on 24–32 compute cores.

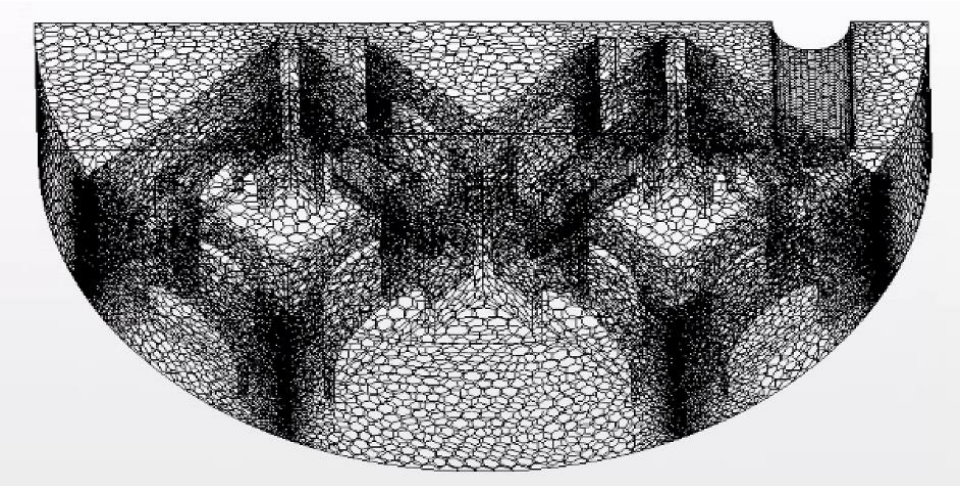

Figure D-33. Computational model and grid (coarse) for the half-symmetry model.

One half (central symmetry) of the mouse holes geometry (Figure D-33.) was modeled for the grid selection analyses, and a full symmetry was used for the final runs. Full symmetry for the main validation work was used because of the observed excessive level deformation and non-wetting of the corners formed by the symmetry plane, which was found to be a modeling artifact. The full model had a total volume of 3.032 liters. After calibration tests on the experimental fixture, a filling flow rate of 11.2 cm^3/s was defined, resulting in a total filling time of approximately 270 s. In the simulations, the geometry was not filled to the top, and only 200 s were simulated. The Reynolds number (Re) for such a filling rate and length scale was on the order of single digits (Re~3), which justifies the laminar flow assumption used in the calculations.

D-3.5 Model Validation Results

The first step in validating the computational models was to select a proper discretization grid to provide fast solution with acceptable accuracy. A grid convergence factor was not computed, but rather, the selection was based on achieving a tolerable error for a key property. The conservation of liquid volume was used as the grid selection criterion. After the selection, the model validation was performed with a single computational grid. Three liquids were used to validate the models: water, glycerin, and silicone oil. Their properties were given in Table D-14. The validation was based on the correct simulation of two phenomena: liquid front progression during surface wetting, which was defined by the viscous and surface forces, and a quantification of void detection by liquid level tracking. The second quantity was of special interest in the filling process because it was used to determine the canister's residual void.

Table D-14. Properties of liquids used for validation.

Liquid	Viscosity, Pa-s	Density, kg/m^3
Water	0.0009	997
Glycerin	1.412	1260
Silicone oil	0.339	968

D-3.6 Mass balance and computational grid selection

An important aspect of the filling simulations is to provide a conservative solution balanced with reasonable computing times. To speed up the solution, coarse grids are desirable, because they allow

larger time steps to be taken while keeping the Courant–Friedrichs–Lewy (CFL) number reasonably low. A coarse domain discretization poses questions about proper mass conservation. The liquid volume control in the system is performed during the time integration by defining a liquid volume error as shown in Eq. (8):

$$\text{VolError} = \left(1 - \frac{\int_V V_f dv}{m.t}\right) 100, \%, \tag{8}$$

where, V_f is the liquid fraction in the discretized element, m is the flow rate, and t is the time.
Three grids were generated that differed by the base size, which is a relative parameter when determining the bulk grid size. It must be noted that regardless of the grid base size, the grids were optimized and refined to capture properly the geometry details. Therefore, the actual element size varied, resulting in disproportion to the base size element count. The grids consisted of polyhedral elements. A filling transient of 200 s with water was computed on the grids with the same flow rate of 11.2 cm^3/s, and the statistic is summarized in Table D-15.

Table D-15. Summary results for the grid selection.

	Base size, mm	Number of elements, thousands	Elements per core, thousands	Total compute time, hour	CFL/ time step, μs	Highest velocity residual	Max liquid volume error, %
Grid 1, coarse	25	24	1	18	1.95/2.5	7.0e-2	1.55
Grid 2, medium	5	49	2	27	2.2/2.5	3.5e-2	0.1
Grid 3, fine	2.5	131	4	181	0.4/1	1.13e-3	0.02

The liquid volume error evolution for the entire transient is plotted in Figure D-34. . The maximum computed volume error remained below 2%, which was an acceptable value for the filling simulations. The result led to the conclusion that the optimal grid was the medium-size grid, which provided high enough accuracy and a reasonable compute time of approximately one day. All three grids provided converged solutions with comparable velocity residuals. The fine grid would be chosen for grid convergence, but because the tradeoff was a long computing time, the medium grid was selected for use in the validation study.

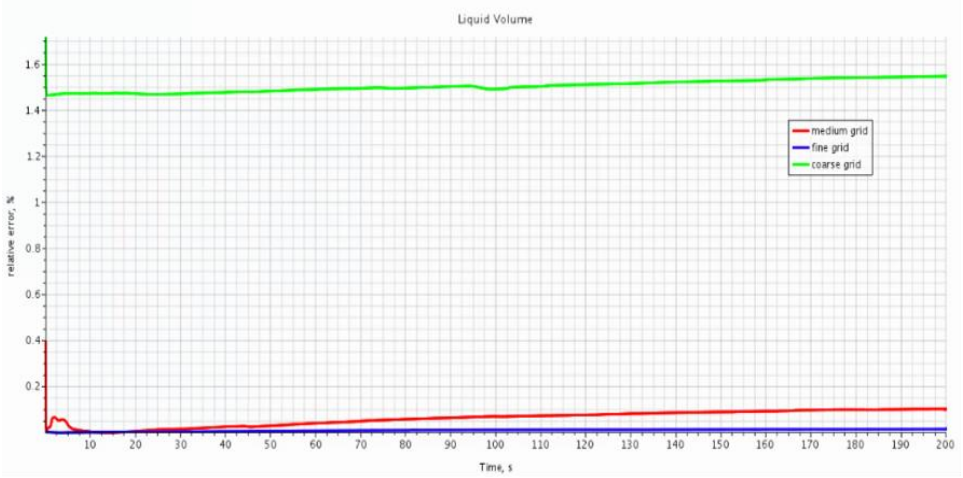

Figure D-34. Liquid volume error time evolution for coarse, medium, and fine computation grids.

D-3.7 Liquid Front Advancement, Surface Wetting

Tracking the liquid gas interface was not the primary objective of this work. However, an accurate prediction of the liquid (free) surface position is important for proper determination of the residual void. During forced injection of filler, the wetting of fuel bundle surfaces (which are quite geometry-intensive in the spacer grids area) affects the level curvature. Viscous and capillarity forces dominate the wetting process. The static and dynamic contact angles at the three-phase (solid, liquid, and gas) interface and the surface tension define the capillarity forces, which, together with the viscous forces, determine the interface position. Extensive research exploring different approaches for contact line movement is detailed by Chun [14], and Dussan [10], providing a good summary of the problem. Many studies focus on the spreading of a small amount of liquid like droplets or thin films [21] with a constant volume. However, during canister filling, a large quantity of liquid was injected by pumping or by gravity, and the surface forces may not have had a dominant effect on the overall level position. Neglecting the surface forces in the simulations helps increase the spatial resolution and substantially reduces the computational burden. Ern [7] analyzed liquid films using direct numerical simulations, and Lan [15] used the laminar VOF method, similar to the method used in this work, to simulate the film deformation caused by surface forces. The study of Lan evaluated the effect of surface forces on a gravity-driven liquid film, demonstrating that the forces modify only the film side shape and have little impact on the bulk film thickness. Furthermore, the study shows that the laminar viscous theory (used below) agrees well with the numerical results for film thickness and velocity.

To assess the importance of surface forces, a two-step approach was taken. First, the computational method employed was evaluated against a simple analytical derivation for liquid spreading caused by viscous forces only, and then an experiment was carried out to confirm that the liquid propagation in the real domain could be accurately predicted with the developed numerical models.

D-3.8 Surface Wetting Simulation and Comparison to a Simplified Viscosity Model

According to the concepts of wetting dynamics formulated by Cazabat [6], and assuming that the spreading occurs due to equilibrium between gravity (liquid weight) and viscous forces, the following expression can be derived:

$$\frac{3\mu RU}{h} = h^2 g\rho, \tag{9}$$

where R is the equivalent radius of the wetted spot, m is the liquid viscosity, U is the average film velocity, ρ is the liquid density, h is the film thickness, and g is the gravitational acceleration.

The right side of Eq. (9) is the gravity force per unit film width, and the left side is the balancing viscous force. The derivation of the left side is based on the classic Poiseuille solution for free surface (no drag) with boundary conditions u|y=0=0, and yielding a velocity distribution across the film (y-direction):

$$u(y) = \frac{G}{2\mu} 2hy - y^2, \tag{10}$$

where G is the pressure gradient, and F is the force per unit width.

The integration of Eq. (10) over the film thickness produces the average film velocity U, which leads to the expression for the viscous force in the left side of Eq. (9):

$$U = Fh/3\mu R. \tag{11}$$

Furthermore, a cylindrical (pancake) shape of the wetting spot was assumed, giving an expression for the liquid volume. The liquid volume was defined by the flow rate, which produced the relationship for the film thickness

$$h = Qt/\pi R^2. \tag{12}$$

Substituting h from Eq. (12), and provided that $U = \partial R/\partial t$, Eq. (9) can be integrated,

$$\int_0^R R^7 dR = \frac{g}{3\nu}\left(\frac{Q}{\pi}\right)^3 \int_0^t t^3 dt, \tag{13}$$

which results in an expression for the radius of the wetted spot:

$$R = \left(\frac{2g}{3\nu}\right)^{1/8}\left(\frac{Q}{\pi}\right)^{3/8} t^{1/2}. \tag{14}$$

Eq. (14) was used to evaluate the wetting progression in the numerical simulations, assuming the viscous forces dominate. This depends only on the fluid kinematic viscosity $\nu=\mu/\rho$.

A separate numerical model was developed to simulate an unbounded liquid wetting of a flat surface. The grid resolution was the same as defined above for consistency with the baseline model. Two high viscosity fluids (silicone oil and glycerin), with properties given in Table D-14. Properties of liquids used for validation, were simulated with flow rates of 5.6, 11.2 and 16.8 cm^3/s. The numerical solution produced a wet spot with an uneven shape (Figure D-36. Surface wetting spot growth, left 1 s, middle 5 s, and right 10 s). The liquid ingress occurred from below the surface in the middle.

The average radius R was obtained by calculating the projection area of the wet spot on the surface. To keep the computational domain as small as possible, only 10 seconds of the wetting process were simulated. The size of the computational grid was around 700,000 elements. A combination of two discretization schemes served for reduction of numerical diffusion and for more accurate tracking of the liquid line. The schemes were blended according to the local CFL number. For the majority (>90%) of the elements, the CFL number was between 0.05 and 1.1. The blending factor was set such that all elements with CFLs below 0.07 used first-order upwind, which was inherently bounded, and the remainder of the elements used a second-order high-resolution interface-capturing (HRIC) scheme [8]. Figure D-35. shows the results for the two liquids used. The solid lines show the nominal injection rate of 11.2 cm^3/s.

Results indicate a very good match for the low flow rate (5.6 cm3/s). As the flow rate increased, the discrepancy grew most evident for the case of glycerin. This difference can be attributed to an increased advection as the flow rate increases. In the CFD solution, a full set of NSEs was solved, whereas the analytical expression was based only on a laminar viscous flow. Another factor was the surface shape, which varied in the numerical result. Both combined in a more favorable manner for the silicone oil as seen in Figure D-35. This analytical experiment demonstrates that the numerical method (e.g., VOF implementation, spatial discretization, time-dependent solution) produces results which agree reasonably well with an analytical model of viscous liquid spreading when the surface forces are not considered.

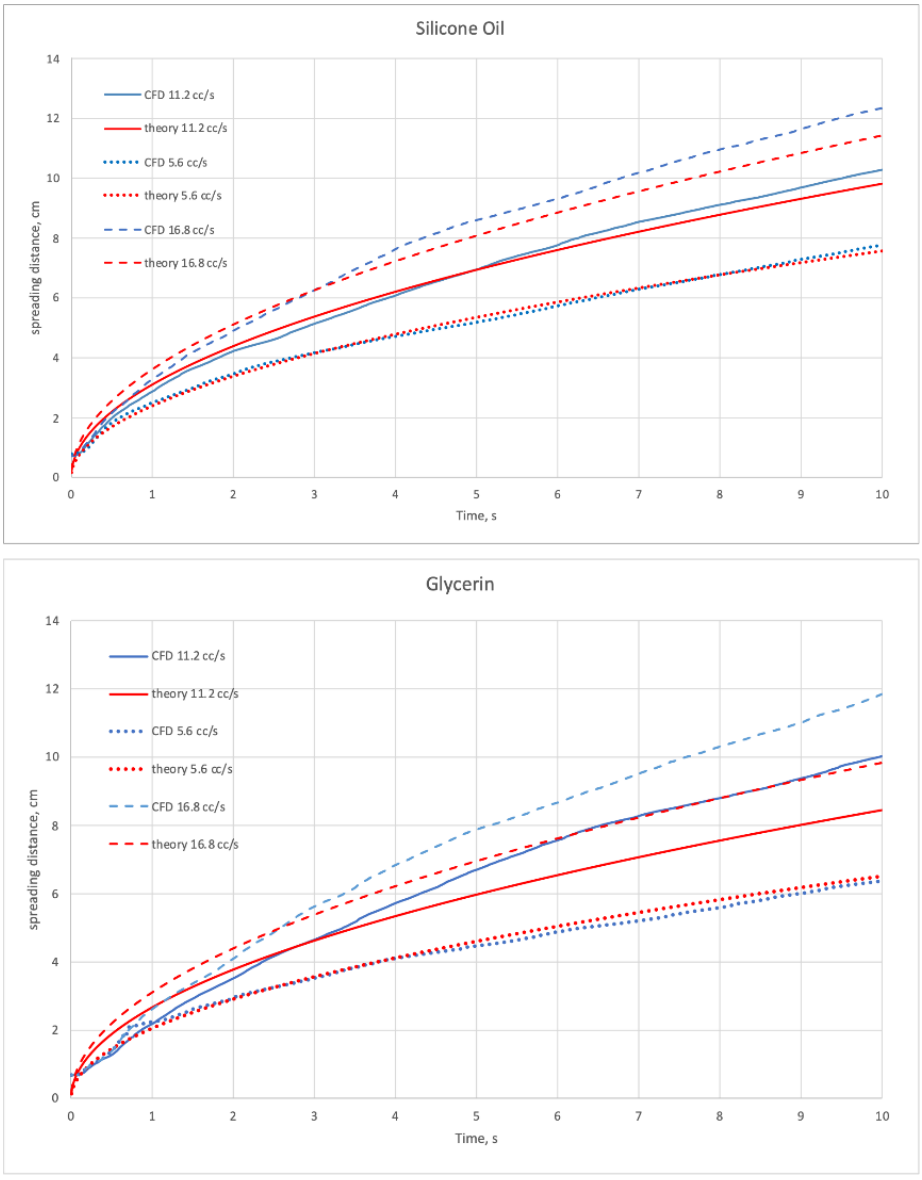

Figure D-35. Verification of numerical result by simplified viscous analytical model of wetting dynamics. Two viscous liquids were simulated with three flow rates. The top plot shows results for silicone oil, and the lower plot shows results for glycerin.

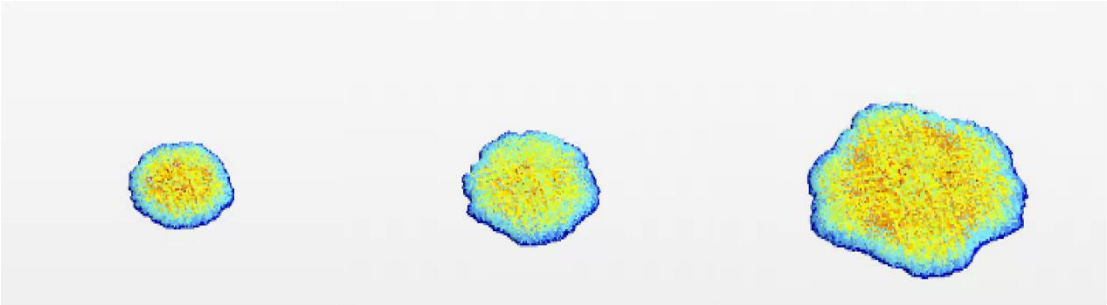

Figure D-36. Surface wetting spot growth, left 1 s, middle 5 s, and right 10 s.

D-3.9 Experimental Verification of the Liquid Front Propagation in the Real Domain

To further verify the model prediction of surface wetting, a short experiment was conducted using the test fixture, as explained in section D-3.2. Two liquids (water and glycerin) were injected with nominal (11.2 cm^3/s) flow rate until the lower bottom surface was fully covered. The liquid line was tracked by photographing the fixture from below. A small amount of colorant was added to improve the contrast without affecting the liquid properties.

Numerical simulations of the same process were also performed, and results were compared by image processing. Both the experiment and the simulation data were exported (from the camera and from the simulation) as images with a predefined resolution. A python script was written to read the images at the pixel level, to recognize the wetted area by color capturing, and to calculate the surface. The script used python image libraries (PILs) to perform these operations [16]. After appropriate cropping around the bottom outer boundary, the relative coverage was calculated. Several sensitivity calculations were run to determine the accuracy of this method, which was lower for the photography because of a larger color dissipation and was higher for the simulation because of the single color used for marking the wet spot. By varying the color identification thresholds, a maximum of 5% coverage uncertainty was calculated.

Different viscosities require different times for the liquids to cover the fixture's bottom surface. The liquid line moves quite different ways in each case. The results for water are shown in Figure D-37.. The calculated surface coverage is shown on the left. The right side shows snapshots of the liquid line motion at predefined times. These snapshots help to explain the differences seen in the line plots. First, the liquid goes around the periphery, and then it wets the central part, which is slightly elevated. This elevation forms a flat area on the plot (between 12 and 25 s) where the coverage does not increase until the corresponding volume is filled. In the simulation, this process is perfect, but in the test, imperfections of surface alignment cause the wetting to occur gradually, and the flat area is smeared. Regardless of these discrepancies, the total wetting times were within 2 seconds' difference. The maximum area coverage deviation was 25% during the wetting of the central elevated section.

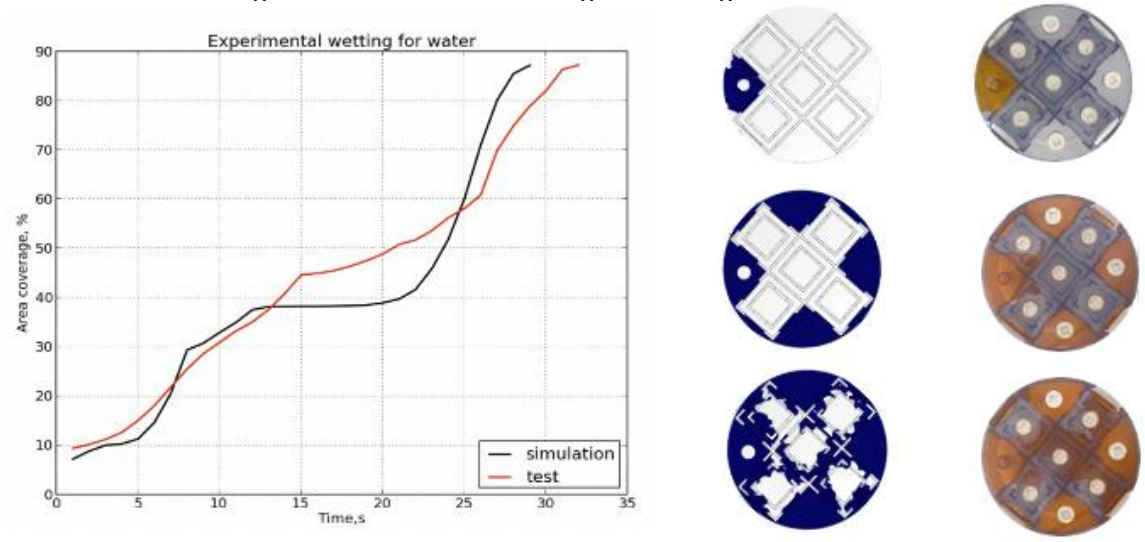

Figure D-37. Wetting of fixture bottom with water. Left: area coverage after image processing of test and numerical data (red + test, black + calculation). Right: snapshots of simulation and experiment showing the liquid line progression at 5, 15 and 25 s of the wetting process.

For glycerin, the liquid built up in the injection point and then covered the bottom evenly, regardless of topology. The liquid line progressed from the injection point to the outermost fixture boundary. These wetting mechanics caused an almost linear liquid line advancement in time (Figure D-38.). However, in the test, an almost full coverage was obtained faster, whereas the final step took longer, leading to the same total wetting time. It was concluded that this observed behavior resulted from the peristaltic pump causing pulses of liquid (expressed more strongly for the more viscous liquid), thus wetting the central section faster than expected.

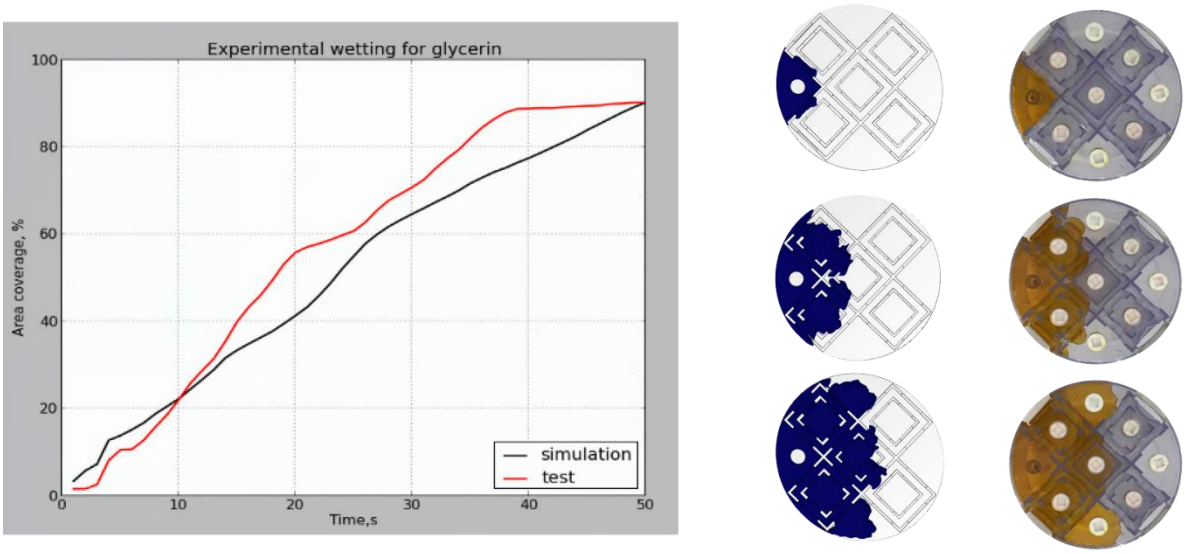

Figure D-38. Wetting of fixture bottom with glycerin. Left: area coverage after image processing of test and numerical data (red = test, black = calculation). Right: snapshots of simulation and experiment showing the liquid line progression at 5, 15 and 25 s of the wetting process.

Overall, the numerical models performed satisfactorily and properly captured the underlying physics of liquid propagation in a complex, real domain. It can be concluded that they were sufficiently suited for the purpose of simulating the filling process of spent fuel canisters.

D-3.10 Residual Void Determination, Uncertainty in the Liquid Volume Calculation

The main objective of the filling simulations is to provide a simple, cost-effective method for determining if a particular DPC is fillable and what the residual void might be. As stated above, the residual void is important for preventing the canister from becoming nuclear critical at some point after it has been permanently disposed. The method of computing the residual void (after the canister is filled) relies on the correct prediction of the liquid level during filling. If the canister's internal geometry is known, then it is possible to define a level-volume function of perfect filling. The deviation of this function from a computed one, as the filling progresses, provides a means to estimate the empty volume retention (void). Because this process is straightforward, the only quantity to evaluate for computational model validation is the liquid volume accuracy when computed by level position.

In the simulation, a level field is formulated by determining the liquid's presence in each computational element. This function is simply the vertical element position for the elements at the boundary of the liquid-gas interface. The level is not even; it has a slope defined mainly by the discretization resolution,

but also by the injection rate, type of liquid, and surface wetting. Figure D-39. illustrates the level field for the case of filling with water. The computed maximum level slope is 10 mm. This slope introduces uncertainty in the volume calculation. Assuming that the level is in a middle position between the maximum and the minimum, the liquid volume can be calculated by summing the individual element volumes that have levels below the average, as shown in Eq. (15).

$$V_{\text{total}} = \sum V_{\text{element}} \text{ if level }_{\text{element}} < \text{ average}, \quad (15)$$

where V_{total} is the total liquid volume, and $V_{element}$ is the element volume in the simulation.

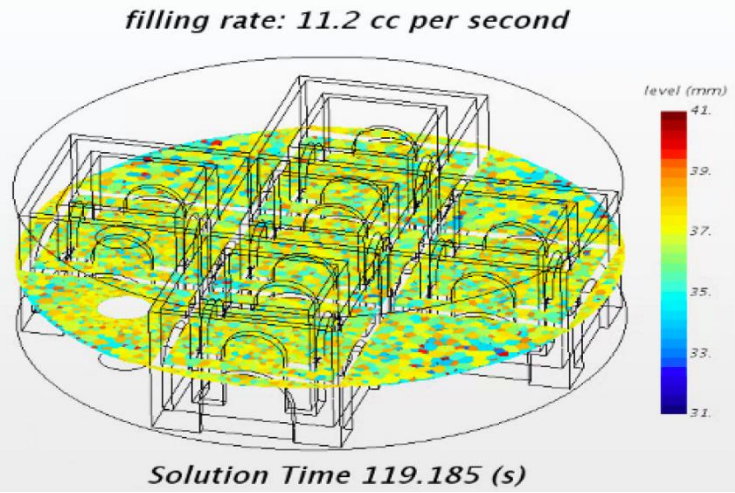

Figure D-39. Level function at an intermediate position during filling with water.

As described in Section D-1.2, level tests were carried out to validate the numerical result. Level probes were used to measure the level, and then the liquid volume was calculated according to a perfect level-volume relationship derived from a CAD drawing of the fixture. In addition, the fixture was weighed to determine the real liquid content.

Figure D-40. shows the liquid volume in the simulation as computed by Eq. (15) (red), the true liquid volume based on the actual liquid content (blue) for two liquids, water (left) and glycerin (right). For comparison, the figure also shows the test results, the weighted liquid volume (black), and the liquid volume by level measurement (yellow). The weight-based (test) and the true (simulation) liquid volumes practically coincide, whereas both level-based volumes fluctuate and are generally lower. After the initial phase of wetting the bottom of the test section (~30 s for water and ~100 s for glycerin), the difference between these volumes remains steady and does not exceed 100 ml. This result validates the simulation model and indicates that a void of more than 100 ml can reliably be detected in the test geometry.

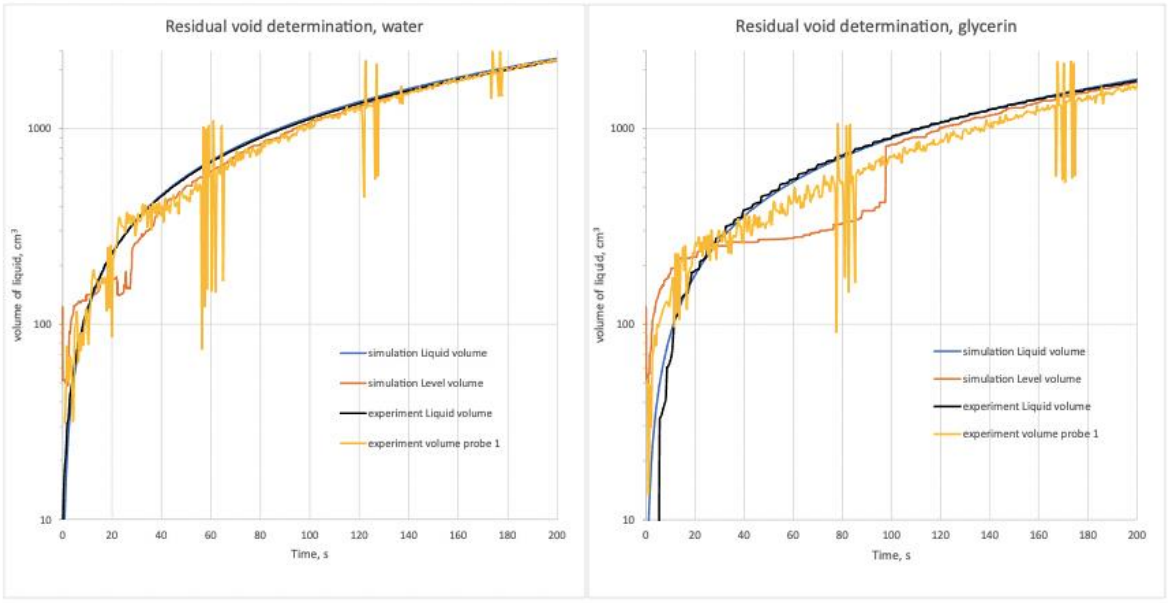

Figure D-40. Liquid volume from filling simulations with water (left) and glycerin (right) calculated by level (red line) and by liquid content (blue line). Validation results from similar experiments are shown with a black line (weight-based volume), and a yellow line (level measurement based). The difference is an absolute measure of the method's sensitivity for void capturing.

As the filling progressed, the deviation remained steady, and for the case of the totally filled domain, the deviation represents about 9%. The simulation result can be processed to compute the relative error during the level-based volume calculation. This error evolution is shown for the two test liquids in Figure D-41. . Initially, because the injection point was at a certain elevation from the fixture floor, the error was almost 100%. Then, during the phase of wetting the bottom, it was still high (30–40% for glycerin and approximately 50% for water), but it decreased gradually and fell under 10% when the fixture was fully filled. Such uncertainty is totally acceptable when providing adequate margin to criticality.

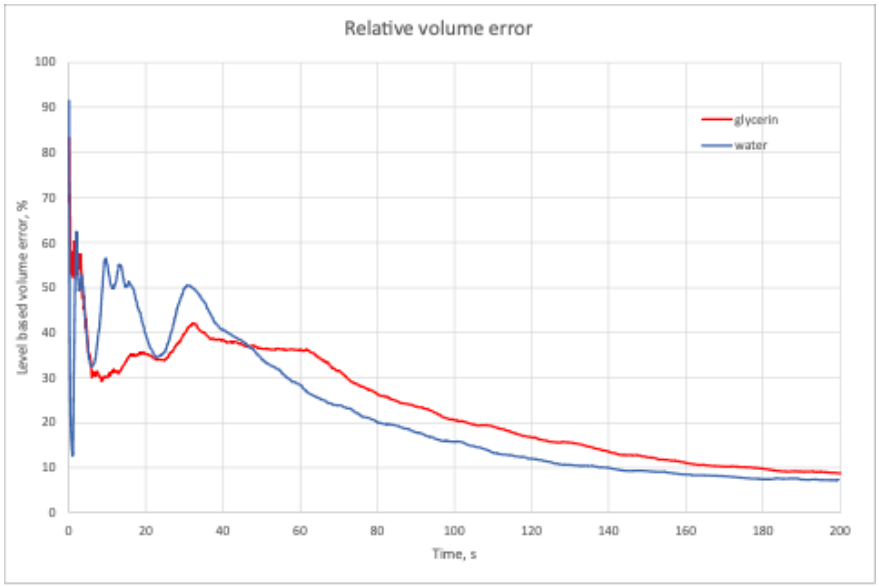

Figure D-41. Error evolution during level-based method for liquid volume calculation. The error serves as a measure of detectable void accuracy.

D-3.11 Conclusions for Validating the DPC Filling Models with Experimental Results

The objective of this work is to validate CFD models based on VOF two-phase approximation for prediction of residual void that may form during filling of DPC with liquid fillers. The problem is studied at the macro scale, so surface forces are neglected for simplification. This aspect was given special attention because it affects the level curvature, which reflects in the accuracy of void prediction. Analytical formulations and experiments were used to validate the modeling approach. Results produce errors within an acceptable range.

The developed models can also be used to simulate filling of real canisters. Experiments can be simulated first and then carried out on a real canister at ORNL to evaluate critical components which, if deteriorated from conditions during storage or transportation, could lead to formation of large, unacceptable voids during the filling with moderator displacement materials.

D-4. Fill Pipe Mercury Experiment

The design of an independent low-volume mercury loop is being addressed through the Phase II test loop experiment and will utilize the current mercury containment of the Spallation Neutron Source - Target Test Facility (SNS – TTF). Development of the Phase II test loop will enable testing of exchangeable test sections and will provide capabilities to simulate realistic flow conditions during the DPC drainpipe filling process. The mercury flow test loop is shown in Figure D-42. , and an exploded view is shown in Figure D-43. .

Figure D-42. Mercury flow loop assembly.

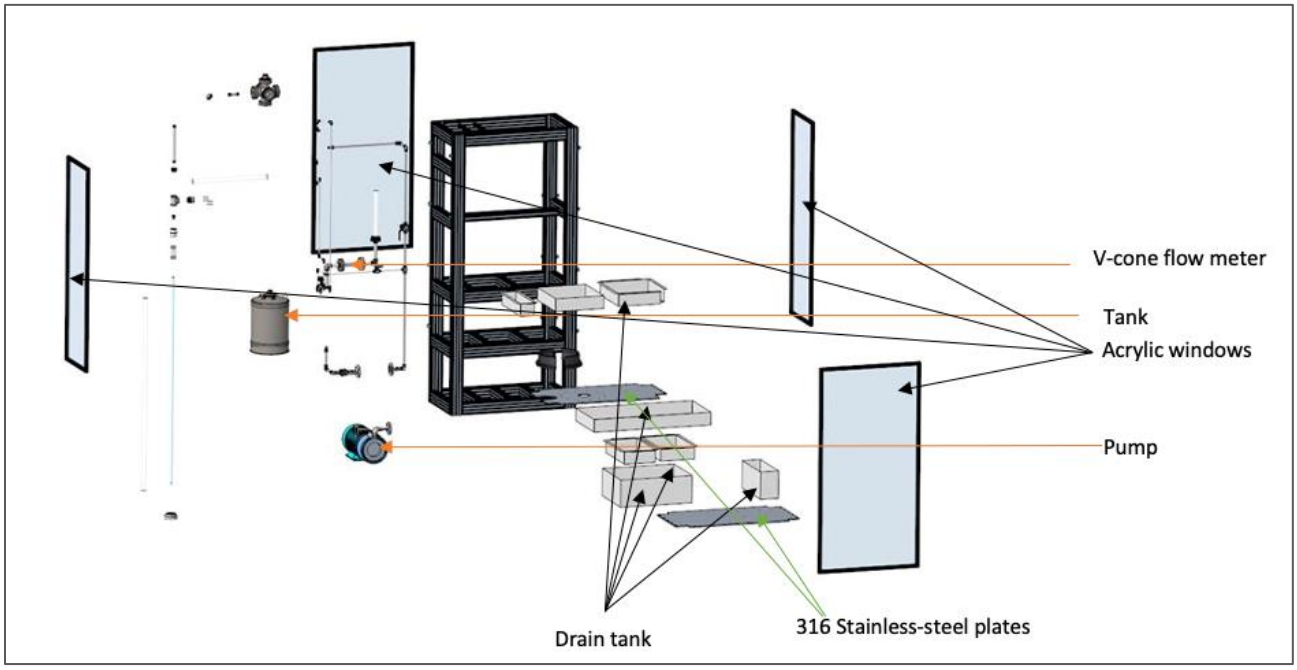

Figure D-43. Exploded view of the flow loop.

D-4.1 Mercury Loop Process Overview and Operation

Figure D-44. shows a simplified diagram of the mercury flow loop with the inner tube, outer tube, v-cone flowmeter, and the pump used to pump the mercury through the loop. The complete setup is also shown in Figure D-42. and Figure D-43. . The loop will serve as a mock-up replicating the proposed process of liquid metal flow into a DPC. Mercury will act as a surrogate for the molten metal flow in the actual DPC canister. The main objectives of this experiment are (1) to study the flow of mercury through the loop at estimated flow rates without backflow, and (2) to study vibrations and stress at different parts of the loop at varied flow rates.

The test section will be made of an exchangeable standardized stainless-steel pipe with coaxial and is contained within acrylic panel enclosures with drain tanks at different levels. The main components of the test setup, aside from the pump, will be assembled outside the TTF containment. Components that are currently in the experiment zone for the test section in the SNS-TTF mercury containment zone will be moved to a separate facility. The assembled loop system will be moved into the TTF containment area with the help of a three-member rigging crew. The roof of the TTF containment will be removed, and the assembled loop system will be placed inside the TTF containment.

An induction motor from VEMP (Russia) will be used to pump mercury into the loop. The tank and support structure of the test loop will be pressure-tested, and structural simulations will be performed. It is estimated that the test loop will require 14 US gallons of mercury, and the tank will be safely tested for 21 US gallons of mercury. The current system was deemed safe without a pressure test because it is made of 316 stainless steel, and no additional pressure tests are required because it will not be pressurized. The effect of mercury on 316 stainless steel for the duration of the experiment will be investigated.

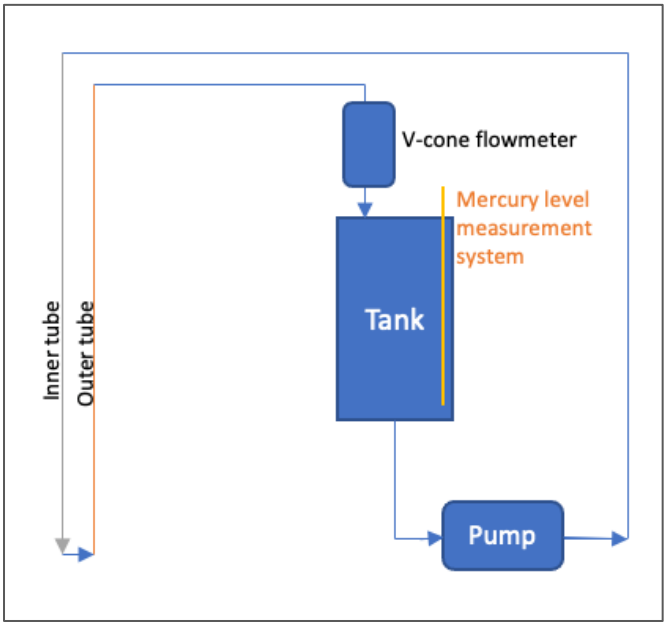

Figure D-44. Simplified schematic of the test loop.

The test section (shown with gray and orange lines in Figure D-44.) has a 43 mm gap between the bottom part of the inner and bottom parts of the external tube. The inner tube initially fills up, and then the outer tube fills where the mercury column rises. Figure D-45. and Figure D-46. show the maximum velocity and pressure zones inside the inner and outer tubes at 60 gallons per min of mass flow rate based on CFD simulations. The maximum velocity predicted in the test section is ~19 m/s and ~19.4×10^6 Pa. Figure D-47. also shows the instantaneous volume fraction contour plots with mercury flowing through the inner tube, displacing air, and rising in the external tube.

The test loop system will be reinforced with steel plates beneath the tank and the motor. One of the concerns for the experiment is the effect of the weight of mercury inside the tank, which would induce stresses on the support structure of the test loop. To remove the ambiguity surrounding the level of stresses to be experienced on the structure, a structural simulation was performed that assumed the mercury volume inside the tank to be 25 gallons.

Figure D-48. shows the contour plots of total displacement and von Mises stresses. The structural simulation confirms that the stresses generated by the 25 gallons of mercury in the tank can be sustained by the structure from the updated design of the test loop. The total deflection and stresses are also not significant enough to cause damage to the test loop support structure during the recurring cycles of experiments.

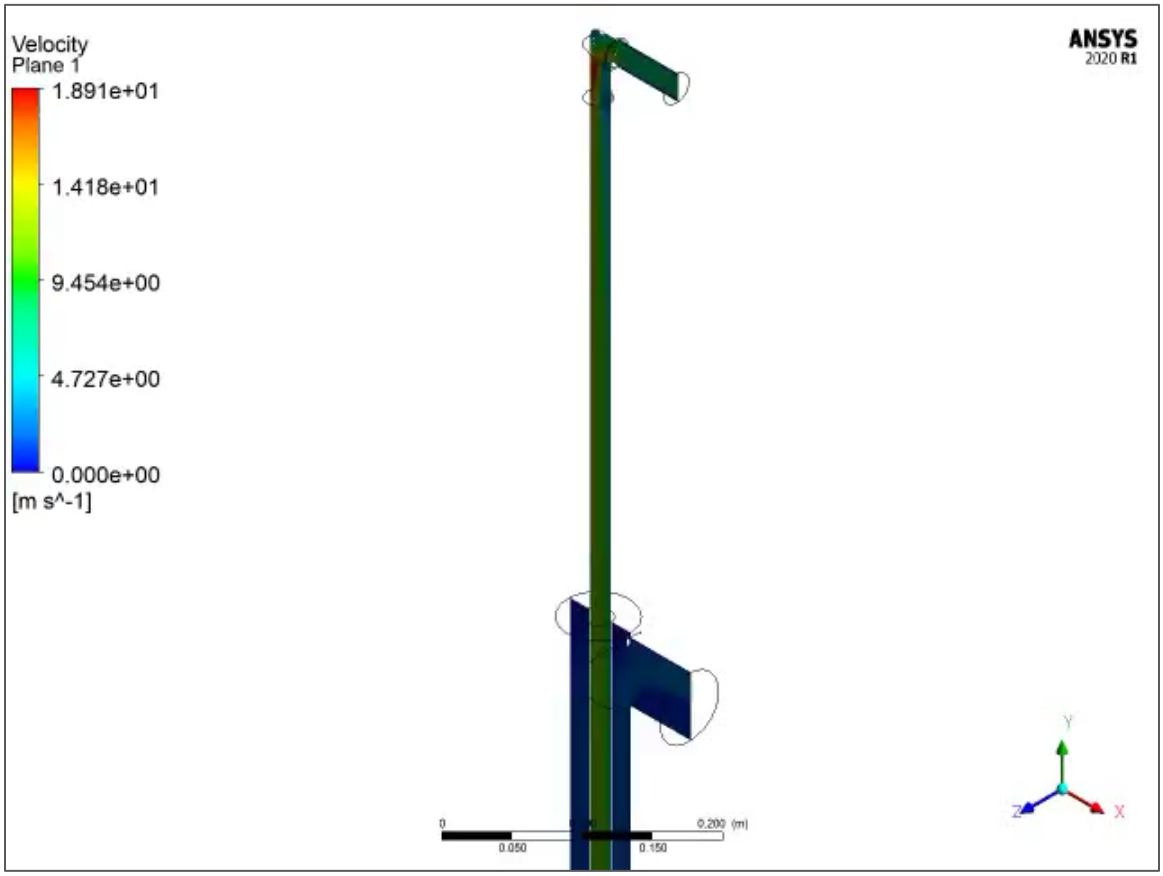

Figure D-45. Mercury flow simulation: velocity contours for mass flow of 60 gallons/min.

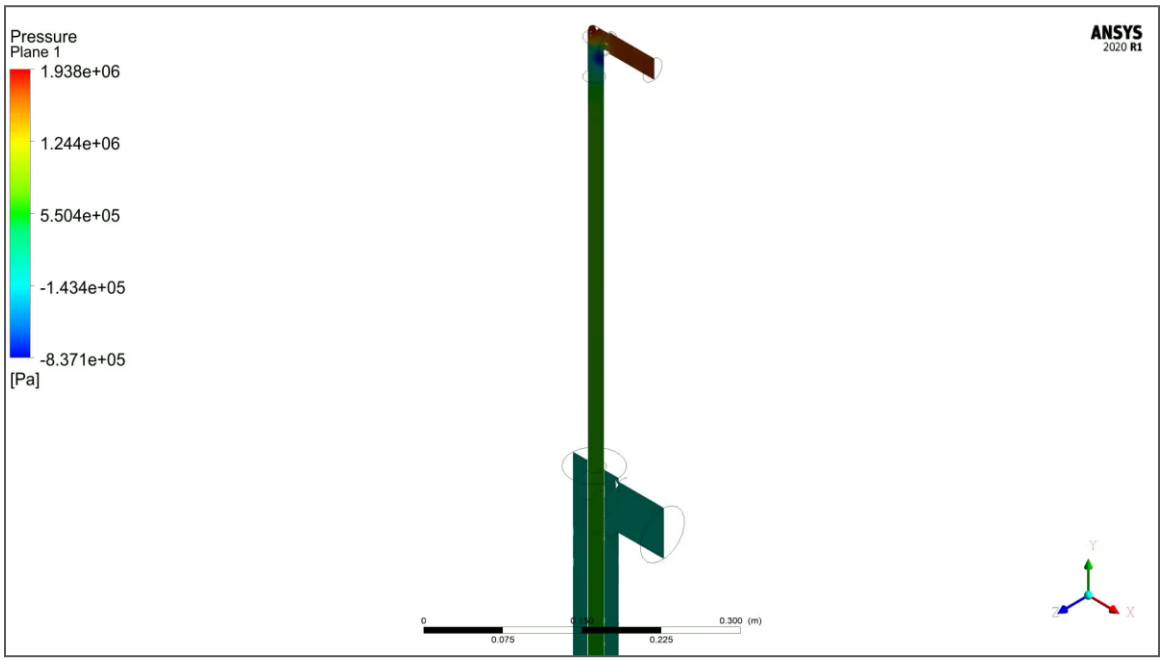

Figure D-46. Mercury flow simulation: pressure contours for mass flow of 60 gallons/min.

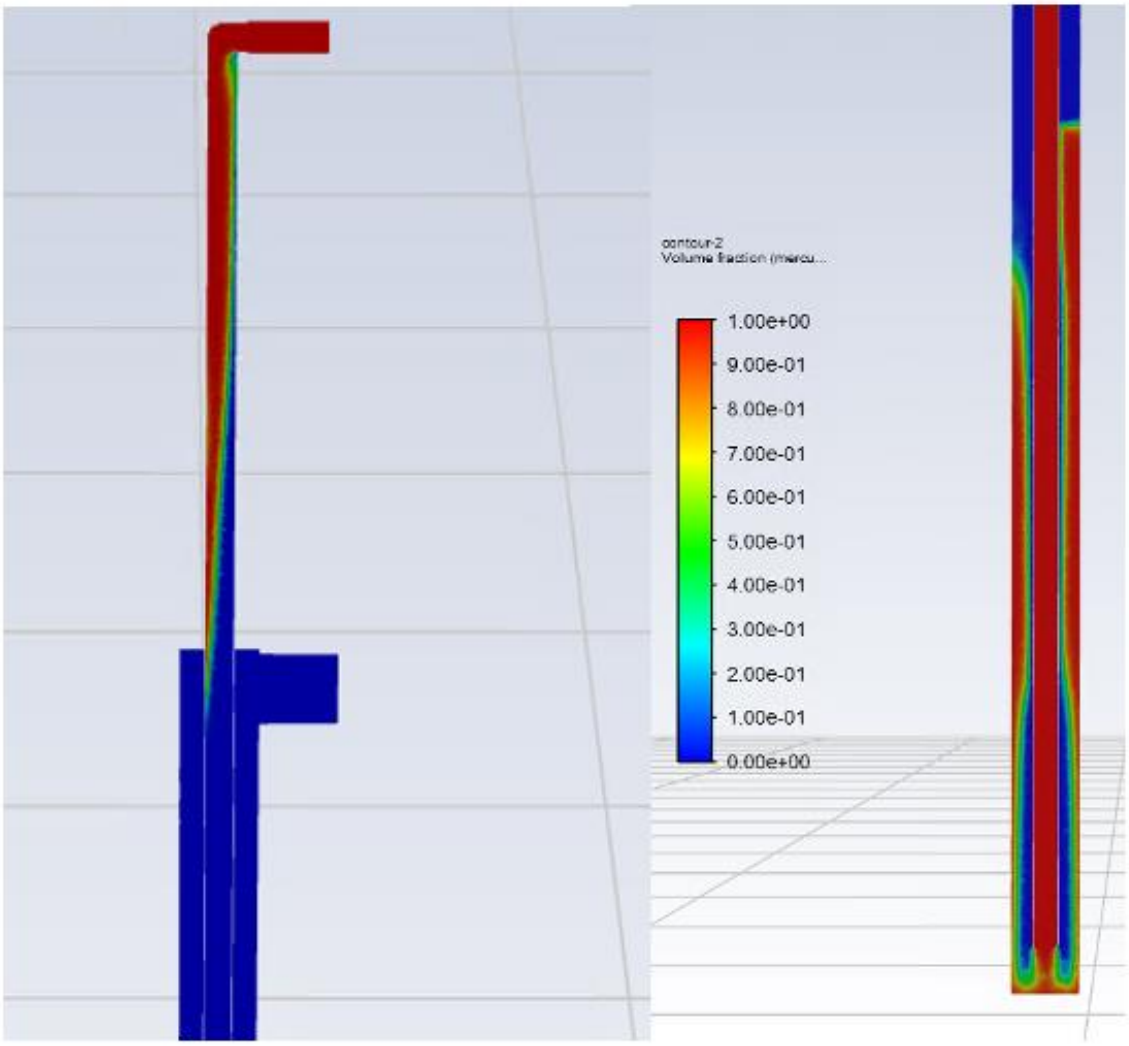

Figure D-47. Mercury flow simulation: volume fraction contour showing mercury at 60 gallons/min, displacing air inside the outer tube.

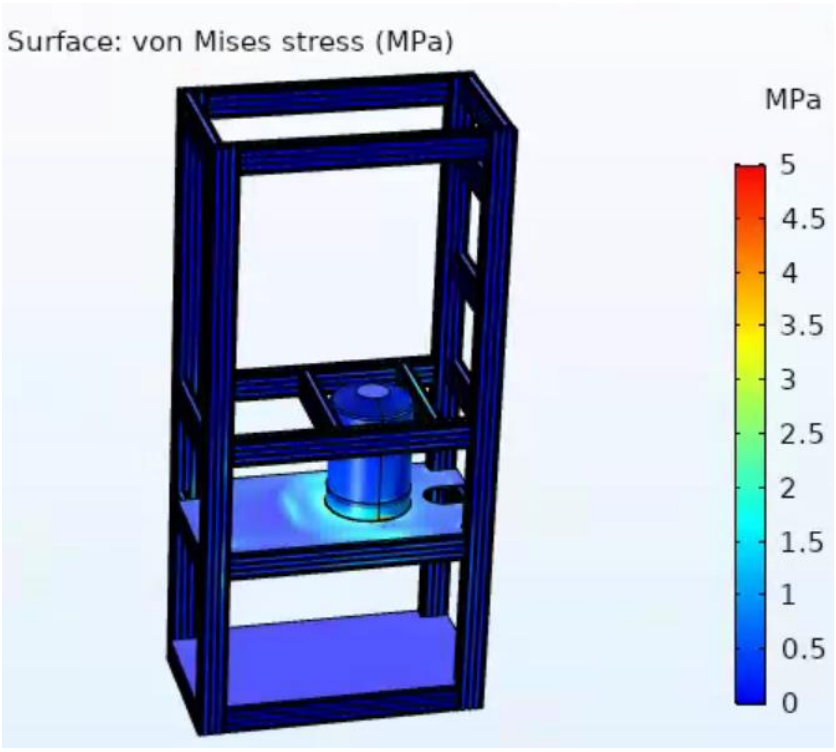

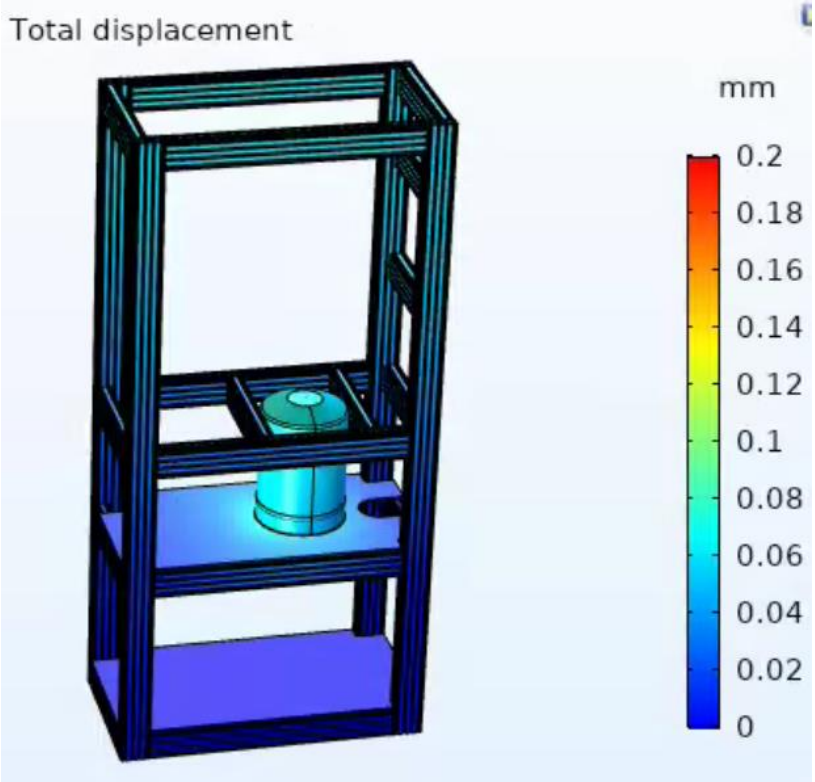

Figure D-48. Structural analysis: contour plot of displacement and von Mises stress for 25 gallons of mercury in the tank performed by Sunday Aduloju, Remote Systems Group, Fusion Energy Division.

D-4.2 Mercury Storage and Disposal

The 10.2 gallons of mercury will be transferred from its original storage container to the tank inside the flow loop using a peristatic pump.

Will be transferred back into the ORNL TTF mercury tank with the help of a peristaltic pump from the drain tap in the bottom of the external tube. It is estimated that out of the 10.2 gallons of mercury stored in the tank, less than 0.01 gallons of mercury will remain inside the loop after the loop is completely drained.

D-4.3 Experiments with the Target

The flow through the test loop will be increased in steps of 0.5 gallons per minute, with a starting flow rate of 0.5 gallons per minute. In each case, the flow rate will be monitored using a custom-built Vcone flowmeter (shown in Figure D-49.) as the flow exits into the storage tank. The level of mercury in the tank will be measured using a Keyence FL100 level sensor. The mercury will be pumped using the induction motor shown in Figure D-50. , which was developed for ORNL by the Institute of Physics, University of Latvia (IPUL), and VEMP, Russia. The motor will be controlled outside the TTF containment zone Keyence level sensor.

to protect against a breach (mercury leak) in the pipe fittings/ flanges, containment bags placed at the flange locations to contain the mercury leak. The maximum pressure in the test section pipes is expected to not exceed 20×10^6 Pascals at the maximum flow rate of 60 gallons/minute. Acrylic windows will be installed to protect against any pressure-induced leakage or high-velocity spraying of mercury from the flanges. The drain tanks will be located at different levels in the flow loop and will prevent the spilling of mercury or contamination of the TTF containment floor.

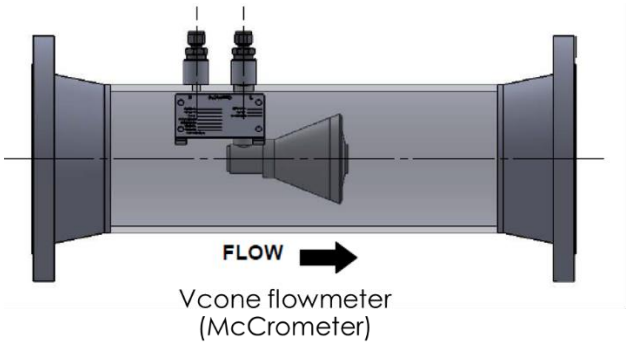

Figure D-49. Vcone flowmeter

D-4.4 Current System Status

The support structure and frame of the system is fully assembled based on an updated design. The tank for mercury storage has been altered in accordance with the provisions the National Board of Boiler and Pressure Vessel Inspection Code, and it has been welded and has completed hydrostatic pressure testing. The tank conforms to ASME code to sustain the required pressures for the experiment. The induction motor is on the lower level. The system currently is located outside the ORNL TTF enclosure where the experiments will be performed.

The system will be fully assembled outside the ORNL TTF enclosure and will be moved into the facility utilizing the existing rigging system. The mercury will be moved to the system storage tank from the TTF containment using a peristaltic pump. The wiring and connections to the electronic and electric systems with be brought out of the ORNL TTF enclosure via specific ports and will be connected to a control and monitoring system outside the ORNL TTF enclosure.

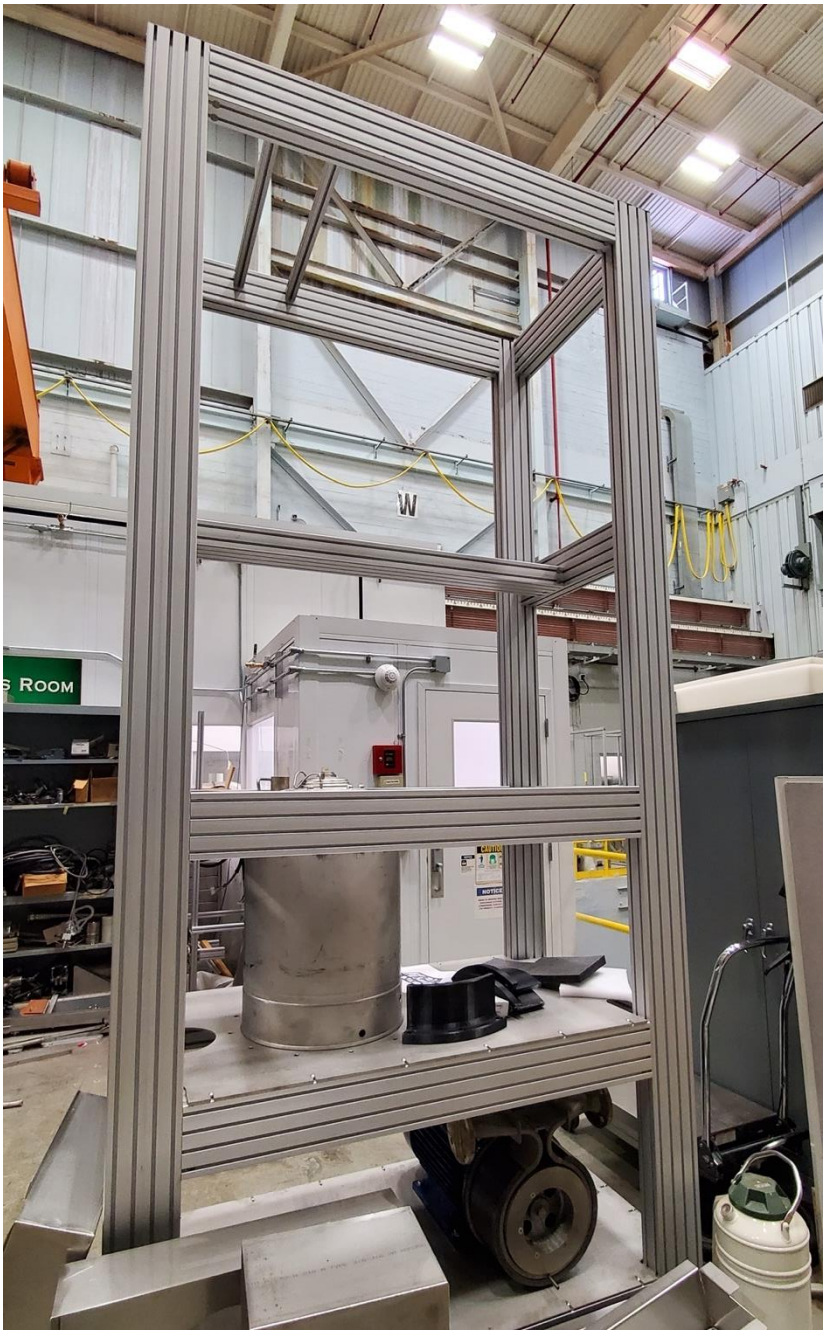

Figure D-50. Current state of assembled system outside TTF containment.

D-5. DPC Container Delivery

A DPC that was originally slated for use by the San Onofre Nuclear Generating Station in California but was never used to store spent fuel was delivered to ORNL (see Figure D-51.). The DPC is over 16 feet tall and weighs approximately 22 tons empty. ORNL is one of three national labs selected to receive DPCs from DOE for ongoing nuclear storage research projects.

Figure D-51. DPC after delivery to ORNL, still in protective covering.

As part of a multi-lab effort to explore enhancements that could extend capabilities of the canisters for the extreme long term, ORNL is exploring the use of metal encapsulation of fuel bundles. To enable this, the metal must be poured in molten form. One of the first experiments will determine whether the residual heat inside the canister containing the fuel will be sufficient to reach the required temperature of > 300ºC in about 4–5 days with sufficient insulation placed around the surface area of the canister. Analytical and numerical simulations have shown that this time frame is sufficient but demonstrating this using an actual canister will bolster confidence for the metal filling option being pursued by ORNL.

This page is intentionally blank

D-6. Future Work

The tin casting experiment and subsequent analysis demonstrates that there is little void formation, and that the voids can be detected and monitored in real time. The observed void formation was not widespread, and its location may not have significant impact on possible DPC long-term performance. Micropore defect, which is well known to occur in the last regions to solidify, is isolated and not connected with any other cracking or long void defect, such as interdendritic porosity, that would lead to any water intrusion. The formation of voids will be further analyzed to determine (1) the results of a more detailed criticality safety analysis which evaluates their impact and (2) the final material selection and potential for inclusion of neutron absorbers in the material.

This page is intentionally blank

D-7. References

1. A.S. Sabau and S. Viswanathan, "Microporosity Prediction in Aluminum Alloy Castings," *Metals and Metallurgical Transactions, B*, 2002, Vol. 33B, pp. 243–255.
2. A.S. Sabau, "Predicting Interdendritic Cavity Defects during Casting Solidification," *JOM*, 2004, Vol. 56, pp. 54–56.
3. A.S. Sabau, W.D. Porter, S. Roy, and A. Shyam, "Process Simulation Role in the Development of New Alloys Based on an Integrated Computational Materials Engineering Approach," paper IMECE2014-37982, *Proceedings of the ASME 2014 Int. Mech. Eng. Congress & Exposition* IMECE2014, Nov. 14–20, 2014, Montreal, Quebec, Canada.
4. A.S. Sabau, "Numerical Simulation of the Investment Casting Process," *Transactions of American Foundry Society*, 2005, Vol. 113, paper 05-160, pp. 407–417.
5. A.S. Sabau, "Measurement of Heat Flux at Metal-Mold Interface during Casting Solidification," *International Journal of Cast Metals Research*, 2006, Vol. 19, pp. 188–194.
6. D. Guérin, V. Morin, D. Chaussy and J-L. Auriault. "Thermal Conductivity of Handsheets, Papers and Model Coating Layers." *In The Science of Papermaking, Trans. of the XIIth Fund. Res. Symp.* Oxford, 2001, (C.F. Baker, ed.), pp 927–945, FRC, Manchester, 2018. DOI: 10.15376/frc.2001.2.927.
7. A. Cazabat, M. Stuart. "Dynamics of Wetting: Effects of Surface Roughness." S.L.: *J. Phys Chem.*, 1985.
8. A. Ern, R. Joubaud, T. Levievre. "Numerical Study of a Thin Liquid Film Flowing Down an Inclined Wavy Plane. s.l.: *HAL Archives Ouvertes*, 2012.
9. CD-Adapco. 2015. STAR-CCM+ Theory Guide. 2015.
10. D. Greif, B. Wiesler, A. Alajbegovic. "Two-Phase Tank Filling Simulations of an Automobile Tank System." MIT, ed. K.J. Bathe: *Computational Fluid and Solid Mechanics*, 2003.
11. E. Dussan. "On The Spreading of Liquids on Solid Surfaces: Static and Dynamic Contact Lines." s.l.: *Annual Rev. Fluid Mech.*, 1979.
12. E. Popov, K. Banerjee. "Dual-Purpose Canister Filling Simulation and Validation: Part I - Simulations." s.l.: ANS Winter Meeting, 2019.
13. E. Popov, K. Banerjee, J. Scaglione. "Dual Purpose Canister Filling Assessment to Support Direct Disposal." Orlando, FL: ANS Winter Meeting, 2018.
14. F. Buscariolo et al. "Multiphase Fuel Filling Simulation Methodology to Evaluate Different Filler Neck Designs." s.l.: SAE International, 2015. 36-0297.
15. H. Chun, L. Scriven. "Hydrodynamic Model of Steady Movement of a Solid/Liquid/Fluid Contact Line." s.l.: *J. of Colloid and Interface Science*, vol. 35, 1, 1971.
16. H. Lan, J. Wegener, B. Armaly, J. Drallmeier. "Developing Laminar Gravity Driven Thin Liquid Film Flow Down and Iclined Plane." s.l. : *Journal of Fluids Engineering* vol. 132, 2010.
17. "Pillow 8.3.2," Python Image Library, s.l.: https://pypi.org/project/Pillow/, 2020, accessed September 2021.
18. M. Heitsch, D. Baraldi, P. Moretto."Simulation of the Fast Filling of Hydrogen Tanks." s.l. : International Conference on Hydrogen Safety, September 16-18, Corsica, France, 2009.
19. N. Cetiner. Experimental work, personal communication. 2018.
20. N. Kim, G. Kim."The Numerical Simulation of the Water-Filling in the Water Tank with Two Ingates." s.l: KSCE *Journal of Civil Engineering*, 2007. vol. 11, 4.
21. R. Banerjee, X. Bai, D. Pugh, K. Isaac. "CFD Simulations of Critical Components in Fuel Filling Systems." s.l: SAE International, 2002. 01-0573.
22. S. Kalliadasis, H. Chang. "Dynamics of Liquid Spreading on Solid Surfaces. s.l. *Ind. Eng. Chem. Res.* 35, 1996.
23. Siemens. "Simcenter STAR-CCM+," https://mdx.plm.automation.siemens.com/star-ccm-plus. 2020, accessed September 2021.

24. Stratasys. Article: SOMOS Partnership. https://www.stratasysdirect.com/technologies/stereolithography/stereolithography-somos-collaboration. Accessed September 2021.
25. R. Tavakoli, "On the Prediction of Shrinkage Defects by Thermal Criterion Functions." *International Journal of Advanced Manufacturing Technology* 74.1 (2014): pp. 569–79. Web.
26. J. Campbell, *Complete Casting Handbook: Metal Casting Processes, Metallurgy, Techniques and Design*, Elsevier Science & Technology, 2015. *ProQuest Ebook Central*, https://ebookcentral.proquest.com/lib/oakridge/detail.action?docID=2128309.
27. E. Niyama, T. Uchida, M. Morikama, and S. Saito, Predicting Shrinkage in Large Steel Castings from Temperature Gradient Calculations, AFS Int. Cast Met. J., Vol 6, 1981, p 16–22
28. Carlson, K. D., & Beckermann, C. (2009). Prediction of shrinkage pore volume fraction using a dimensionless Niyama criterion. *Metallurgical and Materials Transactions A*, *40*(1), 163-175